Development of next generation biodegradable drug-eluting coronary artery stents

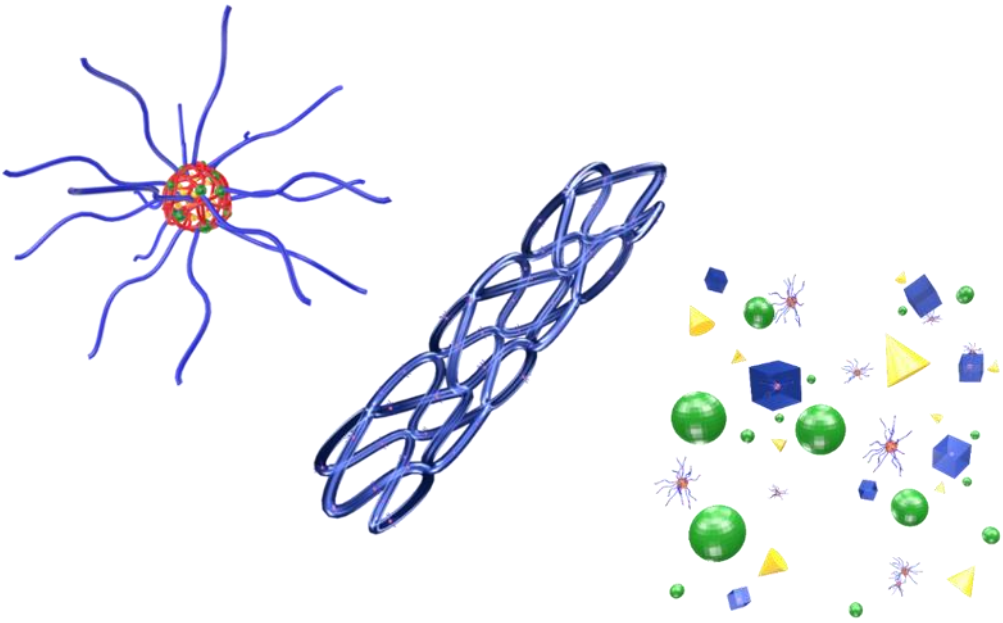

by

Katarzyna Anna Somszor

ORCID ID: 0000-0003-1510-6580

December 2019

Submitted in total fulfilment of the requirements of the degree of Doctor of Philosophy

Department of Biomedical Engineering

The University of Melbourne

Abstract

Cardiovascular diseases are a leading cause of mortality globally, causing approximately 17 million deaths annually. Additionally, this number is predicted to rise to 23 million by 2030. The most common type of cardiovascular disease is coronary heart disease, a disease of coronary arteries that supply oxygen rich blood to the heart. Coronary artery disease is the build-up of a waxy substance called a plaque inside the coronary artery which leads to its narrowing and blockage. In current medical practice, coronary heart disease is commonly treated through balloon angioplasty and stenting to open the artery. Current stents are drug-eluting, metallic, and permanent, and recipients require prolonged anti-platelet therapy. Permanent stenting is not required. The diseased vessel can heal within 6 months to 1 year after intervention. As such, the concept of biodegradable stents has emerged as the alternative to conventional stenting, in which the stent degrades away leaving behind only the healed vessel. The first generation of biodegradable stents has been linked to higher rates of late stage thrombosis, and it has been suggested that this is due to increased strut thicknesses that cause disturbance to the laminar blood flow and result in activation of thrombogenic pathways.

The aim of this thesis is to develop customizable, biodegradable, multi drug eluting coronary artery stents by using polymer chemistry, materials science, and additive manufacturing. The novel materials developed in this work are to be blood-compatible, biodegradable, have sufficient mechanical properties, promote endothelialisation, have multi-drug eluting properties, and be processable through additive manufacturing techniques. To achieve this, we used the following approaches: (1) Design and additive manufacturing of custom-made biodegradable nanocomposite based coronary artery stents via MEW (2) Design and synthesis of biocompatible and biodegradable core-cross linked star-brush polymers for antithrombotic

drugs (3) Development of multi-drug eluting biodegradable nanocomposite-star polymer materials for application as coronary artery stents utilizing MEW.

To accomplish this, we first developed biodegradable polycaprolactone-reduced graphene oxide nanocomposites with increased strength and fabricated them into stent-like structures via MEW. We illustrated that these materials have increased mechanical strength (enabling the fabrication of stents with thinner struts), that MEW is able to produce well-defined stent structures with struts as thin as 60 μm, and that we can use the technology to tailor the stent diameter, geometry, strut thickness, and strut spacing, potentiating personalised stent design.

We then designed and synthesized a class of core-cross linked star-brush polymers that exhibited hydrophobic blocks in their outer shell, hydrophilic segments in their inner brush shell and in their core. These polymeric platforms allowed the encapsulation of hydrophilic drugs without the need for conjugation of the drug to the carrier. Drug loading properties of synthesized polymers were studied using two clinically used anti-thrombotic drugs. Drug release profiles were obtained at physiological and acidic conditions. The cytocompatibility of the polymers was assessed through acute toxicity studies on human umbilical vein endothelial cells.

Finally, we developed multi-drug eluting biodegradable materials and confirmed their printability via MEW. We illustrated dual drug elution of an anti-thrombotic agent (heparin) from bulk of the material via incorporation of synthesized star polymers and elution of an anti-proliferative agent (rapamycin) from the surface via electro spraying of the outer layer. Fabricated materials were characterized in terms of their mechanical performance, crystallinity, thermal behaviour, biological interactions, degradation, and dual drug elution. These materials

were found to deliver anti-proliferative drugs in a controlled manner, slowly release anti-coagulating agents, and show excellent cytocompatibility *in vitro*.

These results illustrated the development of a biodegradable and multi-drug eluting stent prototype. A novel fabrication technique was used for the fabrication of the device and allowed for customized stents design and production of thin struts (~60 µm). Further, the use of rGO as a nanocomposite material allowed for improved mechanical strength, and the inclusion of the star polymers enabled the development of a well-defined dual drug delivery These results support the use of this novel material system and fabrication technology for the development of next generation biodegradable coronary artery stents.

Declaration

This is to certify that

i. this thesis comprises only my original work towards the PhD,

ii. due acknowledgement has been made in the text to all other material used, and

iii. the thesis is less than 100,000 words in length, exclusive of tables, figures, bibliography and appendices.

Katarzyna Anna Somszor

Acknowledgments

First, I would like to thank my supervisors, Dr Daniel Heath, Prof. Andrea O'Connor and Prof. Greg Qiao for their support and guidance during my PhD. Your experience, input, and help throughout my studies were tremendous, and I would like to thank you for believing in me, giving me the opportunity to grow academically and professionally, and always ensuring that I stay on track with my research. Each one of you provided me with your specialized knowledge and enabled me to receive the help I needed. I have learned a lot thanks to you, not only scientifically but also personally, and I am very grateful for that.

I would like to also thank Dr Fatemeh Karimi, Dr Tom McKenzie, Dr Qiang Fu for their help and support during my studies. Fatemeh, Tom, Qiang – thanks to you I was able to learn a lot about polymer science, synthesis, materials and research. Your guidance allowed me to grow and become a better researcher. I would like to thank you for being there for me when I needed your advice and support. You always encouraged me to keep on trying and never give up, especially in the moments when my research did not go well. Thanks to your kindness and generous help, I was able to progress with my project, learn new techniques and grow. I would never be able to be where I am today without your help.

Also, I would like to thank all the members from Polymer Science Group, Tissue Engineering Group, and Ellis Research Group for their support during my studies. I would like to thank Prof. Amanda Ellis for providing me with the opportunity to conduct research in her lab and supporting me in very difficult moments of my PhD. I would like to thank all members of the Polymer Science for teaching me polymer science techniques and making me feel that I belong to the group.

Additionally, I would like to thank and acknowledge researchers from Queensland University of Technology (QUT), Dr Onur Bas, Tara Shabab and Prof. Dietmar Hutmacher, for their support and contribution to this project, as well as making me feel extremely welcomed during my research visit at QUT.

I would like to express my gratitude to the O'Brien Institute of Microsurgery (Melbourne, Australia) for their kind donation of Smooth Muscle Cells for my research. I would like to thank Prof. Wayne Morrison and Associate Prof. Geraldine Mitchell for their feedback on my project while presenting my research at the O'Brien Institute of Microsurgery.

Also, I would like to thank all team members of Exopharm Pty Ltd for their endless support during my PhD and always believing in me. I would like to thank Dr Gregor Lichtfuss and Dr Ian Dixon for giving me a unique opportunity to learn about biopharmaceutical field from a commercial perspective while pursuing my PhD. Gregor, you have been a great mentor and one of my biggest supporters – thank you for believing in me from day one, always being there for me, and giving me such a unique opportunity to grow professionally and personally.

Finally, I would like to thank my family and friends for always being there for me with their support. I would like to thank my sister and my parents, for believing in me and encouraging me to pursue this degree. I would also like to thank my partner, for always supporting me, believing in my capabilities, being by my side in the worst moments and encouraging me to follow my dreams.

Patent

This PhD work is to be used towards a provisional patent application.

Table of Contents

Abstract **1**

Declaration **4**

Acknowledgments **5**

Patent **7**

Table of Contents **8**

List of Figures **13**

List of Tables **24**

List of Abbreviations **27**

1. Literature Review **1**

1.1. Abstract 1

1.2. Background 1

1.3. A timeline of coronary artery stents development 4

1.3.1. Angioplasty and bare metal stents 4

1.3.2. Drug eluting stents: First, second and third generation 6

1.3.3. Fourth generation (bioabsorbable) 10

1.4. Commercial fabrication techniques and materials for polymeric stents 12

1.4.1. Extrusion blow moulding followed by laser cutting 15

1.4.2. Die drawing 17

1.4.3. Solvent based spraying 18

1.4.4. Microfiber monofilament processing 18

1.5. Clinical outcomes from the first generation of biodegradable stents 19

1.6. Using materials science and advanced fabrication techniques to address critical challenges with biodegradable stent technology.....24

1.6.1. Potential and challenges of additive manufacturing in personalized stent fabrication 25

1.6.2. 3D printing/Fused Deposition Modelling 26

1.6.3. Photolithography/Stereolithography 31

1.6.4. Melt electrowriting.....31

1.7. Critical comparison between commercial and lab-based techniques 33

1.8. Scope of the work 36

1.8.1. Designing the ideal bioabsorbable and drug-eluting stent.....36

1.9. Conclusions.....45

1.10. Objectives 49

1.11. Thesis Outline 49

1.12. References.....53

2. Additively manufactured biodegradable reduced graphene oxide-polycaprolactone coronary artery stents via MEW 71

2.1. Abstract.....71

2.2. Introduction.....72

2.3. Experimental methods 74

2.3.1. Materials 74

2.3.2. Preparation and characterization of composites 74

2.3.3. Mechanical tests.....75

2.3.4. Rheology 75
2.3.5. Differential scanning calorimetry and Thermogravimetric analysis 76
2.3.6. Fabrication and characterization of stents via melt electrowriting 76
2.3.7. Tensile tests on melt electrowritten fibres 77
2.3.8. Three-point bending test on melt electrowritten stents 77
2.3.9. Biological interactions 77
2.3.10. Statistical analysis 80
2.4. Results and Discussion 80
2.4.1. Preparation and characterization of composites 80
2.4.2. Mechanical tests 83
2.4.3. Rheology 86
2.4.4. Differential scanning calorimetry and Thermogravimetric analysis 88
2.4.5. Fabrication and characterization of melt electrowritten stents 91
2.4.6. Three-point bending tests on melt electrowritten stents 97
2.4.7. Biological interactions 98
2.5. Conclusion 105
2.6. References 105
3. Core cross linked biocompatible and biodegradable star brush polymers for hydrophilic antithrombotic drugs 112
3.1. Abstract 112
3.2. Introduction 113
3.3. Methods 118
3.3.1. Materials 118
3.3.2. Synthesis of core-cross linked star-brush polymers 118

3.3.3. Characterization of star-brush polymers 119
3.3.4. Drug loading 120
3.3.5. In-vitro drug release 121
3.3.6. Cytotoxicity assay 122
3.3.7. Adhesion and proliferation of human umbilical vein endothelial cells 122
3.3.8. Statistical analysis 123
3.4. Results and Discussion 124
3.4.1. Synthesis of core-cross linked star-brush polymers 124
3.4.2. Drug loading and in-vitro drug release 142
3.1.1 Cytotoxicity assay 149
3.4.3. Adhesion and proliferation of human umbilical vein endothelial cells 150
3.5. Conclusion 152
3.6. References 152
4. Additively manufactured multi drug eluting biodegradable reduced graphene oxide-polycaprolactone-star polymer coronary artery stents 168
4.1. Abstract 168
4.2. Introduction 169
4.3. Methods 173
4.3.1. Materials 173
4.3.2. Preparation and characterization of composites 174
4.3.3. Mechanical tests 174
4.3.4. Rheology 175
4.3.5. Differential scanning calorimetry and Thermogravimetric analysis 176
4.3.6. Melt electrowriting of stents 176

4.3.7. Rapamycin coating....177
4.3.8. Drug elution....177
4.3.9. Degradation....178
4.3.10. Biological interactions....178
4.3.11. Statistical analysis....182
4.4. Results and Discussion....182
4.4.1. Mechanical tests....182
4.4.2. Rheology....185
4.4.3. Differential scanning calorimetry and Thermogravimetric analysis....186
4.4.4. Melt electrowriting of stents....189
4.4.5. Rapamycin coating....190
4.4.6. Drug elution....191
4.4.7. Degradation....198
4.4.8. Biological interactions....201
4.5. Conclusion....209
4.6. References....210
5. Conclusions and Future Perspectives....214
5.1. Thesis conclusions....214
5.2. Future perspectives....218
Appendices....222
A. Chapter 2 Appendix....222
B. Chapter 3 Appendix....224
C. Chapter 4 Appendix....229

List of Figures

Figure 1.1: History of coronary artery stent progression. Adapted from references 2-4.....5

Figure 1.2: Schematic of fabrication process for polymeric biodegradable stents (Absorb BVS by Abbott Vascular). Adapted from ref 63. 13

Figure 1.3: Optical coherence tomography images illustrating representative examples of challenges associated with biodegradable stents: (A) strut malposition; (B) incomplete lesion coverage, possible ruptured plaque (white arrow), and uncovered thrombus (white asterisk); (C) underdeployment; (D) acute disruption; (E) overlap of scaffolds; (F) late discontinuity; (G) peri-strut low-intensity area (corresponding to inflammation around struts); (H) uncovered struts; and (I) neoatherosclerosis. Figure reproduced with permission from ref 9. Copyright 2017, Europa Group.....20

Figure 1.4: Schematic outline for the influence of strut thickness and stet design on physiological endothelial shear stresses within the artery. Reproduced with permission from ref 7. Copyright 2017, Lippincott Williams & Wilkins.....22

Figure 1.5: 3D printing of multidrug eluting patient-specific polymeric biodegradable stent. (a) Schematic of 3D printing of personalized stents. The process begins with CT imaging of the cross-section of the coronary artery and the diseases plaque. Custom made CAD design of the biodegradable scaffold is prepared utilizing the CT images of the patient. Upon the successful fabrication of the prototype using custom-build extrusion 3D printing setup, the device is implanted, which is followed by multi-drug elution and degradation. CT imaging is performed to assess healing of the artery. (b) CT images of the coronary artery and stent design (c) CT images of the pig heart with implanted scaffold (d) Custom-built extrusion setup (e)Steps involved in the ex-vivo implantation of the scaffold in the pig's artery (f)

Biodegradable drug-eluting polymeric stent. Reproduced with permission from ref 97. Copyright 2017, Wiley.....28

Figure 1.6: Representation of laboratory-based fabrication methods for polymeric coronary artery stents (a) Schematic of 3D printing setup (b) 3D printed PCL/PLGA/PEG vascular scaffolds (c) (d) SEM images of drug-eluting scaffolds. Reproduced with permission from ref 102. Copyright 2015, Elsevier. (e) (f) 3D printed PCL stents with various strut thickness. Reproduced with permission from ref 95. Copyright 2018, Elsevier. (g) 3D printed methacrylated poly(1-12 dodecamethylene citrate) stent. Reproduced with permission from ref 96. Copyright 2018, Elsevier. (h) Stent design and SEM images of the 3D printed composite scaffolds. Reproduced with permission from ref 97. Copyright 2017, Wiley. (i) MEW setup including a nozzle with high voltage and produced jet with polymer. Scale bar 2µm. (j) Design of a tube produced via MEW with control over length, translational, tangential, effective and rotational velocities. (k) Illustration of the pivot angle between pivot points and resulting porosity in melt electrowritten scaffolds. Reproduced with permission from ref 99. Copyright 2018, Elsevier. (l) Experimental setup for laser cutting of polymeric tubes in 3D using fibre laser and laser cut polymeric mats. Reproduced with permission from ref 96, 106. Copyright 2017, Elsevier. 30

Figure 1.7: The schematic showing the difference between solution-based electrospinning and melt electrospinning writing methods with resulting tubular scaffolds. (a) Comparison of solution electrospinning and melt electrowriting techniques. The polymer melt in MEW leads to a more stabilized jet compared to the use of polymer solution in ES and better control of the 3D features. Reproduced with permission from ref 98. Copyright 2015, IOP Publishing. (b) Electrospun PCL tubular scaffolds and the resulting fibrous structures. Reproduced with permission from ref 127. Copyright 2009, Elsevier. (c) Melt electrowritten PCL tubular

scaffolds and the resulting fibre structures. Reproduced with permission from ref 99. Copyright 2018, Elsevier. 32

Figure 1.8: In Chapter 2, we develop reduced graphene oxide-polycaprolactone stents with varying pore size, degree of curvature, size of curvature, fibre diameter, stent diameter utilizing melt electrowriting. 50

Figure 1.9: In Chapter 3, we synthesized biodegradable , biocompatible core-cross linked star-brush polymers for hydrophilic, anti-thrombotic drugs. 51

Figure 1.10: In Chapter 4, we fabricated PCL/rGO/CCS materials, evaluated their printability and studied biodegradation as well as multi-drug elution of two clinically used drugs (heparin and rapamycin).....53

Figure 2.1: Raman spectra of PCL, PCL/rGO, rGO and GO materials used. D and G correspond to D Band and G Band respectively. 82

Figure 2.2: Representative (a) full tensile stress-strain curves, (b) tensile stress-strain curves over the elastic region, (c) full compressive stress-strain curves, and (d) compressive stress strain curves over the elastic region curves for melt cast PCL and PCL-rGO nanocomposites with 0.1 wt%, 0.3 wt%, 0.6 wt% and 1.0 wt% rGO. (e) full tensile stress-strain curves curves for melt electrowritten filaments of PCL and PCL-rGO 0.1 wt% nanocomposites. (f) tensile stress-strain curves over the elastic region curves for melt electrowritten filaments of PCL and PCL-rGO 0.1 wt% nanocomposites.....83

Figure 2.3: Rheology characterization of PCL and PCL-rGO 0.1 wt%. (a) Viscosity curve as a function of shear rate at the temperatures of 70, 90 and 120ºC for PCL. (b) and PCL-rGO 0.1 wt%. (c) Temperature sweep for PCL and PCL-rGO 0.1 wt%. (d) Frequency sweep for PCL and PCL-rGO 0.1 wt%.....88

Figure 2.4: Thermal analysis for PCL, PCL-rGO 0.1 wt% and melt electrowritten PCL-rGO 0.1 wt%. (a) TGA curves for all materials (b) DSC curves (c) Melting temperatures after 1st,

2nd and 3rd heating cycles (d) Crystallization temperatures after 1st, 2nd and 3rd cycle. Asterisks (*) represent statistical difference where **P<0.01 and *P<0.05, (n= 3). 89

Figure 2.5: Fabrication of stent-like structures from PCL-rGO 0.1 wt% nanocomposites using MEW: (a) D= 2mm, multi structures, (b) D= 3.5 mm, 0.5 mm x 0.5 mm pore size, (c) D= 3.5 mm, 1mm x 1mm pore size (d) D= 3.5 mm, multi pore size (e) D= 3.5 mm, multi-curve (f, g) D= 3.5 mm, multi-architecture (h) D= 3.5 mm, curvy architecture (i) D= 5mm, multi-architecture.....94

Figure 2.6: SEM images of melt electrowritten scaffolds with varying stent diameter (a-c), architecture (a-l), pore size (d-f), strut thickness (g-i), and strut curvature (j-l).....96

Figure 2.7: Three-point bending tests on melt electrowritten scaffolds with varying pore size and number of printed layers. 97

Figure 2.8: (a) Three-point bending tests for scaffolds with varying stent architectures and pore size (b) Flexural stiffness as a function of stent geometry for scaffolds with pore size of 0.5mm x 0.5mm and 3 layers, 0.5 mm x 0.5mm and 5 layers, 1mm x 1mm and 3 layers, 1mm x 1mm and 5 layers. 98

Figure 2.9: Serum and protein adsorption curves for PCL and PCL-rGO (0.1 wt% and 0.3 wt%) composites.....100

Figure 2.10: Quantification of HUVECs adhesion and proliferation over 7 days of culture. The cells were seeded at a density of 1.7 $\times 10^4$ cells per cm^2. Asterisks (*) represent statistical difference where **P<0.01 and *P<0.05, (n= 3).....101

Figure 2.11: Representative images of hUVECs adhesion and proliferation on various surfaces over 7 days. Scale bar represents 100 µm.....102

Figure 2.12: (a) Platelet adhesion on glass, PCL, PCL-rGO (0.1wt%) and PCL-rGO (0.3wt%). (b) Morphology of adhered platelets on glass, PCL, PCL-rGO (0.1wt%), PCL-rGO (0.3wt%). Asterisks (*) represent statistical difference where **P<0.01 and *P<0.05, (n= 3).....103

Figure 2.13: Representative images of platelet adhesion on (a) glass (b) PCL (c) PCL-rGO (0.1wt%) (d) PCL-rGO (0.3wt%). Scale bars are 5µm. 104

Figure 3.1: Schematic of synthesis pathway.....117

Figure 3.2: DMF GPC of synthesized brushes with varying number of repeat units (PEG40, PEG20, PEG15 and PEG10).....124

Figure 3.3: Representative ^{1}HNMR spectrum of synthesized brush with the corresponding reaction pathway. 125

Figure 3.4: DMF GPC of synthesized CCS-OH and respective PEG brush before cross-linking with PEG diacrylate (Mw = 250 Da). CCS-OHs purified via dialysis in DI water for 7 days. 129

Figure 3.5: DLS characterization of synthesized CCS-OHs. Average size of hydrodynamic diameter 12.5 nm. 130

Figure 3.6: DMF GPC of representative CCS-PCL.....131

Figure 3.7: Representative ^{1}HNMR spectrum of CCS-PCL with the corresponding reaction pathway. 133

Figure 3.8: Drug release profiles for dextran and heparin at pH = 7.4 and pH = 5. 145

Figure 3.9: HUVECs viability in the presence of various concentrations of star polymers. Asterisks (*) represent statistical difference where **P<0.01 and *P<0.05, (n= 3).....150

Figure 3.10: Representative images of HUVES adhesion and proliferation on various surfaces over 7 days. Scale bar represents 100 µm.....151

Figure 3.11: Quantification of HUVECs adhesion and proliferation over 7 days of culture. The cells were seeded at a density of 1.7×10^4 cells per cm^2. Asterisks (*) represent statistical difference where **P<0.01 and *P<0.05, (n= 3). 151

Figure 4.1: Mechanical characterization of CCS/PCL-rGO (0.1wt%) composites. (a) Tensile stress-strain curves. (b) Tensile Young's Modulus for composites with varying content of CCS

in PCL-rGO (0.1wt%). (c) Compressive stress-strain curves (d) Compressive Young's Modulus for composites with varying content of CCS in PCL-rGO (0.1 wt%). All quantitative data are expressed as mean ± standard deviations with a minimum of n = 3 repeats.....183

Figure 4.2: Rheology characterization of printing material. (a) Viscosity vs shear rate for PCL-rGO (0.1wt%) and PCL-rGO (0.1wt%)-CCS(10wt%) at printing temperatures of 90ºC(b) Temperature sweeps for PCL-rGO (0.1wt%) and PCL-rGO(0.1wt%)-CCS(10wt%) (c) Frequency sweeps for PCL-rGO (0.1wt%) and PCL-rGO(0.1.wt%)-CCS(10wt%). 185

Figure 4.3: (a) TGA curves for CCS embedded in PCL-rGO (0.1 wt%) matrix at 10, 20 and 40 wt%, PCL-rGO (0.1wt%), heparin loaded CCS (10wt%) in PCL-rGO (0.1wt%) matrix, and pure heparin. (b) Heat flow curves for PCL-rGO (0.1wt%)-CCS(10wt%), PCL-rGO (0.1wt%)-CCS(20wt%), PCL-rGO(0.1wt%)-CCS(40wt%), and PCL-rGO(0.1wt%). (c) Melting temperatures for PCL-rGO (0.1wt%)-CCS(10wt%), PCL-rGO (0.1wt%)-CCS(20wt%), PCL-rGO(0.1wt%)-CCS(40wt%), and PCL-rGO(0.1wt%) after 1st, 2nd and 3rd heating cycles. (d) Crystallization temperatures for PCL-rGO (0.1wt%)-CCS(10wt%), PCL-rGO (0.1wt%)-CCS(20wt%), PCL-rGO(0.1wt%)-CCS(40wt%), and PCL-rGO(0.1wt%) after 1st, 2nd cooling cycles. Asterisks (*) represent statistical difference where **P<0.01 and *P<0.05, (n= 3)..187

Figure 4.4: Drug release profiles of heparin and rapamycin at pH = 7.4 and pH = 5. All quantitative data are expressed as mean ± standard deviations with a minimum of n = 3 repeats. Square symbols show heparin release; triangle symbols show rapamycin release. Rap corresponds to rapamycin. 192

Figure 4.5: Degradation curves for melt electrowritten scaffolds with varying pore size and number of layers. All quantitative data are expressed as mean ± standard deviations with a minimum of n = 3 repeats. X corresponds to the data point at which the scaffold fully degraded into small fibre pieces and mass could not be measured. 199

Figure 4.6: Representative images of accelerated scaffold degradation at 0h, 10h, 28h, and 32h of degradation. 201

Figure 4.7: Representative images of hUVECS adhesion and proliferation on glass and materials with different CCS content in PCL, and PCL-rGO (0.1wt%). Scale bars are 100 µm. 203

Figure 4.8: Quantification of HUVECs adhesion and proliferation over 7 days of culture. The cells were seeded at a density of 1.7×10^4 cells per cm^2. Asterisks (*) represent statistical difference where **P<0.01 and *P<0.05, (n= 3). 204

Figure 4.9: Representative images of SMCs adhesion and proliferation on various surfaces over 4 days. Scale bar represents 100 µm. rGO/CCS/PCL-rap1 corresponds to the 0.1wt% rGO/CCS (10wt%)/PCL material with 2.5mg of rapamycin in 3 mL polymer solution in DCM. rGO/CCS/PCL-rap2 corresponds to the starting concentration of 5 mg of rapamycin in 3 mL polymer solution in DCM. 205

Figure 4.10: Quantification of SMCs adhesion and proliferation over 4 days of culture. The cells were seeded at a density of 1.7×10^4 cells per cm^2. rGO/CCS/PCL-rap1 corresponds to the 0.1wt% rGO/CCS (10wt%)/PCL material with 2.5mg of rapamycin in 3 mL polymer solution in DCM. rGO/CCS/PCL-rap2 corresponds to the starting concentration of 5 mg of rapamycin in 3 mL polymer solution in DCM. Asterisks (*) represent statistical difference where **P<0.01 and *P<0.05 (n= 3). 206

Figure 4.11: (a) Platelet adhesion on glass, PCL-rGO(0.1wt%)-heparin loaded CCS(10wt%), PCL-rGO(0.1wt%)-heparin loaded CCS(20wt%), and PCL-rGO(0.1wt%)- heparin loaded CCS(40wt%). (b) Morphology of adhered platelets on glass, PCL-rGO(0.1wt%)-CCS(10wt%), PCL-rGO(0.1wt%)-CCS(20wt%), and PCL-rGO(0.1wt%)-CCS(40wt%). Asterisks (*) represent statistical difference where **P<0.01 and *P<0.05, (n= 3). 207

Figure 4.12: Representative images of platelet adhesion on (a) glass (b) PCL-rGO(0.1wt%)-CCS(10wt%) (c) PCL-rGO(0.1wt%)-CCS(20wt%) (d) PCL-rGO(0.1wt%)-CCS(40wt%). Scale bars are 5μm. 208

Figure B. 1: DMF GPC spectra of CCS-OH formed from PEG-40 arm with varying ratio of cross linker (PEG diacrylate) to PEG brush (PEG40). PEG40 was used as a precursor brush and cross-linked with PEG diacrylate (PEGDA, MW=250 Da) at the ratios of PEF brush (PEG 40) : PEDGA (cross linker): 1:10, 1:15, 1:20, 1:25, 1:30. 224

Figure B.2: DMF GPC of PEG10 arm and synthesized CCS after addition of cross-liner at the ratio of 1:15 [PEG10]:[PEGDA]. 225

Figure B.3: DMF GPC of PEG15 arm and synthesized CCS after addition of cross linker at the ratio of 1:15 [PEG15]:[PEGDA].....225

Figure B.4: DMF GPC of PEG20 arm and synthesized CCS after addition of cross linker at the ratio of 1:15 [PEG20]:[PEGDA].....226

Figure B.5: DMF GPC spectra of CCS-PCL after ring opening polymerization of caprolactone utilizing CCS-OH as a precursor. 226

Figure B.6: UV-Vis spectrum of FTIC Dextran (Mw = 20 kDa) at 0.01 mg/ml.....227

Figure B.7: Standard curve of FTIC Dextran (Mw = 20 kDa). 228

Figure B.8: UV-spectra of Heparin-Azure A complex. The band observed at approximately 510 nm corresponds to heparin-azure interactions. The band at 620 nm corresponds to uncomplexed heparin by Azure A dye. The absorption band at 620nm decreases with increasing heparin concentration, due to the falling concentration of Azure A. The decrease in absorbance at 620 nm is proportional to the increase of free heparin concentration.....228

Figure C.1: Modelling of the kinetics release of rapamycin at pH =5. Experimental data was fit into first-order kinetics model. 229

Figure C.2: Modelling of the kinetics release of rapamycin at pH =7.4. Experimental data was fit into first-order kinetics model. 230

Figure C.3: Fitting of rapamycin release (pH = 5) into Higuchi model. 230

Figure C.4: Fitting of rapamycin release (pH = 7.4) into Higuchi model. 231

Figure C.5: Fitting of heparin release from CCS(10wt%)/PCL-rGO at pH = 7.4 into Higuchi model.....231

Figure C.6: Fitting of heparin release from CCS(10wt%)/PCL-rGO at pH = 7.4 into the Power model.....232

Figure C.7: Fitting of heparin release from CCS(10wt%)/PCL-rGO at pH = 5 into the Power model.....232

Figure C.8: Fitting of heparin release from CCS(20wt%)/PCL-rGO at pH = 7.4 into the Power model.....233

Figure C.9:Fitting of heparin release from CCS(20wt%)/PCL-rGO at pH = 5 into the Power model.....233

Figure C.10: Fitting of heparin release from CCS(40wt%)/PCL-rGO at pH = 7.4 into the Power model. 234

Figure C.11: Fitting of heparin release from CCS(40wt%)/PCL-rGO at pH = 5 into the Power model.....234

Figure C.12: Fitting of heparin release from CCS-rap/PCL-rGO at pH = 7.4 into the Power model.....235

Figure C.13: Fitting of heparin release from CCS-rap/PCL-rGO at pH = 5 into the Power model.....235

Figure C.14: Modelling of rapamycin release (pH = 5) using the Power model.....236

Figure C.15: Modelling of rapamycin release (pH = 7.4) using the Power model.....236

Figure C.16: Fitting of heparin release from CCS(10wt%)/PCL-rGO at pH = 7.4 into the Hixon Crowell model.....237

Figure C.17: Modelling of rapamycin release (pH = 5) using the Hixon-Crowell model....237

Figure C.18: Modelling of rapamycin release (pH = 7.4) using the Hixon-Crowell model.238

Figure C.19: Fitting of heparin release from CCS(10wt%)/PCL-rGO at pH = 7.4 into the Weibull model.....238

Figure C.20: Fitting of heparin release from CCS(10wt%)/PCL-rGO at pH = 5 into the Weibull model.....239

Figure C.21: Fitting of heparin release from CCS(20wt%)/PCL-rGO at pH = 7.4 into the Weibull model.....239

Figure C.22: Fitting of heparin release from CCS(20wt%)/PCL-rGO at pH = 5 into the Weibull model.....240

Figure C.23: Fitting of heparin release from CCS(40wt%)/PCL-rGO at pH = 7.4 into the Weibull model.....240

Figure C.24: Fitting of heparin release from CCS(40wt%)/PCL-rGO at pH = 5 into the Weibull model.....241

Figure C.25: Fitting of heparin release from CCS-rap/PCL-rGO at pH = 7.4 into the Weibull model.....241

Figure C.26: Fitting of heparin release from CCS-rap/PCL-rGO at pH = 5 into the Weibull model.....242

Figure C.27: Modelling of rapamycin release (pH = 5) using the Weibull model. 242

Figure C.28: Modelling of rapamycin release (pH = 7.4) using the Weibull model. 243

Figure C.29: Fitting of heparin release from CCS(10wt%)/PCL-rGO at pH = 7.4 into the Exponential model. 243

Figure C.30: Fitting of heparin release from CCS(10wt%)/PCL-rGO at pH = 5 into the Exponential model. 244

Figure C.31: Fitting of heparin release from CCS(20wt%)/PCL-rGO at pH = 7.4 into the Exponential model. 244

Figure C.32: Fitting of heparin release from CCS(20wt%)/PCL-rGO at pH = 5 into the Exponential model. 245

Figure C.33: Fitting of heparin release from CCS(40wt%)/PCL-rGO at pH = 7.4 into the Exponential model. 245

Figure C.34: Fitting of heparin release from CCS(40wt%)/PCL-rGO at pH = 5 into the Exponential model. 246

Figure C.35: Fitting of heparin release from CCS-rap/PCL-rGO at pH = 7.4 into the Exponential model. 246

Figure C.36: Fitting of heparin release from CCS-rap/PCL-rGO at pH = 5 into the Exponential model.....247

Figure C.37: Fitting of rapamycin release at pH = 5 into the Exponential model.....247

Figure C.38: Fitting of rapamycin release at pH = 7.4 into the Exponential model.....248

Figure C.39: Standard curve for Rapamycin measured at 280 nm. 248

Figure C.40: Representative HIM image of electrospun PCL/rapamycin fibres. Scale bar corresponds to 1µm.....249

Figure C.41: Representative HIM image of electrospun PCL/rapamycin fibres. Scale bar corresponds to 5µm.....249

List of Tables

Table 1.1: Presentation of the range of materials and drugs used in currently developed stents together with FDA status and clinical trials [4, 7]. Late scaffold thrombosis is defined as 30 days to 1 year after scaffold implantation. Very late scaffold thrombosis is defined as 1 year after implantation [9]. 7

Table 1.2: Bioabsorbable polymeric scaffolds. PLLA – poly-L-lactic acid, PLA – poly-lactic acid, PDLA -poly D-lactide , PLGA – poly lactic-co-glycolic acid, TDP – tyrosine derived polycarbonate, DTDP – desaminotyrosine derived polycarbonate [48] 12

Table 1.3: Commercially utilized techniques for processing polymers as biodegradable stents [48]. 14

Table 1.4: Emerging laboratory-based techniques for processing polymers into biodegradable stents [66] 25

Table 1.5: Effect of additives, fillers, and reinforcement additives on polymers. 42

Table 2.1: Mechanical characterization of PCL-rGO nanocomposites. 86

Table 3.1: Characterization of synthesized brushes. (a) L= Me6TREN. (b) Conversion at 3h. Calculated from HNMR. (c) Calculated from ^{1}HNMR. 126

Table 3.2: Overview of synthesized CCS with varying cross-linker ratios and precursor CCS-OHs. DMF GPCs and HNMR spectra of synthesized CCSs in supporting information. (a) L = Me_6TREN. (b) [Br] = bromide, [PEG MEA] = PEG methyl ethyl acrylate (Mw = 480 Da)(c) Approximated from DMF GPC and ^{1}HNMR. 127

Table 3.3: Encapsulation strategies for hydrophilic drugs previously reported in the literature[46]. 135

Table 3.4: Overview of previously synthesized systems which exhibit hydrophobic arms and hydrophilic cores for a comparison of synthesized CCS-PCL stars in this study. Abbreviations are defined in the list of abbreviations (pages XXVII-XXXIV).....138

Table 3.5: Drug loading content and efficiencies for two antithrombotic drugs used (heparin and dextran). 144

Table 3.6: Overview of heparin, dextran or other antithrombotic drug encapsulation properties of different carrier systems and comparison to this study. Drug encapsulation rate (ER) (%) – maximum reported in the study, EF = encapsulation efficiency, NK = nattokinase, DLC = drug loading content, DL – drug loading properties (include either EF or DLC based on which one is reported in the study.....148

Table 4.1: Mechanical characterization of melt-cast CCS-PCL-rGO composites. All quantitative data are expressed as mean ± standard deviations with a minimum of n = 3 repeats. 184

Table 4.2: DSC characterization of PCL-rGO (0.1wt%) composited with varying content of CCS. ΔH – enthalpy; Xc – crystallinity.....189

Table 4.3: Kinetics mechanism investigated for release of heparin and rapamycin. C_t – amount of the drug released at time t; C_0 – initial concentration of drug at time t = 0; K_0 – zero-order rate constant; t – time; K_t – first order rate constant; C- total amount of drug release; D – diffusion coefficient of the drug molecule; qt – total amount of drug in a unit volume of a matrix; C_s – dimensional solubility of drug in polymer matrix; C_t/C_∞ - fraction of drug release at time t; K – rate constant; n- release exponent; K_{HC} - Hixon-Crowell rate constant; T – lag time measured as a result of dissolution process; a – scale parameter that describes time dependence; b- shape of dissolution curve; C_L – initial drug loading through the system; n – exponent that varies with geometry; r – system half thickness; C_{max} – maximum dissolution; α - location/scale parameter; β - dissolution rate per unit of time (shape parameter).....196

Table A.1: Protein adsorption on PCL, PCL-rGO (0.1wt%), and PCL-rGO (0.3wt%). 222

Table B.1: Characterization of synthesized CCS-PCL polymers. (a) [XL] = cross linker PEG diacrylate (MW = 250 Da) (b) Calculated from DMF GPC. 227

List of Abbreviations

β-CD	Beta cyclodextrin
0D	Zero-Dimensional
1D	One-Dimensional
^{1}HNMR	Proton nuclear magnetic resonance
2D	Two-Dimensional
3D	Three-Dimensional
AA	Acrylic acid
AADG	Aspartylglycosamine
AC-G2 PAMAM	Acetylated generation 2 Poly(amidoamine)dendrimer
AE	Aminoester
ANOVA	Analysis of Variation
ATRP	Atom Transfer Radical Polymerization
b	Block polymer
BSA	Bovine Serum Albumin
BVS	Bioresorbable Vascular Scaffold
CA-PEG	Carboxy Poly(ethylene glycol) Amine
CCS	Core cross linked star polymer
CD	Cyclodextrin
CHESG	Cholesterol enzymatically synthesized glycogen
Chol	Cholesterol
CHP	Chaperone, cholesterol-bearing pullulan
CL	ε-caprolactone

Co	Copolymer
CT	Computed Tomography
CX	Phosgene oxime
Da	Dalton
DAPI	4´,6-diamino-2-phenylindole
DCM	Dichloromethane
DEE	Diethyl ether
DEX	Dextran
DHBA	Dihydroxybenzoic acid
DLC	Drug loading content
DLE	Drug loading efficiency
DLS	Dynamic light scattering
DMAEMA	Methacrylic acid 2-(dimethylamino)ethyl ester
DMF	Dimethylformamide
DMSO	Dimethylsulfoxide
DOPC	1,2-dioleoyl-sn-glycero-3-phosphocholine
DPPC	Dipalmitoylphosphatidylcholine
DPPG	Dipalmitoylphosphatidylglycerol
DSC	Differential Scanning Calorimetry
dsDNA	Double stranded DNA
DSPE	1,2-Distearoyl-sn-glycero-3-phosphorylethanolamine
DTDP	Des-amino tyrosine derived polycarbonate
EBM	Endothelial Basal Medium
EBMTM	Endothelial Cell Growth Basal Medium

EC	Endothelial Cell
EDTA	Ethylenediaminetetraacetic acid
EF	Encapsulation efficacy
ER	Encapsulation rate
FA	Folic acid
FAK	Focal Adhesion Kinase
FBS	Fetal Bovine Serum
FCS	Fetal Calf Serum
FDA	U.S Food and Drug Administration
FU	Fluorouracil
g	Graft polymer
G'	Storage Modulus
G''	Loss Modulus
GFP	Green Fluorescent Protein
GLU	Glucose
GO	Graphene Oxide
GPC	Gel Permeation Chromatography
H40	Boltorn H40
HA	Hyaluronic acid
hbFGF-1	Human basic fibroblast growth factor
HBP	Heparin-binding peptide
HEBriB	2-hydroxyethyl α-bromoisobutyrate
HEGF	Human Epidermal growth factor
HEP	Heparin

HGP	Hyperbranched poly(glycidol)
HIM	Helium Ion Microscopy
HPA	p-hydroxyphenyl acetic acid
HPHEEP	Hypernranched polyphosphate
HPβCD	2-Hydroxypropyl-beta-cyclodextrin
HSPC	Hydrogenated soy phosphatidylcholine
HUVECs	Human Umbilical Vein Endothelial Cells
kDa	Kilodalton
kNA	Kilonewton
LTSL	Dipalmitoylphosphatidylcholine-3-Methylpentyl (4-sulphamoylphenyl)carbamate -1,2-Distearoyl-sn-glycero-3-phosphorylethanolamine- poly(ethylene glycol)
Lys	Lysine
MBA	N,N-Methylenebisacrylamide
MC	Microcapsule
Me_6TREN	Tris(2-(diethylamino)ethyl)amine
MEO2MA	2-(2-methoxyethoxy)ethyl methacrylate
MEW	Melt electrowriting
MMA	Methyl methacrylate
Mn	Number-average molecular weight
mPCL	Medical grade Poly(ε-caprolactone)
MRI	Magnetic Resonance Imaging
MS	Microsponges, Microspheres
MSA	Methane sulfonic acid
MSC	Mesenchymal stem cell

MSPC	3-Methylpentyl(4-sulphamoylphenyl)carbamate
Mw	Weight-average molecular weight
MWCO	Molecular weight cut off
Nd YAG	Neodymium-doped yttrium aluminium garnet
NK	Nattokinase
NMR	Nuclear Magnetic Resonance
NO	Nitric Oxide
NP	Nanoparticle
OEGA	Oligo (ethylene glycol) acrylate
OEGMA	Oligo(ethylene glycol) methacrylate
OrnAA	Ornithine methacrylamide
PAA	Peroxyacetic acid
PAMAM	Poly(amidoamine)
PBA	Phenylboronic acid
PBS	Phosphate Buffer Saline
PCL	Poly(ε-caprolactone)
PDA	1,4-Bis(acryloyl)piperazine
PDI	Polydispersity
PDLA	Poly D-lactide
PDLLA	Poly-d,l-lactic acid
PDMAEMA	Poly(N,N-dimethylaminoethylmethacrylate)
PEA	Phenethylamine
PEDOT	Poly(3,4-ethylenedioxythiophene)
PEG	Poly(ethylene glycol)

PEG MEA	Poly(ethylene glycol) methyl ether acrylate
PEGDA	Poly(ethylene glycol) diacrylate
PEGMA	Poly(ethylene glycol) methyl ether methacrylate
PEO	Poly(ethylene oxide)
PEVA	Poly(ethyelene-co-vinyl) acetate
$PG_{OH}MA$	Poly(glycidyl methacrylate)
PLA	Poly-lactic acid
PLGA	Poly(lactic-co-glycolic acid)
PLLA	Poly-L-lactic acid
PLP	Pyridoxal 5′-phosphate hydrate
PMBA	Poly n-butyl methacrylate
PMMA	Poly(methyl methacrylate)
PN	Pyridoxine
PNA ECD	Poly(*N*-isopropylacrylamide-*co*-acrylic acid/aminated β-cyclodextrin)
PNIPAM	Poly-N-isopropyl acrylamide
POEGA	Poly Oligo (ethylene glycol) acrylate
pOrnAA	Poly(ornithine methacrylamide)
PPEGMA	Poly(poly(ethylene glycol) methyl ether monomethacrylate)
PS	Polystyrene
QCM	Quartz Crystal Microbalance
RAFT	Reversible addition fragmentation chain transfer polymerization
RAPA	Rapamycin
RGO	Reduced Graphene Oxide
ROP	Ring Opening Polymerization

RS	Eudragit RS (Copolymer of Ethyl prop-2-enoate; methyl 2-methylprop-2-enoate; trimethyl-[2-(2-methylprop-2-enoyloxy)ethyl]azanium; chloride)
s	Star polymer
seATRP	Simplified electrochemically mediated Atom Transfer Radical Polymerization
SEM	Scanning Electron Microscope
SIBS	Poly(styrene-b-isobutylene-b-styrene)
SMCs	Smooth Muscle Cells
sPCL	Star Poly(ε-caprolactone)
sPEG	Star Poly(ethylene glycol)
TBA	4-thio-butyl-amidine
TCPS	Tissue Culture Polystyrene
TDP	Tyrosine derived polycarbonate
TEA	Triethanolamine
TEM	Transmission Electron Microscope
TGA	Thermogravimetric analysis
TGF-β	Transforming Growth Factor-β
THF	Tetrahydrofuran
TREN	Tris(2-aminoethyl)amine)
TRITC	Tetramethyl rhodamine
TSL	Dipalmitoylphosphatidylcholine-1,2-Distearoyl-sn-glycero-3-phosphorylethanolamine- poly(ethylene glycol)
TTSL	Dipalmitoylphosphatidylcholine-Hydrogenated soy phosphatidylcholine -Cholesterol-1,2-Distearoyl-sn-glycero-3-phosphorylethanolamine-poly(ethylene glycol)
UV	Ultraviolet
UV-ATRP	Ultraviolet-Induced Atom Transfer Radical Polymerization

VEGF	Vascular Endothelial Growth Factor
VP	*N*-vinyl-2-pyrrolidone
X-ray	Energetic High-Frequency Electromagnetic Radiation
γ-CD	Gamma cyclodextrin

1. Literature Review

1.1. Abstract

A substantial amount of research is currently occurring that is focused on the development of biodegradable coronary artery stents. However, the clinical implementation of this technology has still significant challenges to overcome. The first generation of clinically used and FDA approved biodegradable stents was linked to higher rates of late stage thrombosis and this led to the withdrawal of the device from market in 2017. Current challenges are related to the development of materials and fabrication processes that can produce biodegradable stents with long term *in vivo* safety and superior clinical performance when compared to the current gold standard of drug eluting metallic stents. In this review, we critically analyse the current material systems and the commercially used and emerging laboratory-based technologies for fabrication of polymeric biodegradable stents. A critical comparison between industrial and research-based methods is outlined with a focus on emerging methods and materials to address the limitations of currently used fabrication techniques.

1.2. Background

Coronary artery stents are intravascular medical devices used in the treatment of coronary heart disease. The first coronary artery stent was used in 1986, and new generations of the device have been developed since then to address the limitations of previous ones. The current focus is the development of fully biodegradable and drug-eluting stents that would support the artery only as long as it is needed and then gradually degrade away leaving behind a healed vessel. However, the first generation of bioabsorbable scaffolds resulted in higher rates of late stage thrombosis, and this led to the withdrawal of the first FDA-approved bioabsorbable device from the market in 2017. The current challenge lies in the development of materials and fabrication processes that can produce a bioabsorbable scaffold with long term safety *in vivo* and superior clinical performance relative to the current generation of drug-eluting metallic

stents. In this review, we critically analyse the current material systems and the commercially-used and emerging laboratory-based technologies for fabrication of polymeric biodegradable drug-eluting stents. A critical comparison between industrial and research-based methods is outlined with a focus on emerging methods and materials to address the limitations of currently used fabrication techniques.

Cardiovascular diseases are leading causes of mortality globally, causing approximately 17 million deaths annually. Additionally, this number is predicted to rise to 23 million by 2030[1]. This group of diseases refers to disorders of the heart and the blood vessels. The most common disorder is known as coronary heart disease, a disease of coronary arteries that supply oxygen-rich blood to the heart. Patients with this condition have an accumulation of cholesterol, known as a plaque, inside the walls of the blood vessel. The growth of this plaque leads to the narrowing and eventually blockage of the artery and reduces the supply of oxygenated blood that reaches the heart muscle. This reduced blood supply can lead to heart attack and potentially death. Every year, approximately 7.4 million people die due to coronary heart disease[2].

In current medical practice, coronary heart disease is commonly treated through balloon angioplasty and stenting (also referred to as percutaneous coronary intervention). During this procedure a catheter is inserted through the skin and into the vasculature. The distal end of the catheter is fitted with a balloon than can be expanded on demand. The catheter is maneuvered such that the balloon is located within the narrowed section of the artery and inflated to expand the narrowed artery (balloon angioplasty). Upon removal of the balloon, blood flow is restored through the vessel. Balloon angioplasty is often not sufficient to maintain vessel patency, as many vessels will experience recoil following the angioplasty procedure. To prevent recoil, a stent is also placed within the vessel. The stent is a cylindrical device made of a metallic wire

mesh. It is expanded within the diseased section of the vessel and provides mechanical support to the vessel to prevent recoil [3]. The device has been clinically used since its development in 1986, and several generations of the device have been developed as we will describe in this review [4]. Current clinically used coronary artery stents are drug-eluting, metallic, and permanent. However, the permanent nature of the stents can lead to several complications, such as re-narrowing of the artery despite of the presence of stent (in stent restenosis), need of prolonged anti-platelet therapy, high rate of repeat procedures, and decrease in quality of life for the patient [4].

Permanent stenting is not required. The diseased vessel has the potential to heal within 6 months to 1 year after intervention [5-6]. In fact, the permanent presence of a foreign material (metallic stent) introduces additional variables in the healing process and can disturb it [5]. For instance, the permanent presence of a metallic scaffold can disrupt the healing, lead to higher rates of blood clot and scar tissue formation, and lead to the recurrence of restenosis[5, 7-8]. In recent years, the development of a biodegradable coronary artery stent has gained significant attention. Such a stent would support the vessel while it heals and then degrade away, leaving behind a functioning artery. This technology would eliminate the complications associated with permanent stenting and represent a major step forward in the treatment of coronary heart disease.

The first generation of biodegradable stents was linked to higher rates of late stage thrombosis and adverse cardiac events compared to the current gold standard, drug eluting metallic stents. As such, the device was removed from the market in 2017. These higher rates of adverse cardiac events have been associated with several factors relative to the device design [9], and can be divided into three main categories including 1) thrombogenicity of the stent material and

biodegradation products, 2) inflammation of the blood vessel, and 3) changes in the shear stress experienced by the endothelial cells due to disturbances in blood flow caused by the stent[9]. Clinical results from this first generation bioabsorbable scaffolds show a clear technological gap in both materials science and manufacturing technologies that must be addressed to enable the development of clinically successful biodegradable coronary artery stents.

In this review, we first describe the history of coronary artery stent development, we then go on to discuss the materials that have been used in the development of polymeric and biodegradable coronary artery stents, outline the fabrication technologies that are commercially used to fabricate these devices, and then describe the clinical outcomes of these devices. Following this thorough description of the field, we discuss emerging developments in materials science and polymer processing techniques that can be used to address many of the current limitations of the technology, and we finally outline where future impactful research can be done.

1.3. A timeline of coronary artery stents development

1.3.1. Angioplasty and bare metal stents

Native blood vessels are composed of three different layers: the adventitia, the media, and the intima, all of which are critical to maintaining the regulatory functions and physiology of a blood vessels. The outer layer, known as the adventitia, provides structural support and compromised of collagen type I and II and elastin fibres embedded in fibroblasts. The middle layer, the media, is composed of smooth muscle cells which are contractile, as well as proteoglycans, elastic, and collagen type I, III and V. The most innermost layer, known as tunica intima, is compromised of endothelial cells with collagen IV fibres and laminin[42]. In this layer, endothelial cells are in a quiescent state and one of their physiological functions is

maintenance of blood vessel thromboresistance by production of anticoagulant factors and nitric oxide[42-43].

A timeline for the development of stenting technologies is schematically shown in **Figure 1.1**. The first catheter-based treatment for coronary artery disease was angioplasty, a procedure that was first performed in 1977. During the procedure, a surgeon will open a compromised artery through the intravascular expansion of a balloon. As the balloon expands, the artery will be dilated, and blood flow will be restored through the vessel upon removal of the balloon. However, angioplasty alone is often not sufficient due to arterial recoil (the tendency of an artery to return to its previous diameter before angioplasty) and neointimal hyperplasia (thickening of the intimal layer of the blood vessel after angioplasty), both of which reduce the diameter of the blood vessel and reduce the supply of oxygen-rich blood to the heart [4, 10].

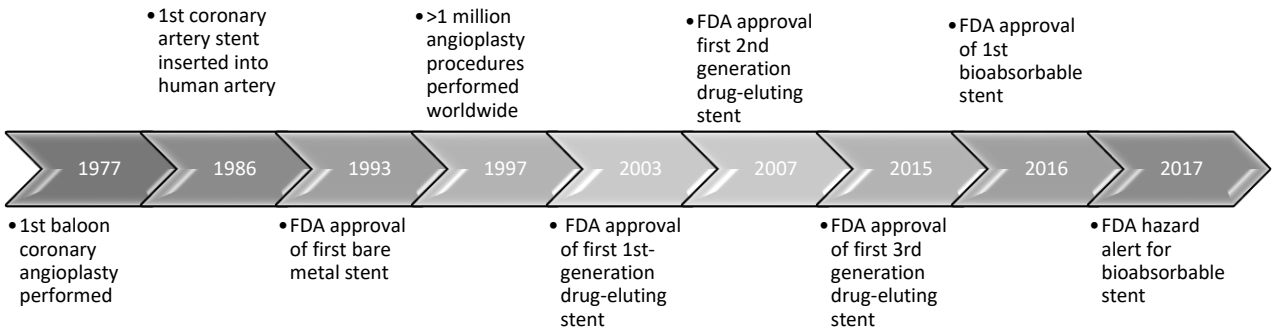

Figure 1.1: History of coronary artery stent progression. Adapted from references 2-4.

To address the shortcomings of angioplasty alone, angioplasty followed by stenting was introduced. In this new procedure, a stent is expanded into the diseased section of the artery following angioplasty to provide sufficient mechanical support to maintain vessel patency. The use of stenting with angioplasty increased the number of successful procedures [11-12]. However,

narrowing of the vessel despite of the use of stent (in-stent restenosis) was still a significant problem, occurring in approximately 15 % of patients [4]. Restenosis happens as a result of the injury to the artery wall during the insertion of a catheter and is related to new tissue growth during healing which becomes excessive. Additionally, the presence of a permanent stent in the artery following the procedure affects the blood vessel lining, therefore leading to higher probability of blood clots and scar tissue formation. Together, this can lead to blockage of the artery in the same location (restenosis) [4, 13].

1.3.2. Drug eluting stents: First, second and third generation

Drug eluting stents were introduced to address the challenge of in stent restenosis present with bare metal stents. These generations of stents are used as local drug delivery vehicles of therapeutic agents that minimise in-stent restenosis. To date, there have been three generations of drug eluting metallic stents, and the development of this technology is compiled in **Table 1.1**. The first generation of drug eluting stents were made of stainless steel and coated with a layer of polymer such as polyethyelene-co-vinyl acetate, poly(n-butyl methacrylate), Parylene C, or poly(styrene-b-isobutylene-b-styrene), which is impregnated with one of two antiproliferative drugs, either sirolimus or paclitaxel [4, 14]. The drugs are locally released, and they act to reduce in-stent restenosis by limiting the overgrowth of intimal tissue. Clinical data showed that the use of drug-eluting stents successfully decreased in-stent restenosis, rates of target lesion revascularization, and cardiac events compared to bare metal stents [15].

Table 1.1: Presentation of the range of materials and drugs used in currently developed stents together with FDA status and clinical trials [4, 7]. Late scaffold thrombosis is defined as 30 days to 1 year after scaffold implantation. Very late scaffold thrombosis is defined as 1 year after implantation [9].

Generation	Stent materials	Drug coating	FDA status	Side effects	Ref
Permanent, metallic, and drug eluting stents					
First	*Bulk material:* Stainless steel *Coating:* Polyethylene-co-vinyl acetate, Poly(n-butyl methacrylate), Parylene C, Poly(styrene-b-isobutylene-b-styrene)	Sirolimus Paclitaxel	2 approvals: Cypher (Cordis) Taxus (Boston Scientific)	-Delayed endothelialization -Stent thrombosis -Non-uniform drug delivery and device expansion -Poor deliverability	4, 14, 16-21
Second	*Bulk material:* Cobalt-chromium, Platinum-chromium *Coating:* Fluoropolymers, Poly(n-butyl methacrylate), Poly(vinylidene fluoride co hexafluoropropylene), *BioLinx™ polymer*	Zotarolimus Everolimus	7 approvals: Xience V, Xience Prime (Abbott Vascular) Promus, Taxus Ion, Promus Element (Boston Scientific) Endeavor, Resolute (Medtronic)	-Increased late scaffold thrombosis and target lesion revascularization -Chronic inflammation -In-stent neoatherosclerosis -Need for dual anti-platelet therapy long-term -Permanent presence of the device	4, 22-31
Third	*Bulk material:* Platinum-chromium *Coating:* Biodegradable Polymers Poly-lactic acid Poly-L-lactide Poly-L-lactide-co-glycolide Poly-D,L-lactide-co-glycolide Poly-vinyl pyrrolidine Poly-lactide-shellac	Umirolimus Sirolimus Everolimus Paclitaxel	1 approval Synergy™ (Boston Scientific)	-No data on possible decrease in required length of dual anti-platelet therapy -Permanent presence of scaffold -Chronic inflammation -In-stent atherosclerosis -Resistance to MRI - Increase in target lesion revascularization long term	4, 8, 32-35
Bioresorbable and polymeric stents					
Fourth: Bioabsorbable	Poly-L-lactic acid Tyrosine-derived polycarbonate Poly-D,L-lactic acid Salicylic acid Magnesium/metal Magnesium alloy	None Everolimus Sirolimus Myolimus Novolimus	No approval	-Higher rates of late and very late stent thrombosis -Strut malposition -Higher rates of target lesion failure, cardiac death, target vessel myocardial infraction, target lesion revascularization -Lack of full scaffold radiopacity except one scaffold (Fantom)	7-9, 36-40

Once restenosis due to neointimal hyperplasia was minimised, stent thrombosis (the formation of a blood clot on the surface of the device) became the next most concerning issue, and further improvements were needed to decrease the rate of stent thrombosis [13]. There are three main drivers of stent thrombosis: 1) pro-thrombogenic disturbances to blood flow caused by the presence of the stent, 2) exposure of the pro-thrombogenic stent material to the blood flow due to poor endothelialisation, and 3) discontinuation of antiplatelet therapy by the patient.

Several stent-related factors have been associated with the development of thrombosis. The first is related to the design of the stent itself and the selection of materials used to fabricate the device. While a great deal of research has focused on designing the stent structure so that the device has minimal impact on the fluid flow through the device, the shape, size, and distance that the stent struts protrude into the lumen will always cause some degree of disturbance to the blood flow. This disturbance promotes thrombosis by disruption the laminar blood flow and change endothelial shear stresses within the artery. This further leads to shear-induced activation of platelets by overexpression of integrin $\alpha_{IIb}\beta_3$ followed by stabilization of platelet aggregates and thrombus formation [7, 9].

Beyond the fundamental design of the stent, factors associated with the deployment of the stent or stents in an artery can influence thrombosis. Under ideal circumstances, a stent should be fully deployed such that the stent is pressed flush against the vessel wall. However, sometimes stent malposition (separation of strut from the intimal surface of the arterial wall) [41] or stent underexpansion (stent does not expand to the full desired diameter) occur. These factors also further act to disrupt blood flow and expose more of the pro-thrombogenic stent surface to the blood. These challenges can be further exacerbated for challenging lesions such as those that

are long or present at bifurcations in the blood vessel. In these instances, a surgeon may be required to implant multiple stents in a single site, further potentiating thrombosis.

Drug-eluting stents were also found to impair reendothelialization after implantation, slow the healing process, and promote the expression of tissue factors leading to prothrombogenic and inflammatory conditions [20]. These issues were addressed with the development of second-generation metallic and drug-eluting stents. These stents were made of less inflammatory materials such as cobalt-chromium and platinum-chromium and eluted newer antiproliferative drugs such as zotarolimus and everolimus[4]. Several combinations of metallic materials were investigated including stainless steel, cobalt-chromium, and platinum-chromium as well as different polymers for the drug eluting layer such as fluoropolymers, poly(n-butyl methacrylate), poly(vinylidene fluoride co hexafluoropropylene) or specifically developed commercial polymers (e.g., BioLinx^{TM})[23,25]. These stents improved endothelization compared to first-generation devices. Additionally, the combination of new materials resulted in improved mechanical properties of the material and allowed for the fabrication of stents with thinner struts [23]. The thinner struts are desirable as they allow disturbances to blood flow to be minimised and expose less pro-thrombogenic stent surface to the blood flow.

While the second generation stents reduced the thrombogenicity of the devices, clinical trials revealed higher rates of target lesion revascularization (repeat revascularization procedure for a vessel already containing a stent), potentially limiting the long term safety of the devices, and prompting the development of third generation metallic and drug eluting stents [4]. Improvements were made by incorporating additives into the main platform, using new coatings of biodegradable polymers, and development of polymer-free coatings. The four main

anti-proliferative agents used in third-generation stents were sirolimus, everolimus, paclitaxel and umirolimus [4, 8].

As of 2018, there is one everolimus eluting stent approved for use in the U.S made of platinum chromium alloy covered with Poly-D,L-lactide-co-glycolide, which elutes everolimus (Synergy ™) [4]. Clinical results for third-generation stents show significant reduction of target lesion revascularization compared to bare metal stents [17]. Everolimus-eluting cobalt chromium stent showed the best clinical outcomes with reduction of stent thrombosis, myocardial infarction and risk of target lesion revascularization. Some research suggests that the use of biodegradable polymers may lead to a decrease in the time required for anti-platelet therapy; however, additional clinical trials are required [4].

Synergy™ stent is everolimus-eluting platinum chromium coronary stent which promotes early healing due to its thin struts (74 µm) and excellent stent coverage with low stent thrombosis. In the study, Synergy™ stent was compared in terms of its pre-clinical performance with other stents that have thicker struts (120 µm – 150 µm)[44]. Results showed rapid endothelialisation of Synergy™ stent with strut coverage as high as 84 %, as compared to 13-68 % for other scaffolds with thicker struts[45]. The polymer coating with everolimus is a biodegradable polymer (PLGA) which gets absorbed as everolimus is being eluted[46-47]. Synergy stent is the first FDA approved stent which utilizes a bioabsorbable polymer as an outer coating for elution of a biodegradable polymer embedded everolimus, and which has very thin struts compared to previous scaffolds[4].

1.3.3. Fourth generation (bioabsorbable)

Despite the significant advances that have been made in stent design, patients still require prolonged use of dual antiplatelet therapy. The prolonged use of these drugs is a burden on the

healthcare budget, poses risks for the patient such as severe bleeding, and discontinuation of the therapy potentiates late stage thrombosis. As such, there is significant interest in developing a next generation of stents that removes the need for the prolonged antiplatelet therapy. Additionally, permanent stenting is not required. The vessels show the ability to heal themselves between 6 months and 1 year post-surgery. There is currently widespread interest in the development of biodegradable stents through combining the properties of the vessel to heal and the desire to minimise prolonged antiplatelet therapy. These medical devices would support the vessel until healing can occur and then degrade away to leave behind a functioning artery. This type of stent could potentially decrease the risk of scaffold thrombosis and reduce the need for dual anti-platelet therapy [4, 7].

Several biodegradable stents are currently being developed or are in clinical trials. The devices are either made from biodegradable metals (e.g., magnesium or iron) or polymers. This review focuses on polymeric biodegradable stents, and current devices are detailed in **Table 1.2**. The majority use Poly-L-lactic acid or Poly-D,L-lactic acid as a stent material, tyrosine-derived polycarbonate, or salicylic acid. Anti-proliferative agents, if used, include everolimus, sirolimus, myolimus, novolimus. Long-term clinical data comparing bioabsorable scaffolds with bare metal stents is not extensive, and no comparison of target lesion revascularization rate has been made, to the authors' knowledge [4].

Table 1.2: Bioabsorbable polymeric scaffolds. PLLA – poly-L-lactic acid, PLA – poly-lactic acid, PDLA -poly D-lactide , PLGA – poly lactic-co-glycolic acid, TDP – tyrosine derived polycarbonate, DTDP – desaminotyrosine derived polycarbonate [48]

Stent name	Company	Bulk Polymer	Strut thickness	Fabrication	Status	Country	Ref
Absorb BVS	Abbott Vascular	PLLA	150 µm	Extrusion, blow molding	FDA hazard alert TGA unapproved Out of market	United States	4, 9, 38, 48-49
REVA ReZolve ReZolve 2 Fantom	Reva Medical	TDP TDP TDP DTDP	200 µm 230 µm - 125 µm	-	Discontinued Clinical trials Clinical trials Clinical trials	United States	4, 48, 50
ART Pure	Arterial Remodeling Technologies	PLA	-	Post processing annealing	Clinical trials	France	4, 48
DESolve 150 DESolve 100 DESolve Cx DESolve NTx	Elixir Medical	PLA PLLA	150 µm 100 µm 120 µm -	Solvent based spraying, annealing	CE Mark CE Mark Clinical trials Under development	United States	48, 51-53
MeRes stent MeRes100	Meril Life Sciences	PLA PLLA	>200 µm -	-	Animal study Clinical trials	India	48, 53-54
FORTITUDE APTITUDE MAGNITUDE	Amaranth Medical Inc.	PLLA PLLA PLLA	150-200 µm 115 µm 100 µm	Multilayer processing	Clinical trials Clinical trials Clinical trials	United States	48, 55-57
XINSORB	Huaan Biotechnology Group Co., Ltd	PLLA	160 µm	-	Clinical trials	China	48, 58
IDEAL (1st) IDEAL (2nd)	Bioabsorbable Therapeutics Inc. Xenogenics Corporation	PLLA/Salicylates	200 µm 175 µm	-	Clinical trials Under development	United States United States	48
ArterioSorb 120 ArterioSorb 95	Arterius Ltd.	PLLA	120 µm 95 µm	Solid die drawing	Under development	United Kingdom	48, 59-60
Mirage BRMS	Manli Cardiology	PLLA	125 µm	Microfiber monofilament with directional alignment	Clinical trials	Singapore	48, 61-62
ON-AVS	OrbusNeich	PLLA/PDLA	150 µm	-	Under development	United States	48
Avatar	S3V Vascular technologies	-	-	-	Animal study	India	48
Stanza BRS	480 Biomedical	PLGA	-	-	Under development	United States	48, 53
ReNATURAL	Cardionovum GmbH	PLLA	-	-	Under development	Germany	48

1.4. Commercial fabrication techniques and materials for polymeric stents

Currently, polymeric stents are commonly made through extrusion-based blow moulding techniques. A generalised process flow diagram is illustrated in **Figure 1.2**. Initially, polymer

pellets are melted, and the melt is extruded through a die to form a polymer tube, sometimes followed by a blow moulding step. After extrusion, the tube is machined, usually through laser cutting, to generate the desired strut pattern. Metallic stents, and sometimes polymeric stents, then undergo an annealing step to improve the mechanical properties, lower the risk of strut breakage, and improve fatigue resistance. A surface treatment such as electro polishing or ultrasonic cleaning is sometimes performed, to ensure that the surface is defect-free [63]. A drug eluting layer is deposited on the surface of the polymer utilizing various techniques such as dip coating or electrospraying. In the process, a drug is usually dissolved in a polymer solution and deposited together with a thin layer of a polymer. In the final steps, a stent is crimped onto the balloon before being inserted into patient's artery, and then expanded at the lesion site (**Figure 1.2**).

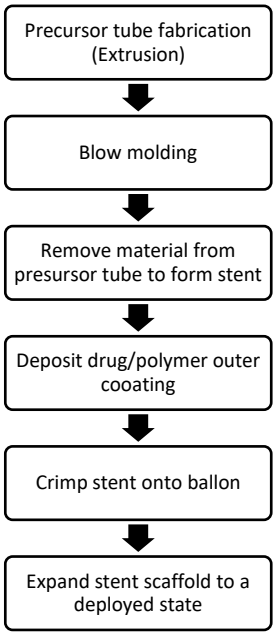

Figure 1.2: Schematic of fabrication process for polymeric biodegradable stents (Absorb BVS by Abbott Vascular). Adapted from ref 63.

Since this study focuses on the development of polymeric stents, a brief overview of the most common currently available industrial methods is described below and compiled in **Table 1.3**.

Table 1.3: Commercially utilized techniques for processing polymers as biodegradable stents [48].

Technique	Process characteristics	Advantages	Disadvantages	Ref
Methods of producing precursor tubes				
Extrusion	• Polymer heated up to the molten state • Extrusion through die using a screw pump • Polymer chains oriented in the direction of flow (longitudinal chain orientation)	• Well established manufacturing protocols • Scalable	• Requires melting of the polymer (above T_m) • Production of a tube without porosity • Limitations in shape of the structure due to die and flow	63-65
Melt Mould Injection Casting	• Melt the polymer • Injection into the mould followed by curing	• Fast production • Low cost	• High temperature • Melting required	66
Blow Moulding	• Material prepared as soft polymeric parison • Injection of the material into the mould • Air blown for tube expansion • Stretching and selective orientation of polymer chains	• Preferential alignment of polymer chains • Selective orientation • Low pressure • Improved mechanical properties	• High temperature • Limited final structures by the shape of a cavity	63
Die drawing	• Polymer heated up • Solid material drawn through a conical die of reducing cross-section • Polymer chains oriented in the direction of the motion • Material pulled into various final shapes	• Improved mechanical, thermal properties • Selective molecular orientation	• High temperature	67
Solvent based spraying	• Polymer dissolved in suitable solvent and sprayed onto the collector • Organic solvent evaporated	• Use of organic solvent • Drugs can be incorporated by co-dissolving with polymer in the solvent	• Poor mechanical properties • Need for very controlled environment for reproducibility	68
Microfiber monofilament	• Fabrication of highly orientated circular polylactide filaments with directional mechanical properties	• Control of mechanical properties • Ambient temperature for some steps of the process	• Process requires melt extrusion	48
Methods of machining tubes to produce stents				
Laser machining	• Laser cutting of precursor scaffolds (tubes) fabricated via above methods for	• Fabrication of desired geometries	• Deposition of the removed material on the surface	66, 69-70

	production of a stent with struts	from tubular scaffolds	• Oxidation of the cut • Burr formation	
Nd:YAG laser			• Extra steps for removal of materials (etching, pickling)	
		• Thin structures (50-100 µm)	• Heat affected zones	
Femtosecond laser			• Not suitable for some polymers	
Excimer laser		• Thin structures (30 µm) • High resolution • Lack of heat affected zones	• Some of the material melts because of cutting • Very expensive • Low resolution and beam quality	
Additional treatments				
Annealing	• Heating of the polymer to an elevated temperature for a certain duration	• Removal of residual solvent • Removal of residual stresses and defects in the material • Improved crystallinity	• Need for elevated temperature	[68]

1.4.1. Extrusion blow moulding followed by laser cutting

Extrusion is the most common technique used to produce the polymeric tubes that are later machined into stents. In this process, a polymer resin with the desired additives is melted and extruded through a die to produce a tubular structure. The tube is then enclosed in a cooled mould and air is blown into the tube to inflate it into the final shape. Once the polymer has solidified, the mould is opened, and the part is ejected.

The tubular scaffolds must then be laser machining to create the desired geometry. The most commonly used laser for the machining of metallic stents is the neodymium: yttrium-aluminium-garnet (Nd:YAG) solid-state laser with wavelength of 1064 nm. While the laser has been utilized for machining of previous generations of stents it does have major drawbacks

including the creation of large heat affected zones and dross adherence [66]. The laser machining of polymeric bioabsorbable stents differs significantly from their metallic counterparts because of different optical and thermal properties of the materials. Commonly, femtosecond and excimer lasers are used in the production of polymeric stents. Femtosecond lasers emit optical pulses with ultrashort pulses in the domain of femtoseconds, thus depositing the laser energy into the electrons of the material on a very short time scale compared to transfer time of the energy to the bulk of the material. This results in minimal thermal stresses and increased ablation efficiency [69]. The major downside of the use of femtosecond for fabrication of stents is its high cost. Another type of commercially used laser is the excimer laser which is an ultraviolet laser [70]. This laser is advantageous as it results in minimal heat affected zones. However, the resolution of the cuts and beam quality are lower compared to Nd:YAG or femtosecond lasers.

Some of the most common additional treatments after production of a scaffolds include annealing and electropolishing. Annealing can be performed to facilitate deformation of stent during expansions, as well as to remove surface irregularities and decrease roughness. Additionally, annealing can be used to tailor mechanical properties such as tensile elongation at break, ultimate tensile strength, ductility and grain size[71-73]. Electropolishing is a technique in which material is removed via electrochemical process to improve surface of a device. In this process, a material or scaffold is immersed in a temperature-controlled bath of electrolyte and current is passed through the solution[74]. The process reduces the roughness of the surface and sometimes is performed after acidic pickling. Both of these techniques ensure the surface smoothness and enable better biocompatibility of a scaffold[75].

There are multiple techniques of depositing drug-eluting polymer layer such as dip coating, electro treated coating, plasma-treated coating and spray-coating [76]. Dip coating involves the submerging of the stent in a solution of a drug or polymer/drug in a solvent. Afterwards, the stent is left to dry which allows the evaporation of the solvent. The technique allows variation in polymer and drug; however, it can lead to complications such as bridging, pooling, and lack of uniformity of a dip coated polymer/drug layer[77-79]. Electro treated coatings are based on the use of electrical stimulus to assist in drug/polymer deposition onto the stent surface, or alternatively, to increase polymerization on previously deposited drug layer[76]. Electrophoretic deposition, a technique which utilizes an electric field to attract charged particles onto the stent surface, results in the formation of a drug layer[80-81]. Plasma treated coating are still undertaken at a laboratory scale, which involve exposing the base metal or polymer coated stent surface to a plasma beam in order to enhance chemical bonds in the drug release via polymer cross linking[76]. Spray coating is one of the most often utilized technique in which an apparatus is used to spray polymer/drug solution onto a stent, enabling consistent deposit of a uniform drug release layer. This method allows high variability of coating designs, therefore leads to better optimization in release profiles. This technique usually exhibits logarithmic release curves with a characteristic burst release profile due to the presence of a drug at the boundary between the stent and the vessel, which is then followed by a decrease in the release rate to enable long-term therapeutic effects[76, 82].

1.4.2. Die drawing

In the die drawing technique, polymer is heated up and drawn through a conical die with reducing cross sections at a set velocity. This results in the transition of amorphous polymer into the oriented polymer chains and allows control of biaxial or uniaxial orientation [67]. The

final product is often improved in its mechanical and thermal properties as a result of processing steps [83].

1.4.3. Solvent based spraying

Solvent based spraying on a commercial level, known more commonly as electrospinning or electrospraying on a laboratory scale level, requires dissolving of the polymer in a suitable solvent and then applying a certain voltage to produce fibres [84]. The fibres are collected onto a rotating rod for fabrication of a tubular scaffold. Although the process has several advantages over other commercially used methods, namely low temperature and porosity of the produced scaffold, the requirements for the reproducibility and mass production of scaffold are significant compared to other processes. Solvent based spraying allows the addition of drugs, simply by co-dissolving in the solvent with polymer, as well as other additives to tailor the properties of the final scaffold[85-87].

1.4.4. Microfiber monofilament processing

Microfiber monofilament processing is one of the few industrial processes which does not require elevated temperature for majority of the steps of the process. In this technology, highly oriented filaments are produced with directional mechanical properties that follow scaffold's radial strength requirements. In this technique, monofilaments are integrated into the circular geometry and then onto the desired strut structures. The process starts with highly oriented circular polylactide monofilament and has three major steps which include melt extrusion, followed by drawing of the monofilament fibres and finished up by the annealing process. The fibres have preferential direction which can influence their properties and match the specific needs for the scaffold. Devices which are produced with this technique have multiple axial microfibers and radiopaque markers attached to them at the ambient temperature in the final steps [48].

1.5. Clinical outcomes from the first generation of biodegradable stents

In July 2016, FDA approved the use of the first biodegradable coronary artery stent, the Absorb GT1 ™ Bioresorbable Vascular Scaffold (BVS). The stent was a fully degradable device made from poly-L-lactide coated with a thin layer of everolimus-eluting poly-D,L-lactide. However, the FDA released a statement in March 2017 reporting that recipients of the Absorb bioresorbable vascular scaffold experienced higher rates of adverse cardiac events including heart attack, death, and the need for additional procedures to reopen the vessel [88-89]. This hazard report resulted in the Absorb scaffold being pulled from the market in 2017.

The BVS was the first FDA approved fully-resorbable stent device, and its clinical failure illustrates that significant research needs to be done to address the shortcomings associated with the first generation of the device, particularly late and very late stage thrombosis. **Figure 1.3** displays optical coherence tomography images that illustrate some of the challenges associated with the *in-vivo* performance of the devices including (**Figure 1.3A**) strut malposition, (**Figure 1.3B**) incomplete coverage of the lesion, (**Figure 1.3C**) under deployment of the stent, (**Figure 1.3D**) acute disruption related to irregularities of a scaffold at baseline, (**Figure 1.3E**) irregularities in the device surface due to overlap of multiple scaffolds, (**Figure 1.3F**) a late discontinuity resulting in the protrusion of struts into the lumen, (**Figure 1.3G**) peri-strut low intensity area that indicates inflammation around the struts, (**Figure 1.3H**) uncovered struts, exposing pro-thrombogenic surface to the blood flow; and (**Figure 1.3I**) neoatherosclerosis. All of these challenges impede the clinical success of these devices by causing pro-thrombogenic changes in blood flow, exposing pro-thrombogenic scaffold material to the blood flow, and can cause inflammation around the struts.

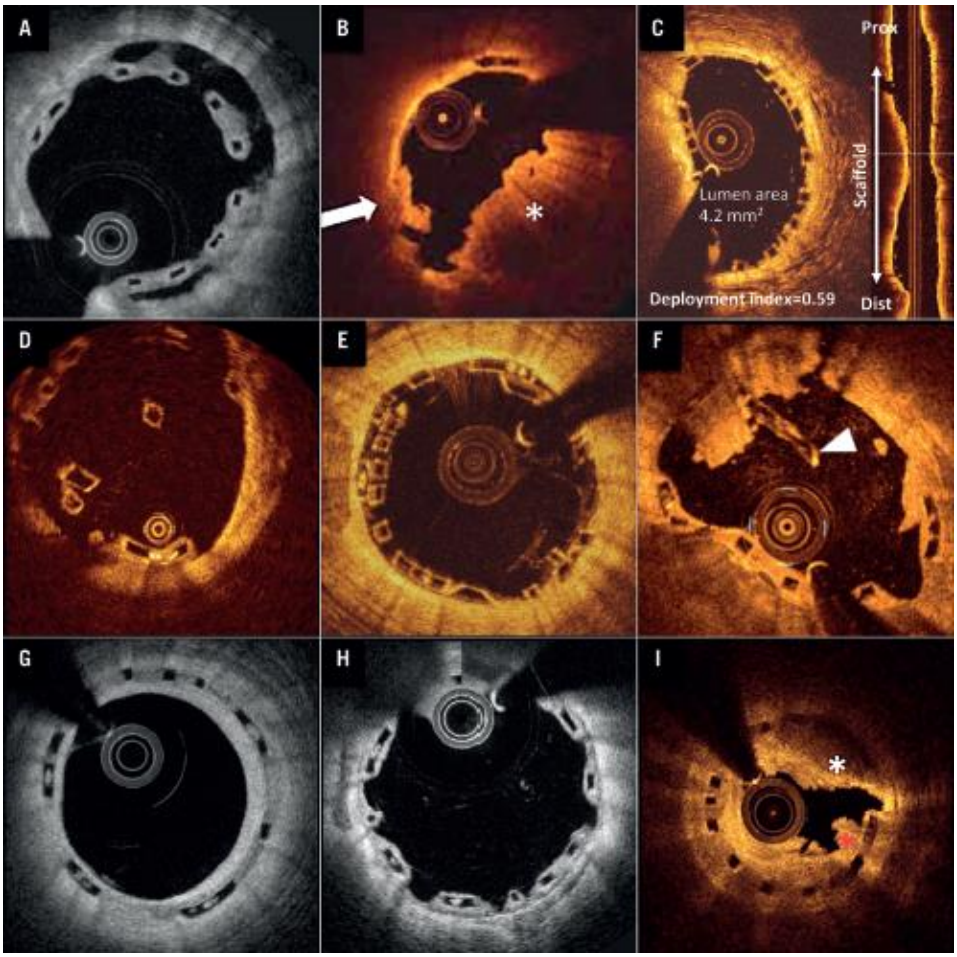

Figure 1.3: Optical coherence tomography images illustrating representative examples of challenges associated with biodegradable stents: (A) strut malposition; (B) incomplete lesion coverage, possible ruptured plaque (white arrow), and uncovered thrombus (white asterisk); (C) underdeployment; (D) acute disruption; (E) overlap of scaffolds; (F) late discontinuity; (G) peri-strut low-intensity area (corresponding to inflammation around struts); (H) uncovered struts; and (I) neoatherosclerosis. Figure reproduced with permission from ref 9. Copyright 2017, Europa Group.

The failure of the Absorb device led to the investigation of causes and provided both clinicians and researchers with insights into biodegradable stents safety long term *in vivo*. As shown in **Figure 1.3**, there are several causes responsible for the device failure, which can be related to: (1) mechanical disruption of physiological conditions (i.e., laminar blood flow and endothelial shear stresses) due to a large profile of a device and thick struts, (2) thrombogenicity of the polymer as it degrades and its degradation products (3) inflammation around struts. Causes such as strut malposition (**Figure 1.3A**), acute disruption (**Figure 1.3D)** and late discontinuity

(**Figure 1.3F**) are related to the biodegradation process. It was found that during the degradation process, degrading struts began to interfere with blood flow and detach from the scaffold, leading to strut malposition (**Figure 1.3A**). This process was happening in a manner that was disruptive to the physiological blood flow and endothelial shear stresses, therefore causing more thrombogenic conditions. Additionally, the Absorb device was found to degrade in large polymer pieces, which was causing acute disruption (**Figure 1.3D**) and late discontinuity (**Figure 1.3F**), as the blood flow was continuously exposed to large pieces of thrombogenic polymer and its biodegradation products. Other causes of a device failure were related to the thick struts of the Absorb scaffold (≈160 μm)[88-89], which resulted in impaired strut coverage by the neointimal tissue formation and inflammation around struts[4-8].

The neointimal coverage is an important aspect of stent implantation as it allows the vessel to come back to its natural state after implantation. In an ideal situation, the stent should be covered by newly formed neo-endothelium which is not always the case in permanent scaffolds. By the permanent presence of a metallic scaffold, a natural physiology of a vessel and its healing process is disrupted which affects blood lining, and can lead to higher rates of blood clots and scar tissue being formed, therefore leading to recurrence of restenosis[5, 7-8]. A scaffold is required in a coronary artery only for a few months after implantation to prevent restenosis related to vessel remodelling and acute recoil[4, 6]. The permanent presence of a stent can lead to many complications mentioned above. Therefore, biodegradable stents were believed to hold the potential of allowing the vessel to remain in its natural state after re-blocking the artery, and allow it to heal without adverse side effects, as compared to permanent scaffolds. Although the Absorb device showed impaired formation of the neointimal coverage, the reasons behind this were different as those in permanent scaffolds. In the Absorb scaffold, thick struts and larger cross-sectional profile of a device were believed to be the reasons behind

the impaired neointimal coverage. Therefore, finding the balance between the biodegradability of a device, optimal device cross-sectional profile, and thin struts, is critical for the formation of a neointimal tissue[4-8].

Strut thickness has a direct impact on the blood flow within the artery post implantation (**Figure 1.4**)[7]. Struts which are thick (> 80 μm) disrupt the laminar blood flow and change endothelial shear stresses within the artery. This further leads to shear-induced activation of platelets by overexpression of integrin $\alpha_{IIb}\beta_3$ followed by stabilization of platelet aggreges and thrombus formation. In the case of the Absorb scaffold, its thick struts (≈ 160 μm) were found to be correlated to the scaffold thrombosis and long-term safety *in-vivo*, due to the deceleration of neointimal tissue formation, disruption of blood flow and changes in endothelial shear stresses, as shown in **Figure 1.4** [4-8]. Several different designs and materials have been utilized for fabrication of biodegradable coronary artery stents, with aims at developing the most optimal

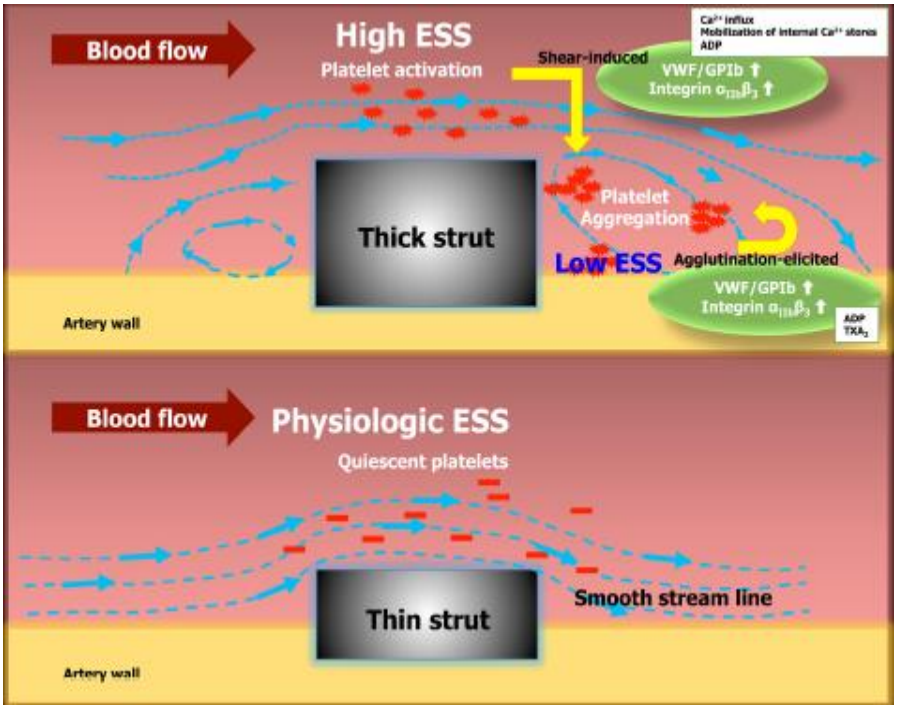

Figure 1.4: Schematic outline for the influence of strut thickness and stet design on physiological endothelial shear stresses within the artery. Reproduced with permission from ref 7. Copyright 2017, Lippincott Williams & Wilkins.

one. These polymeric materials vary in crystallinity, composition and arrangement of the polymeric chains, which then further translates to various performance in terms of degradation and inflammation, which could lead to scaffold thrombosis [4-8]. These studies aim at understanding the behaviour of the device in-vivo, after exposure to flow and shear-stresses within the artery, based on the differences in composition, designs, and degradation profiles. Consequently, studies report different behaviours in terms of inflammation and bio absorption based on composition and structure of the device [4-8]. They combine modelling and clinical evaluation of the devices which ultimately suggests that thick protruding struts induce flow disturbances and changes to endothelial shear microgradients. These shear microgradients have been shown to have three phases: shear acceleration phase, peak shear phase, and shear deceleration phase. The first of these phases correlates to platelets being in the central phase of the flow, and suddenly undergoing acceleration due to shear microgradient. In the next phase, these accelerated platelets are thought to adhere to exposed thrombogenic surfaces through platelet membrane glycoproteins, leading to further recruitment of the platelets into the downstream deceleration zone. In the deceleration zone, platelets are believed to decelerate through decreasing hemodynamic drag forces. As a result, reduced shear stresses within this zone lead to formation of integrin $\alpha_{IIb}\beta_3$ adhesion contacts. This flow behaviour is believed to be strongly related to changes in laminar flow, with magnitude of disturbance dependent on the protrusion of the struts into the lumen[4-8]. Other studies further built on current understanding of the impact of stent and scaffold material, as well as strut design and thickness both on the flow within the artery and on the thrombosis[128]. These studies were based on the careful analysis of different designs and materials, to gain an understanding into the relationship between the material, design and the mechanisms of thrombotic complications from the pre-clinical and clinical viewpoints[128]. These studies investigated materials ranging from stent alloys, magnesium, polymers and their derivatives such as PLLA, PDLA, PGA,

PCL, and those of mixed composition, therefore mixed hydrophilicity and hydrophobicity. Materials were compared in terms of their mechanical performance, corrosion resistance, biocompatibility, recoil, and biodegradability. The study combined the investigation and analysis of pre-clinical and clinical findings on the influence of strut and stent design, with computational fluid dynamics, and showed that excessive strut density and greater thickness increases local blood flow disturbances contributing to thrombogenicity[128].

Stent design, surface curvature and their influence on the flow were correlated with drug distribution and anti-proliferative properties on the atherosclerotic arterial wall. In the study, strut spacing, curvature and design were correlated with their influence on the rates of restenosis and drug coating distribution, as well as neointimal coverage of the stent. In terms of hydrophilicity and hydrophobicity of the material, and their influence on the flow within the artery, not many studies were conducted. Materials were usually analysed in terms of their crystallinity, strength, and adsorption time, as these three factors were found to be the most crucial in the determination on their applicability for the stent application[128].

1.6. Using materials science and advanced fabrication techniques to address critical challenges with biodegradable stent technology

The development of clinically successful biodegradable stents will require advances in material science and fabrication techniques to address the root causes of the failure experienced by the first generation of devices. In the next sections of this review, we will explore some of the advances in fabrication techniques and materials development that are occurring or could be implemented to enable development of clinically successful biodegradable stents.

1.6.1. Potential and challenges of additive manufacturing in personalized stent fabrication

Current industrial techniques for fabrication of polymeric stents usually involve extrusion or injection moulding, followed by melt blowing and laser cutting to obtain the final structure. Electropolishing and chemical post-treatment are generally utilized in the final steps to minimize surface irregularities [90]. These techniques lack personalized sizing, reguire high temperatures and do not allow drug-loading into the bulk of the device. The biodegradable scaffolds produced by these methods have struts with thickness from 100 µm to 250 µm [4, 48, 91], significantly thicker than the traditional non-degradable stents which range from 60 µm to 80 µm in thickness[91]. Current polymeric scaffolds either require thick struts for sufficient radial support, or lack the necessary mechanical properties *in vivo.*

The current methods of stent fabrication result in standard sizes that may not fit a desired patient's vessel or disease state, leading to difficulties in selecting the appropriate device, lengthier procedures, device-vessel mismatch, and post-procedure complications [7, 92]. Additive manufacturing technologies have potential to generate personalised and patient-specific stents, as described in **Table 1.4**.

Table 1.4: Emerging laboratory-based techniques for processing polymers into biodegradable stents [66]

Fabrication	Process characteristics	Advantages	Disadvantages	Ref
Fused Deposition Modelling	• 3D printing technique utilizing melt extrusion where many thin layers of polymer are deposited on top of one another • Materials melted for extrusion • Capable of fabricating 3D structures with feature sizes in the 100s of microns	• Micron level resolution • Short processing time	• Laying down the material in layers (limited designs) • Irregular surface • Limited to polymer melts	[93]
Photolithography	• Method utilized for tissue engineering yet to be explored for stent fabrication • Use of mask to photopolymerize and then cross-link polymers to fabricate 3D scaffolds	• Polymer can be loaded with additives and drugs	• High cost • Slow fabrication • Difficult to scale up for mass production	[94]

Stereolithography	• Maskless fabrication utilizing photopolymerization to cross-link polymers and generate 3D scaffold	• Automated • Fast • Easy fabrication of scaffolds with varying pore size	• Feature size limited to laser width	[94]
3D printing from solution or melt	• Polymer melted or dissolved in a suitable solvent • Melt extrusion of the polymer • Layer by layer formation of 3D structures	• Personalized size • Easy to adapt design • Addition of drugs and additives	• Low resolution • High temperature • Surface roughness • Limitations in nozzle size	[95-96]
3D printing with additives/nano fillers	• Additives melted/dissolved together with polymer • Co extrusion of the polymer melts with additives at adjusted parameters (temperature, purge pressure)	• Tailor of properties of the scaffold by selective choice of additives	• Optimization required for process parameters	[97]
Melt electrowriting	• Polymer melted and extruded through the nozzle • Voltage applied onto the polymer melt to draw the desired 3D structure • Continuous deposition of layers of material to obtain the final 3D design	• Complex structures fabrication with very high resolution (µm) • No need for laser cutting to produce a stent with struts • Allow drug and additives loading into the bulk of the material • Porosity of the scaffold • No solvent required • Reproducible	• Need to melt the material • Limitations in resolution	[98-99]

1.6.2. 3D printing/Fused Deposition Modelling

Melt extrusion 3D printing promising fabrication technique that received vast attention in recent years. In this process, the polymer is heated above its melting temperature in the cartridge, or dissolved in a solvent, and then the material is extruded through a nozzle by applying a certain system pressure. Once the material is extruded, it is cooled down in the case of melt extrusion or solvent is evaporated, in the case of solvent-assisted 3D printing. By continuous deposition of layers of the materials and custom-written programs, desired 3D structures can be created. Some research studies report fabrication of 3D printed stents, with strut thickness of 300 µm, and more lately 150 µm, yet these are quite far from industrial or commercial use [95, 97, 100]. The thickness of 80 µm, present in metallic stents, has been clinically shown to be the best-performing in metallic scaffolds [91, 101]. Fabrication of biodegradable,

polymeric stents with strut thickness close to 80 μm via 3D printing is limited by the nozzle size required to extrude the polymer melt through it and often times by the mechanism of material deposition in layer-by-layer manner. Although it is possible to 3D print a tubular structure, there is often significant roughness of the outer layer due to multi-layer extrusion of the material. Currently, 3D printed polymeric devices reported in the literature are with strut thickness of 500 - 600 μm [95], 300 μm[97], 150 μm [100].

More recently, studies have been performed that introduce nanofillers into the polymer matrix for enhancement of the mechanical and biological properties of biodegradable coronary scaffolds [97]. The feasibility of 3D printing of polymer-carbon composite has been shown with novel approach of utilization of medical images of patient's arteries onto the stent design (**Figure 1.5, Figure 1.6h**) [97]. The study is one of the first that successfully shows the concept of personalized 3D printing of biodegradable stents with patient specific approach. Additionally, the dual drug elution profile of the device, with combinatorial drug release of anti-coagulation drugs and investigation of the deployment of the stent in the swine heart, show its potential for more detailed animal studies. Some of the limitations of the study remain the strut thickness, which is close to 300 μm, and evaluation of clinical long-term performance of the scaffolds.

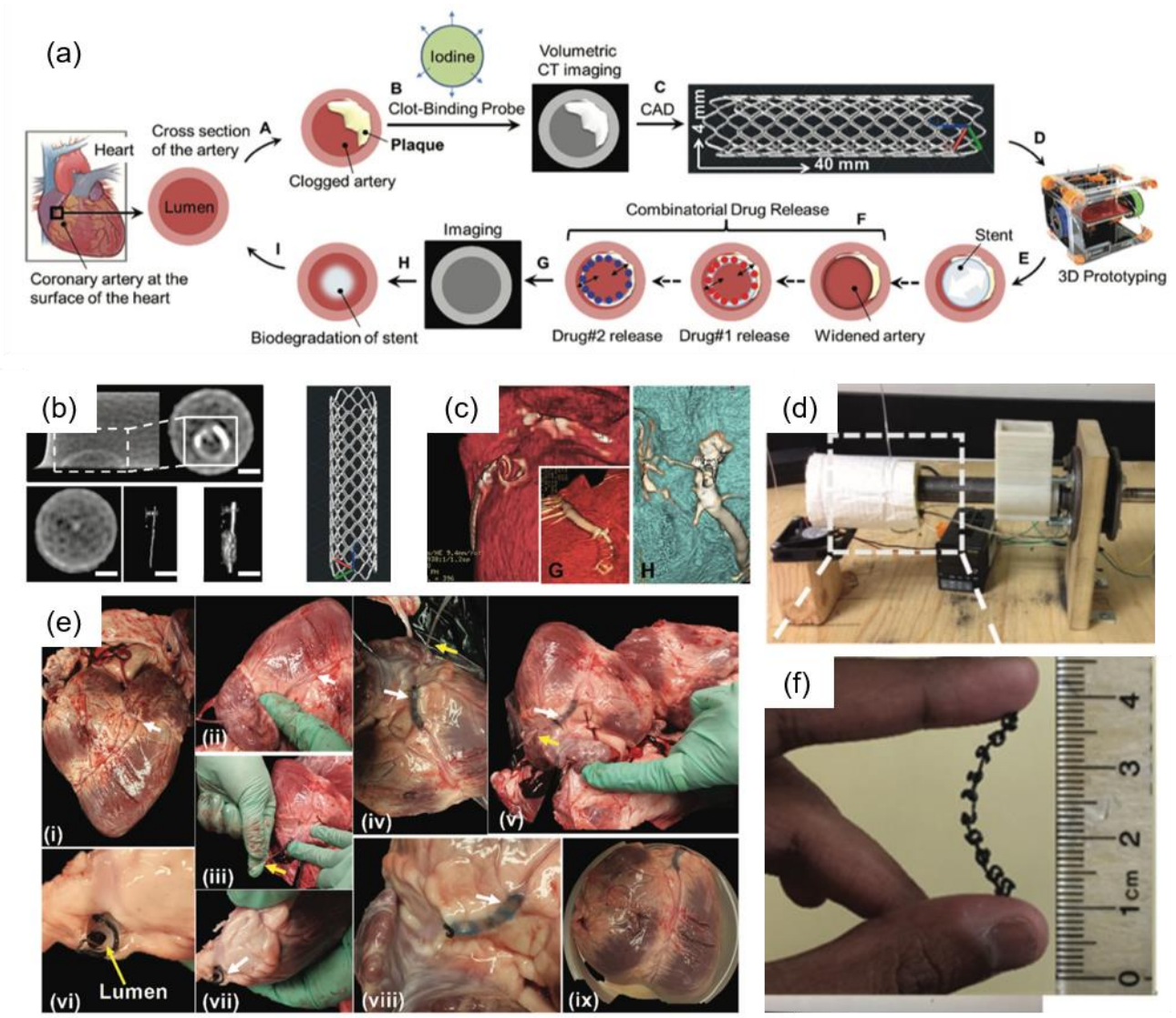

Figure 1.5: 3D printing of multidrug eluting patient-specific polymeric biodegradable stent. (a) Schematic of 3D printing of personalized stents. The process begins with CT imaging of the cross-section of the coronary artery and the diseases plaque. Custom made CAD design of the biodegradable scaffold is prepared utilizing the CT images of the patient. Upon the successful fabrication of the prototype using custom-build extrusion 3D printing setup, the device is implanted, which is followed by multi-drug elution and degradation. CT imaging is performed to assess healing of the artery. (b) CT images of the coronary artery and stent design (c) CT images of the pig heart with implanted scaffold (d) Custom-built extrusion setup (e)Steps involved in the ex-vivo implantation of the scaffold in the pig's artery (f) Biodegradable drug-eluting polymeric stent. Reproduced with permission from ref 97. Copyright 2017, Wiley.

In the other studies (**Figure 1.6a-d**), authors characterized biological performance of 3D printed PCL scaffold with sirolimus/PEG/PLGA coating deposited via spray technique with strut size from 300 – 1300 μm [102]. The study performed animal tests using pigs, with no fatalities following up the device insertion and up to 4 weeks after stenting. Some inflammatory response has been observed around the struts with decreased amount in sirolimus coated stents. Process parameters of 3D printing and its influence of the physical features of 3D printed PCL stent has been investigated [95]. Different parameters such as printing nozzle temperature, flow rate, speed, and trajectories were evaluated in terms of its effect on final stent structure (**Figure 1.6e-f**). Devices were further characterized in terms of their radial behaviour. Additionally, the influence of nozzle, flow rate, and printing speed on resulting strut thickness has been quantified. The results suggest that higher nozzle temperature led to lower strut thickness - 195μm was reported as the lowest the device could reach. Higher flowrate has been correlated with higher strut thickness and higher printing speed has been correlated to lower strut thickness [95]. Similarly, other studies investigate the processing parameters for 3D printing using methacrylated poly(1-12 dodecamethylene citrate) (**Figure 1.6g**), and show the optimization process of desired stent like structures with 150 μm strut thickness and radial stiffness compared to the nitinol stents [96].

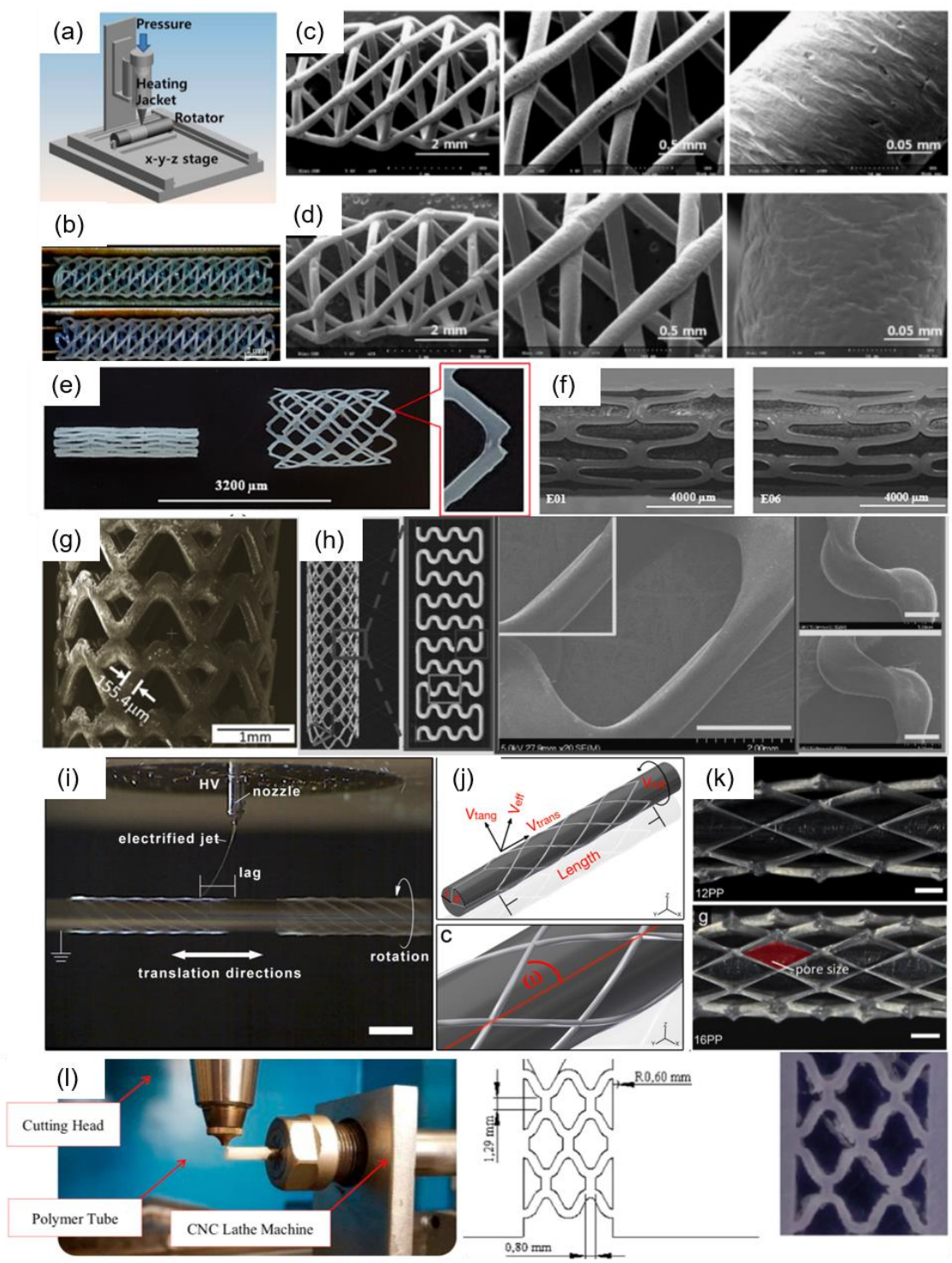

Figure 1.6: Representation of laboratory-based fabrication methods for polymeric coronary artery stents (a) Schematic of 3D printing setup (b) 3D printed PCL/PLGA/PEG vascular scaffolds (c) (d) SEM images of drug-eluting scaffolds. Reproduced with permission from ref 102. Copyright 2015, Elsevier. (e) (f) 3D printed PCL stents with various strut thickness. Reproduced with permission from ref 95. Copyright 2018, Elsevier. (g) 3D printed methacrylated poly(1-12 dodecamethylene citrate) stent. Reproduced with permission from ref 96. Copyright 2018, Elsevier. (h) Stent design and SEM images of the 3D printed composite scaffolds. Reproduced with permission from ref 97. Copyright 2017, Wiley. (i) MEW setup including a nozzle with high voltage and produced jet with polymer. Scale bar 2µm. (j) Design of a tube produced via MEW with control over length, translational, tangential, effective and rotational velocities. (k) Illustration of the pivot angle between pivot points and resulting porosity in melt electrowritten scaffolds. Reproduced with permission from ref 99. Copyright 2018, Elsevier. (l) Experimental setup for laser cutting of polymeric tubes in 3D using fibre laser and laser cut polymeric mats. Reproduced with permission from ref 96, 106. Copyright 2017, Elsevier.

1.6.3. Photolithography/Stereolithography

Photolithography utilized a mask to photopolymerize and cross-link polymers, resulting in a three-dimensional scaffold. The technique allows uniform encapsulation of cells, and easy control of pore size through variation over polymer type and concentration. In its mask-based form, it requires manual and prefabrication of multiple photomasks for multi-layer scaffolds therefore is difficult to scale up and requires significant amount of time for fabrication of a final device[94].

Stereolithography is a photolithography-based process which uses a maskless photopolymerization to cross-link polymers and produce a three-dimensional scaffold[94]. Some of the main advantages include its automation, fast processing, ease of fabrication of structures with different parameters such as pore size or elasticity. However, the feature size that can be polymerized is limited to the beam width of the laser[94].

1.6.4. Melt electrowriting

MEW is an emerging technique which utilizes melt extrusion and applied voltage for fabrication of highly ordered 3D structures with various application in biomedical field [103]. In this method, a polymer with high viscosity and low conductivity results in a melt flow which is followed by cooling down of the electrified jet and solidification of deposited material. Studies has shown the feasibility of use of the technique for fabrication of scaffolds with sub-micron filaments [98, 104]. The technique allows fabrication of structures with typical fibre diameters from 5 to 30 μm and allows writing of the material to millimetre heights [98]. Previous studies investigated the influence of instrument parameters on melt electrowriting of PCL and characterized the resulting scaffolds in terms of its crystallinity and fibre orientation [99, 104].

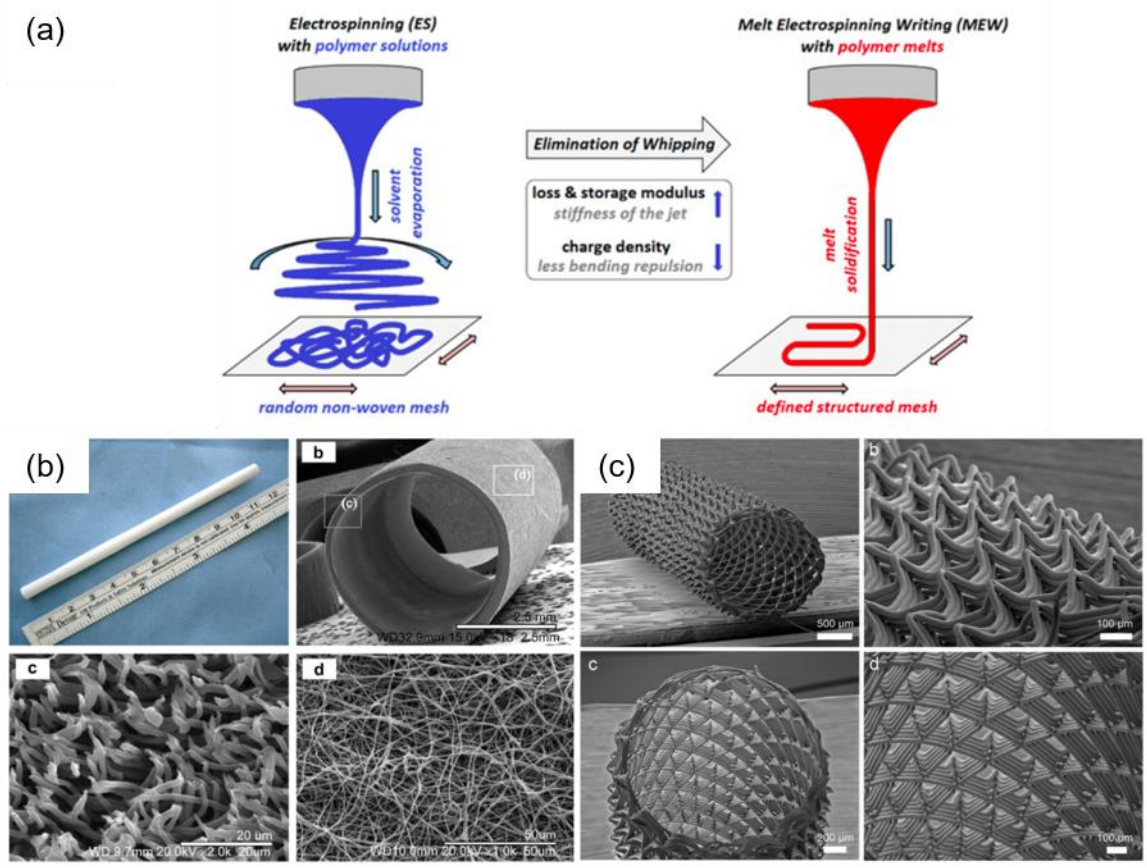

Figure 1.7: The schematic showing the difference between solution-based electrospinning and melt electrospinning writing methods with resulting tubular scaffolds. (a) Comparison of solution electrospinning and melt electrowriting techniques. The polymer melt in MEW leads to a more stabilized jet compared to the use of polymer solution in ES and better control of the 3D features. Reproduced with permission from ref 98. Copyright 2015, IOP Publishing. (b) Electrospun PCL tubular scaffolds and the resulting fibrous structures. Reproduced with permission from ref 127. Copyright 2009, Elsevier. (c) Melt electrowritten PCL tubular scaffolds and the resulting fibre structures. Reproduced with permission from ref 99. Copyright 2018, Elsevier.

The feasibility of additive manufacturing of tubes with desired pore size, angle between the filaments, and printed length has been shown (**Figure 1.6i-k**)[99]. The study shows the potential of the technique for fabrication of custom-designed, personalised scaffolds with well controlled parameters. One of the major advantages of the MEW technique is an easy control of the device design via custom-written software, porosity of the scaffolds, and reproducibility [103]. Additionally, the mechanical properties of melt electrowritten devices are higher compared to electrospun scaffolds due to use of polymer melt rather than a solution in the fabrication process. Also, in the case of electrospun scaffolds, fibres are not fused together, unless annealing step is used – this weakens the overall structure of the scaffold. It is also suggested

that the use of a melt in the MEW process rather than polymer solution results in a stabilized jet and more control in the deposition of the material (**Figure 1.7a**) [98]. While tubular structures have been fabricated using MEW, the technique has not yet been explored for the fabrication of coronary artery stents.

1.7. Critical comparison between commercial and lab-based techniques

Current manufacturing techniques for fabrication of polymeric biodegradable stents range from extrusion, blow moulding, die drawing, microfiber monofilament processing, solvent based spraying and post-processing techniques including annealing, electropolishing and laser cutting. The majority of these methods require high temperatures at some point in the process, do not provide individual sizing, and are used for mass-production of thousands of similar tubes, rather than patient specific devices. Additionally, the drug loading takes places through the coating of a stent, rather than through incorporation into the bulk of a device. Other major limitation of current manufacturing techniques and materials used is the strut thickness of produced devices, which ranges from 100 μm to more than 200 μm. Although there are some biodegradable polymeric devices currently under development, with targeted strut thickness below 100 μm, they are not available on the market and more intensive research and development as well as lengthy clinical trials are required for their approval. The main challenges to be overcome for the clinical application of the bioabsorbable scaffold are the scalable fabrication of devices with thin struts, sufficient radial force and long-term safety in vivo.

Currently in industry, the limitations of the materials and fabrication techniques are mainly addressed by post-processing techniques such as thermal treatment (annealing), micro-braiding

which involves the stretching of the fibres to increase the strength of them, or by forming of interconnected networks between the fibres.

Emerging additive manufacturing techniques hold the potential to address the limitations of manufacturing practices by their custom-design approaches to printing and production of personalized scaffolds, feasibility of use of many polymers, polymer composites or polymer derivatives as an input material, easy control of the size of the scaffold, and reproducibility of the technique. 3D printing of medical devices is bringing lots of attention not only in coronary artery field but overall in biomanufacturing of medical devices with several new regulations coming up from FDA in regard to 3D printing of medical implants [105]. As mentioned previously, several studies showed the feasibility of 3D printing of polymeric biodegradable coronary stents with different polymers and studied the influence of the nozzle type, printing speed, or temperature on strut thickness. The most recent reports of coronary stent fabrication utilize additive manufacturing techniques, with the use of various polymers such as PCL [95, 102, 106], methacrylated poly(1-12 dodecamethylene citrate) [96] or polymer composites [97]. The limitation still lies in thick struts of devices, yet the field progression may soon be able to address the issue with novel 3D printing techniques which utilize electric fields.

This brings us closer to MEW technique, which extrudes material that is then collected on the translating collector by applying pressure, heating the polymer and applying voltage. The method allows writing of the polymer in three different directions with control of the height of the structure and its final shape. Studies have shown the feasibility of MEW of tubular scaffolds with control of pore diameter, length, and distance between the strands of the material. The technique, similar to 3D printing, allows the control of the device design and opens up the possibility of its use for fabrication of patient specific scaffolds on demand. Additionally, the

technology has high resolution and better control of the printing, as compared to 3D printing, and usually requires lower temperatures. As mentioned above (Section 1.6.4), studies have been performed which showed the feasibility of production of a well-controlled tube with desired properties thus it shows high potential for the future application in biomanufacturing of polymeric biodegradable stents.

Solution electrospinning is a technique that recently found its way into the industry, with Elixir Medical company utilizing it for fabrication of biodegradable scaffolds with post-processing steps involving annealing. Little information is presented on the laser cutting of the tubes produced with this technique, thus we cannot comment on it with regard to other techniques. Usually in the laboratory setting, electrospinning is a process highly influenced by many factors such as humidity, temperature, or system design, and its reproducibility requires tight controls on all of these variables, often difficult in the research laboratory. The use of the technique for industrial scale process requires well controlled environment and protocols.

Laser processing, utilized both in industry and slightly less studied in academia, is a common post processing technique for polymeric tubes to note. Industrially used laser usually range from Nd:YAG, femto-second and excimer laser, with the latter two usually more applicable to transparent polymers. Although lasers allow fabrication of thin structures down to 30 μm with high resolution, their use is very expensive and usually only utilized in industrial environment. The remaining issue with the use of the laser is its thermal effect on the polymer and production of the heat affected zones.

Solution electrospinning with annealing followed by laser cutting, 3D printing and melt electrowriting are the most promising and researched techniques for fabrication of polymeric

biodegradable scaffolds with application in stents. The low temperature of the solution electrospinning makes it an appealing technique as annealing can be further used to improve the mechanical performance of the material, or alternatively the addition of reinforcing fillers to the polymer solution before electrospinning. 3D printing and melt electrowriting both offer the custom-made design alongside a personalized patient-centric approach but still require high temperatures to melt the material. MEW seems to have an advantage over 3D printing due to better control of the device filaments and easy production of more complex 3D structures like coronary artery stents.

1.8. Scope of the work

1.8.1. Designing the ideal bioabsorbable and drug-eluting stent

The clinical failure of the first generation of bioresorbable stents illustrates that there are key improvements that need to be made before this technology can reach its commercial and clinical impact. Some of these advances can be made through improved selection and design of materials and others can be achieved through the use of emerging fabrication processes.

1.8.1.1. Materials development

From a materials point of view, there are many key characteristics for an "ideal biodegradable drug-eluting stent". Some of the major ones include its mechanical integrity: the device requires sufficient ductility to perform well under scaffold expansion process during deployment as previous clinical cases with under-expansion of the scaffold have been linked to device thrombosis or later device failure [7, 9]. Additionally, it must have high tensile strength and stiffness to allow fabrication of thin struts (≈ 80 μm) without loss in radial strength of the scaffold.

To fabricate an ideal stent, a material is required which has high tensile strength, high elongation at break, and high radial strength (compressive strength), to minimize strut thickness, therefore decrease the likelihood of changes in blood flow. At the same time, this material needs to be biodegradable, biocompatible and haemocompatible. High tensile strength after expansion allows a lower volume of foreign material in the artery thus a decreased inflammatory response. The elongation at break of the scaffolds must be high as well, to allow the wide range of scaffold expansion and proper deployment during the angioplasty. Thinner struts of the biodegradable scaffold permit a fabrication of a device with smaller cross-sectional profile therefore improving its flexibility, deliverability and leading to easier implantation for the clinician and less risk of procedure related complications.

It is important to note that current polymeric materials do not have all the necessary properties needed for development of the ideal coronary artery stent from materials point of view. As we outlined previously, the ideal stent should be characterized by high tensile strength, high elongation at break, and high ductility. From a mechanics point of view, as the elongation at breaks increases, usually the material's tensile strength decreases. This is also correlated to the ductility of the material as a material with low tensile strength is usually characterized by high ductility, and a material with medium tensile strength, with medium ductility. The current challenge from materials viewpoint for biodegradable coronary stents lies in the balance between high tensile strength, high elongation at break, and enhanced ductility. Finding the suitable approach to achieve these three mechanical characteristics in one biodegradable polymeric material is a significant challenge in the field of polymer science itself [7, 107-108].

Current limitations of bioabsorbable devices are the following: 1) low tensile strength and stiffness of the materials which leads to thick struts required for sufficient vessel support and

prevention of the acute recoil; 2) insufficient ductility of the materials which directly influences the expansion range of the device during the angioplasty procedure and scaffold retention on the balloon catheter[7]; 3) loss of mechanical properties during the vessel remodelling given that the degradation of the device happens too rapidly [90, 109-110]. Polymers which have been previously used for manufacturing of the biodegradable stents include PLA, PLLA, PDLA[107]. These materials are significantly lower in terms of their tensile strength, modulus, and elongation at break compared to metallic scaffolds which utilize cobalt chromium or platinum chromium alloys. The gap between the low mechanical performance of polymers and high requirement for radial support for the vessel is currently addressed with the use of larger amount of the polymer, therefore larger volume of the device. This directly leads to a larger cross section of the stent and thicker struts which has adverse clinical effects as mentioned previously[7].

Although initially the focus was to utilize PLA, PLLA, and PDLA for fabrication of bioabsorbable scaffolds [107], PCL has recently brought more attention as a possible candidate for fabrication of biodegradable stents due to its low melting temperature, high elongation at break, and high tensile strength [95, 102, 106, 111]. PCL is polymer composed of hexanoate repeat units from the class of aliphatic polyesters[112]. PCL has been widely studied for its physical, thermal and mechanical properties, which depend upon its molecular weight, as well as degradation mechanisms. In general, PCL has limitations related to its glass transition temperature (< -60 ºC), elastic properties, tensile and compressive behaviour compared to other polymeric materials such as PLA[112]. However, PCL is characterized by long degradation time (2 - 3 years), which is longer as compare do other polymers utilized for fabrication of stents such as PLLA[112]. Longer degradation time of PCL could be problematic as it could lead to more inflammatory responses due to long exposure of the polymer in the artery, or other

clinical complications. These drawbacks of PCL could be addressed by clinical studies of PCL stents and perhaps provide more in depth understanding of complications that could arise. Additionally, a viable method to improve mechanical performance of PCL and direct its biological, thermal or physical behaviour to desired characteristics is to blend it with reinforcing additives such as carbon-based nanomaterials.

There are many reinforcing additives available for fabrication of a composite to enhance the mechanical strength of a material and tailor its properties such as organic or inorganic additives in various dimensional forms[113-114] (**Table 1.5**). Different additives have been studied with various dimensional sizes such as zero-dimensional (nanoparticles, dots), one-dimensional (nanotubes, nanorods, nanowires), two-dimensional (planar, sheets, nanofilms, nanolayers, nanocoating), three-dimensional (hierarchical structures) – both in organic and inorganic forms[113-114]. Zero-dimensional (0 D) materials can be amorphous or crystalline, and exist individually or incorporated in matrix, and compose of metal, ceramic or polymer. One-dimensional (1 D) nanomaterials are needle like shaped, and similarly to zero-dimensional material can be amorphous or crystalline, and made of metal, ceramic or a polymer. Two-dimensional (2 D) nanomaterials exhibit plate-like shapes and are deposited on a substrate. Similarly, to other materials, two-dimensional materials can be metallic, ceramic, polymeric and amorphous or crystalline. Three-dimensional (3 D) nanomaterials are composed of highly hierarchical structures and can be metallic, ceramic or polymeric. From functional point of view, there are many additives previously studies such as reinforcing, conductive, semi-conductive, insulating, piezo-electric, magnetic, coupling, extender filers or plasticizers (**Table 1.5**). Each of these functional additives has a different effect on polymer properties after its introduction into polymer matrix and by a precise choice of a functional additive, properties of material can be adjusted to desired application. Reinforcing additives are usually carbon based,

fibrous or glass, and they have been all reported to increase the tensile strength of materials after their inclusion into the polymeric matrices[114]. Conductive, semi-conductive, and piezoelectric additives are excellent choices for applications in which conductivity can enable material processing or influence electrical outputs. Magnetic additives can be useful in applications that use magnetic forces to direct interactions with cells or other biological functions. Other additive types such as extender fillers or plasticizers, can influence the material to promote its processing under desired conditions.

Some of the requirements for a composite to work as a stent material are enhancing its tensile strength and modulus without loss of flexural stiffness and compromise on elongation at break, increase in compressive strength, improvement of melt-flow properties (if fabricated via additive manufacturing utilizing melts). From a biological point of view, thrombogenicity, inflammatory response and biodistribution are some of the most crucial aspects. Once the stent begins to degrade, the composite material will slowly dissolve leading to small pieces of a composite in human body which can cause problems with accumulation in different organs and tissues. Nanocomposite materials which are naturally exerted though the body with minimal accumulation are preferred to be used in application relating to implantable devices such as stents. There are many filler types which could be potentially used as reinforcing additives for polymers **(Table 1.5).** Reinforcing additives offer great mechanical strength after incorporation of a filler and one of the most promising fillers are carbon-based, or graphene-based fillers due to their properties.

Graphene based materials have been widely studied due to their excellent mechanical strength, thermal conductivity, electrical conductivity, and ability to direct cell behaviour[115-117]. Studies have been performed which investigated biodistribution of graphene-based materials after

administration to animals via different routes. The effects of rGO were studied by oral administration to mouse [118]. It was shown that most of the rGO nanosheets appeared to be removed from the body 15 days to 2 months post-administration. The study suggests that rGO migrated into the blood after oral administration and circulated through entre system. The rGO nanosheets were mainly located (in descending order) in the kidney, stomach, liver, lung and blood 1 day post-treatment, indicating that a considerable amount of rGO penetrated the main organs through intestinal absorption. 60 days after administration of rGO, the concentration in liver, kidneys and brain was below the detection limit of the instrumentation [118-119].

Similarly, several studies have been performed in which inflammatory response after graphene distribution was studied [119]. In these studies, different route of administration was investigated such as nasal inhalation, intra tracheal instillation, pharyngal aspiration, intravenous injection, intraperitoneal injection. In case of nasal inhalation, graphene and graphene oxide was tested with various concentration and sizes. In was found that lower concentrations, below 3 mg/m^3, do not induce inflammation. Studies on intra tracheal instillation revealed that larger size of GO provides inflammation while smaller does not. The sizes investigated were from 10 nm to 800 nm. Pharyngal aspiration studies showed no inflammatory response with small size graphene (50 nm - 350 nm) and some response in large sizes (750 nm - 130 nm). More studies were performed on intravenous injection of graphene, graphene oxide and combinations of GO with dextran or PEG. In most of the cases inflammatory response would depend on concentration, with higher concentrations (10 mg/kg) producing some inflammatory response but the studies were not consistent. The rest of the studies, on intraperitoneal response of graphene oxide injection, confirmed stronger inflammatory response with large size graphene oxide (750 nm – 1300 nm) [118-121].

Table 1.5: Effect of additives, fillers, and reinforcement additives on polymers.

Additive/Filler	Common materials	Effect on polymer properties	Biodistribution/ Thrombogenicity	Ref
		Functional Types		
Reinforcing	Carbon, fibrous materials, glass	-Increases tensile strength -Increases flexural modulus	-Biodistribution and inflammatory response based on composition, size, concentration of a nanofiller -Renal and blood excretion with reports of accumulation in spleen and liver -Functionality dependent biodistribution and thrombogenicity -Lack of studies in human and large cohort clinical trials	119, 122-125
Conductive	Aluminium powders, carbon filler, graphite	-Improves electrical and thermal conductivity		
Semi conductive	Transition metal dichalcogenides	-Provides tailorable conductivity		
Insulating	Graphene oxide	-Increases mechanical strength -Limits conductivity		
Piezoelectric	Lead zirconate titanate, barium titanate, chitin, collagen	-Mechanical actuating properties		
Magnetic	Ferrous oxides, nickel, cobalt, cobalt-platinum	-Provides magnetic functionality		
Coupling agents	Silanes, titanates	-Improves interface bonding between polymer matrix and fibres		
Extender fillers	Calcium carbonate, silica	-Reduces material cost		
Plasticizers	Monomeric liquids, low-molecular weight materials	-Improves melt flow properties -Enhances flexibility		
		Hierarchical types		
0 D	Nanoparticles, dots (metallic, ceramic, polymeric)	-Dependent upon composition of the filler	-Removal from the body within months after administration	117-119
1 D	Nanotubes, nanorods, nanowires (carbon nanotube, halloysite nanotubes)	-Dependent upon composition of the filler	-Exerted primarily through kidneys -Exertion dependent upon size of nanofiller, composition and concentration - Biodistribution primarily through kidney, stomach, liver, lungs and blood	
2 D	Nanofilms, nanolayer, nanocoating, nanosheet (layered silicate, graphene, MXene, BN, MOS_2, WS_2)	-Dependent upon composition of the filler		
3 D	Hierarchical structures (MOF)	-Dependent upon composition of the filler	-Inflammatory response dependent upon size of nanofiller, concentration and method of administration -Lack of consistency in reported studies and clinical studies in human	

Additionally, other reports suggest that biodistribution of nanofillers is dependent upon the route of administration, concentration, size and composition of the nanofiller. Usually, higher concentrations of nanofillers lead to more profound inflammatory response and longer time to exert the nanofiller through kidneys, and longer accumulation in other organs[119]. Size of a

nanofiller is another important aspect which affects its biodistribution and accumulation, with larger sizes of nanofillers leading to inflammatory response[122-123].

1.8.1.2. Degradation and drug elution

In terms of degradation and drug elution, the stent should resist vessel recoil during the arterial remodelling and healing process for at least 6 – 12 months, with no loss in mechanical strength and no influence on the surrounding tissue after it has healed [126]. The biodegradation period has to be sufficiently long to allow for the required vessel support and degrade as small polymer pieces rather than large chunks that can then lead to inflammation. A porous device could potentially be clinically beneficial through small fibre degradation rather than larger parts of polymer.

Drug elution from a device is usually required at initial stages, in the form of anti-proliferative drugs such as everolimus and sirolimus, to prevent in-stent restenosis (re-narrowing of the artery despite use of stent). Drug elution of anti-thrombotic agents from the device could potentially reduce platelet adhesion and aggregation therefore reduce the risk of thrombosis during the scaffold degradation and potentially improve its safety in vivo long term.

While anti-proliferative drugs are hydrophobic in nature and are usually incorporated onto the device surface via their embedding in hydrophobic polymer, majority of anti-thrombotic agents are hydrophilic in nature. This is problematic for local drug delivery of anti-thrombotic drugs from a hydrophobic scaffold at the later stages of the device lifetime. A potential strategy to address these limitations could be development of drug delivery platforms which are hydrophobic in their exterior, and hydrophilic in their interior, therefore allowing the encapsulation of hydrophilic drug internally, and homogenous blending of the hydrophobic exterior within the hydrophobic matrix of a device.

1.8.1.3. Radiopacity

Additionally, the ideal stent would exhibit full radiopacity on clinically used X-ray, MRI and CT to allow the tracking of the stent location and biodegradation in vivo as well as improve implantation process. The majority of biodegradable polymeric stents are made of polymers which are not radiopaque under clinically used X-ray, which was the case with the Absorb BVS scaffold. Having the radiopacity would enable better implantation to prevent under expansion and incomplete lesion coverage and could potentially enable real time monitoring of stent degradation. However, most of the contrast agents are hydrophilic in nature, therefore incorporating them into the stent is a similar challenge to hydrophilic anti-thrombotic drug encapsulation. Alternatively, use of contrast agents which are more hydrophobic in nature such as lipiodol could be a potential solution as the hydrophobic contrast agent could be simply blended into the hydrophobic polymer matrix. Accomplishing radiopacity of a device, combined with drug eluting properties, without jeopardising the mechanical properties is difficult yet critical.

1.8.1.4. Fabrication techniques

In terms of the fabrication techniques, the ideal stent would be fabricated in a process that allows personalized sizing, does not require high processing temperature thus allows drug-loading into the bulk of the device. The technique would allow fabrication of a porous scaffold with sufficient mechanical properties to allow vessel support.

The “ideal stent” would exhibit porosity and allow degradation in small fibre pieces rather than big chunks of polymer melt. A scaffold which consists of nano-scale fibres and which is porous would preferentially degrade in surface degradation mechanisms rather than bulk degradation. Additionally, a porous scaffold could potentially lead to a better clinical outcome due to

promotion of cell differentiation and endothelialisation, without platelet adhesion and aggregation. Device-vessel mismatch has been previously linked to stent thrombosis therefore a fabrication process that allows personalized sizing and matches its profile to the patient's vessel could potentially lead to better clinical performance.

The key challenge in the field of biodegradable polymeric coronary artery stents is to achieve a balance between: 1) scaffold properties such as porosity, proper mechanical performance, desired degradation, full radiopacity; 2) drug-eluting profile including multi-drug elution over time, combination of anti-proliferative drugs and anti-thrombotic drugs; 3) manufacturing process which is low temperature, low cost and allows fast mass production 4) clinical performance with superior outcomes of biodegradable devices relative to the currently used second generation metallic stents, excellent deliverability and long term safety *in vivo.* Achieving this balance is a task that requires interdisciplinary efforts of materials scientists, biomedical engineers, clinicians and industry practitioners to achieve a positive outcome and make bioabsorbable drug-eluting stents a reality rather than an emerging yet inferior technology.

1.9. Conclusions

Development of the next generation, bioabsorbable, drug-eluting coronary artery stents is the common direction of many scholars, researchers and industrial companies in the field. The ideal devices would be fully biodegradable, have superior mechanical properties as well as thinner struts compared to previously developed bioabsorbable scaffolds, deliver anti-platelet and anti-proliferative drugs over their lifetime, would not cause early or late scaffold thrombosis, and display visibility under clinically used X-ray.

Fabrication of a device that has thin sturts, high radial strength and elongation at break is the key issue in successful development of bioabsorbable scaffolds. Improving the manufacturing technique to obtain a stent with thinner struts to current biodegradable scaffolds could potentially lead to better coverage of lesions and decrease the likelihood of flow disturbance and changes in endothelial shear stress and scaffold thrombosis.

Long term scaffold thrombosis remains the significant threat and issue to biodegradable polymeric stents given the previous history of Absorb device. So far, drug-eluting polymeric stents have coatings with anti-proliferative drugs to address in-stent restenosis (re-narrowing of the artery despite use of stent). In the case of these devices, as they degrade away, the drug-eluting coating erodes first leaving the large density of bulk polymer inside the artery with no active drugs but high thrombogenic potential. Minimizing the activation of thrombogenic pathways through local drug delivery, during late device degradation, has not been addressed before. Delivery of drugs which interact with integrin $\alpha_{IIB\,\beta_3}$ at later stages of device has not been studied and could possibly lead to low rates of late and very late scaffold thrombosis. So far, no devices addressing this issue have been developed.

Looking at the field from a materials point of view, development of novel polymeric systems via new synthesis pathways could be a potential future direction in the field. The desired material system would need to display superior mechanical properties to currently used second generation metallic drug-eluting stents, and high values of tensile modulus, tensile strength, elongation at break, and durability. Additionally, it would need to be radiopaque under clinically used X-ray and not cause thrombosis or inflammation long term *in-vivo*. From processing point of view, it would need to have low melting temperature or good solubility in common green solvents, so it does not require high processing temperatures or toxic solvents.

Synthesis of a material with these properties could potentially solve the issue of current biodegradable polymer yet long regulatory pathways and clinical trials required would slow down its potential presence on the market. Additionally, any new material requires series of testing in terms of its biodegradation, long-term mechanical performance during the degradation process, and toxicity studies.

In terms of manufacturing process, the current field tends to move towards personalized fabrication techniques such as 3D printing or MEW[95, 97, 100]. Patient specific approach and custom-made devices could potentially address the problem of device-vessel mismatch and significantly decrease the time required to match the device with patient's artery. 3D printing is a promising future direction in the field of medical device manufacturing, yet limitations related to low resolution, nozzle size and fabrication of thin struts remain to be solved. As of now, medical devices made through 3D printing have thick struts (> 150 μm) and more research and development are needed to optimize the process or design novel polymeric materials for further reduction in strut thickness. MEW is a promising technique that could be utilized for fabrication of polymeric biodegradable stents given the starting material holds the required mechanical properties for the stent to be sufficiently stiff in radial direction.

Substantial advancement has been made in polymeric biodegradable scaffolds over last 10 years, with many emerging laboratory and commercial systems being developed. Although these devices show the fast progress in the field, there is clear need for more clinical data to ensure their safety and understand their possible side effects long term. Current polymeric material systems do not have all the necessary properties of a "perfect stent material" in terms of the mechanics, radiopacity, and clinical performance long term in vivo. More research and development in the field of biodegradable polymers is needed with novel biocompatible

materials synthesized or utilization of various polymeric composites. Combination of materials with additives, or design of a new polymer, could potentially solve the limitations of current devices. Additionally, scaffold thrombosis remains the major complication that needs to be tested long term, given the history of the previous Absorb device, thus novel materials need to be anti-thrombotic long term.

Majority of current manufacturing techniques require high temperature, do not permit drug loading into the bulk of the material and do not provide personalized sizing. Patient specific on-demand fabrication of medical devices are current trends in the field with lots of potential to transform clinical setting and manufacturing. 3D printing and MEW have several advantages over conventional fabrication techniques of stents, but many limitations need to be addressed to fully incorporate its use in medical field such as low resolution, limited thickness of stent struts and high temperature of printing.

Given the rapid growth of the biomanufacturing field and continuous development of novel biomaterials, it is very likely that within next 10 - 20 years, many emerging polymeric systems will be developed, with wide range of mechanical properties and excellent biocompatibility, as well as new ways of processing them for application in on-demand manufacturing of medical devices like coronary artery stents. Intensive research and development both in polymers and processing technologies will move the field forward and enable the development of many next generations of coronary artery stents that ultimately will address the limitations of current devices.

1.10. Objectives

The aim of this thesis is to develop customizable, biodegradable, multi drug eluting coronary artery stents by utilization of additive manufacturing, and through design and development of polymer-based material systems. These materials are to be haemocompatible, biodegradable, promote endothelialisation, have sufficient mechanical properties and multi-drug eluting properties as well as be processable through additive manufacturing techniques such as MEW. In order to do this, we used the following approaches:

1. Additive manufacturing of custom-made biodegradable nanocomposite-based coronary artery stents via MEW
2. Synthesis of biocompatible and biodegradable core cross-linked star-brush polymers for antithrombotic drugs
3. Development of multi-drug eluting biodegradable nanocomposite-star polymer materials for application as coronary artery stents utilizing MEW

1.11. Thesis Outline

In **Chapter 1**, current manufacturing techniques and material systems for fabrication of biodegradable, drug eluting stents were discussed and reviewed. We evaluated industrially used processing techniques for fabrication of coronary artery scaffolds and outlined emerging laboratory techniques with their advantages and disadvantages from processing point of view. Additionally, we described material systems currently used for coronary artery stent application with focus on polymeric stents and outlined the limitations of current materials as well as characteristics of an ideal stent material.

In **Chapter 2**, customized, biodegradable nanocomposite-enriched polymeric stents were developed by utilization of novel fabrication technique - MEW. These materials were fabricated with different ratio of rGO relative to PCL to study the influence of its inclusion on mechanics, thermal properties, crystallinity, rheology, printability and biological interactions. We chose to use PCL as a base polymer due to its low melting temperature, biocompatibility, relatively high tensile strength, high elongation at break, as well as its current FDA approval status. rGO was chosen as a nanofiller due to its excellent mechanical performance, hemocompatibility, thermal conductivity, and capability to direct cell behaviour and enhance cellular interactions. In this study, we addressed the limitations of biodegradable stents by developing devices with strut thickness as low as 60 µm, utilizing MEW. We also illustrated the feasibility of customization of scaffolds through fabrication of stents with different pore size, stent diameter, geometry and strut thickness. Our results showed that by incorporation of

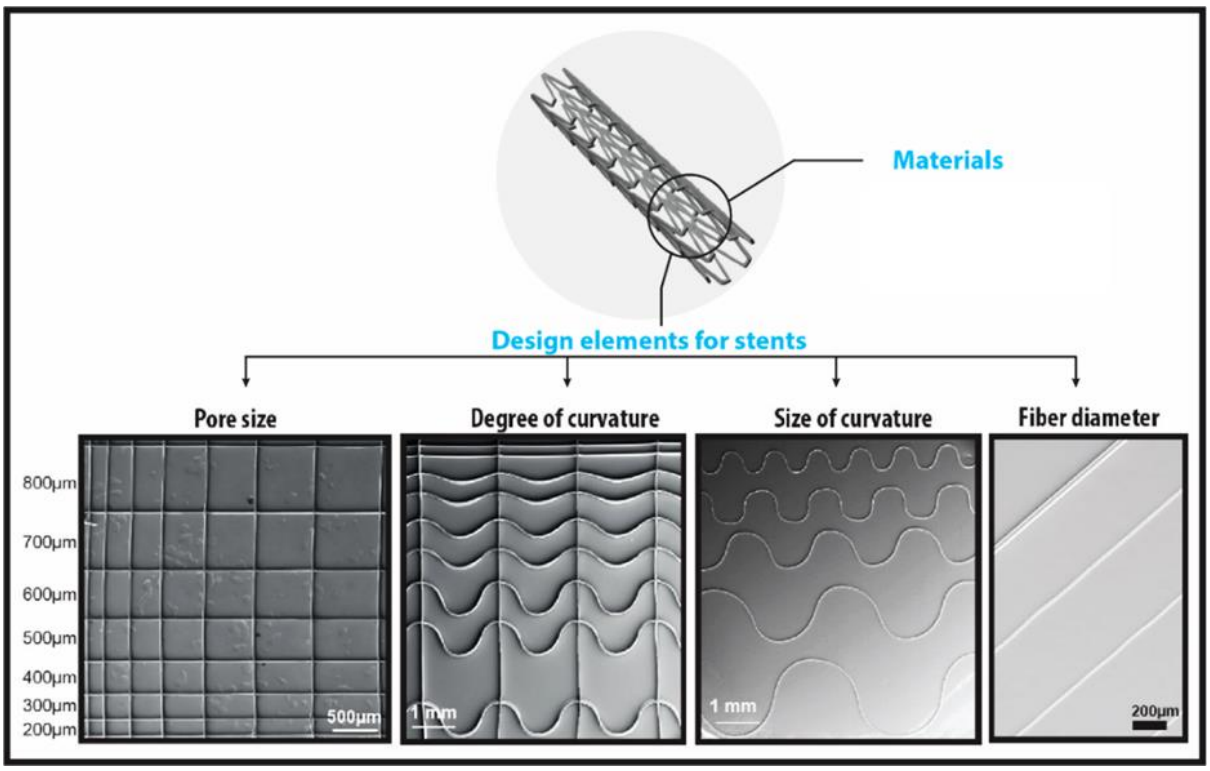

Figure 1.8: In Chapter 2, we develop reduced graphene oxide-polycaprolactone stents with varying pore size, degree of curvature, size of curvature, fibre diameter, stent diameter utilizing MEW.

rGO into PCL matrix, we improved mechanical performance of materials, enhanced cell proliferation, and fabricated devices with thin struts (60 µm).

In **Chapter 3**, we developed novel polymeric architectures to investigate their loading capabilities and release profiles in context of two clinically used antithrombotic drugs. These architectures were synthesized via photo-induced atom transfer polymerization (UV-ATRP) to form a class of hydrophilic brushes, and core-cross linked star-brush polymers and ring opening polymerization (ROP) to grow hydrophobic arms from a hydrophilic star-brush cores. Synthesized star-brush polymers were composed of hydrophobic exterior (PCL), hydrophilic interior (PEG-based), and hydrophilic core cross linked core (PEG diacrylate). These polymeric platforms were evaluated in terms of their loading and release of anti-thrombotic drugs at physiological and acidic conditions. Additionally, biological interactions of cells with developed materials were studied. Cytotoxicity, adhesion and proliferation of human umbilical vein endothelial cells were assessed while in contact with synthesized materials. The results showed increased hUVECs proliferation on materials with synthesized stars embedded in polymeric matrix, and release profiles showed more rapid release of dextran at acidic conditions compared to physiological, and no significant changes in release in heparin in two pHs.

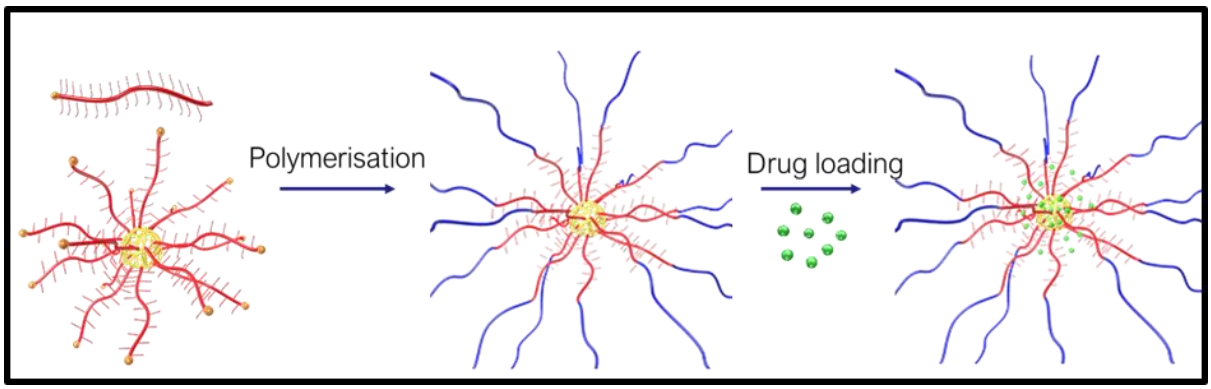

Figure 1.9: In Chapter 3, we synthesized biodegradable , biocompatible core-cross linked star-brush polymers for hydrophilic, anti-thrombotic drugs.

In **Chapter 4**, we combined our techniques and synthesized materials from **Chapter 2** and **Chapter 3**, to develop multi-drug eluting biodegradable materials for application as coronary artery stents. In this study, we fabricated reduced rGO/PCL/CCS materials and evaluated them in terms of printability using MEW system, mechanical performance, thermal behaviour, crystallinity, drug elution, degradation and biological interactions with three different cell types (hUVECs, SMCs, platelets). Our results showed that at lower CCS in PCL/rGO, there was no compromise on materials tensile and compressive Young's Modulus, and that higher CCS loadings led to a decrease in both tensile and compressive performance was observed. Dual drug elution of anti-thrombotic drug (heparin), and anti-proliferative drug (rapamycin) was studied in physiological and acidic conditions and showed controlled release of rapamycin, and slower release of heparin. Degradation of scaffolds with varying pore size and number of layers was investigated and showed that scaffolds with smaller pore size and larger number of layers degrade slower. In terms of biological interactions, our results showed improved endothelialisation due to graphene-enrichment and star presence in polymeric matrix, reduced smooth muscle cell proliferation correlated to rapamycin elution, and reduced platelet adhesion due to heparin elution and material composition.

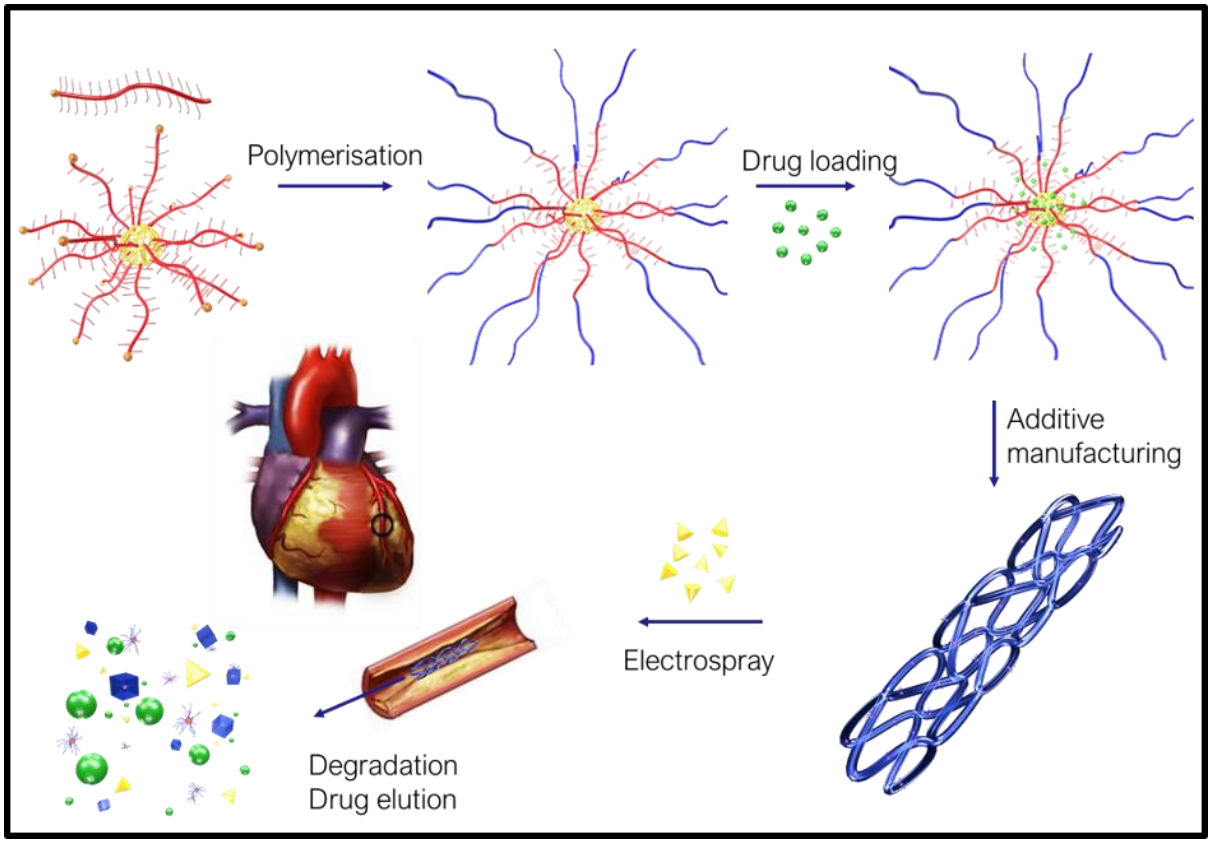

Figure 1.10: In Chapter 4, we fabricated PCL/rGO/CCS materials, evaluated their printability and studied biodegradation as well as multi-drug elution of two clinically used drugs (heparin and rapamycin).

1.12. References

1. Vilahur, G.; Badimon, J. J.; Bugiardini, R.; Badimon, L., Perspectives: The burden of cardiovascular risk factors and coronary heart disease in Europe and worldwide. *European Heart Journal Supplements* **2014,** *16* (suppl A), A7-A11.

2. Mendis, S., Global progress in prevention of cardiovascular disease. *Cardiovasc Diagn Ther* **2017,** *7* (Suppl 1), S32-S38.

3. Sigwart, U., Living history of medicine: vascular scaffolding, from dream to reality. *Eur Heart J* **2017,** *38* (16), 1245-1248.

4. Kalra, A.; Rehman, H.; Khera, S.; Thyagarajan, B.; Bhatt, D. L.; Kleiman, N. S.; Yeh, R. W., New-Generation Coronary Stents: Current Data and Future Directions. *Curr Atheroscler Rep* **2017,** *19* (3), 14.

5. Puricel, S.; Cook, S.; Arroyo, D., Coronary healing after stenting: wounds, faith, and the quest for the perfect stent. *European Heart Journal - Cardiovascular Imaging* **2015,** *17* (1), 12-14.

6. Mintz Gary, S.; Popma Jeffrey, J.; Pichard Augusto, D.; Kent Kenneth, M.; Satler Lowell, F.; Chiu Wong, S.; Hong Mun, K.; Kovach Julie, A.; Leon Martin, B., Arterial Remodeling After Coronary Angioplasty. *Circulation* **1996,** *94* (1), 35-43.

7. Sotomi, Y.; Onuma, Y.; Collet, C.; Tenekecioglu, E.; Virmani, R.; Kleiman, N. S.; Serruys, P. W., Bioresorbable Scaffold: The Emerging Reality and Future Directions. *Circ Res* **2017,** *120* (8), 1341-1352.

8. Sammel, A. M.; Chen, D.; Jepson, N., New generation coronary stent technology--is the future biodegradable? *Heart Lung Circ* **2013,** *22* (7), 495-506.

9. Sotomi, Y.; Suwannasom, P.; Serruys, P. W.; Onuma, Y., Possible mechanical causes of scaffold thrombosis: insights from case reports with intracoronary imaging. *EuroIntervention* **2017,** *12* (14), 1747-1756.

10. Katz, G.; Harchandani, B.; Shah, B., Drug-eluting stents: the past, present, and future. *Curr Atheroscler Rep* **2015,** *17* (3), 485.

11. Fischman , D. L.; Leon , M. B.; Baim , D. S.; Schatz , R. A.; Savage , M. P.; Penn , I.; Detre , K.; Veltri , L.; Ricci , D.; Nobuyoshi , M.; Cleman , M.; Heuser , R.; Almond , D.; Teirstein , P. S.; Fish , R. D.; Colombo , A.; Brinker , J.; Moses , J.; Shaknovich , A.; Hirshfeld , J.; Bailey , S.; Ellis , S.; Rake , R.; Goldberg , S., A Randomized Comparison of Coronary-Stent Placement and Balloon Angioplasty in the Treatment of Coronary Artery Disease. *New England Journal of Medicine* **1994,** *331* (8), 496-501.

12. Serruys , P. W.; de Jaegere , P.; Kiemeneij , F.; Macaya , C.; Rutsch , W.; Heyndrickx , G.; Emanuelsson , H.; Marco , J.; Legrand , V.; Materne , P.; Belardi , J.; Sigwart , U.; Colombo , A.; Goy , J. J.; van den Heuvel , P.; Delcan , J.; Morel , M.-a., A Comparison of

Balloon-Expandable-Stent Implantation with Balloon Angioplasty in Patients with Coronary Artery Disease. *New England Journal of Medicine* **1994,** *331* (8), 489-495.

13. Iqbal, J.; Gunn, J.; Serruys, P. W., Coronary stents: historical development, current status and future directions. *Br Med Bull* **2013,** *106*, 193-211.

14. Wolf, K. V.; Zong, Z.; Meng, J.; Orana, A.; Rahbar, N.; Balss, K. M.; Papandreou, G.; Maryanoff, C. A.; Soboyejo, W., An investigation of adhesion in drug-eluting stent layers. *Journal of Biomedical Materials Research Part A* **2008,** *87A* (1), 272-281.

15. Stettler, C.; Wandel, S.; Allemann, S.; Kastrati, A.; Morice, M. C.; Schömig, A.; Pfisterer, M. E.; Stone, G. W.; Leon, M. B.; de Lezo, J. S.; Goy, J.-J.; Park, S.-J.; Sabaté, M.; Suttorp, M. J.; Kelbaek, H.; Spaulding, C.; Menichelli, M.; Vermeersch, P.; Dirksen, M. T.; Cervinka, P.; Petronio, A. S.; Nordmann, A. J.; Diem, P.; Meier, B.; Zwahlen, M.; Reichenbach, S.; Trelle, S.; Windecker, S.; Jüni, P., Outcomes associated with drug-eluting and bare-metal stents: a collaborative network meta-analysis. *The Lancet* **2007,** *370* (9591), 937-948.

16. Serruys, P. W.; Onuma, Y.; Garg, S.; Vranckx, P.; De Bruyne, B.; Morice, M.-C.; Colombo, A.; Macaya, C.; Richardt, G.; Fajadet, J.; Hamm, C.; Schuijer, M.; Rademaker, T.; Wittebols, K.; Stoll, H. P., 5-Year Clinical Outcomes of the ARTS II (Arterial Revascularization Therapies Study II) of the Sirolimus-Eluting Stent in the Treatment of Patients With Multivessel De Novo Coronary Artery Lesions. *Journal of the American College of Cardiology* **2010,** *55* (11), 1093-1101.

17. Bangalore, S.; Toklu, B.; Amoroso, N.; Fusaro, M.; Kumar, S.; Hannan, E. L.; Faxon, D. P.; Feit, F., Bare metal stents, durable polymer drug eluting stents, and biodegradable polymer drug eluting stents for coronary artery disease: mixed treatment comparison meta-analysis. *BMJ* **2013,** *347*, f6625.

18. Palmerini, T.; Biondi-Zoccai, G.; Riva, D. D.; Stettler, C.; Sangiorgi, D.; D'Ascenzo, F.; Kimura, T.; Briguori, C.; Sabatè, M.; Kim, H.-S.; De Waha, A.; Kedhi, E.; Smits, P. C.; Kaiser, C.; Sardella, G.; Marullo, A.; Kirtane, A. J.; Leon, M. B.; Stone, G. W., Stent thrombosis with drug-eluting and bare-metal stents: evidence from a comprehensive network meta-analysis. *The Lancet* **2012,** *379* (9824), 1393-1402.

19. Bavry, A. A.; Kumbhani, D. J.; Helton, T. J.; Borek, P. P.; Mood, G. R.; Bhatt, D. L., Late Thrombosis of Drug-Eluting Stents: A Meta-Analysis of Randomized Clinical Trials. *The American Journal of Medicine* **2006,** *119* (12), 1056-1061.

20. Luscher, T. F.; Steffel, J.; Eberli, F. R.; Joner, M.; Nakazawa, G.; Tanner, F. C.; Virmani, R., Drug-eluting stent and coronary thrombosis: biological mechanisms and clinical implications. *Circulation* **2007,** *115* (8), 1051-8.

21. Finn Aloke, V.; Nakazawa, G.; Joner, M.; Kolodgie Frank, D.; Mont Erik, K.; Gold Herman, K.; Virmani, R., Vascular Responses to Drug Eluting Stents. *Arteriosclerosis, Thrombosis, and Vascular Biology* **2007,** *27* (7), 1500-1510.

22. Otsuka, F.; Cheng, Q.; Yahagi, K.; Acampado, E.; Sheehy, A.; Yazdani, S. K.; Sakakura, K.; Euller, K.; Perkins, L. E. L.; Kolodgie, F. D.; Virmani, R.; Joner, M., Acute Thrombogenicity of a Durable Polymer Everolimus-Eluting Stent Relative to Contemporary Drug-Eluting Stents With Biodegradable Polymer Coatings Assessed Ex Vivo in a Swine Shunt Model. *JACC Cardiovasc Interv* **2015,** *8* (9), 1248-1260.

23. Kereiakes, D. J.; Cox, D. A.; Hermiller, J. B.; Midei, M. G.; Bachinsky, W. B.; Nukta, E. D.; Leon, M. B.; Fink, S.; Marin, L.; Lansky, A. J., Usefulness of a cobalt chromium coronary stent alloy. *The American Journal of Cardiology* **2003,** *92* (4), 463-466.

24. Wiemer, M.; Serruys, P. W.; Miquel-Hebert, K.; Neumann, F.-J.; Piek, J. J.; Grube, E.; Haase, J.; Thuesen, L.; Hamm, C., Five-year long-term clinical follow-up of the XIENCE V everolimus eluting coronary stent system in the treatment of patients with de novo coronary

artery lesions: The SPIRIT FIRST trial. *Catheterization and Cardiovascular Interventions* **2010,** *75* (7), 997-1003.

25. Planer, D.; Smits, P. C.; Kereiakes, D. J.; Kedhi, E.; Fahy, M.; Xu, K.; Serruys, P. W.; Stone, G. W., Comparison of Everolimus- and Paclitaxel-Eluting Stents in Patients With Acute and Stable Coronary Syndromes: Pooled Results From the SPIRIT (A Clinical Evaluation of the XIENCE V Everolimus Eluting Coronary Stent System) and COMPARE (A Trial of Everolimus-Eluting Stents and Paclitaxel-Eluting Stents for Coronary Revascularization in Daily Practice) Trials. *JACC: Cardiovascular Interventions* **2011,** *4* (10), 1104-1115.

26. Stone, G. W.; Rizvi, A.; Sudhir, K.; Newman, W.; Applegate, R. J.; Cannon, L. A.; Maddux, J. T.; Cutlip, D. E.; Simonton, C. A.; Sood, P.; Kereiakes, D. J., Randomized Comparison of Everolimus- and Paclitaxel-Eluting Stents: 2-Year Follow-Up From the SPIRIT (Clinical Evaluation of the XIENCE V Everolimus Eluting Coronary Stent System) IV Trial. *Journal of the American College of Cardiology* **2011,** *58* (1), 19-25.

27. Serruys, P. W.; Silber, S.; Garg, S.; van Geuns, R. J.; Richardt, G.; Buszman, P. E.; Kelbæk, H.; van Boven, A. J.; Hofma, S. H.; Linke, A.; Klauss, V.; Wijns, W.; Macaya, C.; Garot, P.; DiMario, C.; Manoharan, G.; Kornowski, R.; Ischinger, T.; Bartorelli, A.; Ronden, J.; Bressers, M.; Gobbens, P.; Negoita, M.; van Leeuwen, F.; Windecker, S., Comparison of Zotarolimus-Eluting and Everolimus-Eluting Coronary Stents. *New England Journal of Medicine* **2010,** *363* (2), 136-146.

28. von Birgelen, C.; Basalus, M. W. Z.; Tandjung, K.; van Houwelingen, K. G.; Stoel, M. G.; Louwerenburg, J. W.; Linssen, G. C. M.; Saïd, S. A. M.; Kleijne, M. A. W. J.; Sen, H.; Löwik, M. M.; van der Palen, J.; Verhorst, P. M. J.; de Man, F. H. A. F., A Randomized Controlled Trial in Second-Generation Zotarolimus-Eluting Resolute Stents Versus Everolimus-Eluting Xience V Stents in Real-World Patients: The TWENTE Trial. *Journal of the American College of Cardiology* **2012,** *59* (15), 1350-1361.

29. Stone, G. W.; Teirstein, P. S.; Meredith, I. T.; Farah, B.; Dubois, C. L.; Feldman, R. L.; Dens, J.; Hagiwara, N.; Allocco, D. J.; Dawkins, K. D., A Prospective, Randomized Evaluation of a Novel Everolimus-Eluting Coronary Stent: The PLATINUM (A Prospective, Randomized, Multicenter Trial to Assess an Everolimus-Eluting Coronary Stent System [PROMUS Element] for the Treatment of up to Two De Novo Coronary Artery Lesions) Trial. *Journal of the American College of Cardiology* **2011,** *57* (16), 1700-1708.

30. Park, S.-J.; Kang, S.-J.; Virmani, R.; Nakano, M.; Ueda, Y., In-Stent Neoatherosclerosis: A Final Common Pathway of Late Stent Failure. *Journal of the American College of Cardiology* **2012,** *59* (23), 2051-2057.

31. Virmani, R.; Farb, A., Pathology of in-stent restenosis. *Current Opinion in Lipidology* **1999,** *10* (6).

32. Oliveira, M. D. P.; Ribeiro, E. E.; Campos, C. M.; Ribeiro, H. B.; Faillace, B. L. R.; Lopes, A. C.; Esper, R. B.; Meirelles, G. X.; Perin, M. A.; Abizaid, A.; Lemos, P. A., Four-year clinical follow-up of the first-in-man randomized comparison of a novel sirolimus eluting stent with abluminal biodegradable polymer and ultra-thin strut cobalt-chromium alloy: the INSPIRON-I trial. *Cardiovasc Diagn Ther* **2015,** *5* (4), 264-270.

33. Windecker, S.; Serruys, P. W.; Wandel, S.; Buszman, P.; Trznadel, S.; Linke, A.; Lenk, K.; Ischinger, T.; Klauss, V.; Eberli, F.; Corti, R.; Wijns, W.; Morice, M.-C.; di Mario, C.; Davies, S.; van Geuns, R.-J.; Eerdmans, P.; van Es, G.-A.; Meier, B.; Jüni, P., Biolimus-eluting stent with biodegradable polymer versus sirolimus-eluting stent with durable polymer for coronary revascularisation (LEADERS): a randomised non-inferiority trial. *The Lancet* **2008,** *372* (9644), 1163-1173.

34. Kereiakes Dean, J.; Meredith Ian, T.; Windecker, S.; Lee Jobe, R.; Mehta Shamir, R.; Sarembock Ian, J.; Feldman Robert, L.; Stein, B.; Dubois, C.; Grady, T.; Saito, S.; Kimura, T.; Christen, T.; Allocco Dominic, J.; Dawkins Keith, D., Efficacy and Safety of a Novel

Bioabsorbable Polymer-Coated, Everolimus-Eluting Coronary Stent. *Circulation: Cardiovascular Interventions* **2015,** *8* (4), e002372.

35. Byrne, R. A.; Mehilli, J.; Iijima, R.; Schulz, S.; Pache, J.; Seyfarth, M.; Schömig, A.; Kastrati, A.; for the Intracoronary, S.; Angiographic Results: Test Efficacy of 3 Limus-Eluting, S., A polymer-free dual drug-eluting stent in patients with coronary artery disease: a randomized trial vs. polymer-based drug-eluting stents. *European Heart Journal* **2009,** *30* (8), 923-931.

36. Onuma, Y.; Serruys, P. W.; Gomez, J.; de Bruyne, B.; Dudek, D.; Thuesen, L.; Smits, P.; Chevalier, B.; McClean, D.; Koolen, J.; Windecker, S.; Whitbourn, R.; Meredith, I.; Garcia-Garcia, H.; Ormiston, J. A.; on behalf of the, A. C. A.; investigators, B., Comparison of in vivo acute stent recoil between the bioresorbable everolimus-eluting coronary scaffolds (revision 1.0 and 1.1) and the metallic everolimus-eluting stent. *Catheterization and Cardiovascular Interventions* **2011,** *78* (1), 3-12.

37. Diletti, R.; Serruys, P. W.; Farooq, V.; Sudhir, K.; Dorange, C.; Miquel-Hebert, K.; Veldhof, S.; Rapoza, R.; Onuma, Y.; Garcia-Garcia, H. M.; Chevalier, B., ABSORB II randomized controlled trial: A clinical evaluation to compare the safety, efficacy, and performance of the Absorb everolimus-eluting bioresorbable vascular scaffold system against the XIENCE everolimus-eluting coronary stent system in the treatment of subjects with ischemic heart disease caused by de novo native coronary artery lesions: Rationale and study design. *American Heart Journal* **2012,** *164* (5), 654-663.

38. Alexandre, A. A.; J. Ribamar Costa, J.; Antonio, L. B.; Robert, J. W.; Robert-Jan, M. v. G.; Bernard, C.; Tejas, P.; Ashok, S.; Marrianne, S.; Cécile, D.; Wai-Fung, C.; Krishnankutty, S.; Patrick, W. S., The ABSORB EXTEND study: preliminary report of the twelve-month clinical outcomes in the first 512 patients enrolled. *EuroIntervention* **2015,** *10* (12), 1396-1401.

39. Jabara, R.; Chronos, N.; Robinson, K., Novel bioabsorbable salicylate-based polymer as a drug-eluting stent coating. *Catheterization and Cardiovascular Interventions* **2008,** *72* (2), 186-194.

40. Campos, M. C.; Muramatsu, T.; Iqbal, J.; Zhang, Y.-J.; Onuma, Y.; Garcia-Garcia, M. H.; Haude, M.; Lemos, A. P.; Warnack, B.; Serruys, W. P., Bioresorbable Drug-Eluting Magnesium-Alloy Scaffold for Treatment of Coronary Artery Disease. *International Journal of Molecular Sciences* **2013,** *14* (12).

41. Karalis, I.; Ahmed, T. A.; Jukema, J. W., Late acquired stent malapposition: why, when and how to handle? *Heart* **2012,** *98* (20), 1529-36.

42. Karimi, F.; O'Connor, A. J.; Qiao, G. G.; Heath, D. E., Integrin Clustering Matters: A Review of Biomaterials Functionalized with Multivalent Integrin-Binding Ligands to Improve Cell Adhesion, Migration, Differentiation, Angiogenesis, and Biomedical Device Integration. *Advanced Healthcare Materials* **2018,** *7* (12), 1701324.

43. Michiels, C., Endothelial cell functions. *Journal of Cellular Physiology* **2003,** *196* (3), 430-443.

44. SYNERGY Stent Early Healing With Thinner Struts. https://www.bostonscientific.com/en-EU/products/stents-coronary/synergy-stent-system/early-healing.html.

45. Finn Aloke, V.; Joner, M.; Nakazawa, G.; Kolodgie, F.; Newell, J.; John Mike, C.; Gold Herman, K.; Virmani, R., Pathological Correlates of Late Drug-Eluting Stent Thrombosis. *Circulation* **2007,** *115* (18), 2435-2441.

46. Wilson, G. J.; Marks, A.; Berg, K. J.; Eppihimer, M.; Sushkova, N.; Hawley, S. P.; Robertson, K. A.; Knapp, D.; Pennington, D. E.; Chen, Y.-L.; Foss, A.; Huibregtse, B.; Dawkins, K. D., The SYNERGY biodegradable polymer everolimus eluting coronary stent:

Porcine vascular compatibility and polymer safety study. *Catheterization and Cardiovascular Interventions* **2015,** *86* (6), E247-E257.

47. Kereiakes Dean, J.; Windecker, S.; Jobe, R. L.; Mehta Shamir, R.; Sarembock Ian, J.; Feldman Robert, L.; Stein, B.; Dubois, C.; Grady, T.; Saito, S.; Kimura, T.; Underwood, P.; Allocco Dominic, J.; Meredith Ian, T., Clinical Outcomes Following Implantation of Thin-Strut, Bioabsorbable Polymer-Coated, Everolimus-Eluting SYNERGY Stents. *Circulation: Cardiovascular Interventions* **2019,** *12* (9), e008152.

48. McMahon, S.; Bertollo, N.; Cearbhaill, E. D. O.; Salber, J.; Pierucci, L.; Duffy, P.; Dürig, T.; Bi, V.; Wang, W., Bio-resorbable polymer stents: a review of material progress and prospects. *Progress in Polymer Science* **2018,** *83*, 79-96.

49. Absorb GT1 Bioresorbable Vascular Scaffold (BVS) by Abbott Vascular: Letter to Health Care Providers - FDA Investigating Increased Rate of Major Adverse Cardiac Events. https://www.fda.gov/safety/medwatch/safetyinformation/safetyalertsforhumanmedicalproducts/ucm547256.htm.

50. Fantom Presentation at Next-Generation Session (Reva). https://www.sec.gov/Archives/edgar/data/1496268/000110465915070858/a15-21188_1ex99d1.htm.

51. Abizaid, A.; Ribamar Costa, J., Jr., The unmet needs: How future technologies will address current limitations of bioresorbable scaffold technology. *Catheter Cardiovasc Interv* **2016,** *88* (S1), 54-59.

52. Boeder, N. F.; Dorr, O.; Bauer, T.; Mattesini, A.; Elsasser, A.; Liebetrau, C.; Achenbach, S.; Hamm, C. W.; Nef, H. M., Impact of strut thickness on acute mechanical performance: A comparison study using optical coherence tomography between DESolve 150 and DESolve 100. *Int J Cardiol* **2017,** *246*, 74-79.

53. Akinapelli, A.; Chen, J. P.; Roy, K.; Donnelly, J.; Dawkins, K.; Huibregtse, B.; Hou, D., Current State of Bioabsorbable Polymer-Coated Drug-Eluting Stents. *Curr Cardiol Rev* **2017,** *13* (2), 139-154.

54. Ashok, S.; Yoshinobu, O.; Ricardo, A. C.; Praveen, C.; Vinay, K. B.; Cholenahally, N. M.; Ajaykumar, U. M.; Kumar, V. K. A.; Pravin Kumar, G.; Gurpreet, S. W.; Mathew, S. K.; Uprenda, K., First-in-human evaluation of a novel poly-L-lactide based sirolimus-eluting bioresorbable vascular scaffold for the treatment of de novo native coronary artery lesions: MeRes-1 trial. *EuroIntervention* **2017,** *13* (4), 415-423.

55. Buccheri, S.; Capodanno, D., Bioabsorbable stents: only bad news? *European Heart Journal Supplements* **2019,** *21* (Supplement_B), B28-B30.

56. Regazzoli, D.; Leone, P. P.; Colombo, A.; Latib, A., New generation bioresorbable scaffold technologies: an update on novel devices and clinical results. *Journal of thoracic disease* **2017,** *9* (Suppl 9), S979-S985.

57. Sakamoto, A.; Jinnouchi, H.; Torii, S.; Virmani, R.; Finn, V. A., Understanding the Impact of Stent and Scaffold Material and Strut Design on Coronary Artery Thrombosis from the Basic and Clinical Points of View. *Bioengineering* **2018,** *5* (3).

58. Dziewierz, A.; Dudek, D., Current perspectives on the role of bioresorbable scaffolds in the management of coronary artery disease. *Kardiol Pol* **2018,** *76* (7), 1043-1054.

59. Takahashi, K.; Katagiri, Y.; Tomaniak, M.; Chichareon, P.; Modolo, R.; Kogame, N.; Chang, C.-C.; Ono, M.; Kawashima, H.; Gao, C.; Bullett, N.; Ahmed, N.; Al-Lamee, K.; Al-Lamee, R.; Serruys, P.; Onuma, Y., TCT-186 Preclinical Evaluation of a Novel Thin-Strut PLLA Bioresorbable Scaffold in Porcine Coronary Artery at 6-Month Follow-Up. *Journal of the American College of Cardiology* **2019,** *74* (13 Supplement), B185.

60. Yuki, K.; Ryo, T.; Kuniaki, T.; Erhan, T.; Taku, A.; Ply, C.; Mariusz, T.; Jan, J. P.; Joanna, J. W.; Nial, B.; Naveed, A.; Kadem, A.-L.; Guy, L.; Pieter, H. K.; Jouke, D.; Johan, H.

C. R.; Eric, K. W. P.; Christos, V. B.; Frank, J. H. G.; Patrick, W. S.; Yoshinobu, O., Preclinical evaluation of a thin-strut bioresorbable scaffold (ArterioSorb): acute-phase invasive imaging assessment and hemodynamic implication. *EuroIntervention* **2019**.

61. Huang, C.-H.; Lee, S.-Y.; Horng, S.; Guy, L.-G.; Yu, T.-B., In vitro and in vivo degradation of microfiber bioresorbable coronary scaffold. *Journal of Biomedical Materials Research Part B: Applied Biomaterials* **2018,** *106* (5), 1842-1850.

62. Erhan, T.; Ryo, T.; Christos, V. B.; Yohei, S.; Rafael, C.; Yaping, Z.; Carlos, C.; Tom, C.; Pannipa, S.; Yoshinobu, O.; Patrick, W. S., Difference in haemodynamic microenvironment in vessels scaffolded with Absorb BVS and Mirage BRMS: insights from a preclinical endothelial shear stress study. *EuroIntervention* **2017,** *13* (11), 1328-1335.

63. Lord, B. H. Polymeric stents and method of manufacturing same. US8370120B2, 2013.

64. David C. Gale, B. H., Anthony J. Abbate, Timothy A. Limon, Klaus Kleine Manufacturing process for polymeric stents. 2011.

65. Yunbing Wang, S. D. P., Carina V.Harold Bioabsorbable polymeric stent with improved structural and molecular weight integrity. 2009.

66. Martinez, A. W.; Chaikof, E. L., Microfabrication and nanotechnology in stent design. *Wiley Interdiscip Rev Nanomed Nanobiotechnol* **2011,** *3* (3), 256-68.

67. Al-Lamee K, K. A., Coates D, Thompson G, Caton-Rose P Method of producing a tube for use in the formation of a stent and such tube. 2014.

68. Zheng, X. Biodegradable endoprostheses and methods for their fabrication. 2007.

69. Terakawa, M., Femtosecond Laser Processing of Biodegradable Polymers. *Applied Sciences* **2018,** *8* (7).

70. Dyer, P. E., Excimer laser polymer ablation: twenty years on. *Applied Physics A* **2003,** *77*, 167-173.

71. Poncin, P., Stent Tubing: Understanding the Desired Attributes. In *Materials & Processes for Medical Devices Conference*, ASM The Materials Information Society: 2003.

72. Poncin, P., Comparing and Optimizing Co-Cr Tubing for Stent Application. In *Materials & Processes for Medical Devices Conference*, 2004.

73. Welch, T. R.; Eberhart, R. C.; Reisch, J.; Chuong, C.-J., Influence of Thermal Annealing on the Mechanical Properties of PLLA Coiled Stents. *Cardiovascular Engineering and Technology* **2014,** *5* (3), 270-280.

74. Kim, J.; Park, J.-K.; Kim, H. K.; Unnithan, A. R.; Kim, C. S.; Park, C. H., Optimization of Electropolishing on NiTi Alloy Stents and Its Influence on Corrosion Behavior. *Journal of Nanoscience and Nanotechnology* **2017,** *17* (4), 2333-2339.

75. Gellér, Z. E.; Albrecht, K.; Dobránszky, J., Electropolishing of Coronary Stents. *Materials Science Forum* **2008,** *589*, 367-372.

76. Livingston, M.; Tan, A., Coating Techniques and Release Kinetics of Drug-Eluting Stents. *J Med Device* **2019,** *10* (1), 10.1115/1.4031718.

77. Levy, Y.; Mandler, D.; Weinberger, J.; Domb, A. J., Evaluation of drug-eluting stents' coating durability—Clinical and regulatory implications. *Journal of Biomedical Materials Research Part B: Applied Biomaterials* **2009,** *91B* (1), 441-451.

78. Bakhshi, R.; Edirisinghe, M. J.; Darbyshire, A.; Ahmad, Z.; Seifalian, A. M., Electrohydrodynamic Jetting Behaviour of Polyhedral Oligomeric Silsesquioxane Nanocomposite. *Journal of Biomaterials Applications* **2008,** *23* (4), 293-309.

79. Park, S.; Bhang, S. H.; La, W.-G.; Seo, J.; Kim, B.-S.; Char, K., Dual roles of hyaluronic acids in multilayer films capturing nanocarriers for drug-eluting coatings. *Biomaterials* **2012,** *33* (21), 5468-5477.

80. Nukala, R. K.; Boyapally, H.; Slipper, I. J.; Mendham, A. P.; Douroumis, D., The Application of Electrostatic Dry Powder Deposition Technology to Coat Drug-Eluting Stents. *Pharmaceutical Research* **2010,** *27* (1), 72-81.

81. Liu, Y.; Wang, W.; Acharya, G.; Shim, Y.-B.; Choe, E. S.; Lee, C. H., Advanced stent coating for drug delivery and in vivo biocompatibility. *Journal of Nanoparticle Research* **2013,** *15* (10), 1962.

82. Shanshan, C.; Lili, T.; Yingxue, T.; Bingchun, Z.; Ke, Y., Study of drug-eluting coating on metal coronary stent. *Materials Science and Engineering: C* **2013,** *33* (3), 1476-1480.

83. Ang, H. Y.; Bulluck, H.; Wong, P.; Venkatraman, S. S.; Huang, Y.; Foin, N., Bioresorbable stents: Current and upcoming bioresorbable technologies. *Int J Cardiol* **2017,** *228*, 931-939.

84. Huang, Z.-M.; Zhang, Y. Z.; Kotaki, M.; Ramakrishna, S., A review on polymer nanofibers by electrospinning and their applications in nanocomposites. *Composites Science and Technology* **2003,** *63* (15), 2223-2253.

85. Son, Y. J.; Kim, W. J.; Yoo, H. S., Therapeutic applications of electrospun nanofibers for drug delivery systems. *Arch Pharm Res* **2014,** *37* (1), 69-78.

86. Ramazani, S.; Karimi, M., Aligned poly(epsilon-caprolactone)/graphene oxide and reduced graphene oxide nanocomposite nanofibers: Morphological, mechanical and structural properties. *Mater Sci Eng C Mater Biol Appl* **2015,** *56*, 325-34.

87. Sarvari, R.; Sattari, S.; Massoumi, B.; Agbolaghi, S.; Beygi-Khosrowshahi, Y.; Kahaie-Khosrowshahi, A., Composite electrospun nanofibers of reduced graphene oxide grafted with poly(3-dodecylthiophene) and poly(3-thiophene ethanol) and blended with polycaprolactone. *J Biomater Sci Polym Ed* **2017,** *28* (15), 1740-1761.

88. Raber, L.; Brugaletta, S.; Yamaji, K.; O'Sullivan, C. J.; Otsuki, S.; Koppara, T.; Taniwaki, M.; Onuma, Y.; Freixa, X.; Eberli, F. R.; Serruys, P. W.; Joner, M.; Sabate, M.;

Windecker, S., Very Late Scaffold Thrombosis: Intracoronary Imaging and Histopathological and Spectroscopic Findings. *J Am Coll Cardiol* **2015,** *66* (17), 1901-14.

89. Ishibashi, Y.; Onuma, Y.; Muramatsu, T.; Nakatani, S.; Iqbal, J.; Garcia-Garcia, H. M.; Bartorelli, A. L.; Whitbourn, R.; Abizaid, A.; Serruys, P. W.; Investigators, A. E., Lessons learned from acute and late scaffold failures in the ABSORB EXTEND trial. *EuroIntervention* **2014,** *10* (4), 449-57.

90. Nordin, J. A.; Nasution, A. K.; Hermawan, H., Can the Current Stent Manufacturing Process be Used for Making Metallic Biodegradable Stents. *Advanced Materials Research* **2013,** *746*, 416-421.

91. Foin, N.; Lee, R. D.; Torii, R.; Guitierrez-Chico, J. L.; Mattesini, A.; Nijjer, S.; Sen, S.; Petraco, R.; Davies, J. E.; Di Mario, C.; Joner, M.; Virmani, R.; Wong, P., Impact of stent strut design in metallic stents and biodegradable scaffolds. *Int J Cardiol* **2014,** *177* (3), 800-8.

92. Lord, B. H. Polymeric Stents and Method of Manufacturing Same. 2010.

93. Yamada, A.; Niikura, F.; Ikuta, K., A three-dimensional microfabrication system for biodegradable polymers with high resolution and biocompatibility. *Journal of Micromechanics and Microengineering* **2008,** *18* (2).

94. Bajaj, P.; Schweller, R. M.; Khademhosseini, A.; West, J. L.; Bashir, R., 3D biofabrication strategies for tissue engineering and regenerative medicine. *Annu Rev Biomed Eng* **2014,** *16*, 247-76.

95. Guerra, A. J.; Ciurana, J., 3D-printed bioabsordable polycaprolactone stent: The effect of process parameters on its physical features. *Materials & Design* **2018,** *137*, 430-437.

96. Ware, H. O. T.; Farsheed, A. C.; Akar, B.; Duan, C.; Chen, X.; Ameer, G.; Sun, C., High-speed on-demand 3D printed bioresorbable vascular scaffolds. *Materials Today Chemistry* **2018,** *7*, 25-34.

97. Misra, S. K.; Ostadhossein, F.; Babu, R.; Kus, J.; Tankasala, D.; Sutrisno, A.; Walsh, K. A.; Bromfield, C. R.; Pan, D., 3D-Printed Multidrug-Eluting Stent from Graphene-Nanoplatelet-Doped Biodegradable Polymer Composite. *Adv Healthc Mater* **2017,** *6* (11).

98. Hochleitner, G.; Jungst, T.; Brown, T. D.; Hahn, K.; Moseke, C.; Jakob, F.; Dalton, P. D.; Groll, J., Additive manufacturing of scaffolds with sub-micron filaments via melt electrospinning writing. *Biofabrication* **2015,** *7* (3), 035002.

99. McColl, E.; Groll, J.; Jungst, T.; Dalton, P. D., Design and fabrication of melt electrowritten tubes using intuitive software. *Materials & Design* **2018,** *155*, 46-58.

100. Ware, H. O. T.; Farsheed, A. C.; Baker, E.; Ameer, G.; Sun, C., Fabrication Speed Optimization for High-resolution 3D-printing of Bioresorbable Vascular Scaffolds. *Procedia CIRP* **2017,** *65*, 131-138.

101. Jabara, R.; Geva, S.; Ribeiro, H.; Chen, J.; Hou, D.; Li, J.; King, S.; Chronos, N.; Robinson, K., A third generation ultra-thin strut cobalt chromium stent: histopathological evaluation in porcine coronary arteries. *EuroIntervention* **2009,** *5* (5), 619-626.

102. Park, S. A.; Lee, S. J.; Lim, K. S.; Bae, I. H.; Lee, J. H.; Kim, W. D.; Jeong, M. H.; Park, J.-K., In vivo evaluation and characterization of a bio-absorbable drug-coated stent fabricated using a 3D-printing system. *Materials Letters* **2015,** *141*, 355-358.

103. Hochleitner, G.; Fursattel, E.; Giesa, R.; Groll, J.; Schmidt, H. W.; Dalton, P. D., Melt Electrowriting of Thermoplastic Elastomers. *Macromol Rapid Commun* **2018,** *39* (10), e1800055.

104. Castilho, M.; Feyen, D.; Flandes-Iparraguirre, M.; Hochleitner, G.; Groll, J.; Doevendans, P. A. F.; Vermonden, T.; Ito, K.; Sluijter, J. P. G.; Malda, J., Melt Electrospinning Writing of Poly-Hydroxymethylglycolide-co-epsilon-Caprolactone-Based Scaffolds for Cardiac Tissue Engineering. *Adv Healthc Mater* **2017,** *6* (18).

105. U.S Department of Health and Human Services, F., Technical Considerations for Additive Manufactured Medical Devices - Guidance fod Industry and Food and Drug Administration Staff. **2017**.

106. Guerra, A. J.; Ciurana, J., Fibre laser cutting of polymer tubes for stents manufacturing. *Procedia Manufacturing* **2017,** (13), 190-196.

107. Borhani, S.; Hassanajili, S.; Ahmadi Tafti, S. H.; Rabbani, S., Cardiovascular stents: overview, evolution, and next generation. *Prog Biomater* **2018,** *7* (3), 175-205.

108. Hermawan, H.; Dubé, D.; Mantovani, D., 16 - Degradable metallic biomaterials for cardiovascular applications. In *Metals for Biomedical Devices*, Niinomi, M., Ed. Woodhead Publishing: 2010; pp 379-404.

109. Li, Y.; Chu, Z.; Li, X.; Ding, X.; Guo, M.; Zhao, H.; Yao, J.; Wang, L.; Cai, Q.; Fan, Y., The effect of mechanical loads on the degradation of aliphatic biodegradable polyesters. *Regen Biomater* **2017,** *4* (3), 179-190.

110. Guildford, A.; Santin, M.; Phillips, G. J., 7 - Cardiovascular stents. In *Biomaterials and Devices for the Circulatory System*, Gourlay, T.; Black, R. A., Eds. Woodhead Publishing: 2010; pp 173-216.

111. Guerra, A. J.; Farjas, J.; Ciurana, J., Fibre laser cutting of polycaprolactone sheet for stents manufacturing: A feasibility study. *Optics & Laser Technology* **2017,** *95*, 113-123.

112. Guarino, V.; Gentile, G.; Sorrentino, L.; Ambrosio, L., Polycaprolactone: Synthesis, Properties, and Applications. In *Encyclopedia of Polymer Science and Technology*, 2017; pp 1-36.

113. Fu, S.; Sun, Z.; Huang, P.; Li, Y.; Hu, N., Some basic aspects of polymer nanocomposites: A critical review. *Nano Materials Science* **2019,** *1* (1), 2-30.

114. Dantas de Oliveira, A.; Augusto Gonçalves Beatrice, C., Polymer Nanocomposites with Different Types of Nanofiller. In *Nanocomposites - Recent Evolutions*, 2019.

115. Yang, K.; Feng, L.; Shi, X.; Liu, Z., Nano-graphene in biomedicine: theranostic applications. *Chem Soc Rev* **2013,** *42* (2), 530-47.

116. Suvarnaphaet, P.; Pechprasarn, S., Graphene-Based Materials for Biosensors: A Review. *Sensors (Basel)* **2017,** *17* (10).

117. Sanchez, V. C.; Jachak, A.; Hurt, R. H.; Kane, A. B., Biological interactions of graphene-family nanomaterials: an interdisciplinary review. *Chem Res Toxicol* **2012,** *25* (1), 15-34.

118. Zhang, D.; Zhang, Z.; Liu, Y.; Chu, M.; Yang, C.; Li, W.; Shao, Y.; Yue, Y.; Xu, R., The short- and long-term effects of orally administered high-dose reduced graphene oxide nanosheets on mouse behaviors. *Biomaterials* **2015,** *68*, 100-13.

119. Ema, M.; Gamo, M.; Honda, K., A review of toxicity studies on graphene-based nanomaterials in laboratory animals. *Regul Toxicol Pharmacol* **2017,** *85*, 7-24.

120. Holt, B. D.; Wright, Z. M.; Arnold, A. M.; Sydlik, S. A., Graphene oxide as a scaffold for bone regeneration. *Wiley Interdiscip Rev Nanomed Nanobiotechnol* **2017,** *9* (3).

121. Xu, S.; Zhang, Z.; Chu, M., Long-term toxicity of reduced graphene oxide nanosheets: Effects on female mouse reproductive ability and offspring development. *Biomaterials* **2015,** *54*, 188-200.

122. Bhattacharya, K.; Mukherjee, S. P.; Gallud, A.; Burkert, S. C.; Bistarelli, S.; Bellucci, S.; Bottini, M.; Star, A.; Fadeel, B., Biological interactions of carbon-based nanomaterials: From coronation to degradation. *Nanomedicine: Nanotechnology, Biology and Medicine* **2016,** *12* (2), 333-351.

123. Yang, L.; Kuang, H.; Zhang, W.; Aguilar, Z. P.; Xiong, Y.; Lai, W.; Xu, H.; Wei, H., Size dependent biodistribution and toxicokinetics of iron oxide magnetic nanoparticles in mice. *Nanoscale* **2015,** *7* (2), 625-36.

124. Kumar, R.; Roy, I.; Ohulchanskky, T. Y.; Vathy, L. A.; Bergey, E. J.; Sajjad, M.; Prasad, P. N., In vivo biodistribution and clearance studies using multimodal organically modified silica nanoparticles. *ACS Nano* **2010,** *4* (2), 699-708.

125. Dumala, N.; Mangalampalli, B.; Chinde, S.; Kumari, S. I.; Mahoob, M.; Rahman, M. F.; Grover, P., Genotoxicity study of nickel oxide nanoparticles in female Wistar rats after acute oral exposure. *Mutagenesis* **2017,** *32* (4), 417-427.

126. Im, S. H.; Jung, Y.; Kim, S. H., Current status and future direction of biodegradable metallic and polymeric vascular scaffolds for next-generation stents. *Acta Biomater* **2017,** *60*, 3-22.

127. Lee, S. J.; Oh, S. H.; Liu, J.; Soker, S.; Atala, A.; Yoo, J. J., The use of thermal treatments to enhance the mechanical properties of electrospun poly(epsilon-caprolactone) scaffolds. *Biomaterials* **2008,** *29* (10), 1422-30.

128. Sakamoto, A.; Jinnouchi, H.; Torii, S.; Virmani, R.; Finn, V. A., Understanding the Impact of Stent and Scaffold Material and Strut Design on Coronary Artery Thrombosis from the Basic and Clinical Points of View. *Bioengineering* **2018,** *5* (3).

2. Additively manufactured biodegradable reduced graphene oxide-polycaprolactone coronary artery stents via MEW

2.1. Abstract

Coronary artery stents are intravascular medical devices used to treat coronary heart disease. Current stents are drug-eluting, metallic, and permanent, and recipients require prolonged anti-platelet therapy. The concept of biodegradable stents has emerged as an alternative to conventional stents, in which the stent degrades away leaving behind only the healed vessel. The first generation of biodegradable stents has been linked to higher rates of late stage thrombosis, and it has been suggested that this is due to increased strut thicknesses that causes disturbances to the laminar blood flow and results in the activation of thrombogenic pathways. A current challenge lies in the fabrication of a device with thin struts yet sufficient mechanical properties to maintain vessel patency. Additionally, the ability to directly fabricate stents in a bottom up fashion would potentiate personalised stent design based on an individual's anatomy and disease state. In this study, we address these challenges by developing a biodegradable PCL-rGO nanocomposite with increased strength and fabricating this composite into stent-like structures via MEW. We illustrate that these materials have increased mechanical strength, that MEW is able to produce well-defined stent structures with struts as thin as 60 μm, and that MEW can be used to tailor the strut thickness, strut spacing, strut geometry, and diameter of the stent, potentiating personalised stent design.

2.2. Introduction

Coronary heart disease is a leading cause of death globally [1]. Angioplasty and stenting is the most common treatment. During angioplasty, a baloon is inflated within the target lesion to open the vessel and to restore blood flow. Following balloon angioplasty, a stent is then deployed to support the re-opened vessel and maintain blood flow. Millions of these procedures are performed annually [2]. The current generation of coronary artery stents are permanent, metallic, and are coated with a drug-impregnated and biodegradable polymer layer to allow short term drug elution. While these devices have been met with clinical success, they have several disadvantages. Specifically, the stents are permanent, can lead to late-stage thrombosis, and require patients to remain on prolonged antiplatelet therapy [3].

Permanent stenting is not required. The blood vessel can heal after 6 months to a year [4]. As such, biodegradable coronary artery stents have recently emerged as an attractive alternative to permanent stenting. The device would support the vessel during the healing process and then degrade away, leaving behind a functioning artery. This technology could alleviate the risk of late stage complications and minimise the need for prolonged antiplatelet therapy [4].

Despite the potential advantages of biodegradable stents, the first clinically available bioabsorbable coronary artery stent – Abbott Vascular's Absorb Bioresorbable Vascular Scaffold – was linked to higher rates of late stage thrombosis during clinical trials, resulting in its removal from the market in 2017 [5]. The clinical failure of the Absorb Stent has been attributed to poor material selection. The device was fabricated from PLLA, and this material has significantly lower strength and modulus compared to traditional metallic materials [6]. As such, the device was fabricated with significantly thicker stuts (~150 μm) to provide the

necessary mechanical support to maintain vessel patency. This is in comparison to the strut thickness of approximately 80 µm in conventional metallic stents such as Synergy or Xience.

The biodegradable stent's thicker struts are a main driver for thromosis. Specifically, the thicker struts result in more pro-thrombogenic material and degradation products present within the blood vessel, result in inflammation of the vessel, and cause significant and pro-thrombogenic changes to the blood flow and the shear stress experienced by endothelial cells [3, 7-8]. Specifically, struts with thicknesses greater than 80 µm have been suggested to initiate a cascade of thrombotic events [3, 6-10].

Developing material systems and fabrication technologies that enable the fabrication of biodegradable stents with thin struts and sufficient mechanical properties is one of the major challenges that must be addressed before these devices can fulfil their clinical and economic potential. Additionally, the development of fabrication techniques that enable the fabrication of personalised stents designed for a patient's unique anatomy and disease state would mark a significant advance in the field.

In this study, we aim to advance biodegradable coronary artery stent technology through two main aims. First, we aim to develop a material system that possesses significantly greater mechanical properties, enabling the fabrication of devices with thinner struts. Second, we aim to use emerging fabrication techniques that will allow for the direct fabrication of personalised stents in a bottom-up fashion with appropriate strut thicknesses (<80 µm). Specifically, we tested the hypotheses that nanocomposites of PCL and rGO will possess significantly greater strength compared to the biodegradable polymer alone and that the emerging fabrication

technology of MEW can be used to fabricate stents with a customisable design and appropriate strut thicknesses of <80μm.

These hypotheses were supported by the data. We illustrate that the MEW can be used to fabricate stents from PCL-rGO nanocomposites with customisable stent diameter, strut thickness, strut spacing, and strut geometry. Additionally, stent-like structures with struts as thin as 60 μm were achieved. Furthermore, PCL-rGO nanocomposites exhibited significantly greater mechanical properties, in a dose dependent manner. To the best of our knowledge, this is the first study to report the utilization of MEW for fabrication of biodegradable coronary artery stents, the first illustration that PCL-rGO nanocomposites can fabricated into devices using MEW, and that MEW can be used to generate customisable stent-like structures with an advanced level of geometry and customizable design using MEW.

2.3. Experimental methods

2.3.1. Materials

PCL pellets (average molecular weight 70,000 – 90,000 Da) were purchased from Sigma-Aldrich, acetone from Chem Supply, GO (5 mg/ml in ethanol) from ACS Material LLC. All chemicals and solvents were used as received.

2.3.2. Preparation and characterization of composites

PCL pellets (2 g) were dissolved in acetone (5 mL) and a GO solution was added to the PCL/acetone solution to obtain 0.1, 0.3, 0.6 and 1 wt% GO/PCL solutions. Solutions were stirred for 24 h, with additional sonication for approximately 1h prior to use, to allow dispersion of GO. GO was thermally reduced to obtain reduced graphene oxide (rGO) at 150 ºC.

2.3.3. Mechanical tests

2.3.3.1. Tensile tests on moulds

Samples were prepared using standardized moulds with dimensions of approximately 10 mm height, 1.7 mm thickness and 1.5 mm width. PCL and PCL-rGO composites (0.1, 0.3, 0.6 and 1 wt%) were heated to 90 ºC and cast in the moulds. Tensile tests were performed using Instron 5567 and 2kN load cell at the tensile rate of 0.1 mm/s. For the analysis of the data, results were used from the tensile load of 2 N for all samples.

2.3.3.2. Compressive tests on moulds

Samples were prepared using standardized moulds with dimensions of approximately 1.45 mm height and 4 mm diameter. PCL and PCL-rGO composites (0.1, 0.3, 0.6 and 1 wt%) were heated up to 90 ºC and cast in the moulds. Samples were compressed at a constant rate of 0.01 mm/s. All compression experiments were performed in PBS at 37 ºC using Instron 5848 Micro tester and a 500 N load cell. For the analysis of the data, results were used from the compressive load of -0.5 N for all samples till the last data point.

2.3.4. Rheology

Rheology tests were performed using Twin Drive Rheometer MCR 702 (Anton Paar) on PCL and PCL-rGO melts (0.1, 0.3, 0.6 and 1 wt%). Viscosity was measured as a function of shear rate from 0.01 /s till 1000 /s at temperatures of 70 ºC, 90 ºC and 120 ºC. Temperature sweeps were performed at the frequency of 1Hz, shear strain of 1 % and the rate of 0.3 ºC/s. Frequency sweeps were performed from 0.01 Hz to 100 Hz, at the printing temperatures of the materials, and 1 % shear strain (oscillatory). All measurements were performed using cone-plate geometry with diameter of 25 mm, 2º angle and 0.102 mm gap.

2.3.5. Differential scanning calorimetry and Thermogravimetric analysis

DSC and TGA of the materierials were performed using an STA-8000 (Perkin Elmer). Dual DSC/TGA analysis was performed on approximately 10 mg samples at the heating/cooling rates of 10 ºC/min. Samples were allowed to reach thermal equilibrium for 30 min between the runs. 3 heating/cooling cycles were performed between 20 ºC to 150 ºC, followed by a thermogravimetric analysis from 20 ºC to 1000 ºC. Degree of crystallinity (X_c), was derived from the first heating cycle to include the thermal history after printing. X_c was calculated according to the following equation (2.1).

$$X_c = \frac{\Delta H_f}{\Delta H^\circ_f} \times \%PCL^{-1} \quad (2.1)$$

Where ΔH_f and $\Delta H^\circ_f{}^{-1}$ are the measured heat of fusion of the samples (normed to PCL content $\%PCL$ and the heat of fusion of 100% crystalline PCL (136 J g^{-1}), respectively[9]. Melting and crystallization temperatures for each sample were obtained from 1st, 2nd and 3rd heating and cooling cycles respectively.

2.3.6. Fabrication and characterization of stents via melt electrowriting

The custom-made MEW device with a high voltage source (DX250R, EMCO, Hallein, Austria) and a controller (Digit Multimeter 2100, Keithley, Cleveland, USA) was used with a gas-pressured feeding system. Stent-like structures with varying diameter, strut architecture, strut spacing, and strut thickness were produced using MEW using PCL-rGO (0.1 wt%) at a temperature of 90 ºC, a pressure of 2.5 bar, a voltage of 3.8 V, a nozzle size of 23 G. The diameters of printed stents include 2 mm, 3.5 mm and 5 mm. The strut spacing ranged from 0.5 mm x 0.5 mm, 1 mm x 1 mm. The architectures of printed devices included curved and

right-angle structures. The deposition of scaffolds was guided by G-code (MACH 3 CNS software, ARTSOFT, Livermore Falls, USA) with a designed x,y pore sizes.

2.3.7. Tensile tests on melt electrowritten fibres

PCL and PCL-rGO (0.1 wt%) fibers were prepared by MEW. For PCL fibers, material was printed at a temperature of 110 ºC, Pressure 2.5 bar, Voltage of 3.8 V. For PCL-rGO (0.1 wt%), fibres were printed at 90 ºC, Pressure 2.5 bar and Voltage of 3.8V. Tensile tests were performed using Instron Micro tester 5848 and 5N load cell at the tensile rate of 0.1 mm/s. The fibre thickness was obtained via SEM imaging and mechanical results were normalized for each fibre by its cross-sectional area. For the analysis of the data, PCL results were used from the tare load of 0.001 N to the end of the run. PCL-rGO 0.1 wt% data was used from the tare load of 0.01 N till the end of the run.

2.3.8. Three-point bending test on melt electrowritten stents

3-point bending tests were performed following ASTM F2606-08 (Standard guide for three-point bending of balloon expandable vascular stents and stent systems)[10]. Span length between the lower supports was set to 16 mm. The maximum displacement and rate of the displacement of the upper load applicator were 1.75 mm and 0.1 mm/s respectively.

2.3.9. Biological interactions

2.3.9.1. Protein adsorption

QCM sensor chips (QSense, QSX301) were cleaned with piranha solution (a 3:1 mixture of concentrated sulfuric acid and hydrogen peroxide) to remove surface contaminants and rinsed with deoinized water, ethanol, and dried under nitrogen. The chips were spin coated with 100µl of 1 % (w/v) PCL in acetone solution, PCL-rGO (0.1 wt%) and PCL-rGO (0.3 wt%) at 3000

rpm for 20 s, then dried at room temperature for 24 h. The adsorption of fetal bovine serum (2 % w/v, FBS Gibco, ThermoFisher Scientific), rich in a variety of proteins such as albumin and other serum proteins, in PBS was measured in real-time using a QCM with dissipation monitoring (Q-sense QCM-D E4). After loading the polymer coated chips into the QCM-D instrument, PBS was injected and system was allowed to equilibrate. After confirming a stable baseline, the serum solution was injected. After approximately 1h, the frequency curve reached its new baseline, and PBS was injected to rinse away non-adsorbed proteins. Frequency and dissipation shifts were monitored in real time at 3^{rd} ,5^{th} and 7^{th} crystals and reported at the 3^{rd} crystal. All experiments were performed under static conditions and gold coated quartz crystal was used as a control.

2.3.9.2. Human umbilical vein endothelial cells

Cell culture surfaces were prepared by coating the growth surfaces of 8-well chamber slide with glass slide bottom (Lab-Tek) with 50 µL of a 5 % polymer solution in acetone. The chamber slides were then covered with aluminium foil and allowed to dry at ambient condition for 48 h. Chamber slides were sterilized through UV exposure for 1 h in a sterile biological safety cabinet. Wells were rinsed twice with PBS and incubated overnight in PBS at 37 °C before the introduction of cells. Pooled donor hUVECs were purchased from Lonza (Australia) and maintained in CloneticsTM EGMTM-2 BulletKitTM containing Endothelial Basal Medium-2 (EBMTM-2 Medium) supplemented with BulletKitTM as recommended by supplier. Cells were cultured at 37 °C in a humidified 5 % CO_2 atmosphere. The culture medium was changed every other day. The cultures were passaged at 80 % confluence and lifted using 0.25 % trypsin-EDTA. For all tests, the cells between passages 3 and 5 were used. 500 µL of medium containing 1.2 $\times 10^4$ cells (1.7 $\times 10^4$ cells per cm^2) was added to each well of polymer-coated chamber slides. Uncoated chamber slides were used as control. The cells

were cultured for 7 days, and the culture medium was changed every two days. Cell attachment and growth were determined after 4 h, 4 and 7 days using double stranded DNA (dsDNA) quantification by the Quant-iTTM PicoGreen® dsDNA Assay (Invitrogen) after digestion with papain. Cell surface densities were determined by dividing the obtained cell number by the area of the test surface. The morphology of the adherent endothelial cells were visualised by staining for the nuclei and actin cytoskeleton by using the FAK100 actin cytoskeleton/focal adhesion staining kit (Merck Millipore). Briefly, the cells were fixed after 4 h and 7 days with 4 % paraformaldehyde and were permeabilized with 0.1% Triton X-100 in PBS. The cells were stained with TRITC-phalloidin (1:500), and 4′,6-diamino-2-phenylindole (DAPI, 1:1000). The cells were finally washed and covered with PBS and imaged using a fluorescent microscope (Olympus IX71). Images were analysed using ImageJ software (NIH).

2.3.9.3. Platelet adhesion

Plateles were obtained from the Australian Red Cross Blood service with approval of the University of Melbourne's Human Ethics Review Board. Pre-cleaned 12 mm glass coverslips were dipcoated in 5 % polymer solution in acetone. Coverslips were dried overnight to remove residual solvent and then transferred to the wells of a 24 well plate. Well plates were steralized through exposure to UV radiation for 2 h and equilibrated in PBS overnight. 0.3 mL of platelet suspension was pipetted onto each of the test surfaces and then incubated at 37 ºC for 1 h. After that, samples were gently rinsed by phosphate buffer saline (PBS) to remove non adherent platelets. Adhered platelets on samples were fixed using 4 % paraformaldehyde solution at room temperature for 2 h. Cultures were rinsed three times with deionized water to remove residual salt, dried and analyzed through Helium Ion Micsocropy (ZEISS Microscopy GmbH, Germany). Images were taken of randomly selected fields of view on each test surface. The

number of adherent platelets was counted and divided by the area of the image to calculate the adherent platelet density.

2.3.10. Statistical analysis

All quantitative data are expressed as mean ± standard deviations with a minimum of n = 3 repeats. Statistical analysis was performed by one way analysis of variance (ANOVA) followed by T-test and P-values less than 0.05 were considered statistically significant.

2.4. Results and Discussion

2.4.1. Preparation and characterization of composites

In this study, we chose to fabricate the stents from PCL and rGO. Previous biodegradable stents used polymers such as PLLA [6]. However, we chose to work with PCL as it has many beneficial properties including a proven track record as a biodegradable material in many biomedical applications, a lower melting temperature that facilitates fabrication through melt-based techniques, and superior mechanical properties to PLLA including a higher elongation at break and a high tensile strength [11-14].

Despite the many beneficial properties of PCL, it is inherently weaker than common stent materials such as platinum chromium or cobalt chromium alloys. A viable method to improve mechanical performance of PCL, and thus reduce strut thickness of the stent, is to blend it with a nanomaterial to form a nanocomposite. While many nanomaterials have been used to generate nanocomposites, graphene and its derivatives [GO and rGO] have gained significant attention in the fields of tissue engineering, drug delivery, bio sensing and nanomedicine [15-17].

As the coronary artery stents will be deployed in the vasculature, hemocompatibility is of utmost importance. Interaction between graphene oxide and blood components were

previously analysed by exposing human platelets to GO (2 µg/mL) and rGO (2 and 10 µg/mL). Studies showed that GO can evoke strong aggregatory response in platelets while rGO showed no significant response or minor aggregatory response which was about 10 % of that induced by GO. rGO was found to be much less effective in activating platelets which may be correlated to reduced charge density on graphene surface [18-19]. Previous reports aimed at understanding the mechanisms behind platelet activation after exposure of GO, and suggested GO-induced platelet activation could be attributed to release of intracellular free calcium and activation of nonreceptor protein tyrosine kinases in platelets [18-19]. Authors aimed at further understanding of reduction of activation of platelets by the rGO and could only relate it to previously mentioned differenced in charge density which is reduced on reduced graphene oxide [18-19].
As such, rGO was the nanomaterial that we chose to work with in this contribution due to its superior interactions with blood and the significant enhancement of mechanical properties that can be achieved at very low concentrations.

Four different PCL-rGO composites were prepared by varying the weight fraction of rGO within the composite (0.1, 0.3, 0.6 and 1 wt%). These composites, as well as the pure components, were characterized using Raman spectroscopy. **Figure 2.1** shows representative Raman spectra for the materials used in this study. The spectra obtained for the GO and rGO show peaks at 1350 cm^{-1} and 1580 cm^{-1} respectively, corresponding to the D and G band, respectively[20]. Both D band and G band are characteristic to carbon materials while characterized by Raman spectroscopy[20-21]. The D band has been shown to correspond to the presence of dislocations in the graphene layer, while the G band has been correlated to the in-plane vibration of sp^2 hybridized carbon atoms. The D band is associated with the vibration of disordered graphite, and generally correlated with the defects from vacancies, and results from dislocations in the graphene layer[20-21]. The ratio of the intensity of D peak to the intensity of G

peak can be related to the number of defects present in the material. **Figure 2.1** illustrates that rGO and GO spectra show the same bands; however, the G band in rGO shifts toward lower wavenumbers compared to the G band in GO. D band of GO was found to be at approximately 1360 cm^{-1}, while D band for rGO was found to be at approximately 1342 cm^{-1}.

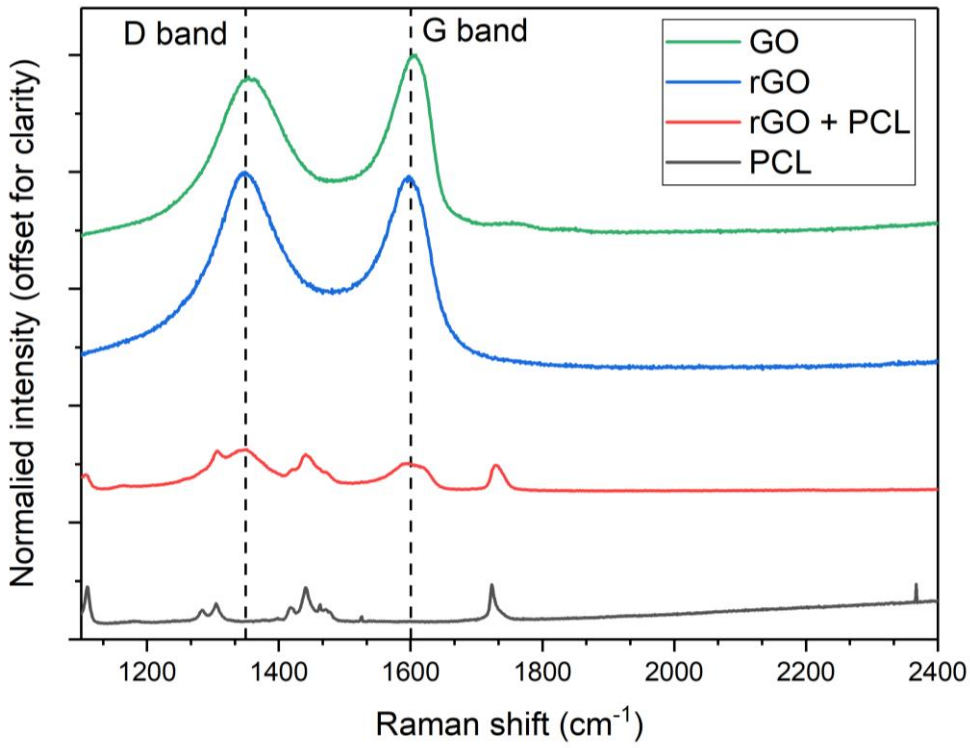

Figure 2.1: Raman spectra of PCL, PCL/rGO, rGO and GO materials used. D and G correspond to D Band and G Band respectively.

Additionally, the intensity ratio of D/G band (I_D/I_G) in rGO samples was found to increase as compared to GO, with values of approximately 1.01 for rGO and 0.95 for GO, which agrees with previous reports[20-21]. I_D/I_G quantifies the density of defects in sp^2 carbons and an increased ratio suggests an increase in the number of smaller graphene domains. This can be also related to the lower content of oxygen groups in the rGOs and more of the graphite like structure. The intensity of the D band increased in rGO, which indicates the formation of new defects in the structures during the reduction process[20].

2.4.2. Mechanical tests

The tensile and compressive properties of the PCL-rGO composites were evaluated to assess the influence of rGO on the mechanical properties of the material. Representative stress-strain curves for the PCL-rGO nanocomposites are shown in **Figure 2.2** and these parameters are tabulated in **Table 2.1**. The tensile tests showed that the modulus of the material increased with increasing rGO content. An increase of more than 2-fold was observed for the PCL-rGO 0.1 wt%, 0.3 wt% and 0.6 wt% groups, while an increase of 3-folds was observed for the PCL-rGO 1 wt% (**Figure 2.2 a-b**). However, the PCL-rGO 0.1 wt%, 0.3 wt% and 0.6 wt% exhibited the highest ultimate tensile strength and a decrease in this property was seen as the rGO content was increased to 1 wt%. Interestingly, the greatest reinforcement of the material was observed with lower nanofiller content (0.1 wt% and 0.3 wt%) which suggests that at lower rGO loadings, the material exhibits homogeneous dispersion of rGO in PCL with no overloading of the matrix.

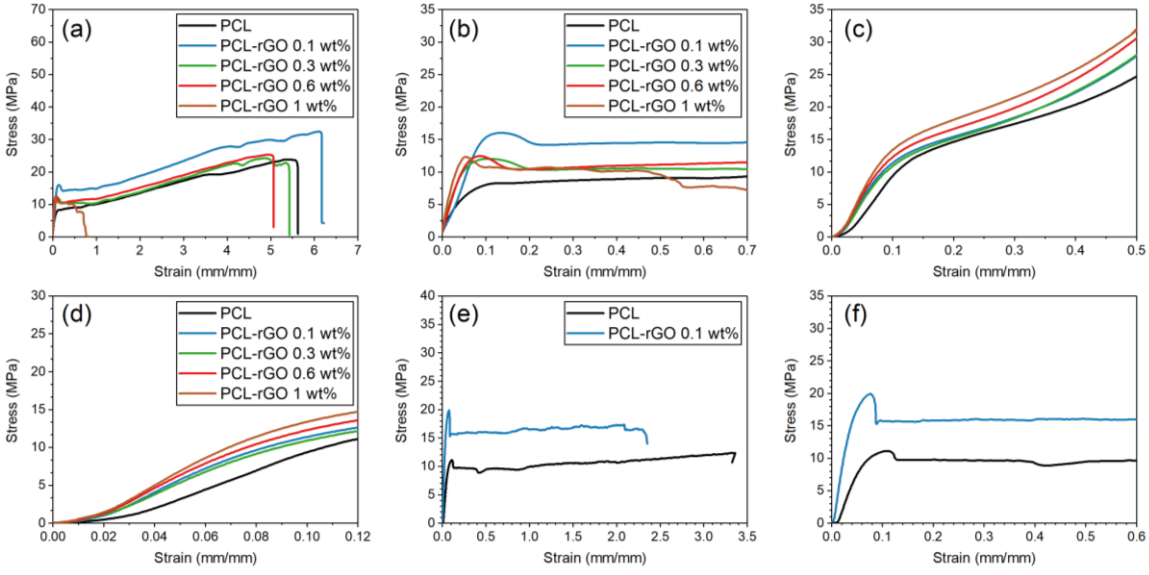

Figure 2.2: Representative (a) full tensile stress-strain curves, (b) tensile stress-strain curves over the elastic region, (c) full compressive stress-strain curves, and (d) compressive stress strain curves over the elastic region curves for melt cast PCL and PCL-rGO nanocomposites with 0.1 wt%, 0.3 wt%, 0.6 wt% and 1.0 wt% rGO. (e) full tensile stress-strain curves curves for melt electrowritten filaments of PCL and PCL-rGO 0.1 wt% nanocomposites. (f) tensile stress-strain curves over the elastic region curves for melt electrowritten filaments of PCL and PCL-rGO 0.1 wt% nanocomposites.

Higher rGO loadings (0.6 wt%, 1 wt%) in PCL show higher Young's Modulus, as compared to lower loadings (0.1 wt%, 0.3 wt%), with lower elongation at break and tensile strength, suggesting that at higher loadings materials become extremely brittle which could be due to overloading of the polymer matrix, formation of graphene aggregates, and worse dispersion of rGO in PCL as compared to low loadings.

Previous studies report that tensile strength and elastic modulus of PCL/Graphene oxide increased with increasing concentration of GO up to 0.3 wt% [17]. The influence of reduced graphene oxide on mechanical properties of electrospun fibers was previously studied [16]. It was shown that with addition of 0.1 wt % of GO and rGO in PCL, the tensile strength of PCL scaffolds increased to over 160 % and 304 % respectively and elastic modulus increased to over 103 and 164 % . Additionally, previous studies report the weakened enhancement of mechanical properties at higher loadings (1 wt%) and correlate it with partial exfoliation of the nanosheets[30].

Other studies report the increase of Young's Modulus of approximately 1.5 folds after incorporation of pure graphene into PCL, at 4 wt%[22]. The concentration tested was higher than those reported in this study. Additionally, differences in preparation of materials were present, which could account for these changes, as slab samples were tested, and nanocomposites were prepared at 250 ºC. Also, the study was performed with pristine graphene rather than reduced graphene oxide[22].

Our tensile results show similar trends to those in the literature and confirm that after incorporation of rGO into PCL at loadings of 0.1 wt% and 0.3 wt%, tensile strength and Young's modulus increase. In this study, we observe a slightly lower increase in tensile

strength of approximately 1.4-fold for 0.1 wt% rGO in PCL, and 1.1-fold for 0.3 wt % rGO in PCL. Previous studies show increase of up to 3 folds in Tensile Strength after incorporation of rGO into PCL at these loadings[30-31]. Studies report the increase in the Elastic Modulus of approximately 1.7-fold after incorporation of 0.1 wt% of rGO in PCL[30-31], which is similar to findings in this study. Our results show an increase of approximately 2 folds after incorporation of rGO at the loadings of 0.1 wt% and 0.3 wt% which is slightly higher than the value. The differences observed could be related to different preparation methods of samples as our composites were melt-casted, while previous studies report changes in electrospun scaffolds [30-31].

Compression tests illustrated that the compressive modulus also increased with increasing rGO content, in a dose dependent manner (**Figure 2.2 c-d, Table 2.1**). Specifically, the PCL-rGO 0.1 wt% exhibited a 35% increase in stiffness while the PCL-rGO 1.0 wt% exhibited a 55% increase in stiffness. Additionally, all nanocomposites exhibit increased strength over the range of strains tested, and none exhibited failure.

It is well documented that processing of nanocomposites can impact their mechanical behaviour due to changes in the micro/nanostructure of the material[23-24]. As such, mechanical tests were performed on melt electrowritten filaments of PCL and the nanocomposites. As described in the printing section below, only the PCL-rGO 0.1 wt% composite exhibited robust printing capacity, so these measurements were only made on the pure PCL and PCL-rGO 0.1 wt% nanocomposite (**Figure 2.2 e-f**). A 2-fold increase in Young's Modulus has been observed in PCL-rGO 0.1 wt% fibers compared to PCL fibers (**Table 2.1**). Similarly, an increase in Ultimate Tensile Strength of approximately 1.5-fold was observed between PCL-rGO 0.1 wt% and PCL melt electrowritten fibres. Upon the full mechanical characterization of materials,

PCL-rGO 0.1 wt% was chosen as a most optimal material to further investigate in terms of printing the final device.

Table 2.1: Mechanical characterization of PCL-rGO nanocomposites.

Tensile properties of melt-cast PCL-rGO nanocomposites

Material	Modulus (MPa)	Ultimate Tensile Strength (MPa)	Strain at break (mm/mm)	Stress at break (MPa)
PCL	131 ± 4.4	24.1 ± 1.1	5.6 ± 0.6	24.0 ± 1.2
PCL/rGO (0.1 wt%)	212 ± 39.2	34.1 ± 5.2	6.6 ± 1.0	33.2 ± 4.6
PCL/rGO (0.3 wt%)	215 ± 18.1	25.7 ± 3.3	5.4 ± 1.5	25.0 ± 3.4
PCL/rGO (0.6 wt%)	240 ± 27.9	24.1 ± 5.3	4.7 ± 1.5	23.7 ± 5.2
PCL/rGO (1 wt%)	286 ± 35.8	11.6 ± 2.2	0.5 ± 0.1	8.7 ± 1.1

Compressive properties of the PCL-rGO nanocomposites

Material	Modulus (MPa)	Stress at 10% strain (MPa)
PCL	121 ± 6.1	7.8 ± 0.5
PCL/rGO (0.1 wt%)	165 ± 5.9	11.3 ± 0.2
PCL/rGO (0.3 wt%)	161 ± 6.2	10.6 ± 0.9
PCL/rGO (0.6 wt%)	175 ± 7.9	11.9 ± 0.8
PCL/rGO (1 wt%)	188 ± 7.5	12.4 ± 0.9

Tensile properties of PCL-rGO fibres produced via MEW

Material	Modulus (MPa)	Ultimate Tensile Strength (MPa)	Strain at break (mm/mm)	Stress at break (MPa)
PCL	205 ± 17.1	13.7 ± 1.4	3.5 ± 2.0	13.5 ± 1.4
PCL/rGO (0.1 wt%)	520 ± 38.9	20.6 ± 1.6	2.9 ± 1.5	17.7 ± 0.9

2.4.3. Rheology

The ability to melt electrowrite a material is dependent on its rheological properties. The melting point of PCL is ~60 ºC. We assessed the viscosity of PCL and the nanocomposite melts at 70 ºC, 90 ºC, and 120 ºC, temperatures relevant to the MEW process. Additionally, the rheology data was collected for PCL-rGO 0.1 wt% as this material was used for fabrication of melt electrowritten scaffold. It was found that the viscosity was both temperature and shear

rate dependent (**Figure 2.3**)**.** Specifically, the viscosity decreased with increasing temperature, and it dropped sharply from a rather steady value when the shear rate of 10 s^{-1} was exceeded. Additionally, we assessed the storage (G') and loss (G'') moduli of the materials over a range of temperatures and shear rates. The storage modulus represents the energy stored in the elastic structure of the sample and gives information about the amount of structure in the sample. The loss modulus represents the viscous part or amount of energy dissipate in the sample. Above 60 ºC, both materials were characterized by higher loss moduli than storage moduli, which is correlated to flow like behaviour and confirms their printability in that regions (**Figure 2.3c**). Frequency sweeps were performed at printing temperatures of PCL and PCL-rGO 0.1 wt% and showed that at lower frequencies storage moduli are higher than loss moduli (solid-like behaviour), while at higher frequencies loss moduli are higher than storage moduli (liquid-like behaviour) (**Figure 2.3d**). These results correspond to the transition of the material from solid like state present at higher frequencies, to liquid like state at higher frequencies, which is due to higher shears on the materials and its transition. This transition relates to higher values of loss modulus at higher frequencies as the materials becomes more liquid-like, therefore more processable under MEW. Our results also suggest liquid like properties above melting temperatures, which is consistent with our ability to print the material at approximately 90ºC.

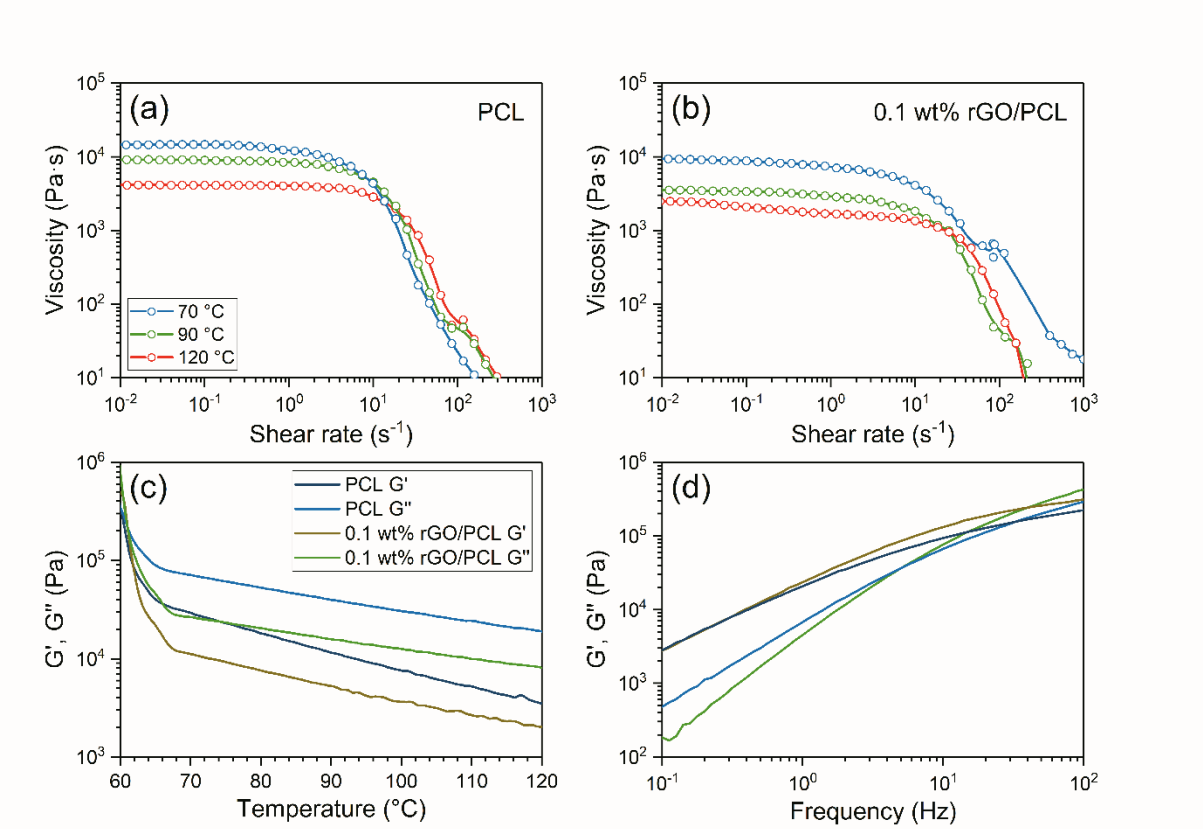

Figure 2.3: Rheology characterization of PCL and PCL-rGO 0.1 wt%. (a) Viscosity curve as a function of shear rate at the temperatures of 70, 90 and 120 ºC for PCL. (b) and PCL-rGO 0.1 wt%. (c) Temperature sweep for PCL and PCL-rGO 0.1 wt%. (d) Frequency sweep for PCL and PCL-rGO 0.1 wt%.

2.4.4. Differential scanning calorimetry and Thermogravimetric analysis

Differential scanning calorimetry (DSC) and thermogravimetric analysis (TGA) were performed on the PCL and PCL-rGO 0.1 wt% before and after printing (**Figure 2.4**) to understand the influence of printing on thermal behaviour of the material and its crystallinity. Three heating cycles were run from 20 ºC to 150 ºC at the heating rate of 10 ºC/min to gain a better understanding of thermal history of the materials as well as the influence of printing on the degree of crystallinity as well as melting and crystallization temperatures. TGA results show that PCL, PCL-rGO 0.1 wt% and PCL-rGO 0.1 wt% after processing, have similar TGA curves and show the initial degradation at temperatures of approximately 375 ºC (**Figure 2.4a**).

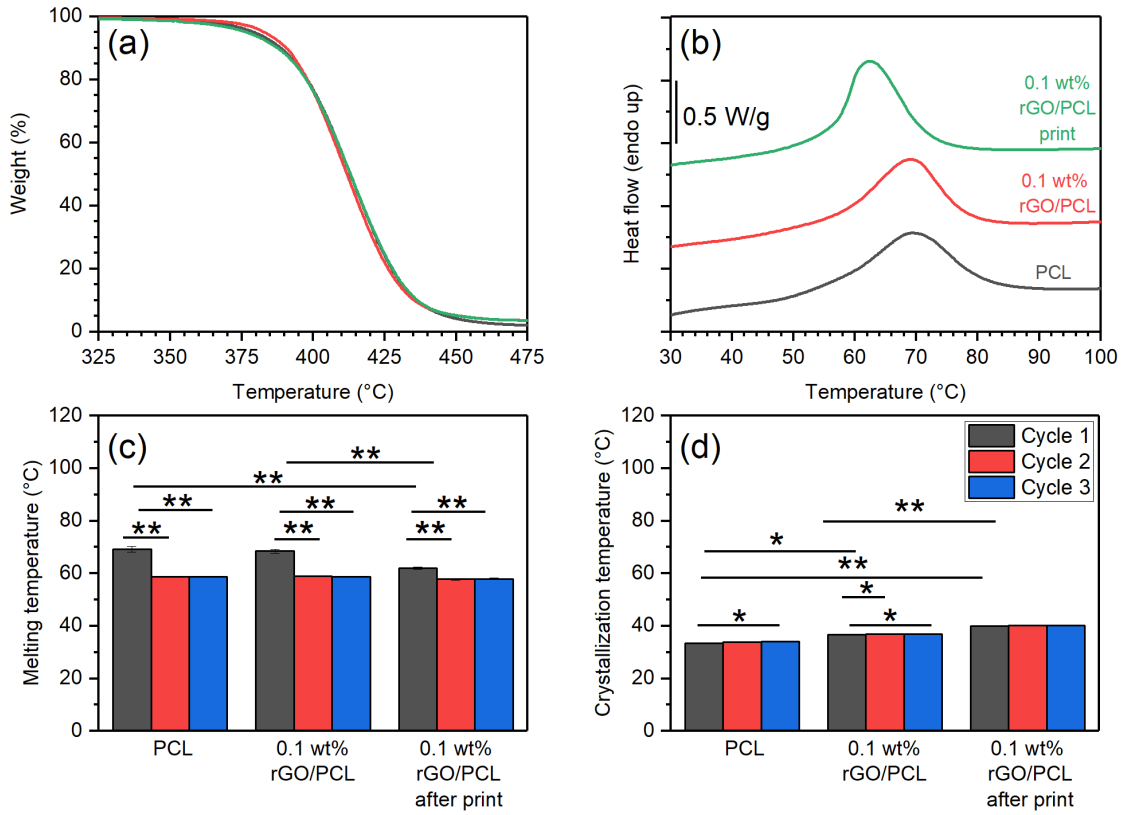

Figure 2.4: Thermal analysis for PCL, PCL-rGO 0.1 wt% and melt electrowritten PCL-rGO 0.1 wt%. (a) TGA curves for all materials (b) DSC curves (c) Melting temperatures after 1st, 2nd and 3rd heating cycles (d) Crystallization temperatures after 1st, 2nd and 3rd cycle. Asterisks (*) represent statistical difference where **P<0.01 and *P<0.05, (n = 3).

DSC results illustrate that melting temperature of PCL before print decreases from 69.2 ºC to 58.8 ºC between first and second heating cycle; however, there is no change in the melting temperature after the second cycle (**Figure 2.4c**). Similarly, the melting temperature of PCL-rGO 0.1 wt% before and after printing, decreases after 1st heating cycle with no significant change after 2nd and 3rd cycles. There is no significant difference between the melting temperatures of PCL and PCL-rGO 0.1 wt% before printing. Additionally, PCL-rGO 0.1 wt% after printing has lower melting temperature after 1st cycle (62 ºC) compared to PCL-rGO 0.1 wt% before printing (68.4 ºC) and pure PCL (69.2 ºC), suggesting the influence of printing on thermal properties of the material (**Figure 2.4c**). The change in thermal properties of the material after printing can be related to thermal history of the polymer, changes in the

arrangement of the polymeric chains after shear-induced extrusion, and changes in the arrangement of the crystalline structure.

DSC results also indicate that there is no significant change in crystallization temperature between the 1st, 2nd or 3rd cooling cycles in PCL-rGO (0.1 wt%) after printing (**Figure 2.4d**). There is a slight increase in crystallization temperatures between 1st and 3rd cycles for PCL and PCL-rGO (0.1 wt%) before printing. The crystallization temperature of PCL-rGO 0.1 wt% (36.7 ºC) is higher compared to PCL (33.5 ºC) after first cooling cycle. This trend continues for 2nd and 3rd cycles with PCL-rGO 0.1 wt% having crystallization temperatures of 36.8 ºC for both cycles and PCL with crystallization temperatures of 33.8 ºC and 34.1ºC for 2nd and 3rd cycle respectively. The increase in the temperature for the crystallization of the polymer upon inclusion of 0.1 wt% rGO is in line with previous reports, whereby the dispersed rGO induces the nucleation of crystalline polymer chains[25-26].

In terms of the crystallization temperatures for PCL-rGO 0.1 wt% before and after printing, processing leads to higher crystallization temperatures of the material (**Figure 2.4d**). Degree of crystallinity for materials before processing was approximated using the formula (1) and found to be approximately 45.7 % for PCL and 52.0% for PCL-rGO 0.1 wt%. There was no significant difference in crystallinity after processing of the materials. Our results indicate an increase in crystallinity after incorporation of rGO into the polymer matrix which is consistent with previous reports of this effect in various polymers[25-27]. rGO has been previously reported to enhance crystallization and orientation of polymeric chains of polycaprolactone in the flow direction[25]. Additionally, higher degree of crystallinity in PCL-rGO 0.1 wt% compared to PCL is related to increased hardness of the material observed in mechanical tests as crystallinity has an impact on mechanical behaviour of polymers[28-29]. rGO has been reported to be an effective

nucleating agent[25-26], which could explain and increase in crystallinity and mechanical properties of PCL-rGO 0.1 wt% compared to PCL.

2.4.5. Fabrication and characterization of melt electrowritten stents

Current industrial techniques for the fabrication of polymeric coronary artery stents involve extrusion or injection moulding, followed by melt blowing, and laser cutting to obtain the final stent structure [30]. The biodegradable stents produced by these methods have struts with thickness from 100 µm to 250 µm [3-4, 31], significantly thicker than the traditional non-degradable stents which have struts that range in thickness from 60 µm to 80 µm [3]. Additionally, these traditional fabrication techniques do not enable the production of personalised stents with unique sizing and strut design based on a patient's unique anatomy and disease state.

Additive manufacturing techniques provide an attractive method for the fabrication of personalised stents, and recent reports have explored this as a means of bottom up stent fabrication using a variety of materials. For instance, stereolithographic 3D printing technologies can print complex structures with a high level of detail, and melt-extrusion based 3D printing techniques such as fused deposition modelling can produce biodegradable stents with personalised stent design. However, these technologies have significant limitations that hinder their translation to the clinic. For instance, stereolithography often requires specialised photo-polymerizable polymers with complex chemistries [11-13 32 22], and conventional melt-extrusion based 3D printing technologies do not have adequate print resolution. They can only produce devices with struts equal to or greater in thickness than those produced commercially (150 µm – 600 µm) [12, 22, 33]. Additive manufacturing techniques with print resolutions of <80 µm are required to enable the customised design of stents with appropriate strut thicknesses.

MEW is an emerging technique that utilises melt extrusion and applied voltage for fabrication of highly ordered 3D structures for various application in the biomedical field [34]. MEW is a nozzle based additive manufacturing technology in which electro-hydrodynamically stabilized molten polymer jets. This technique combines the principles of conventional additive manufacturing by the use of pressure to extrude the material, and heating elements to melt the polymer, with electrospinning, by using of a voltage applied between the needle and a collector to produce a jet. In this method, a polymer with high viscosity and low conductivity results in a melt flow which is followed by cooling down of the electrified jet and solidification of deposited material. Upon contact with a collector, the molten jet solidifies to a fibre which can be deposited in a direct-writing manner. Studies have shown the feasibility of the technique for fabrication of scaffolds with sub-micron filaments [35-36]. The technique allows fabrication of structures with typical fibre diameters from 5 μm to 30 μm and allows writing of the material to millimetre heights [35]. The major advantages of MEW compared to conventionally used electrospinning and 3D printing are the ability to fabricate complex 3D structures with high resolution (< 30μm), controlled porosity of the printed scaffold, and solvent-less processing.

Although MEW has been used for the fabrication of tubular constructs consisting of organized fibre architectures, it has not been explored in context of fabrication of biodegradable coronary artery stents. Additionally, tubular scaffolds presented in the previous literature have not been able to produce the complex patterning required in advanced stenting design. To date, the structures that have been produced can still be considered as fibre-winding technologies rather than true 3D printing. Therefore, only relatively simple design concepts consisting of straight, repeating design elements have been fabricated [34]. Moreover, only a few composite materials compositions (e.g., PCL/hydroxyapatite and PCL/magnesium fluoride) has been investigated with MEW.

Once the window for printability was determined, MEW was used to produce stent-like structures. As shown in **Figure 2.5**, MEW enables the facile fabrication of stents with a wide range of architectures. The stent diameter, pore size, strut thickness, and geometry can all be independently tailored in a bottom up fashion using MEW. Additionally, struts with a thickness as low as 60 μm were produced. Stents were melt electrowritten with diameters of 2 mm, 3.5 mm and 5 mm, a clinically relevant range of diameters. The strut spacing (also described as pore size) was investigated over a range of 0.5 mm x 0.5 mm to 1 mm x 1 mm. Multiple stent architectures were also created including curving structures, right-angled structures, and rectangular shapes with varying strut spacing.

The architectures were varied to show the potential for personalised stent design. This patient-specific approach is becoming increasingly important. Human vessels vary in sizes, and it is often difficult to match the stent size to the patient's plaque and vessel size. Such a mismatch in device-vessel size can lead to significant clinical complications such as life-threatening late stage thrombosis. MEW could provide a facile method of directly fabricating patient-specific stents based on the patient's unique anatomy and disease state.

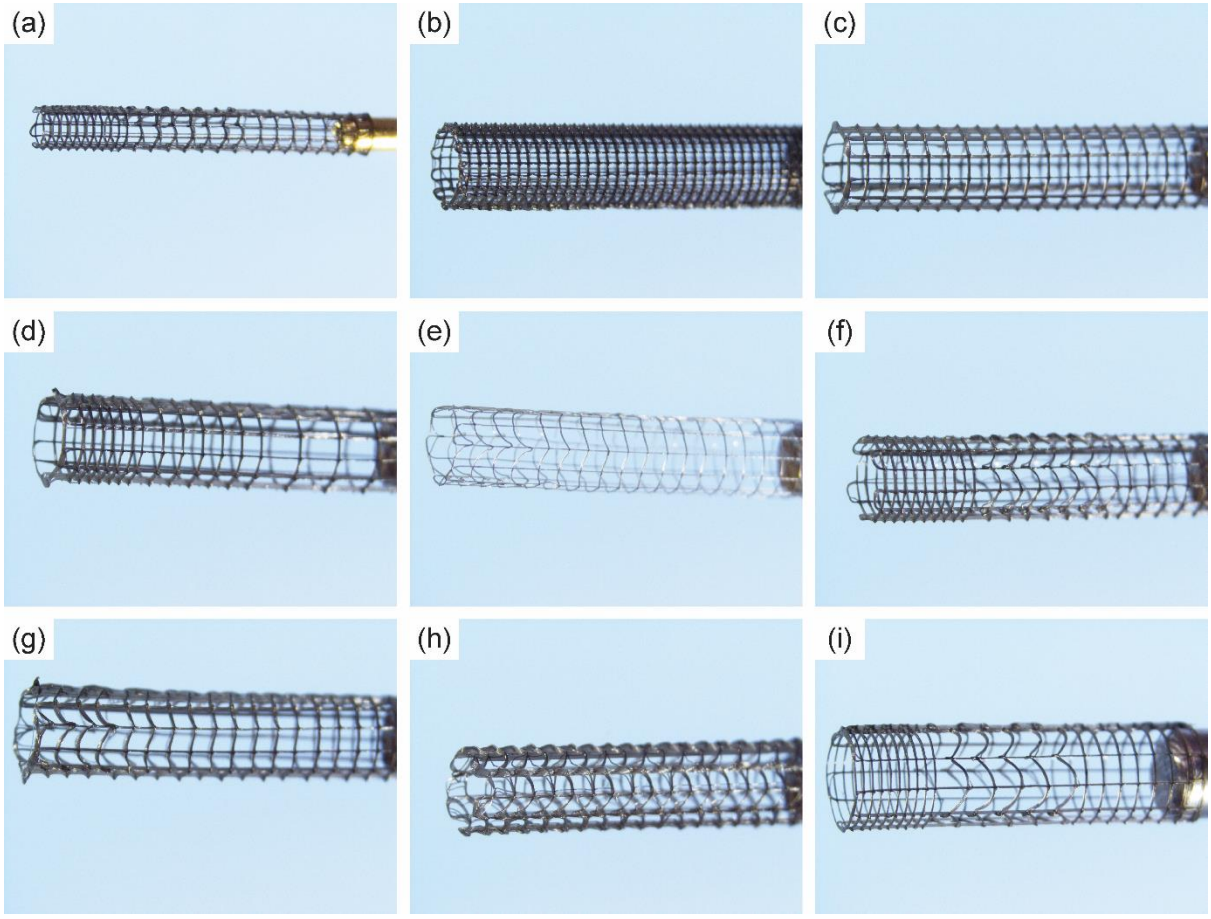

Figure 2.5: Fabrication of stent-like structures from PCL-rGO 0.1 wt% nanocomposites using MEW: (a) D = 2mm, multi structures, (b) D = 3.5 mm, 0.5 mm x 0.5 mm pore size, (c) D= 3.5 mm, 1 mm x 1 mm pore size (d) D = 3.5 mm, multi pore size (e) D = 3.5 mm, multi-curve (f, g) D = 3.5 mm, multi-architecture (h) D = 3.5 mm, curvy architecture (i) D = 5 mm, multi-architecture.

SEM was used to assess the microstructure of the stents (**Figure 2.6**). The SEM images illustrate high fidelity in printing and precise control over the deposited filaments at the microscale. Additionally, as MEW is an additive manufacturing technique, where filaments are deposited on top of one another in a layer-by-layer fashion, this technique provides two independent mechanisms by which the strut size can be tailored. First, the width of the struts can be controlled by controlling the diameter of the deposited filament, and the height of the strut can be controlled by specifying the number of print layers that are deposited. From measurements taken using the SEM images, we found that struts with a minimum fibre thickness of 60 µm could be produced, thicknesses that are similar to what are currently used in when fabricating metallic stents. In this study, we did not aim at reducing strut thickness

below 60 µm, as it would most likely result in insufficient mechanical support for the artery. Our aim was to illustrate our capability to fabricate stents with the thickness of current coronart artery stents, and we did not aim at reducing the strut thickness further. Metallic stents are usually characterized by strut thickness of 60 µm – 80 µm, which is often times optimal for them. However, polymeric materials are generally weaker than metallic ones, thus reducing strut thickness below 60 µm could result in loss of mechanical performance necessary for the application as a coronary artery stent.

Although MEW was previously used for fabrication of tubular scaffolds, this is the first study which shows the utilization of this technique for printing of stent-like structures with high level of complexity. Our results show that printed devices were customizable with their design, strut thickness, diameter, and degree of curvature, which has not been studied before. Only relatively simple design concepts consisting of straight, repeating design elements were fabricated before. Additionally, our study shows the utilization of PCL/rGO as a printing ink, which has not been shown before for its feasibility of printing utilizing MEW. Printing of only few composite materials such as PCL/hydroxyapatite or PCL/magnesium fluoride have been investigated with MEW. Therefore, our study is the first to show that PCL/rGO can be successfully processed into stent-like structures with high degree of resolution, low strut thickness, and customizable design utilizing MEW.

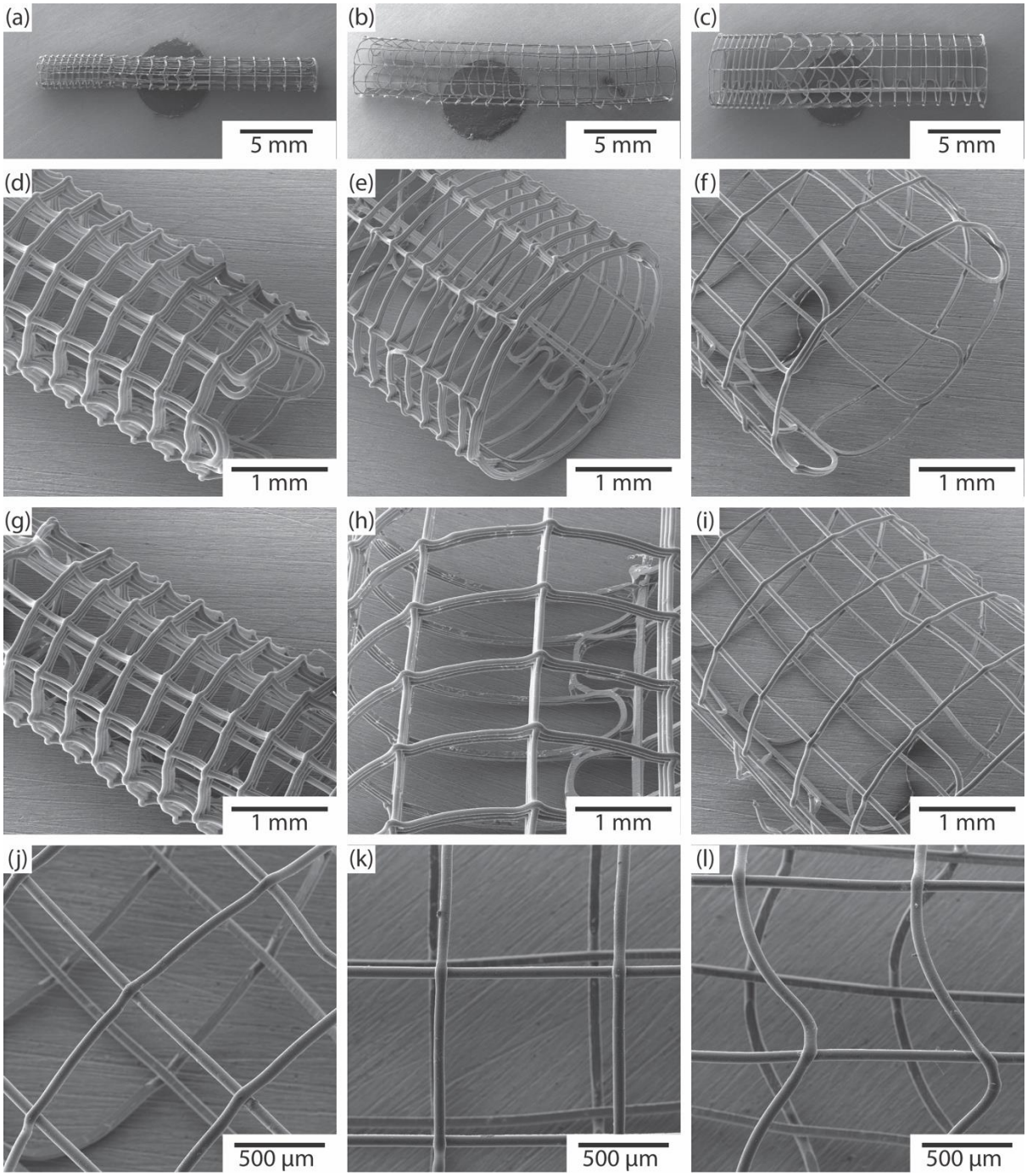

Figure 2.6: SEM images of melt electrowritten scaffolds with varying stent diameter (a-c), architecture (a-l), pore size (d-f), strut thickness (g-i), and strut curvature (j-l).

2.4.6. Three-point bending tests on melt electrowritten stents

Three-point bending tests were performed on melt electrowritten stents (PCL-rGO 0.1 wt%) according to the ASTM F2606-09, the standard guide for three-point bending of balloon expandable vascular stents. Specifically, we assessed the properties of melt electrowritten stents that had varying strut spacing (0.5 mm x 0.5mm, 1mm x 1mm) and number of layers (3 layers, 5 layers) (**Figure 2.7**). Results illustrate that with decreasing strut spacing and increasing number of printed layers on the scaffold, the flexural stiffness increases (**Figure 2.8**). Videos of three-point bending tests on melt electrowritten scaffolds which show how

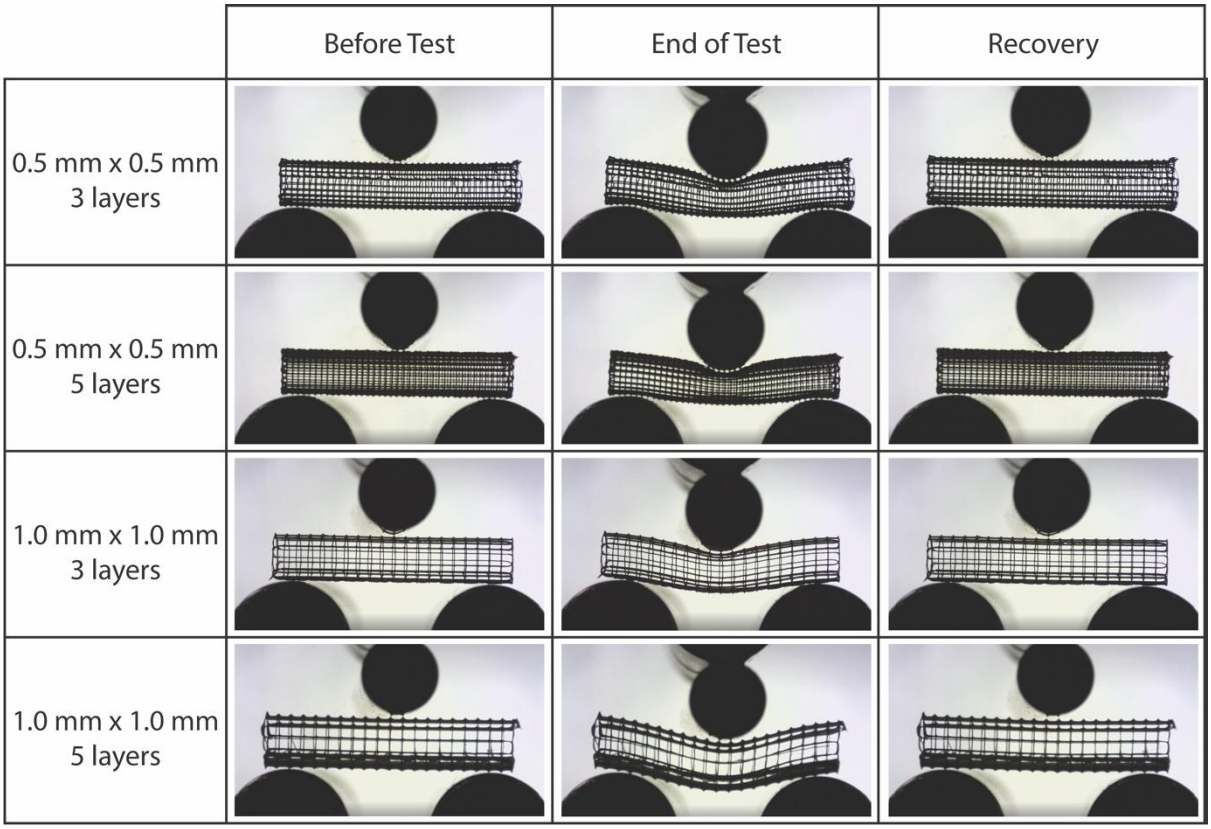

flexural load was applied, as well as full flexural recovery of the devices, are attached in the

Figure 2.7: Three-point bending tests on melt electrowritten scaffolds with varying pore size and number of printed layers.

supplementary information.

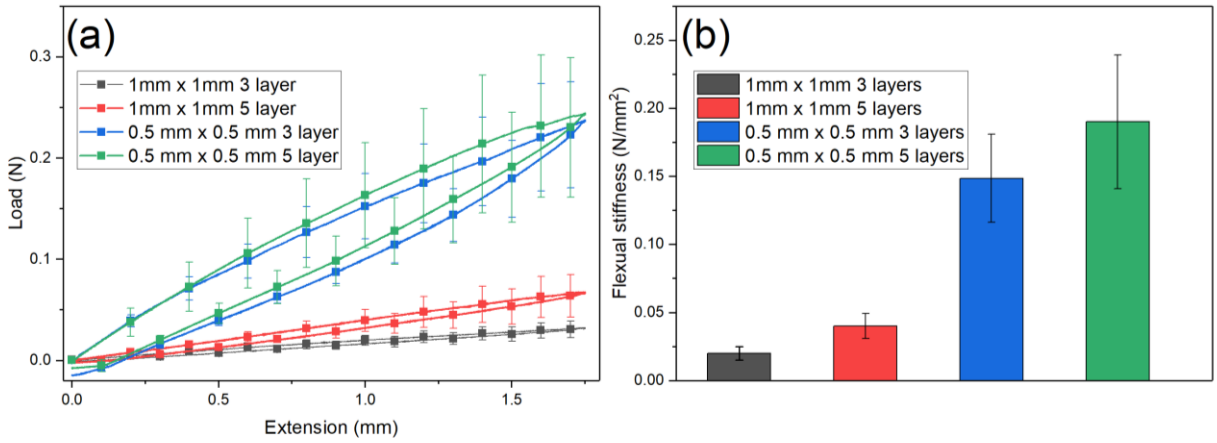

Figure 2.8: (a) Three-point bending tests for scaffolds with varying stent architectures and pore size (b) Flexural stiffness as a function of stent geometry for scaffolds with pore size of 0.5 mm x 0.5 mm and 3 layers, 0.5 mm x 0.5 mm and 5 layers, 1 mm x 1mm and 3 layers, 1 mm x 1 mm and 5 layers.

Stents with pore size of 0.5 mm x 0.5mm and 5 layers of printed materials were found to have the highest flexural stiffness. Our mechanical results from standards and melt electrowritten samples are consistent with previous studies which report increase in Tensile strength, Young's modulus and Elongation at break by inclusion of graphene in polymeric materials due to excellent natural mechanical properties of graphene[16-17, 22, 37-38].

Flexural stiffness of a stent is critical in overall performance of a device – a stent needs to be flexible enough to access the lesion site and adequately cover it [39-40]. High flexural flexibility, high tensile and compressive strength, as well as sufficient elongation at break are all necessary for superior mechanical performance of a biodegradable stent. The mechanical characteristics show that printed stents are very flexible and come back to their original shape after loading which is the desired performance.

2.4.7. Biological interactions

To gain the better understanding of the materials and their biological interactions, three types of biological tests were performed on polymer coatings with PCL, PCL-rGO (0.1 wt%) and

PCL-rGO (0.3 wt%). PCL was chosen as a control material. PCL-rGO (0.1 wt%) was chosen as it was the final material used for MEW of stents. PCL-rGO (0.3 wt%) was additionally studied to better understand the influence of increasing rGO loading on biological performance.

2.4.7.1. Protein adsorption

Protein adsorption studies were performed on polymer surfaces with PCL, PCL-rGO (0.1 wt%) and PCL-rGO (0.3 wt%) coatings (**Figure 2.9**). Protein adsorption was found to increase with increasing rGO content in PCL. Quantification of protein adsorption was performed by approximation of the change in frequency (Hz), as shown in **Table A1** (**Appendix Chapter 2**). Previous studies aimed at understanding the mechanism and reasons behind increased protein adsorption on graphene based materials and suggested that π-π stacking, electrostatic interactions and hydrophobic effects of graphene-based materials are the predominant mechanisms responsible for increased adsorption [41-42]. Reduced graphene oxide was previously reported to be more compatible than graphene oxide, in terms of protein adsorption, as graphene oxide was found to enhance protein adsorption more significantly than reduced graphene oxide due to more surface alterations[41]. Therefore, reduced graphene oxide was chosen in this study as it causes a less profound increase in protein adsorption relative to graphene oxide. In our results, we observed an increase in protein adsorption on PCL-rGO composites, as compared to PCL, with a concentration dependent effect. Higher concentration of rGO in PCL (0.3 wt%) was found to increase protein adsorption more significantly as compared to low concentration (0.1 wt%). This could be related to increase of electrostatic interaction between graphene sheets and proteins, which is more evident at higher concentration of rGO.

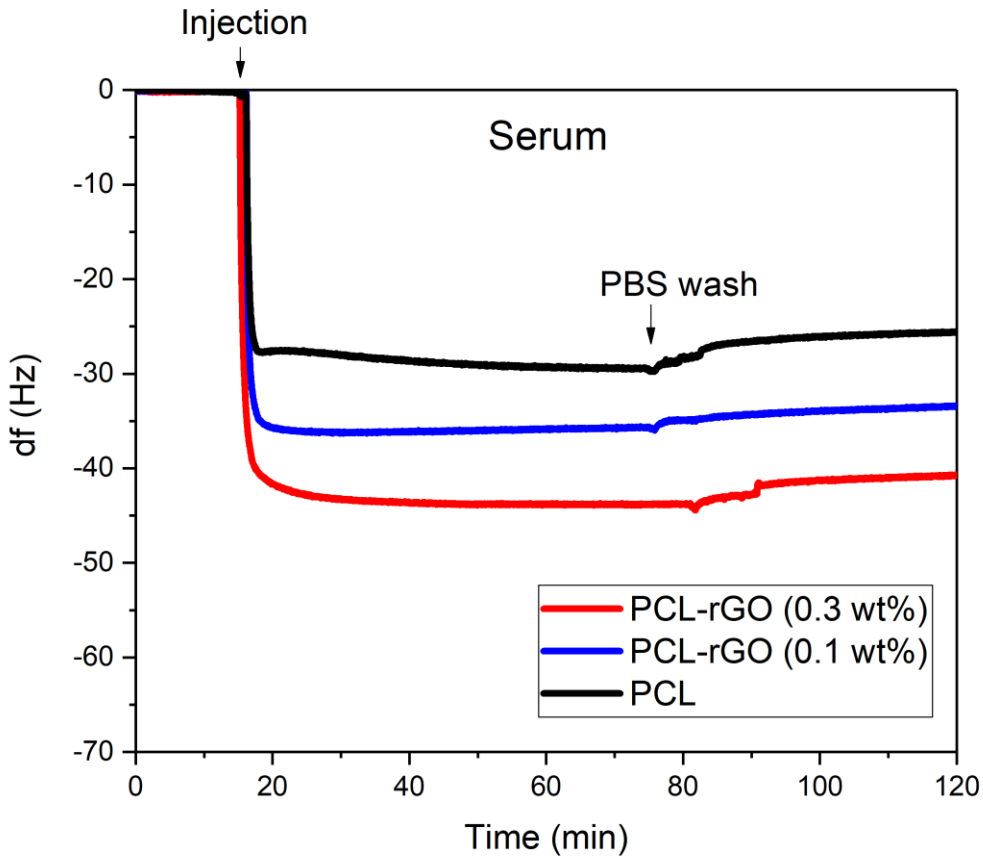

Figure 2.9: Serum and protein adsorption curves for PCL and PCL-rGO (0.1 wt% and 0.3 wt%) composites.

2.4.7.2. Human umbilical vein endothelial cells

The native blood vessel is lined with a monolayer of endothelial cells, referred to as an endothelium. This cell layer plays a vital role in maintaining vascular homeostasis. As such, rapid endothelialisation of coronary artery stents is desired. hUVECs adhesion and proliferation studies were performed on PCL, PCL-rGO 0.1 wt%, and PCL-rGO 0.3 wt% nanocomposites to assess how the addition of the rGO influences endothelial cell-material interactions (**Figure 2.10, Figure 2.11**). The surface density of cells at 4 hours, 4 days, and 7 days post-seeding was determined through a DNA quantification assay. The initial adhesion of hUVECs is similar across all surfaces. However, the addition of the rGO improves the cell proliferation rate in a dose-dependent manner. In fact, the number of hUVECs inhabiting the PCL-rGO 0.3wt% surfaces is equal to or greater than the control surface (glass) across all days

of the study. These results are corroborated by the fluorescence microscopy images taken at 4 hours and 7 days post-seeding (**Figure 2.11**). Similar numbers of cells were observed on all surfaces at the initial adhesion stage; however, only glass and the PCL-rGO 0.3 wt% surfaces were near confluence after the 7 days of culture. These results suggest that the PCL-rGO nanocomposites lead to better endothelialisation compared to pure PCL. These results are in accordance to previous reports in the literature of improved cell proliferation on biomaterial surfaces by inclusion of graphene suggesting the influence of electrostatic interactions and protein adsorption to increased cell proliferation [17, 43-44]

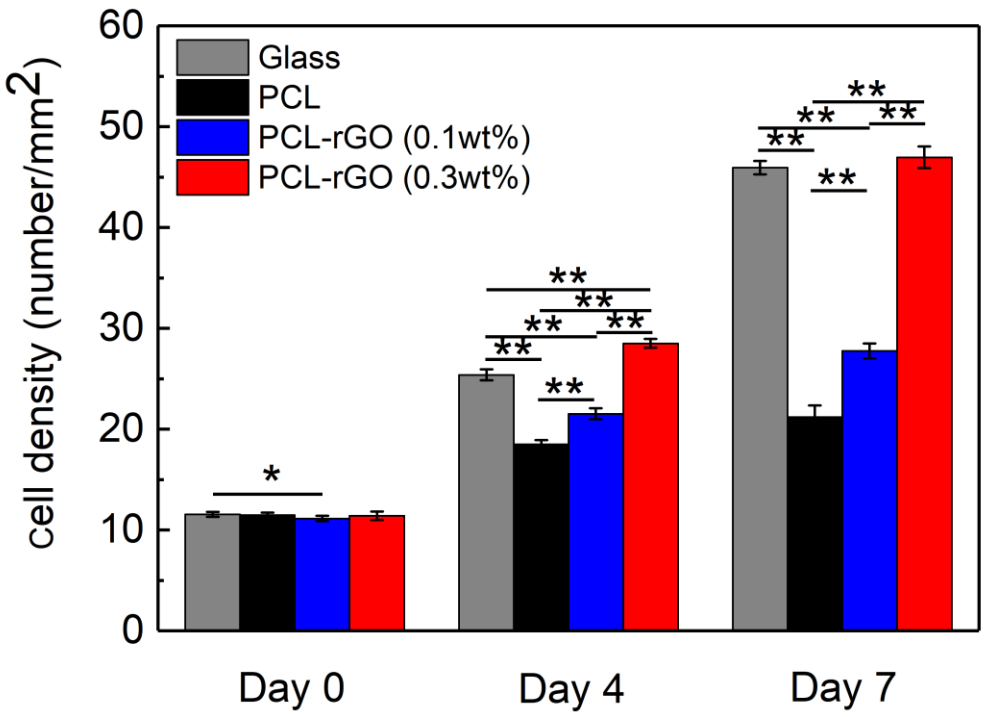

Figure 2.10: Quantification of HUVECs adhesion and proliferation over 7 days of culture. The cells were seeded at a density of 1.7 $\times 10^4$ cells per cm^2. Asterisks (*) represent statistical difference where **P<0.01 and *P<0.05, (n= 3).

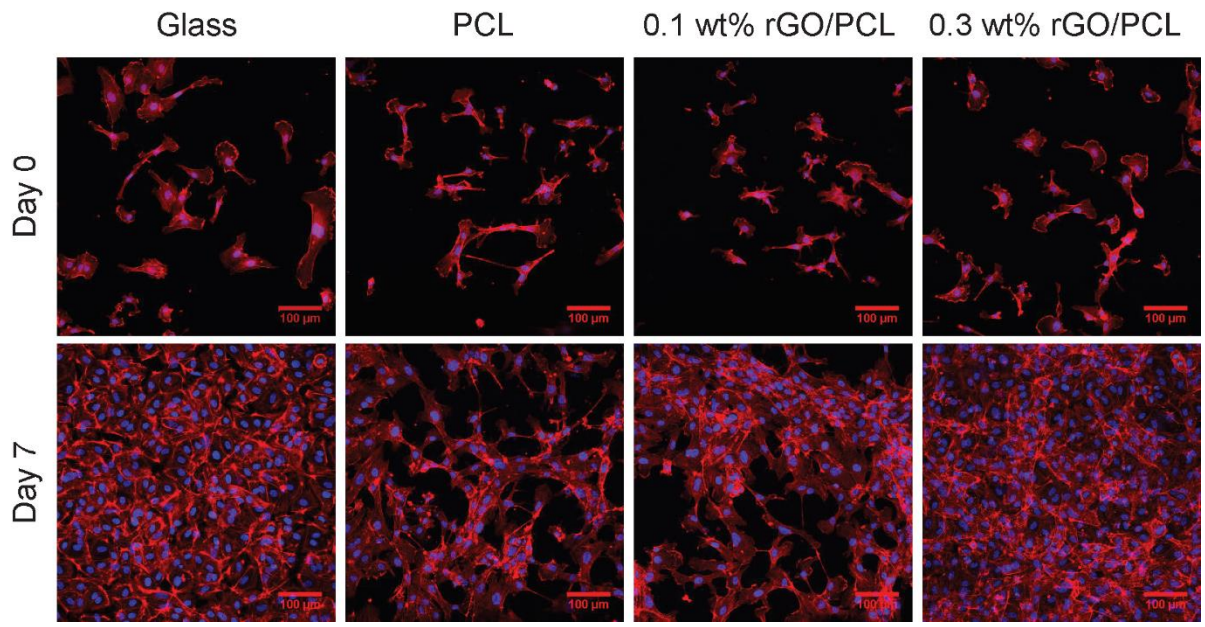

Figure 2.11: Representative images of hUVECs adhesion and proliferation on various surfaces over 7 days. Scale bar represents 100 µm.

2.4.7.3. Platelet adhesion

Platelet adhesion was studied on surfaces coated with PCL, as well as PCL-rGO (0.1 wt% and 0.3 wt%) (**Figure 2.12, Figure 2.13**). The results show similar number of platelets adhering between PCL and PCL-rGO (0.3 wt%), and a slight decrease in a number of adhered platelets on PCL-rGO (0.1 wt%).

Previous studies on platelet adhesion on graphene enriched materials showed that reduced graphene oxide shows excellent haemocopatibility as compared to other graphene based materials and does not evoke strong platelet activation or adhesion responses as compared to other graphene additives such as graphene oxide[18-19]. Studies show that increased protein adsorption on graphene-based materials leads to the surface passivation and reduced adhesion or aggregation of platelets[18]. In this study, we observe increased serum and protein adsorption, and a slight decrease in platelet adhesion on surfaces with rGO 0.1 wt%. Our results also show that at higher rGO concentrations (0.3 wt%) the morphology of platelets trends towards an increasingly spread shape. This suggests more activation of platelets at surfaces with higher

rGO concentrations. At lower concentration (0.1 wt%) there is no statistically significant difference in morphology of platelets, thus activation, as compared to PCL. Platelet activation can lead to increased thrombogenicity of the material and activation of thrombogenicity pathways, therefore lower concentration of rGO (0.1 wt%) was chosen for final printing application[39].

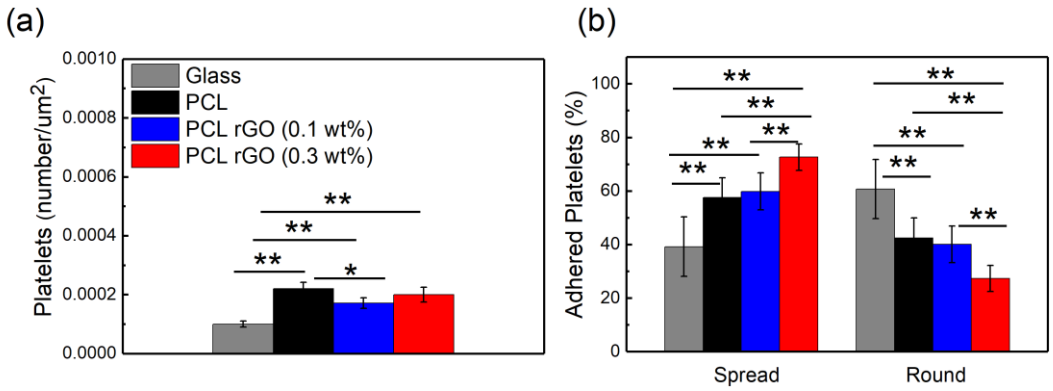

Figure 2.12: (a) Platelet adhesion on glass, PCL, PCL-rGO (0.1 wt%) and PCL-rGO (0.3 wt%). (b) Morphology of adhered platelets on glass, PCL, PCL-rGO (0.1 wt%), PCL-rGO (0.3 wt%). Asterisks (*) represent statistical difference where **P<0.01 and *P<0.05, (n= 3).

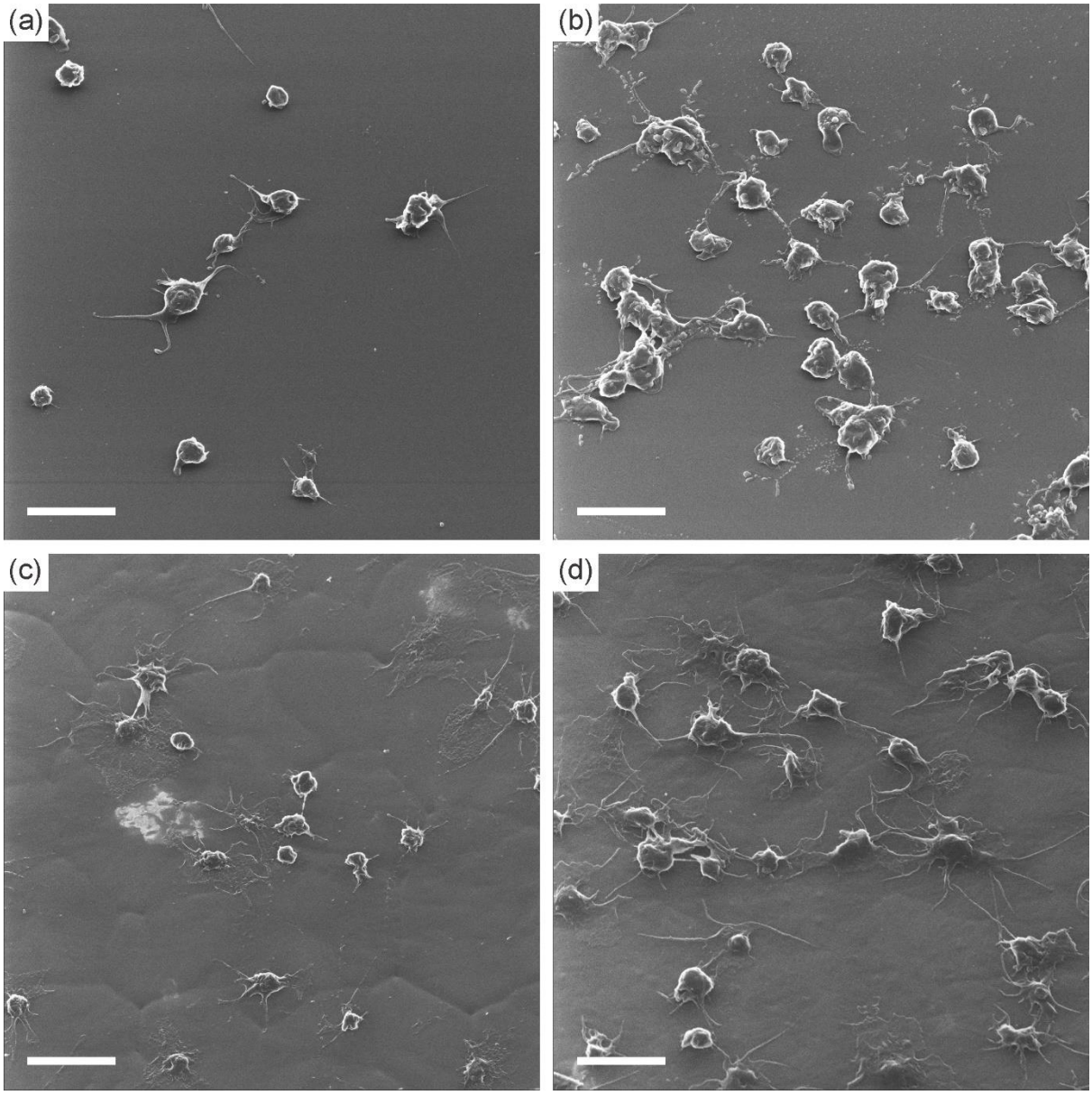

Figure 2.13: Representative images of platelet adhesion on (a) glass (b) PCL (c) PCL-rGO (0.1 wt%) (d) PCL-rGO (0.3 wt%). Scale bars are 5 μm.

2.5. Conclusion

Biodegradable PCL-rGO stent-like structures were fabricated using MEW. The tensile modulus of the PCL-rGO nanocomposites increased by more than 2 folds for composites containing all nanocomposite compositions (0.1 wt% to 1 wt% rGO), compared to PCL, and by 3 folds for PCL-rGO. Additionally, the compressive modulus of the materials also increased for all nanocomposite compositions. Additionally, a class of PCL-rGO 0.1 wt% stents have been printed using MEW system with varying diameters, strut thicknesses, strut spacing, and strut geometries, and strut thicknesses as small as 60 μm were produced. Furthermore, the PCL-rGO 0.1 wt% composites improved endothelial proliferation over 7 days compared to PCL controls with no observed statistically significant increase in platelet activation. This data supports the use of PCL-rGO 0.1 wt% nanocomposites in the development of biodegradable coronary artery stents and the use of MEW as a means of fabricating personalised stents.

2.6. References

1. McAloon, C. J.; Boylan, L. M.; Hamborg, T.; Stallard, N.; Osman, F.; Lim, P. B.; Hayat, S. A., The changing face of cardiovascular disease 2000-2012: An analysis of the world health organisation global health estimates data. *Int J Cardiol* **2016,** *224*, 256-264.

2. Ho, M.-Y.; Chen, C.-C.; Wang, C.-Y.; Chang, S.-H.; Hsieh, M.-J.; Lee, C.-H.; Wu, V.; Hsieh, I. C., The Development of Coronary Artery Stents: From Bare-Metal to Bio-Resorbable Types. *Metals* **2016,** *6* (7).

3. Foin, N.; Lee, R. D.; Torii, R.; Guitierrez-Chico, J. L.; Mattesini, A.; Nijjer, S.; Sen, S.; Petraco, R.; Davies, J. E.; Di Mario, C.; Joner, M.; Virmani, R.; Wong, P., Impact of stent strut design in metallic stents and biodegradable scaffolds. *Int J Cardiol* **2014,** *177* (3), 800-8.

4. Kalra, A.; Rehman, H.; Khera, S.; Thyagarajan, B.; Bhatt, D. L.; Kleiman, N. S.; Yeh, R. W., New-Generation Coronary Stents: Current Data and Future Directions. *Curr Atheroscler Rep* **2017,** *19* (3), 14.

5. Jinnouchi, H.; Torii, S.; Sakamoto, A.; Kolodgie, F. D.; Virmani, R.; Finn, A. V., Fully bioresorbable vascular scaffolds: lessons learned and future directions. *Nat Rev Cardiol* **2019,** *16* (5), 286-304.

6. Borhani, S.; Hassanajili, S.; Ahmadi Tafti, S. H.; Rabbani, S., Cardiovascular stents: overview, evolution, and next generation. *Prog Biomater* **2018,** *7* (3), 175-205.

7. Stiehm, M.; Wustenhagen, C.; Siewert, S.; Ince, H.; Grabow, N.; Schmitz, K. P., Impact of strut dimensions and vessel caliber on thrombosis risk of bioresorbable scaffolds using hemodynamic metrics. *Biomed Tech (Berl)* **2018**.

8. Boeder, N. F.; Dorr, O.; Bauer, T.; Mattesini, A.; Elsasser, A.; Liebetrau, C.; Achenbach, S.; Hamm, C. W.; Nef, H. M., Impact of strut thickness on acute mechanical performance: A comparison study using optical coherence tomography between DESolve 150 and DESolve 100. *Int J Cardiol* **2017,** *246*, 74-79.

9. Hanßke, F.; Bas, O.; Vaquette, C.; Hochleitner, G.; Groll, J.; Kemnitz, E.; Hutmacher, D. W.; Börner, H. G., Via precise interface engineering towards bioinspired composites with improved 3D printing processability and mechanical properties. *Journal of Materials Chemistry B* **2017,** *5* (25), 5037-5047.

10. International, A., Standard guide for three-point bending of baloon expandable vascular stents and stent systems. 2014; Vol. F2606-08.

11. Park, S. A.; Lee, S. J.; Lim, K. S.; Bae, I. H.; Lee, J. H.; Kim, W. D.; Jeong, M. H.; Park, J.-K., In vivo evaluation and characterization of a bio-absorbable drug-coated stent fabricated using a 3D-printing system. *Materials Letters* **2015,** *141*, 355-358.

12. Guerra, A. J.; Ciurana, J., 3D-printed bioabsordable polycaprolactone stent: The effect of process parameters on its physical features. *Materials & Design* **2018,** *137*, 430-437.

13. Guerra, A. J.; Ciurana, J., Fibre laser cutting of polymer tubes for stents manufacturing. *Procedia Manufacturing* **2017,** (13), 190-196.

14. Guerra, A. J.; Farjas, J.; Ciurana, J., Fibre laser cutting of polycaprolactone sheet for stents manufacturing: A feasibility study. *Optics & Laser Technology* **2017,** *95*, 113-123.

15. Wu, S. Y.; An, S. S.; Hulme, J., Current applications of graphene oxide in nanomedicine. *Int J Nanomedicine* **2015,** *10 Spec Iss*, 9-24.

16. Ramazani, S.; Karimi, M., Aligned poly(epsilon-caprolactone)/graphene oxide and reduced graphene oxide nanocomposite nanofibers: Morphological, mechanical and structural properties. *Mater Sci Eng C Mater Biol Appl* **2015,** *56*, 325-34.

17. Song, J.; Gao, H.; Zhu, G.; Cao, X.; Shi, X.; Wang, Y., The preparation and characterization of polycaprolactone/graphene oxide biocomposite nanofiber scaffolds and their application for directing cell behaviors. *Carbon* **2015,** *95*, 1039-1050.

18. Kenry; Loh, K. P.; Lim, C. T., Molecular Hemocompatibility of Graphene Oxide and Its Implication for Antithrombotic Applications. *Small* **2015,** *11* (38), 5105-17.

19. Singh, S.; Singh, M.; Nayak, M.; Kumari, S.; Shrivastava, S.; Grácio, J. J. A.; Dash, D., Thrombus Inducing Property of Atomically Thin Graphene Oxide Sheets. *ACS nano* **2011,** *5* (6), 4987-4996.

20. Muzyka, R.; Drewniak, S.; Pustelny, T.; Chrubasik, M.; Gryglewicz, G., Characterization of Graphite Oxide and Reduced Graphene Oxide Obtained from Different Graphite Precursors and Oxidized by Different Methods Using Raman Spectroscopy. *Materials (Basel)* **2018,** *11* (7).

21. Shen, Y.; Jing, T.; Ren, W.; Zhang, J.; Jiang, Z.-G.; Yu, Z.-Z.; Dasari, A., Chemical and thermal reduction of graphene oxide and its electrically conductive polylactic acid nanocomposites. *Composites Science and Technology* **2012,** *72* (12), 1430-1435.

22. Misra, S. K.; Ostadhossein, F.; Babu, R.; Kus, J.; Tankasala, D.; Sutrisno, A.; Walsh, K. A.; Bromfield, C. R.; Pan, D., 3D-Printed Multidrug-Eluting Stent from Graphene-Nanoplatelet-Doped Biodegradable Polymer Composite. *Adv Healthc Mater* **2017,** *6* (11).

23. Fu, S.; Sun, Z.; Huang, P.; Li, Y.; Hu, N., Some basic aspects of polymer nanocomposites: A critical review. *Nano Materials Science* **2019,** *1* (1), 2-30.

24. Muller, K.; Bugnicourt, E.; Latorre, M.; Jorda, M.; Echegoyen Sanz, Y.; Lagaron, J. M.; Miesbauer, O.; Bianchin, A.; Hankin, S.; Bolz, U.; Perez, G.; Jesdinszki, M.; Lindner, M.; Scheuerer, Z.; Castello, S.; Schmid, M., Review on the Processing and Properties of Polymer Nanocomposites and Nanocoatings and Their Applications in the Packaging, Automotive and Solar Energy Fields. *Nanomaterials (Basel)* **2017,** *7* (4).

25. Wang, B.; Li, Y.; Weng, G.; Jiang, Z.; Chen, P.; Wang, Z.; Gu, Q., Reduced graphene oxide enhances the crystallization and orientation of poly(ε-caprolactone). *Composites Science and Technology* **2014,** *96*, 63-70.

26. Yao, G.; Duan, T.; An, M.; Xu, H.; Tian, F.; Wang, Z., The influence of epitaxial crystallization on the mechanical properties of a high density polyethylene/reduced graphene oxide nanocomposite injection bar. *RSC Advances* **2017,** *7* (35), 21918-21925.

27. Lee, S.; Hong, J.-Y.; Jang, J., The effect of graphene nanofiller on the crystallization behavior and mechanical properties of poly(vinyl alcohol). *Polymer International* **2013,** *62* (6), 901-908.

28. El-Hadi, A.; Schnabel, R.; Straube, E.; Müller, G.; Henning, S., Correlation between degree of crystallinity, morphology, glass temperature, mechanical properties and

biodegradation of poly (3-hydroxyalkanoate) PHAs and their blends. *Polymer Testing* **2002,** *21* (6), 665-674.

29. Pukánszky, B.; Mudra, I.; Staniek, P., Relation of crystalline structure and mechanical properties of nucleated polypropylene. *Journal of Vinyl and Additive Technology* **1997,** *3* (1), 53-57.

30. Martinez, A. W.; Chaikof, E. L., Microfabrication and nanotechnology in stent design. *Wiley Interdiscip Rev Nanomed Nanobiotechnol* **2011,** *3* (3), 256-68.

31. McMahon, S.; Bertollo, N.; Cearbhaill, E. D. O.; Salber, J.; Pierucci, L.; Duffy, P.; Dürig, T.; Bi, V.; Wang, W., Bio-resorbable polymer stents: a review of material progress and prospects. *Progress in Polymer Science* **2018,** *83*, 79-96.

32. Ware, H. O. T.; Farsheed, A. C.; Akar, B.; Duan, C.; Chen, X.; Ameer, G.; Sun, C., High-speed on-demand 3D printed bioresorbable vascular scaffolds. *Materials Today Chemistry* **2018,** *7*, 25-34.

33. Ware, H. O. T.; Farsheed, A. C.; Baker, E.; Ameer, G.; Sun, C., Fabrication Speed Optimization for High-resolution 3D-printing of Bioresorbable Vascular Scaffolds. *Procedia CIRP* **2017,** *65*, 131-138.

34. Hochleitner, G.; Fursattel, E.; Giesa, R.; Groll, J.; Schmidt, H. W.; Dalton, P. D., Melt Electrowriting of Thermoplastic Elastomers. *Macromol Rapid Commun* **2018,** *39* (10), e1800055.

35. Hochleitner, G.; Jungst, T.; Brown, T. D.; Hahn, K.; Moseke, C.; Jakob, F.; Dalton, P. D.; Groll, J., Additive manufacturing of scaffolds with sub-micron filaments via melt electrospinning writing. *Biofabrication* **2015,** *7* (3), 035002.

36. Castilho, M.; Feyen, D.; Flandes-Iparraguirre, M.; Hochleitner, G.; Groll, J.; Doevendans, P. A. F.; Vermonden, T.; Ito, K.; Sluijter, J. P. G.; Malda, J., Melt Electrospinning

Writing of Poly-Hydroxymethylglycolide-co-epsilon-Caprolactone-Based Scaffolds for Cardiac Tissue Engineering. *Adv Healthc Mater* **2017,** *6* (18).

37. Sarvari, R.; Sattari, S.; Massoumi, B.; Agbolaghi, S.; Beygi-Khosrowshahi, Y.; Kahaie-Khosrowshahi, A., Composite electrospun nanofibers of reduced graphene oxide grafted with poly(3-dodecylthiophene) and poly(3-thiophene ethanol) and blended with polycaprolactone. *J Biomater Sci Polym Ed* **2017,** *28* (15), 1740-1761.

38. Wang, B.; Zhang, Y.; Zhang, J.; Li, H.; Chen, P.; Wang, Z.; Gu, Q., Noncovalent Method for Improving the Interaction between Reduced Graphene Oxide and Poly(ε-caprolactone). *Industrial & Engineering Chemistry Research* **2013,** *52* (45), 15824-15828.

39. Sotomi, Y.; Onuma, Y.; Collet, C.; Tenekecioglu, E.; Virmani, R.; Kleiman, N. S.; Serruys, P. W., Bioresorbable Scaffold: The Emerging Reality and Future Directions. *Circ Res* **2017,** *120* (8), 1341-1352.

40. Sotomi, Y.; Suwannasom, P.; Serruys, P. W.; Onuma, Y., Possible mechanical causes of scaffold thrombosis: insights from case reports with intracoronary imaging. *EuroIntervention* **2017,** *12* (14), 1747-1756.

41. Qi, Y.; Chen, W.; Liu, F.; Liu, J.; Zhang, T.; Chen, W., Aggregation morphology is a key factor determining protein adsorption on graphene oxide and reduced graphene oxide nanomaterials. *Environmental Science: Nano* **2019,** *6* (5), 1303-1309.

42. Mao, H.; Chen, W.; Laurent, S.; Thirifays, C.; Burtea, C.; Rezaee, F.; Mahmoudi, M., Hard corona composition and cellular toxicities of the graphene sheets. *Colloids Surf B Biointerfaces* **2013,** *109*, 212-8.

43. Kumawat, M. K.; Thakur, M.; Gurung, R. B.; Srivastava, R., Graphene Quantum Dots for Cell Proliferation, Nucleus Imaging, and Photoluminescent Sensing Applications. *Sci Rep* **2017,** *7* (1), 15858.

44. Zhang, B.; Wei, P.; Zhou, Z.; Wei, T., Interactions of graphene with mammalian cells: Molecular mechanisms and biomedical insights. *Adv Drug Deliv Rev* **2016,** *105* (Pt B), 145-162.

3. Core cross linked biocompatible and biodegradable star brush polymers for hydrophilic antithrombotic drugs

3.1. Abstract

Molecular polymeric architectures such as star polymers are ideal candidates for drug encapsulation due to their biocompatibility, unimolecularity, small size, facile synthesis and well controlled drug release profiles. In this study, we report a synthesis CCSs via a three step process utilizing UV-ATRP and ring opening polymerisation (ROP). In the UV-ATRP step, PEG MEA and HEBriB are used to form polymeric brushes with varying brush lengths. These brushes are cross-linked with the use poly(ethylene glycol) diacrylate to form core-cross linked star polymers with arms that contain functional hydroxyl end groups. Ring opening polymerization of ε-caprolactone is performed in the final step utilizing the end hydroxyl groups. The resulting CCSs consist of hydrophobic PCL blocks in their outer shells, hydrophilic PEG MEA segments in their inner brush shells and hydrophilic PEGDA in their cores. These polymeric platforms allow the encapsulation of hydrophilic drugs without the need for conjugation of the drug to the carrier. The influence of PEG length and cross linker amount on the formation of stars is investigated. Synthesized CCSs are then evaluated for their drug loading properties using fluorescent dextran (20kDa) as model hydrophilic drug, and heparin. The drug loading studies demonstrate drug loading efficiencies of approximately 70% for dextran and 50 % for heparin, as well as a drug loading content of 6.8% and 5% for dextran and heparin, respectively. Drug release profiles of heparin and dextran are then studied at pH = 5 and pH = 7.4 to understand the influence of pH on drug release, utilizing ultraviolet/visible spectrophotometry (UV-VIS). Cytocompatibility of synthesized CCSs is assessed through the cytotoxicity studies on human umbilical vein endothelial cells (hUVECs). Proliferation and

adhesion studies of HUVECs are performed on synthesized surfaces with varying ratios of CCSs in PCL and show no difference in cell adhesion between groups and an increase of hUVECs proliferation with the increase of CCSs content in PCL matrix.

3.2. Introduction

Anticoagulant and antiplatelet drugs are widely used agents in antithrombotic therapy to prevent aggregation of platelets and fibrin [1-2]. Heparin is one of the most common clinically utilized anticoagulants, acting through binding to antithrombin III and leading to the inactivation of thrombin[2]. Heparin has been clinically used for more than 70 years and remains an efficient clinical treatment to prevent formation of blood clots. Additionally, it is a sulphur rich glycosaminoglycan with high water solubility. Another common antithrombotic agent is dextran, an antiplatelet drug, which acts by coating of platelets and endothelial cells thus decreasing adhesion of platelets and inhibiting stabilization of fibrin. The detailed mechanism of its action remains unclear with few reports regarding its influence on the blockage of uptake of tissue plasminogen activator[2]. Dextran is a hydrophilic polysaccharide with glucose units joined by 1:3 and 1:4 glucoside links. Both heparin and dextran are usually administrated intravenously; however, their prolongated local delivery can be achieved through a delivery system.

Heparin and dextran, the two most common antithrombotic drugs, are hydrophilic in nature. The administration of such drugs has been previously studied with the use of various delivery platforms such as reverse micelles[3], bioconjugates[4-5], liposomes[6-7], nanospheres[8], dendrimers[9-11] or other polymeric architectures. These studies show the feasibility of the use of delivery platforms for local antithrombotic drug delivery, however, some of these platforms (e.g., micelles, vesicles, and dendrimers) are based on self-assembly. The self-assembly mechanism

can lead to issues in the stability of the delivery platform, as well as the burst release of a drug due to uncontrolled disassembly below the critical association concentration or upon external stimuli such as pH and temperature[12]. Other systems such as core-shell architectures, hyperbranched polymers, functionalized dendrimers, or star polymers, have the advantage of robustness due to their covalent bonds. Nonetheless, they are often limited by the size of their cavities for drug loading and require more tedious synthesis processes[13]. Star polymers have several advantages over other delivery systems due to their facile preparation, the potential for a scalable synthesis, tuneable chemistry, and tailored core size for the desired application[14]. There are few studies investigating anti-thrombotic, hydrophilic drug delivery utilizing star polymers.

Star polymers can be synthesized via two fundamental approaches: a "core first" and an "arm first". The "core first" method utilizes a multifunctional core as an initiator and enables the growth of polymeric chains from the initiating sites with the variety of living controlled polymerisations[15-16]. The major disadvantage of this method is a low number of arms due to limited number of functional growth sites. This often leads to a small core size and low drug loading efficiency of a synthesized system[14]. The "arm first" method utilizes end-reactive linear polymers as macroinitiators to initiate polymerisation of a cross-linkable monomer in a way that enables arm coupling and core formation[12]. The advantage of this approach is a high number of arms and a large core which enables high drug loading. More recently, a novel method has been studied known as a "brush first" approach[17-19]. This technique is relatively new, as compared to "core-first" and "arm-first" approaches. The method involves macromonomer photopolymerization to form living bottle-brush polymer initiators that are then cross-linked with a multi-functional monomer to generate brush-arm star polymers. The

key advantage of "brush-first" approach is the unique ability to quickly synthesize nanostructures of diverse size and composition in a simple one pot process[17-19].

Controlled (living) radical polymerizations have been widely studied in the field of polymer science for the past decade with ATRP being one of the most intensively explored[20-21]. ATRP is one of the most effective and widely used controlled radical polymerisation methodologies as it allows for synthesis of complex polymer structures in a robust manner with precise control over the chemical composition, polydispersity and uniform growth of polymer chains[20]. Traditionally, ATRP synthesis was copper mediated and required higher concentrations of transition metals and later copper removal. Several studies have been conducted to exploit methodologies to manipulate the activation-deactivation equilibrium between active and dominant species to maximize control during polymerization[22]. These approaches were based on the selection of copper-ligand complexation agents to determine the optimal rate of polymerization and manage deactivating species concentration[22].

More recently, various stimuli have been studied for their control over activation-deactivation equilibrium[23] such as photochemical[24-25], pressure[26], or electrochemical[22, 27]. These stimuli lower the activation energy for initiation and activation steps of synthesis reactions, allowing for the in-situ generation of more active catalysts and faster controller radical polymerization under milder conditions[22]. Previous studies have shown that the controlled living radical polymerisation of methacrylates can be efficiently controlled under visible light[22, 28-29]. Additionally, traditional copper mediated polymerization was also proven to benefit from photo-irradiation by development of copper mediated photo induced controlled radical polymerization systems both in the presence or lack of conventional photo initiators or photosensitisers[30-33]. A recent study reported a visible/sunlight (UV) photoinduced ATRP of

both acrylic and methacrylic monomers with parts per million (ppm) of Cu catalyst with subtle differences to the mechanisms as compared to previous studies[34]. The study addresses the limitation of conventional ATRP in which a high loading of catalyst is required and adds on to previous literature which reports methods to allow ppm-scale concentrations of catalyst to be used through continuous regeneration of Cu^{I} activators[28, 35].

This work builds on previous reports of UV-ATRP of methacrylates[22]. We investigate the formation of polymeric brushes with targeted molecular weights (DP_n = 10 - 40) under UV irradiation ($l_{max} \approx 360$ nm). Here, the photoactivation is induced in $Cu^{II}(Me_6\text{-Tren})Br_2$ (Tren = tris(2-aminoethyl)amine)) with an excess of aliphatic tertiary amine Me_6-Tren. In this study, we report the successful development of a core-cross linked biocompatible and biodegradable star-brush polymers (CCSs) via the "brush first" route, followed by ring opening polymerization (ROP).

In the first step of the synthesis pathway, HEBriB was used as an initiator (MI) and PEG MEA was reacted with it to synthesize PEG based brushes, which were then cross-linked by PEGDA to form core-cross linked star-brush polymers via UV-ATRP. The hydroxyl groups on the arms of these star-brush polymers were then used as initiating sites for ROP of CL (**Figure 3.1**). The key building blocks used to form the CCSs were PCL as the hydrophobic arms, PEG MEA as hydrophilic brush shell, and PEGDA as cross-linked hydrophilic core. The influence of PEG length and the amount of cross-linker on the formation of stars was investigated.

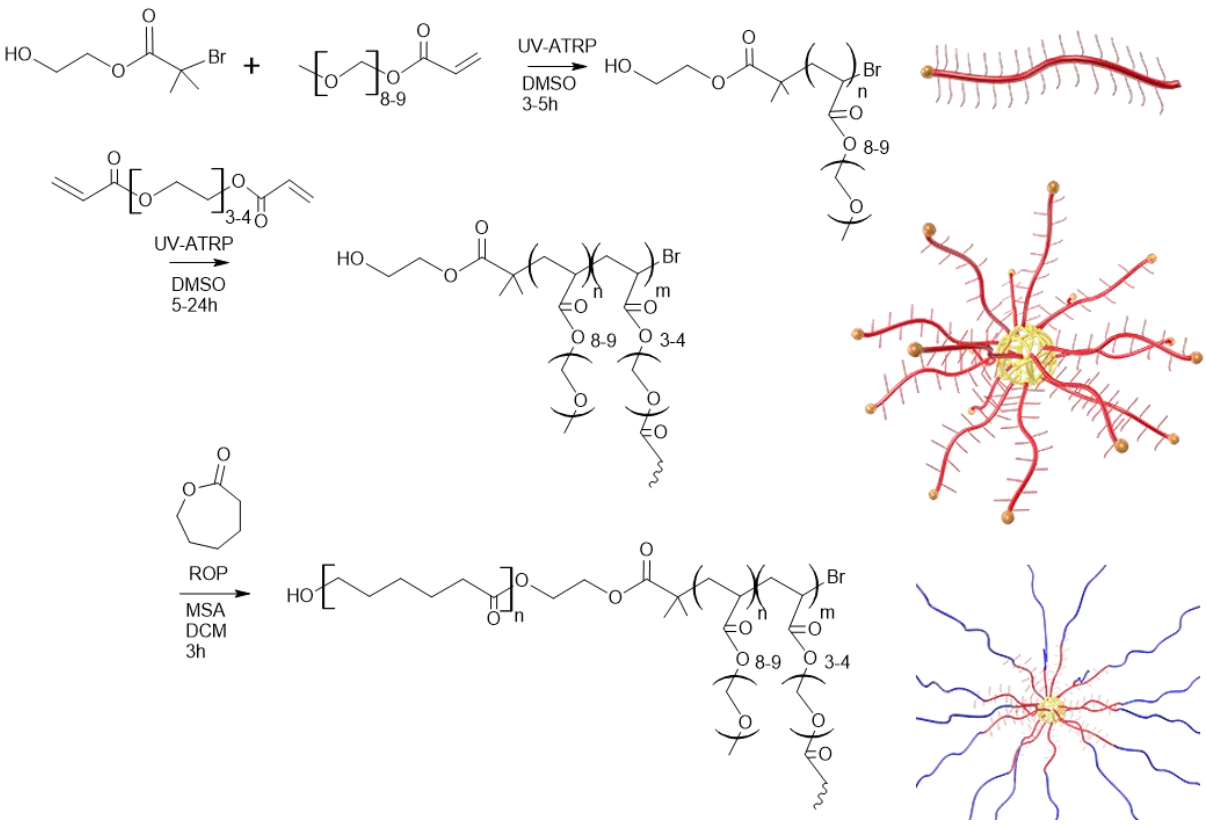

Figure 3.1: Schematic of synthesis pathway.

In this study, the aim was to synthesize a star polymer with hydrophilic brush-core and hydrophobic arms. PEGDA was chosen as a cross-linker due to its hydrophilicity and ability to cross-link under UV light. PEG MEA was chosen to form an inner brush due to its end methyl group and hydrophilic nature of a molecule. PCL was chosen as an outer block due to its hydrophobicity, biocompatibility, and degradable nature. Synthesized star-brush polymers were investigated as molecules for drug loading of hydrophilic drug to allow their incorporation into the hydrophobic matrices. Loaded star polymers were designed to function as hydrophilic drugs carriers to be later incorporated into the hydrophobic, polymeric matrices. Synthesized CCS were found to exhibit approximately 70 % and 50 % drug loading capacity for hydrophilic drugs such as dextran and heparin respectively. Upon successful loading of CCS with dextran and heparin, drug release profiles were obtained at pH = 5 and pH = 7.4. In

vitro cytotoxicity of CCSs, as well as adhesion and proliferation studies of human umbilical vein endothelial cells (hUVECs) on surfaces with varying ratio of CCS in PCL were performed.

3.3. Methods

3.3.1. Materials

ε-Caprolactone (97 %), methane sulfonic acid (MSA, 98 %), copper (II) bromide ($CuBr_2$), poly(ethylene glycol) diacrylate (Mn = 250 Da), poly(ethylene glycol) methyl ether acrylate (Mn = 480 Da), 2-hydroxyethyl acetate, fluorescent isothiocyanate dextran (Mn = 20 kDa), heparin sodium salt from porcine mucosa (Grade I-A, ≥ 180 USP units/mg), Azure A chloride, were purchased from Sigma Aldrich. Dry toluene, dichloromethane and ε-caprolactone were obtained by distillation from calcium hydride before use. Poly(ethylene glycol) diacrylate (Mn = 250 Da) and poly(ethylene glycol)methyl ether acrylate (Mn = 480 Da) were deinhibited by passing through basic alumina columns before use. HEBriB was synthesized via the esterification of 1,2-ethanediol with α-bromoisobutyryl bromide (98 %, Aldrich), purified by flash column chromatography, and characterized by ^{1}H NMR and ^{13}C NMR. Me_6TREN was synthesized according to the procedure reported in the literature[36].

3.3.2. Synthesis of core-cross linked star-brush polymers

Preparation of a series of PCL-PEG MEA-PEGDA CCS polymers was achieved via UV-ATRP of HEBriB and PEG MEA using a “brush-first” one pot strategy with HEBriB as the initiator and PEGDA as the cross-linker. Variation of the PEG MEA: HEBriB as well as MI:PEGDA ratios resulted in CCS polymers of varying hydrophilicity. In a typical process, HEBriB-PEG MEA brush was prepared in the first step. HEBriB (1 equiv.), PEG MEA (40 equiv., 20 equiv., 15 equiv. or 10 equiv.), $CuBr_2$ (0.02 equiv.), Me_6TREN (0.12 equiv.) were dissolved in DMSO at 12.5 wt% concentration of polymer and the mixture was degassed for 30 min. The reaction mixture was then exposed to UV light for 3 h. subsequently, a 100 µL aliquot of the MI solution was taken for ^{1} H NMR analysis to determine the conversion to brush structure. Upon >90%

conversion, PEGDA was added for the cross-linking step at various ratios to the number of synthesized brush arms (10 equiv., 15 equiv., 20 equiv., 25 equiv., or 30 equiv.) in DMSO mixture. The reaction was stirred under UV irradiation for 24 h. After 24 h, the reaction was stopped and a 100 µL aliquot of the solution was taken for ^{1}H NMR analysis and DMF GPC analysis. Upon the confirmation of the molecular weight, number of the arms, and size of the synthesized CCS polymer, the crude mixture was dialyzed against water using dialysis tubes (MWCO = 50 kDa) and freeze dried for 7 days to remove any water content. In the last step to synthesize PCL-PEG MEA-PEGDA CCS polymers, dry CCS (1 equiv.) was dissolved in toluene (3 mL) to remove any residual water using a toluene-water azeotrope under reduced pressure by the high vacuum rotary evaporator. Dry CCS, ε-Caprolactone, MSA (2.1 equiv.) and dry DCM (5 mL) were added via syringe under Argon atmosphere following a previously described protocol[12]. The reaction mixture was stirred for 3-5 h at room temperature. A 100 µL aliquot of the reaction solution was taken for ^{1}H NMR analysis and DMF GPC analysis, respectively. The remainder of the crude reaction was precipitated into the diethyl ether to yield the final CCS polymer and dried under vacuum.

3.3.3. Characterization of star-brush polymers

Molecular weight characterizations were carried out via Gel Permeation Chromatography (GPC) using DMF as the mobile phase unless otherwise stated. The GPC analysis was conducted on a Shimadzu liquid chromatography system equipped with a PostNova PN3621 MALLS detector (λ = 532 nm), Shimadzu RID-10 refractometer (λ = 633 nm), and Shimadzu SPD-20A UV−vis detector using three identical Jordi columns (5 µm bead size, Jordi Gel Fluorinated DVB Mixed Bed) in series operating at 70 °C. DMF (>99%, Aldrich) with 0.05 mol L^{-1} LiBr was employed as the mobile phase at a flow rate of 1 mL min^{-1} following previously described protocols[12]. Calibration curves were used to determine molecular weights

of synthesized polymers by comparison to narrow molecular weight distribution poly(ethylene glycol) standards. When aqueous-phase GPC was employed, a separate Shimadzu liquid chromatography system was utilized, equipped with a Shimadzu RID-10 refractometer (λ = 633 nm), using three Waters Ultrahydrogel columns in series ((i) 250 Å porosity, 6 μm diameter bead size; (ii) and (iii) linear, 10 μm diameter bead size), operating at room temperature. The eluent was milli-Q water containing 20 % v/v acetonitrile and 0.1 % w/v trifluoroacetic acid (TFA) at a flow rate of 1 mL min^{-1} as described in the previous studies[12] . The molecular weight characteristics of the analyte were determined by a comparison to narrow molecular weight distribution poly(ethylene glycol) standards. All samples were filtered through 0.45 μm nylon filters prior to injection. Proton Nuclear Magnetic Resonance (^{1}H NMR) spectroscopy was conducted on a Varian Unity 400 MHz spectrometer operating at 400 MHz, using the solvent chloroform ($CHCl_3$) (Cambridge Isotope Laboratories) as reference and sample concentrations of approximately 10 mg mL^{-1}. Dynamic Light Scattering (DLS) measurements and analysis were performed on a Wyatt DynaoPro NanoStar DLS/SLS instrument with a GaAs laser (658 nm) at an angle of 90 °C and a temperature of 25 ± 0.1 °C. Spectra were obtained at concentrations of 1 mg mL^{-1} in water. UV-Vis spectrometric analysis was performed using a Shimadzu UV-2101 PC UV-Vis scanning spectrophotometer at a scan rate of 1 nm s^{-1}, with paired quartz cuvettes (Starna Pty Ltd) as described in the previous studies[12,37].

3.3.4. Drug loading

CCS polymer (5 mg) was dissolved in 5 mL of THF and fluorescent dextran 20 kDa or heparin (0.5 mg) was dissolved in 1 mL of water. The mixture was stirred for 24 h and afterwards allowed for evaporation of THF. The precipitate of unloaded drug was collected by centrifugation at 1500 rpm (1450 G; rotor size = 13 cm) for 30 minutes and the amount of unloaded drug was determined by measuring the absorbance at 492 nm using calibration curves

generated from standard solutions for fluorescent dextran [12, 37]. For studies with heparin, the calibration curve was obtained with the use of Azure A to form heparin-azure complex and enable calculation of remaining heparin concentration through UV-Vis at 620 nm[38-40]. Drug loading content (DLC) and drug loading efficiency (DLE) were calculated according to the following equations[12],

$$DLC = \frac{Weight\ of\ loaded\ drugs}{Weight\ of\ polymer\ used} \quad (3.1)$$

$$DLE = \frac{Weight\ of\ loaded\ drugs}{Weight\ of\ drugs\ used} \quad (3.2)$$

The supernatant solutions were freeze-dried to yield drug-loaded CCS polymer samples for UV-Vis characterization.

3.3.5. In-vitro drug release

The *in vitro* drug release study was performed using a dialysis method following the previously described protocols[12, 41]. Briefly, freeze dried drug loaded CCS polymer samples (30 mg) were suspended in 2 mL PBS with pH 7.4 and 5, respectively. The solutions were transferred to two dialysis tubes (MWCO = 50 kDa) and dialyzed against the corresponding PBS solutions (pH = 7.4 and pH = 5) in a shaking water bath at 37 ºC[12]. At certain time intervals, 2.0 mL aliquots of the solution outside of the dialysis tubes were taken for UV-Vis analysis and replaced with fresh PBS solution. The concentrations of the released drug were estimated via UV-Vis using the standard curves. Heparin concentration was obtained with the use of Azure A to form heparin-azure complex and enable calculation of remaining heparin through measurement at 620 nm[38-40]. The amount of released dextran was approximated by measuring the absorbance at 492 nm[37].

3.3.6. Cytotoxicity assay

100 µL of medium containing 1 ×10^4 HUVECs (3.1 ×10^4 cells per cm^2) was plated to each well of a 96-well plate. After 12 h, the medium was replaced with 100 µL of fresh medium containing stars polymers with various concentrations from 0 to 500 µg/mL and incubated for 24 h. The cells were then washed twice with PBS and incubated with 110 µL fresh medium containing 10 µL of cell counting kit-8 (CCK-8) solution for a further 3 h[42-43]. Finally, the absorbance of the removed medium was measured at 460 nm using a microplate reader (TECAN M200 infinite Pro). Experiments were performed in triplicate. The cell viability (%) was calculated by the following formula, where [A] is the average absorbance:

$$Cell\ viability\ (\%) = \frac{[A]_{460(sample)} - [A]_{460(blank)}}{[A]_{460(control)} - [A]_{460(blank)}} \quad (3.3)$$

3.3.7. Adhesion and proliferation of human umbilical vein endothelial cells

Surface preparation: Cell culture surfaces were prepared by coating the growth surfaces of 8-well Lab-Tek II chamber slides or Lab-Tek chambered coverglass (for confocal microscopy) with 25 µL of a 2 % polymer solution in acetone. The chamber slides were then covered with aluminium foil and allowed to dry at ambient condition for 48 h. Chamber slides were sterilized through UV exposure for 1 h in a sterile biological safety cabinet. Wells were rinsed twice with PBS and incubated overnight in PBS at 37 °C before the introduction of cells.

Cell culture and maintenance: Pooled donor hUVECs were purchased from Lonza (Australia) and maintained in Clonetics™ EGM™-2 BulletKit™ containing Endothelial Basal Medium-2 (EBM™-2 Medium) supplemented with BulletKit™ as recommended by the supplier. Cells were cultured at 37 °C in a humidified 5 % CO_2 atmosphere. The culture medium was changed every other day. The cultures were passaged at 80 % confluence and

lifted using 0.25 % trypsin-EDTA. For all tests, the cells between passages 3 and 5 were used[44-45].

Adhesion and proliferation: 500 µL of medium containing 1.2 ×10^4 cells (1.71 ×10^4 cells per cm^2) was added to each well of polymer-coated chamber slides. Uncoated chamber slides were used as control. hUVECs were cultured for 7 days and the culture medium was changed every two days. Cell attachment and growth were determined for HUVECs after 4 h, 4 and 7 days using double stranded DNA (dsDNA) quantification by the Quant-iT™ PicoGreen® dsDNA Assay (Invitrogen) after digestion with papain as previously described [44-45]. Cell surface densities were determined by dividing the obtained cell number by the area of the test surface. Experiments were performed in triplicate.

The adherent endothelial cells were stained for the nuclei and actin cytoskeleton by using the FAK100 actin cytoskeleton/focal adhesion staining kit (Merck Millipore) as previously described[44-45]. Briefly, hUVECs were fixed after 4 h and 7 days and SMCs were fixed after 4 h and 4 days with 4 % paraformaldehyde and were permeabilized with 0.1 % Triton X-100 in PBS. The cells were stained with TRITC-phalloidin (1:500), and 4′,6-diamino-2-phenylindole (DAPI, 1:1000). The cells were finally washed and covered with PBS and imaged using a confocal laser scanning microscope (Nikon A1R) at 20 × magnification. Images were generated by optical sectioning in the z-direction and were analysed using ImageJ software (NIH).

3.3.8. Statistical analysis

The student's t test and ANOVA one-way analysis of variances were used to analyse the statistical differences between samples and were considered significant at $^{**}P<0.01$ and $^{*}P<0.05$.

3.4. Results and Discussion

3.4.1. Synthesis of core-cross linked star-brush polymers

Synthesis of the CCS polymers was achieved via three-step reaction, as illustrated in the **Figure 3.1**. In the first part of the synthesis pathway, a class of PEG brushes was synthesized with varying ratio of ATRP initiator to PEG MEA via UV-ATRP (**Figure 3.2, Figure 3.3**) to study the influence of molar ratio of PEG methyl ethyl acrylate to HEBriB (initiator) on the brush formation.

UV-ATRP was chosen as a synthesis method as it is a very robust technique for synthesis of polymers with well-controlled architecture, narrow polydispersity, and uses very low amounts of copper catalysts due to the photo-induction with the UV light [20-21, 28].

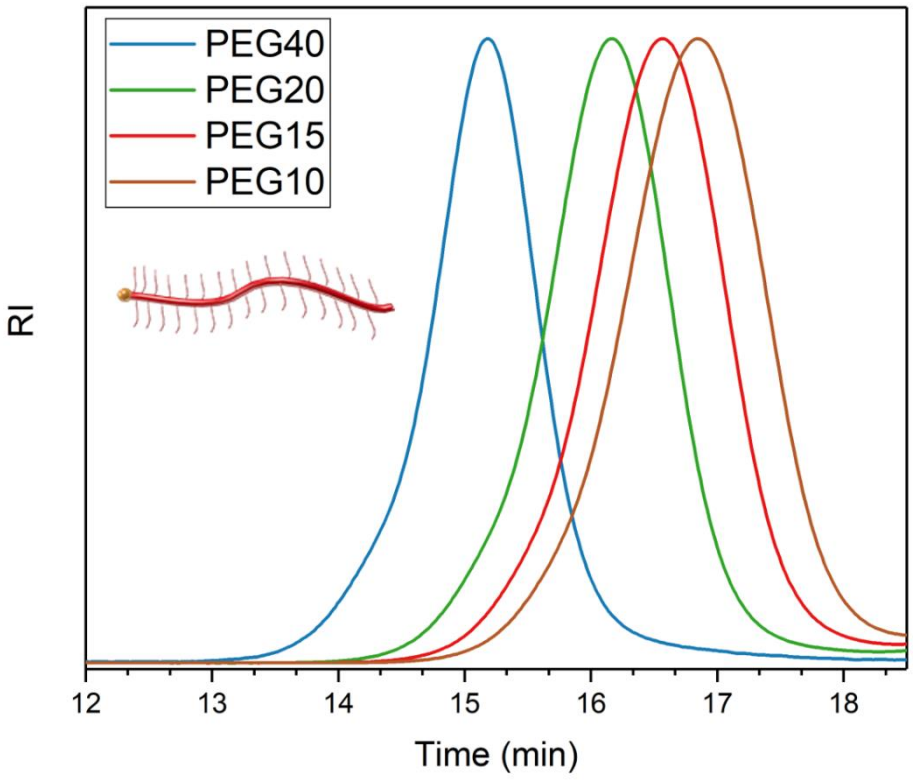

Figure 3.2: DMF GPC of synthesized brushes with varying number of repeat units (PEG40, PEG20, PEG15 and PEG10).

Photoinduced controlled radical polymerization was carried from the deoxygenated mixtures containing HEBriB:PEG MEA:$CuBr_2$:Me_6TREN = 1:40/20/15/10:0.02:0.12 in DMSO at total concentration of 12.5 wt %. ^{1}H NMR analysis was used to estimate the conversion of a PEG MEA monomer into polymer chain. Additionally, prior to the cross-linking of formed brush arms, the conversion and polydispersity of synthesized brush arm polymers were evaluated by GPC with DMF as a mobile phase (**Figure 3.2**). The conversion and kinetics of polymerization reaction was calculated by integrating of the peaks of CH in synthesized brush polymer (a-d peaks in the Figure 3.3) to the peak of CH in unconverted PEG methyl ethyl acrylate peaks (1-3 peaks in the Figure 3.3) in ^{1}H NMR spectrum (**Figure 3.3**).

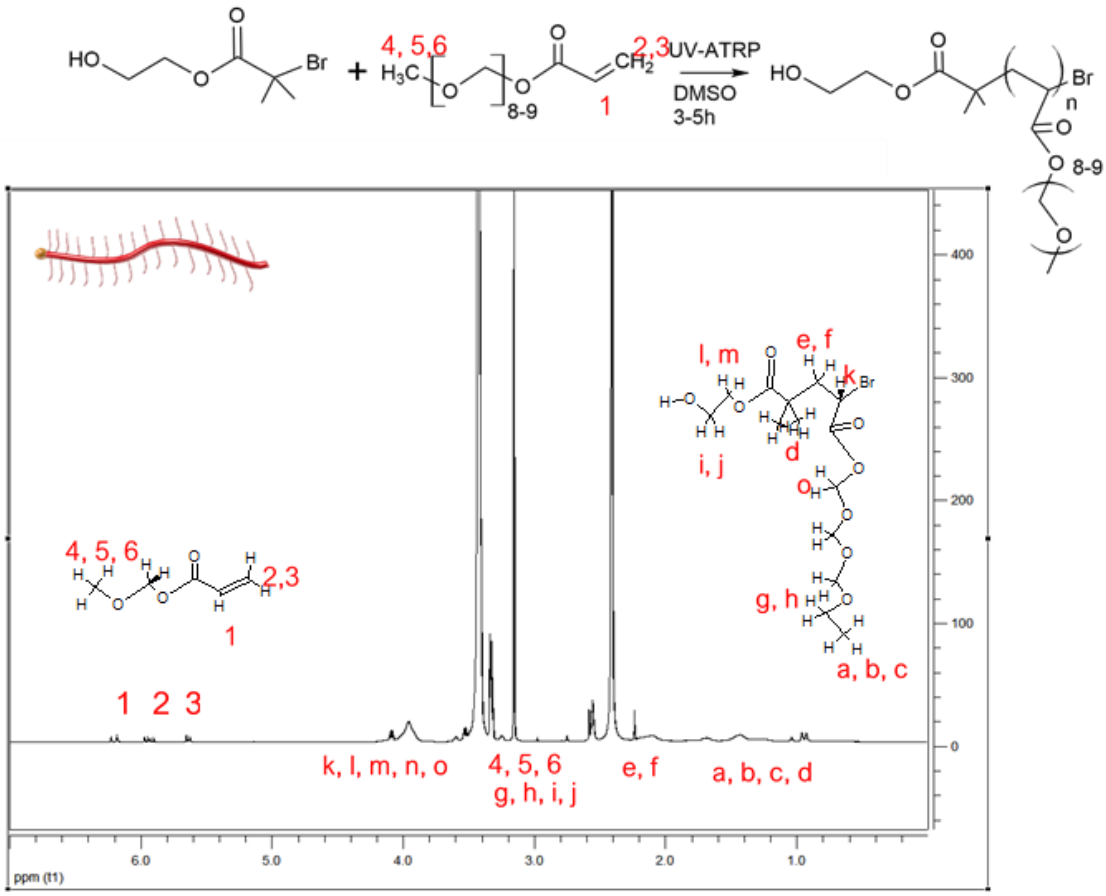

Figure 3.3: Representative ^{1}HNMR spectrum of synthesized brush with the corresponding reaction pathway.

Table 3.1: Characterization of synthesized brushes. (a) L= Me_6TREN. (b) Conversion at 3 h. Calculated from ^{1}HNMR. (c) Calculated from ^{1}HNMR.

PEG brush	$[Cu^{II}]$: [L][a]	[Br] : [PEG MEA]	Conversion	PDI	Mw (kDa)[c]
PEG_{40}	0.02:0.12	1:40	0.8	1.1	17.1
PEG_{20}	0.02:0.12	1:20	0.9	1.1	8.5
PEG_{15}	0.02:0.12	1:15	0.9	1.1	6.6
PEG_{10}	0.02:0.12	1:10	0.9	1.1	4.5

Kinetics investigation showed quantitative conversion of PEG MEA to PEG brushes (PEG_{40}, PEG_{20}, PEG_{15} and PEG_{10}) of approximately 9 0% after 3 - 5 h of the reaction with narrow distribution of molecular weights (PDI = 1.1) (**Table 3.1**). The conversion of PEG methyl ethyl acrylate to PEG brush was additionally evaluated at various time intervals (30 min, 1 h, 1 h 30 min, 2 h, 2 h 30 min, 3 h) to better understand the kinetics of the reaction. All brush polymers reached a conversion of 90 % or higher after 3 h of the reaction. PEG brushes with lower molecular weights and shorter brush chains (DP = 10, 15, 20) achieved a 90 % conversion at a faster rate compared to brushes with higher molecular weights and longer brush chains (DP = 40). For PEG brushes with 40 repeat units, 90 % of conversion was achieved approximately after 4 - 5 h of the reaction. For PEG brushes with 10, 15 and 20 repeat units, 90 % conversion was achieved after 3 h of the reaction. Results indicate that polymer brushes of PEG methyl ethyl acrylate with lower DP (≤20) were polymerized faster than polymers with higher DP.

Following the formation of well-defined class of brushes via photo induced ATRP, PEG brushes were crosslinked using PEGDA crosslinker (Mw = 250 Da) after approximately 3 h of

brush arm polymerization. To better understand the influence of cross linker and PEG brush length on star formation, a class of star polymers with varying cross linker (XL) to PEG brush (B) ratio ([XL]/[B]) was synthesized and the conversion of PEG brush to star was calculated using ^{1}H NMR and GPC analysis (**Table 3.2**). Results indicate that PEG brush with the shortest length of arms and 10 PEGA repeat units converted to core-cross linked stars with high conversion, however, star-star coupling was observed in these stars (**Figure B2, Appendix Chapter 3**). PEG brushes with longest length of arms and 40 PEGA repeat units showed increasing conversion of brush into star polymers with increasing amount of cross-linker used (**Table 3.2**, **Figures B3-B5, Appendix Chapter 3**). The highest conversion was achieved for PEG brushes with medium PEG lengths of 20 and 15 repeat units, with no star-star coupling observed, therefore PEG brush with 20 repeat units was used in the later synthesis steps.

Table 3.2: Overview of synthesized CCS with varying cross-linker ratios and precursor CCS-OHs. DMF GPCs and HNMR spectra of synthesized CCSs in supporting information. (a) L = Me_6TREN. (b) [Br] = bromide, [PEG MEA] = PEG methyl ethyl acrylate (Mw = 480 Da)(c) Approximated from DMF GPC and ^{1}HNMR.

CCS	[Cu^{II}] : [L][a]	[Br] : [PEG MEA][b]	CCS-OH	[XL]:PEG Brush	Conversion[c]
CCS1	0.02:0.12	1:10	PEG_{10}-OH	15:1	0.9
CCS2	0.02:0.12	1:15	PEG_{15}-OH	15:1	0.8
CCS3	0.02:0.12	1:20	PEG_{20}-OH	15:1	0.8
CCS4	0.02:0.12	1:40	PEG_{40}-OH	10:1	0.3
CCS5	0.02:0.12	1:40	PEG_{40}-OH	15:1	0.4
CCS6	0.02:0.12	1:40	PEG_{40}-OH	20:1	0.7
CCS7	0.02:0.12	1:40	PEG_{40}-OH	25:1	0.75
CCS8	0.02:0.12	1:40	PEG_{40}-OH	30:1	0.75

In the final step, ROP of CL was performed utilizing the end hydroxyl groups on the star polymer arms to achieve stars with hydrophobic outer layer. PCL was selected as an outer block of the synthesized star polymers due to its hydrophobicity and degradable nature. Additionally, hydrophobic shell of PCL was used to prevent burst release of hydrophilic drugs and enable slower, controlled release from the inner core. Synthesized star polymers were later incorporated into the hydrophobic PCL matrix, therefore hydrophobic PCL outer blocks of the star polymers were polymerized to allow the compatibility with surrounding PCL matrix and homogenous blending. Non-functional methyl ends of the brush, which compromise of PEG MEA, were chosen to assure that PCL chains would polymerize from hydroxyl groups at the end of star arms rather than inner brush groups. PEGDA was used as a cross-linker due to its hydrophilic nature, cross-linking capability of PEG based synthesized brush polymers, and lack of functional groups that could result in undesired growth of PCL chains from the core of a star polymer. Due to this, limitations in the star design were present. It was necessary to ensure that no functional group was present at the end of brushes to prevent undesired initiation of growth of PCL chains from end groups other than hydroxyl groups of the arms.

As we mentioned previously, photoinduced living radical polymerization of acrylates with low concentrations of copper and its enhancement upon irradiation with UV radiation was used to synthesize block copolymers with excellent conversion and low polydispersity indexes[22]. In the final step of our reaction pathway, the end functional groups on the star-brush arms are utilized for ring-opening polymerization of caprolactone.

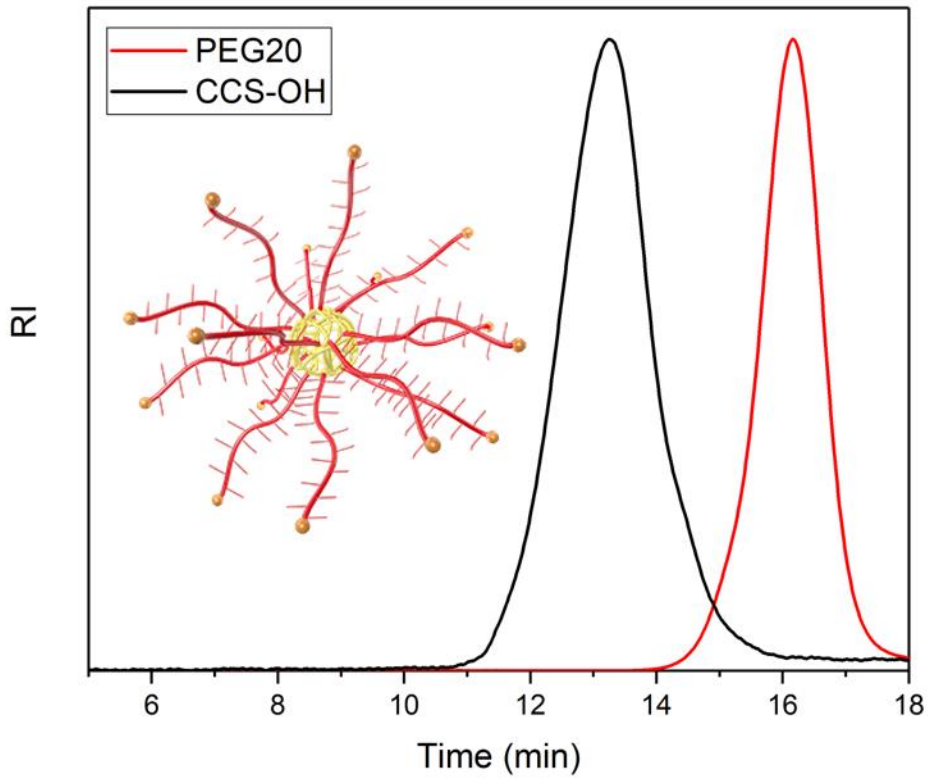

Figure 3.4: DMF GPC of synthesized CCS-OH and respective PEG brush before cross-linking with PEG diacrylate (Mw = 250 Da). CCS-OHs purified via dialysis in DI water for 7 days.

Following the formation of core-cross linked star brush polymers with hydroxyl end groups (CCS-OH), utilizing PEG20 brush and 1:15 ratio of the brush polymer to the cross linker, synthesized stars were dialyzed against water to remove DMSO and the remaining brush-arm. Upon successful removal of DMSO solvent and unconverted brush-arm, synthesized star-brush polymers were freeze dried. Synthesized CCS-OH were characterized via GPC and DLS to confirm a full removal of the unconverted arm. Results showed narrow molecular weight

distribution of synthesized star polymers (PDI = 1.3) (**Figure 3.4**). Molecular weight of synthesized brush and star polymers were approximated via DMF GPC using calibration curves. Additionally, the molecular weight of brushes was estimated utilizing ^{1}H NMR.

The size of synthesized CCS-OH was characterized by DLS (**Figure 3.5**) and hydrodynamic diameter (D_h) was found to be approximately 12.5 nm. This size corresponds to the core of synthesized stars with hydroxyl functional groups, which corresponds to the star polymer before the final ring opening polymerization step.

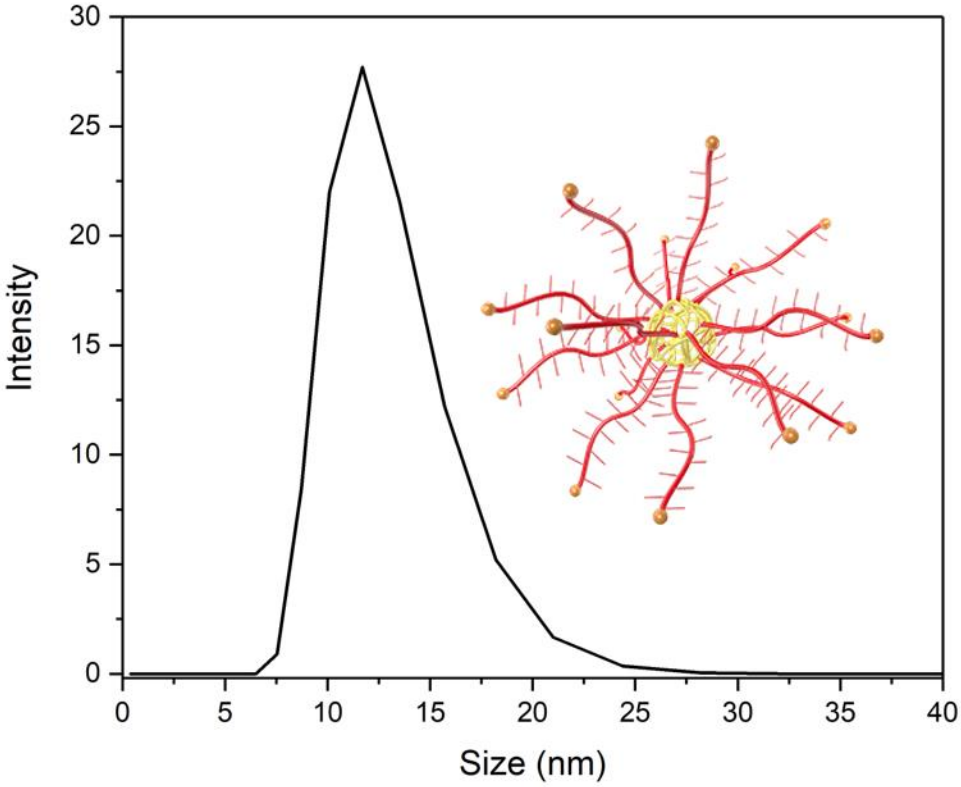

Figure 3.5: DLS characterization of synthesized CCS-OHs. Average size of hydrodynamic diameter 12.5 nm.

Following the synthesis and purification of CCS-OHs, ring opening polymerization of CL was performed. Ring opening polymerization of caprolactone was initiated from the hydroxyl end groups of CCS-OHs in the presence of organic catalyst methane sulfonic acid (MSA, CH_3SO_3H). The resulting polymers formed through the growth of PCL chains from hydroxyl groups to form CCS-PCL as shown in **Figure 3.6**. Synthesized polymers were characterized in terms of their molecular weights and PDI (**Figure B7, Table B2, Appendix Chapter 3**).

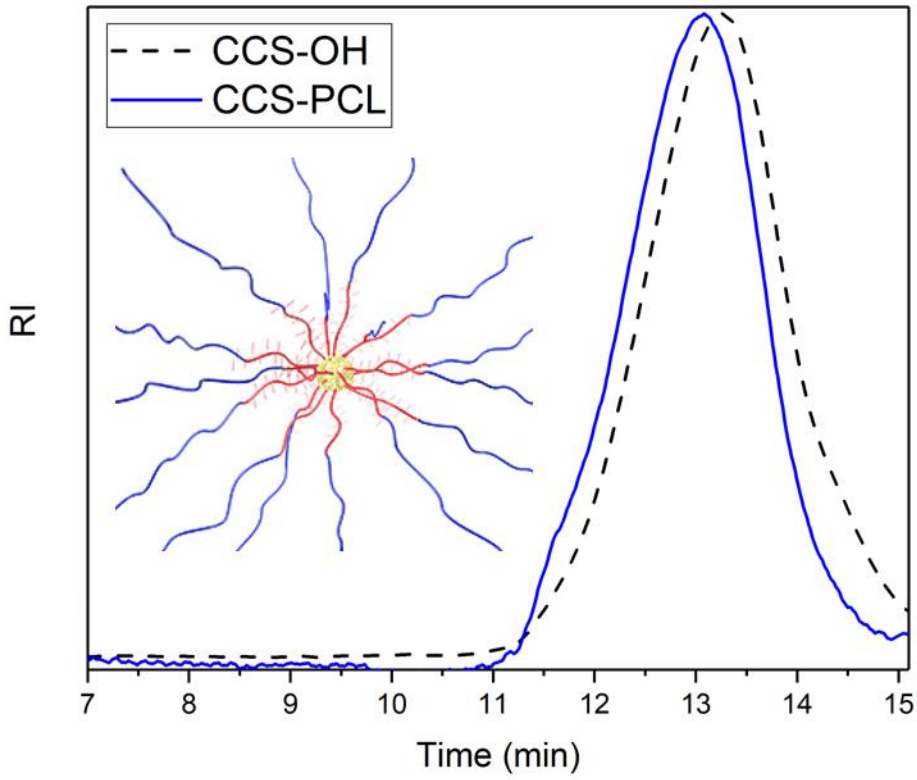

Figure 3.6: DMF GPC of representative CCS-PCL.

As mentioned previously, PCL was chosen as the resulting arm polymer due to its hydrophobic nature and compatibility with the PCL matrix for homogenous blending. The distribution of synthesized CCS-PCL polymers was narrow with PDI = 1.4 -1.6 and the conversion of CL to PCL was very high (> 90 %) after 3 h of the reaction, as shown in ^{1}H NMR spectrum (**Figure**

3.6, Figure 3.7). Very low traces (<10 %) of characteristic peaks of a caprolactone monomer could be observed after 3h of a reaction (**Figure 3.7**).

In this study, the aim was to synthesize a star polymer with hydrophobic PCL arms, inner hydrophilic brush and core-cross linked hydrophilic core. We hypothesized that these molecules could allow the homogenous blending with hydrophobic matrix such as PCL, and prolonged release of hydrophilic drugs through their interaction with a hydrophilic core. Such molecules would be particularly useful in a delivery of a hydrophilic therapeutic from a hydrophobic scaffold and prolonging its release.

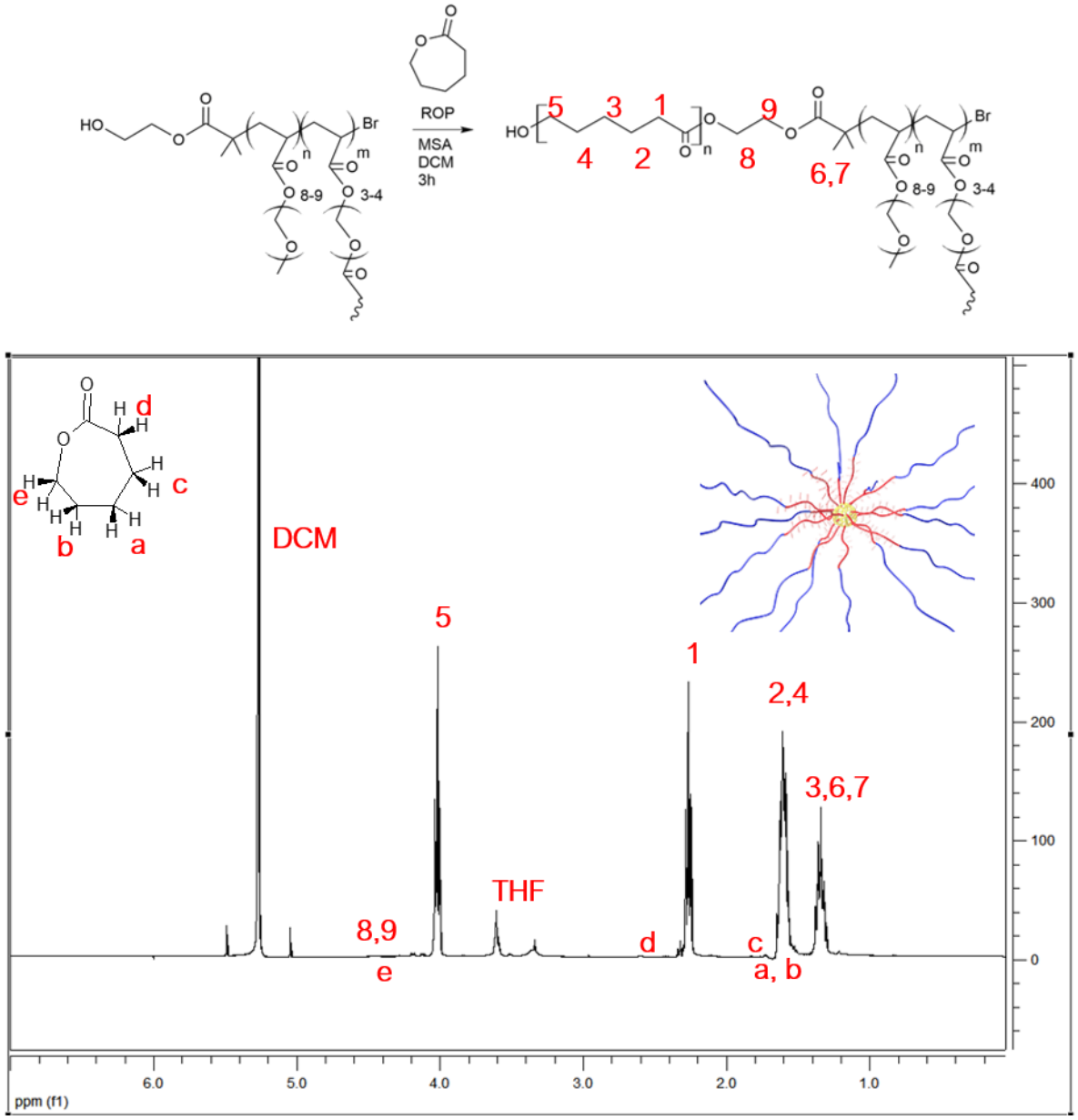

Figure 3.7: Representative ^{1}HNMR spectrum of CCS-PCL with the corresponding reaction pathway.

The reaction pathway designed in this study shows our ability to control synthesis conditions and the design of final star-brush polymers. By variation in PEG brush length, as well as PCL arm lengths, we show the feasibility to tailor star design to the desired application. Synthesized star-brush polymers exhibit hydrophobic PCL arms which allow its homogenous blending with PCL or PCL based matrices. The cross-linked core and its surrounding brush shell are

hydrophilic in nature, as compared to PCL, therefore allowing favourable interactions between the hydrophilic parts of the drug with the hydrophilic core and its brush. This study confirms the feasibility of synthesis of our desired polymeric architecture and its precise tailor of its molecular architecture, polydispersity, and polymer chains lengths.

Some of the advantages of the use of star polymers over other previously reported strategies for delivery of hydrophilic drugs include their flexible composition and ease of tailoring their design to the desired drug or function (e.g., changing the PEG brush length, core size, or core composition), tuneable size (through adjustment of the core and arm sizes), and controlled drug release (**Table 3.3**). Despite these advantages, little attention has been brought to the study of star polymers for hydrophilic drugs, with majority of reports focusing on delivery of hydrophobic molecules[12].

Table 3.3 presents most common strategies for encapsulation and delivery of hydrophilic drugs previously reported in the literature. Some of the techniques, such as reverse micelle or polymer matrix entrapment, have clear advantages such as the ease of preparation, however, issues with the stability of reverse micelles and their disassembly or homogenous dispersion in care of matrix entrapment are present. Star polymers are core-cross linked unimolecular structures; therefore, they are not at risk of disassembly, and through their adjustment of hydrophobicity or hydrophilicity, can be well incorporated into the polymer matrices.

Table 3.3: Encapsulation strategies for hydrophilic drugs previously reported in the literature[46].

Type	Function	Formulation	Advantages	Disadvantages
Polymer nanoparticles	Encapsulation and drug delivery of lipophilic and hydrophilic drugs	Dispersion of polymer prepared beforehand or the polymerization of monomer	-Possibility of tailoring the reaction through pH, drug concentration, monomer type	-Not efficient in loading of macromolecules -Drug can react with polymer in formation during polymerization
Polymer matrix entrapment	Drugs entrapped into polymer matrix and protected			-Dispersion issues due to differences in polymer matrix and drug hydrophilicity/hydrophobicity
Polyester based nanospheres	Encapsulation of drugs with lower risk of reaction between the drug and polymer	Use of preformed polymers; polyesters added to formulation to form nanospheres	-Less risk of reaction between the drug and monomer during polymerization	-Limitations in protein encapsulation due to polymer degradation in the nanoparticle core and production of acidic monomers -Use of organic solvent -Lack of drug dispersibility in polymer
Adsorption onto nanoparticles	Drugs entrapped in an alternative way to polymer nanoparticles	Adsorption on the drug through interaction on the surface of nanoparticle, depends on the nature of the surface	-Prevents the drug from possible degradation -Avoids the possibility of drug and monomer reaction	-Surface modifications affect drug loading
Aqueous core nanocapsules	Core-shell structure with drugs encapsulated in the core	Formation of aqueous droplets in organic phase followed by polymeric interface reinforcement	-High loading efficiency -Protection of the drug against degradation within the nanocapsule	-Complex encapsulation process
Nanocapsules formed from nano-emulsions	System of liquid droplets dispersed in immiscible liquid and	Aqueous droplets	-Narrow size distribution of droplets	-Energy required to form the nanocapsules

	stabilized with surfactants			
Reverse Micelle	Incorporation of drugs into the core	Self-aggregation of amphiphilic polymers	-Wide variety of types possible based on the starting block copolymer	-Mostly studied for hydrophobic drugs as a micelle -Burst release and dynamic nature -Limited stability
Star polymer	Central core surrounded by multiple arms; drugs loaded onto the core	Core first, arm first or couple onto methods	-Flexible composition -Tuneable size and loading -Controlled drug release -Well defined structure	-Complex synthesis and characterization

If we look more closely at the previous reports of synthesis of drug delivery molecules with hydrophilic interior and hydrophobic exterior for application in hydrophilic drug delivery, we can notice a broad range of systems studied such as dendrimers, liposomes, reverse micelles, nano gel, hydro gel, star polymers, particles (micro, nano) or others (bioconjugates, sponges, brushes) (**Table 3.4**). In order to compare synthesized star-brush polymers in this study to previous reports of similar delivery systems, we investigated previous efforts to develop drug delivery platforms for hydrophilic drugs.

The majority of previously synthesized systems utilize poly(amidoamine) (PAMAM) dendrimer as a core to graft from a hydrophobic polymer chain arm. Polymers such as PDLA, PLA and PCL were synthesized via ring-opening polymerizations of their respective monomers utilizing hydroxyl end groups of a PAMAM-OH dendrimer. This synthesis pathway has been intensively investigated with many studies successfully reporting their synthesis[41, 47-48]. The advantage of this technique is its relatively facile synthesis pathway; however, the

limitation lies in the choice of the core to graft from, as well as the lack of control over the core properties as compared to other techniques. Liposomes are encapsulation systems utilized for delivery of hydrophilic drugs. However, their clinical translation is limited by their low solubility, short half-life, oxidation and hydrolysis reactions, risk of leakage, or alternatively the fusion of encapsulated drugs [49-50].

The previously mentioned reverse micelle share similarities to star polymers, as they often contain polymer chains of both a hydrophilic and hydrophobic nature. Hence, they allow encapsulation and interaction based on hydrophilicity/hydrophobicity of their cores, arms and encapsulated molecules. Previous studies have been performed to synthesize reverse micelle with a hydrophobic exterior and a hydrophilic interior, for the delivery of various drugs or the encapsulation of hydrophilic dyes (**Table 3.4**). However, issues with stability of micelles and their disassembly limits their utility for applications in hydrophilic drug delivery as compared to star polymers. Previous studies report nanogel formation utilizing β-cyclodextrins as functional cores to polymerize from for encapsulation of drugs or dyes as presented in **Table 3.4**.

Similarly, studies were conducted to synthesise star polymers utilizing β-cyclodextrins as cores to grow hydrophobic polymers from such as PCL. Other studies report synthesis of star polymers from polysaccharide-based cores to grow hydrophobic arms, or conjugation of a drug via covalent bonding.

Table 3.4: Overview of previously synthesized systems which exhibit hydrophobic arms and hydrophilic cores for a comparison of synthesized CCS-PCL stars in this study. Abbreviations are defined in the list of abbreviations (pages XXVII-XXXIV).

System	Study	Synthesis	Components	Application	Ref
Dendrimer	-Release of drug from PAMAM-PCL dendrimers[51] -Degradation and drug release from star PCL-PAMAM dendrimers[41]	-ROP of CL on PAMAM-OH dendrimer	PAMAM-PCL	Dexamethasone release Prednisone acetate release	[41, 51-54]
	-Synthesis and evaluation of polyester-co-polyether dendrimers[55]	-Core synthesized from butane tetracarboxylic acid and aspartic acid, dendrons from PEO, dihydroxybenzoic acid or gallic acid and PEG monoetherate	PEO-DHBA-PEG	Rhodamine and β-carotene encapsulation	
	-Synthesis of PAMAM-PCL star dendrimer for hydrophilic drug delivery[48]	-Bulk polymerization of lactide with PAMAM dendrimer	PAMAM-PLA	Bovine serum release	
	-Synthesis of dendrimer/star shaped amphiphilic copolymers for curcumin delivery[56]	-Synthesis of polyaminoester blocks and PEG using pentaerythritol as the core initiator for ROP of CL; second ROP on OH groups and attachment of PEG blocks	sPCL-AE-b-(PCL)-b-mPEG	Curcumin release	
	-Synthesis of dendrimer with aliphatic polyester Boltorn H40 as the core, PCL and PEG as outer shell[57]	-Synthesis of H40-PCL-COOH followed by synthesis of H40-PCL-PEG-FA	H40-PCL-PEG-FA	Tumour targeting	
	-Synthesis of thermo	-Conjugation of PEG to PAMAM dendrimer	PAMAM-PEG-PDLLA	Encapsulation camptohecin	

	responsive PAMAM-PEG-PDLLA dendrimer nanoparticles[47]	and ring opening polymerization of DLLA			
Liposome	-Morphine encapsulation in lipid foam (lipid-based particles)[58]	-Use of DepoFoam technology (multivesicular liposomal platform)	-Multivesicular lipid-based particles; phospholipids, DOPC, DPPG	Delivery of morphine	58-60
	-Encapsulation of hydrophilic drugs into hydrophilic part of liposome[58]	-Morphology of vesicle adjusted by the hydrophilic/hydrophobic ration	-Liposomes with lipid bilayers	Encapsulation of irinotecan, vincristine, cytarabine	
Reverse micelle	-Core inversible micelle for hydrophilic drug delivery[61]	-PEG-CA composed of PEG and dendritic octamer of cholic acid (self-assembly into micelle)	PEG-CA	Amyloid fibril inhibiting, congo red encapsulation	61-66
	-Self-assembly of star triblock copolymers based on cyclodextrin core	-Synthesis of CD-(PMMA) utilizing 21Cl-β-CD, followed by polymerization to form CD-(PMMA-b-PDEA) and then final polymer	CD-(PMMA-b-PDEA-b-PPEGMA)	Dox release	
	-Synthesis of thermo responsive polymeric micelles with a hydrophilic poly(glycidol) core[65]	-RAFT polymerization of N-isopropylacrylamide using HGP-based macro RAFT agent	-HGP-PNIPAM	Drug delivery, controlled release	
	-Self-assembly into reverse micelles	-Synthesis of star shaped and linear poly(glycidyl methacrylate) by ATRP as precursors of PGOH; PG-OH MA backbones modified through esterification of hydroxyl groups with acyl chlorides	-Alkylated PG-OH MA	Encapsulation of vasopressin and dyes	

Nanogel	-Cyclodextrin based nanogel via cross linking or self-assembly -Core-shell nanogel[67]	-Incorporation of cross-linking agent of self-assembly of blocks	γCD nanogels HPβCD nanogels CHP nanogel CHESG nanogel	Drug loading	[67-70]
	-Functionalized nanogel[70]	-PEO-b-PMA cross linked to form nanogel; further conjugation to folic acid	PEG-b-PMA with PEG-terminal aldehyde functionality	Targeted therapy for ovarian cancer	
Particles (nano, micro)	-Core cross linked polyvinylpyrrolidone nanoparticles for hydrophilic drugs[71]	-Polyvinylpyrrolidone particles cross-linked with N,N-methylene bis-acrylamide (MBA)	MBA-PVP	Dextran encapsulation	[71-77]
	-Nanocapsules based on Y-shaped miktoarm star block PEO-PCL copolymers[77]	-Ring opening polymerization of CL initiated by PEO lysine macroinitiator; nano assembly on a w/o template	PEO-Lys-PCL	Hydrophilic drug delivery	
	-Self-assembly of hyperbranched polyphosphate nanocarriers[76]	-Polyphosphate nanocarriers formed through self-assembly of amphiphilic hyperbranched multi-arm copolymers (HPHEEP-star-PEEPs)	-HPHEEP-star-PPEPs	Chlorambucil loading	
	-Self assembled nanocages for hydrophilic molecules[78]	-Synthesis of star shaped $PG_{OH}MA$ and further modification to form $PG_{OH}MA$-CX	$PG_{OH}MA$-CX	Encapsulation of vasopressin, myoglobin, albumin	
Star polymer	-Core-shell hyperbranched poly(ester amide)-star-PCL[79]	-Ring opening polymerization of CL with hyperbranched PEA as a macroinitiator	PEA-star-PCL	Encapsulation of polar dyes	[79-86]
	-Star based polymer networks[80]	-Core first synthesis of gel network (MMA-b-DMAEMA)	DMAEMA-star-MMA	Hydrophilic and hydrophobic drug delivery	
	-Synthesis of glucose-based	-Glu(PBA-Br) synthesis followed by seATRP with OEGA	α-D-glucose-(PBA-b-POEGA-Br)	Possibility of use as biomaterials	

	star-like block copolymer[82]				
	-Multi-arm star like block copolymers based on β-CD[84]	- β-CD esterified to produce 21-Br-β-CD; followed by ATRP	β-CD (PAA-b-PS)	-	
	-Pyridoxine based eagle shaped asymmetric star polymers via seATRP	-Vitamin B6 macroinitiator reacted with bromide; pyridoxine-star shaped block copolymer with hydrophilic pyridoxine core and PDMAEMA-b-PNIPAM arms	-PN-(PDMAEMA-b-PNIPAM-Br)	Drug delivery pH sensitive	
	-Incorporation of PCL to cyclodextrin nanocarrier for gene delivery[74]	-Star like amphiphilic cyclodextrin-PCL-PDMAEMA copolymer with cyclodextrin core, PCL segments and PDMAEMA block synthesized using cyclodextrin as initiator to form β-CD-PCL-OH and then synthesize PCL-b-PDMAEMA arm	β-CD-g-(PCL-b-PDMAEMA)	Gene delivery	
Other (brush, microsponge, bioconjugates etc.)	-Development of Eudragit RS1000 based microsponges	-Oil/oil emulsion solvent diffusion for preparation of 5-FU Eudragit RS1000 MS	5-FU-MS	Loading of 5-Fluorouracil	[87-89]
	-Polysaccharide based conjugate[89]	-Covalent conjugation of a drug to a polysaccharide utilizing end functional group	HA-paclitaxel β-C-PEG copolymer-camptohecin Carboxymethyl dextran-captohecin	Paclitaxel, Camptohecin delivery	

Particles were intensively investigated for hydrophilic drug encapsulation ranging from microparticles, nanoparticles, to various types of nanocarriers or microspheres (**Table 3.4**). These drug delivery platforms were utilized for the delivery of various hydrophilic drugs; however, their size is significantly larger compared to unimolecular star polymers and they require complex encapsulation techniques.

Star architectures, which share the highest degree of similarity to the star polymers synthesized in this work, are formed using core shell hyperbranched poly(ester amide)-star-poly(caprolactone), which were investigated for encapsulation of polar dyes. No studies have been reported that utilize hydrophilic PEG derivatives as cores and inner brushes, with PCL arms for hydrophilic anti-thrombotic drugs.

In the next steps of this study, we investigated drug loading capacities of synthesized CCS-PCL for antithrombotic drugs such as dextran (20 kDa), and heparin (17-19 kDa). Both dextran and heparin are hydrophilic polysaccharides with good water solubility. The encapsulation of drug into polymeric architectures (such as star polymers) was studied to investigate its capacity to prolong drug release and control release profiles. Prolonged release of an anti-thrombotic drug using a star polymer could allow its local delivery from a hydrophobic scaffold at later stages of a device lifetime.

3.4.2. Drug loading and in-vitro drug release

To assess the drug encapsulation efficacy of synthesized CCS-PCL polymer, water-soluble anti-thrombotic drugs, dextran and heparin, were selected for drug loading and release studies. Dextran is an anti-thrombotic drug with molecular weight of 17-19 kDa and was used as a model hydrophilic drug for the study. Heparin is a clinically used anti-coagulant drug with

molecular weight similar to that of a chosen dextran. Both drugs have wide clinical application in various thrombotic conditions to decrease the risk of blood clotting and are usually administrated intravenously. Previous studies show that hydrophobic based polymeric implants may fail in later stages of the device lifetime due to the high risk of a device thrombosis often presented in biodegradable polymeric coronary artery stents or vascular grafts[90-92]. Heparin has been shown to improve the biocompatibility of materials with applications in coronary artery stents or vascular grafts, however most of these studies focused on incorporation of a heparin through a scaffold coating rather than its controlled release from the bulk of the device[92]. This study examines the concept of the synthesis of drug-delivery platforms for hydrophilic drugs and its later incorporation into the hydrophobic polymer matrix.

This study aims at investigating the loading capabilities of two clinically relevant hydrophilic drugs (dextran, heparin) into a synthesized delivery system and drug release at acidic and physiological conditions. These delivery platforms have been synthesized to be later incorporated into the hydrophobic PCL or PCL-like matrix. Synthesized CCS-PCL are designed to act as unimolecular systems for anti-thrombotic drug, with the protective outer PCL arms stabilizing the carrier in PCL matrix of the final device and PEG based brush-shell and core to allow the favourable interaction of the hydrophilic drug with it thus allowing its encapsulation in a device. For the purpose of this study, CCS-PCL polymers synthesized with most optimal synthesis conditions were used as models for the evaluation of their drug loading capabilities using dextran and heparin. **Table 3.5** presents drug loading contents and drug loading efficiencies of synthesised CCS-PCL for both heparin and dextran. Synthesized platforms show drug loading contents of approximately 5 % and 7 % for heparin and dextran, respectively. The drug loading efficiencies are approximately 50 % and 69 % for heparin and dextran, respectively. Although heparin and dextran are both polysaccharides with similar

water solubility, the variation in charge is attributed as the main factor in the variation of the drug loading capacity and efficiency between the two drugs. To better understand how star polymers synthesized in this study compare to other drug delivery systems, we compared the drug loading properties of our systems to that of carrier systems previously reported in literature (**Table 3.6**).

Table 3.5: Drug loading content and efficiencies for two antithrombotic drugs used (heparin and dextran).

Drug	Type of activity	MW (kDa)	DLC (%)	DLE (%)
Heparin	Anti-coagulant	17-19	5.0 ± 0.1	49.8 ± 1.0
Dextran	Anti-thrombotic	20	6.8 ± 1.1	69.5 ± 11

Following the study on drug loading, drug release profiles were obtained for both drugs at pH of 5 and 7.4 (**Figure 3.8**). pH = 5 corresponds to the intra-cellular conditions while pH = 7.4 represents physiological conditions. Loaded star polymers were suspended in corresponding PBS solutions and dialyzed against pure PBS (MWCO of dialysis tubing = 50 kDa). The molecular weight cut off was chosen to allow the transport of the drug from the interior to the exterior of the dialysis tubing (MW heparin = 17-19 kDa, MW dextran = 20 kDa), while ensuring that synthesized star polymers stay inside the dialysis tubing (Mw CCS-PCL = 174 kDa). The release of dextran was shown to be more rapid as compared to heparin which could be attributed to its higher hydrophilicity therefore higher affinity towards hydrophilic PBS. No significant difference was observed between release in the neutral PBS (pH = 7.4) and acidic PBS (pH = 5) which could be due to the slow degradation of PCL[12]. The timeframes for drug release studies in this work were up to 300 h which is significantly shorter than average time required for degradation of PCL. Our results indicate that within 24 h, majority of elution of

final drug amount has occurred, with slower release over the next hours for both heparin and dextran.

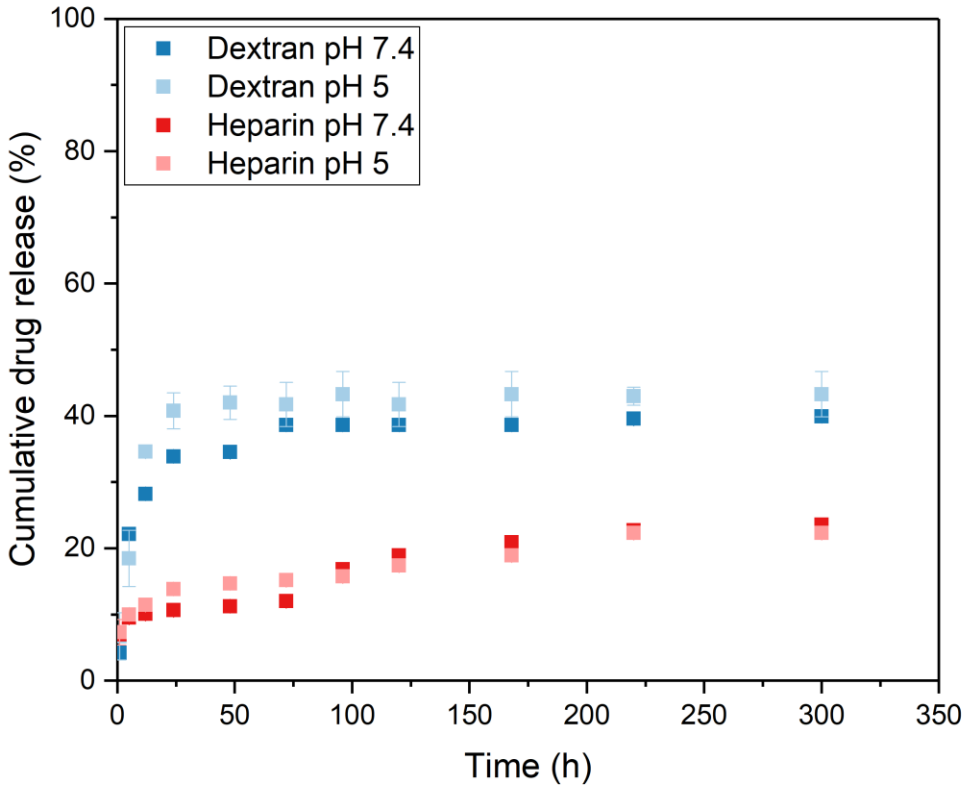

Figure 3.8: Drug release profiles for dextran and heparin at pH = 7.4 and pH = 5.

In order to compare our synthesized system and its drug loading capabilities to other carriers in the literature, we need to look closer at both drugs investigated and types of systems developed. **Table 3.6** shows the overview of previously synthesized and fabricated delivery system for the study of heparin, dextran or other clinically relevant anti-thrombotic, hydrophilic drugs. Several systems have been developed to entrap heparin inside the carrier system such as dendrimers, liposomes, reverse micelles, hydro and nanogels, particles (micro, nano etc.), star polymers or bioconjugates. It is important to note that not all these studies report drug loading efficiencies, or drug loading contents of synthesized systems, therefore our comparisons were limited to the studies which disclosed these values as shown in **Table 3.6**.

Studies which report the results of drug loading efficiencies and drug loading contents, in the context of synthesized systems, vary from entrapment efficiencies of 16 % to 98%. In our study, synthesized star brush polymers were characterized for both drug loading efficiencies and drug loading content of heparin and dextran. Our results are in between these reported in literature, with drug loading efficiency of approximately 70 % for dextran and 50 % for heparin; and drug loading contents of approximately 6.8 % for dextran and 5 % for heparin. Drug loading contents of previously developed carriers were reported only in few studies and ranged from 23 % to 35 % (**Table 3.6**). The broad range of drug loading efficiencies obtained in previous studies can be associated with differences in methods, experimental conditions, definitions of entrapment efficiencies and breadth of systems studied.

Our drug loading results are lower for heparin, as compared to dextran, which can be associated with a negative charge of heparin. A possible improvement of this work would be to investigate other inner blocks such as brushes composed of NIPAM to enhance the cationic charge in the brush and inner core, consequently loading a greater mass of heparin. Additionally, other cross linkers such as MBA (N,N-methylenebisacrylamide) could be used to enhance the interaction of a drug with a core, in the manner similar to the previous reports[93].

Regarding the loading content, values obtained in this study are below 10 %. These values are lower than the drug loading contents reported in the literature, ranging between 23 % and 35 % (**Table 3.6**). Lower drug loading contents of synthesized star polymers could be related to the small size of synthesized platforms and their unimolecular nature. Similarly, increasing drug efficiencies, modifications in star design and use of other cross-linkers, or brush structures, could be investigated as possible solutions of improving the synthesized system.

Our drug release profiles show 34 ± 0.1 % and 40 ± 0.2 % release of dextran at 24 h and 300 h at pH = 7.4 respectively, and 10.6 ± 0.3 % release and 23.6 ± 0.1% release of heparin at pH = 7.4 (**Figure 3.8**). Compared to other studies, dextran release reached approximately 43 % at pH = 5 and 70 % at pH = 7.4 at day 30 of release study[94]. At 24 h of the release, less than 10% of a drug was released, while within 300 h of the release experiment, approximately 30 % and 60 % of dextran was released at pH = 5 and pH = 7.4 respectively. Similarly, other studies report release of dextran from PVP nanoparticles ranging from 10 - 20 % within first 24 h, and 20 – 90 % within 300 h, depending on particle composition[71]. Others report encapsulation of dextran molecules into lysine-based hydrogels with pH dependent release profiles showing 70 - 90 % dextran release within 24 h in pH = 7.4, and less than 8% in pH =3.0 [95]

Dendrimer based PEG-PAMAM hydrogels have also been investigated for their drug loading and release of hydrophilic dextran, reporting a dextran release of approximately 30 - 70 % within 24 h, and 60 -100 % within 300 h based on dendrimer composition[96].

Other studies report heparin release from PLLA/PEG based microspheres of approximately 20-30 % within 25 h and 50 – 60 % within 300 h, depending on microsphere composition[97]. Studies which utilize reverse micelles for encapsulation of heparin report release studies in which more than 60 % of heparin has been released within 24 h[3].

Table 3.6: Overview of heparin, dextran or other antithrombotic drug encapsulation properties of different carrier systems and comparison to this study. Drug encapsulation rate (ER) (%) – maximum reported in the study, EF = encapsulation efficiency, NK = nattokinase, DLC = drug loading content, DL – drug loading properties (include either EF or DLC based on which one is reported in the study.

Carrier	System	Interaction	DL (%)	Drug	Ref
Dendrimer	PAMAM-HPA	Electrostatic	-	Hep	[98]
	Ac-G2 PAMAM		-	Dex	
Liposome	Light activated liposomes			Dex	[99]
	TSL (DPPC:DSPE-PEG) LTSL (DPPC:MSPC:DSPE:PEG) TTSL (DPPC:HSPC:Chol:DSPE:PEG)	Hydrophilic/hydrophobic	-	Dex	[100]
Reverse micelle	Micelle assembly of PLA-b-PEG	Hydrophilic/hydrophobic	-	Hep	[3]
	AADG-MBA		EF=70	Dex	[94]
Hydrogel	Assembly of sPEG-Hep with PEG-HBP	Polysaccharide-protein	-	Hep	[101]
	sPEG-PAMAM hydrogel	-	-	Dex	[96]
	PLP	Hydrophilic/hydrophobic; π-π stacking	LE=42 DLC=23	Dex	[95]
	4 arm sPEG		-	Dex	[102]
Nanogel	P(CD-OrnAA)-FA		-	Dex	[103]
Particles (nano, micro)	Eudragit P-4125F microparticles	Emulsion	ER=78	Hep	[104]
	PMMA-b-PMAETMA nanoparticles	Cationic; Hydrophilic/hydrophobic	EF=98	Hep	[105]
	Hep-PU MS	-	DL=32	Hep	[106]
	PDA-PS NPs	Specific interaction	EF=75	Nk	[107]
	PEDOT/Ms/MnO2	-	-	Hep	[108]
	Hep-CS-PLNs	Hydrophilic/hydrophobic; cationic	EF=88	Hep	[109]
	PLGA NPs	Physical, ionic	-	Hep	[110]
	Alginate beads	Entrapment	EF=85	Hep	[111]

	PEG-PLGA NPs	Emulsion	EF=65	Hep	[112]
	RS/PCL NPs RS/PLGA RS/RL/PLGA NPs	Electrostatic, ionic	EF=56	Hep	[113]
	PLLA-PEG-PLLA MS	Hydrophilic/hydrophobic	EF=16	Hep	[97]
	PVP NPs	Hydrophilic/hydrophobic	EF=70	Dex	[71]
	Co(VP-AA) NPs		EF=40	Dex	[114]
	Gelatin NPs	Hydrophilic/hydrophobic	EF=90	Dex	[115]
	PLGA MSs		-	Dex	[116]
	Chitosan TBA MSs		EF=96	Dex	[117]
	PNA-ECD MCs		-	Dex	[118]
Star polymer	6B-PDMAEMA-HEp	Conjugation	-	Hep	[4]
	8a-sPEG-PLLA	Hydrophilic/hydrophobic	DLC=35	Dex	[119]
Conjugate	PDMAEMA and P(MEO_2MA-co-OEOMA) conjugated with heparin	Conjugation	-	Hep	[120]
	PLA-Hep sPLA-Hep Tetronic-PCL-Heparin micelle	Conjugation	-	Hep	[121]

3.1.1 Cytotoxicity assay

Cytotoxicity of synthesized materials was examined by dissolving the CCS-OHs in sterile cell culture media at various concentrations and incubating with hUVECs as a model mammalian cell line. CCS-OHs were used due to their hydrophilicity as compared to CCS-PCL which is biocompatible. Cell viability was assessed after 24 h (**Figure 3.9**). Cells, in the absence of the polymer, were used as a positive control. Results show that synthesized CCS-OHs are not cytotoxic to hUVEC cells which confirms their use for biomedical application such as incorporation into a polymeric scaffold.

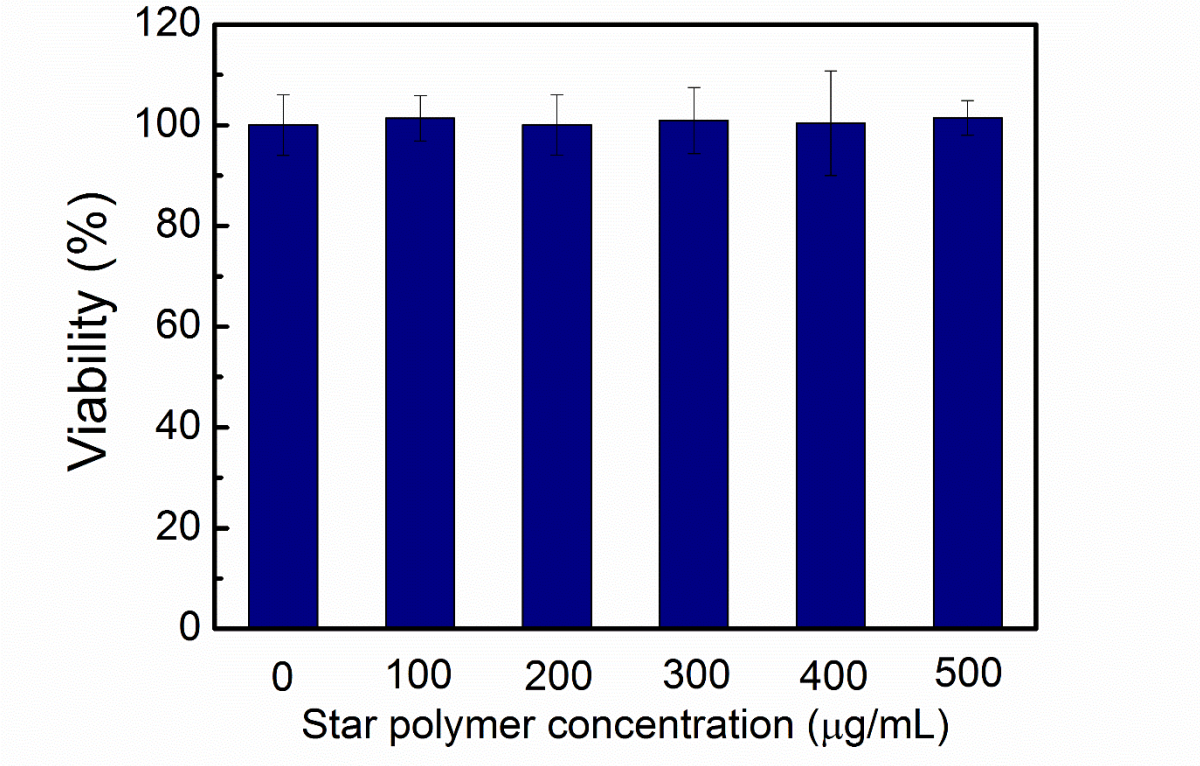

Figure 3.9: HUVECs viability in the presence of various concentrations of star polymers. Asterisks (*) represent statistical difference where **P<0.01 and *P<0.05, (n= 3).

3.4.3. Adhesion and proliferation of human umbilical vein endothelial cells

Adhesion and proliferation of human umbilical vein endothelial cells on surfaces with different rations of CCS in PCL was studied (**Figure 3.10, Figure 3.11**). Adhesion of cells at day 0 and proliferation at days 4 and 7 were quantified. No statistically significant difference in cell adhesion was observed at day 0 between surfaces with different CCS content in PCL. In terms of hUVECs proliferation, it was found that proliferation increases with star content in PCL at day 7 (**Figure 3.10, Figure 3.11**). Different ratios of star in PCL correspond to different hydrophilicity/hydrophobicity of surfaces as with increasing the CCS content in PCL matrix, hydrophilicity increases. Also, the composition of material changes as more of PEG based methacrylates are incorporated into the materials with higher star content. These differences could be the possible causes of change in cell adhesion and proliferation.

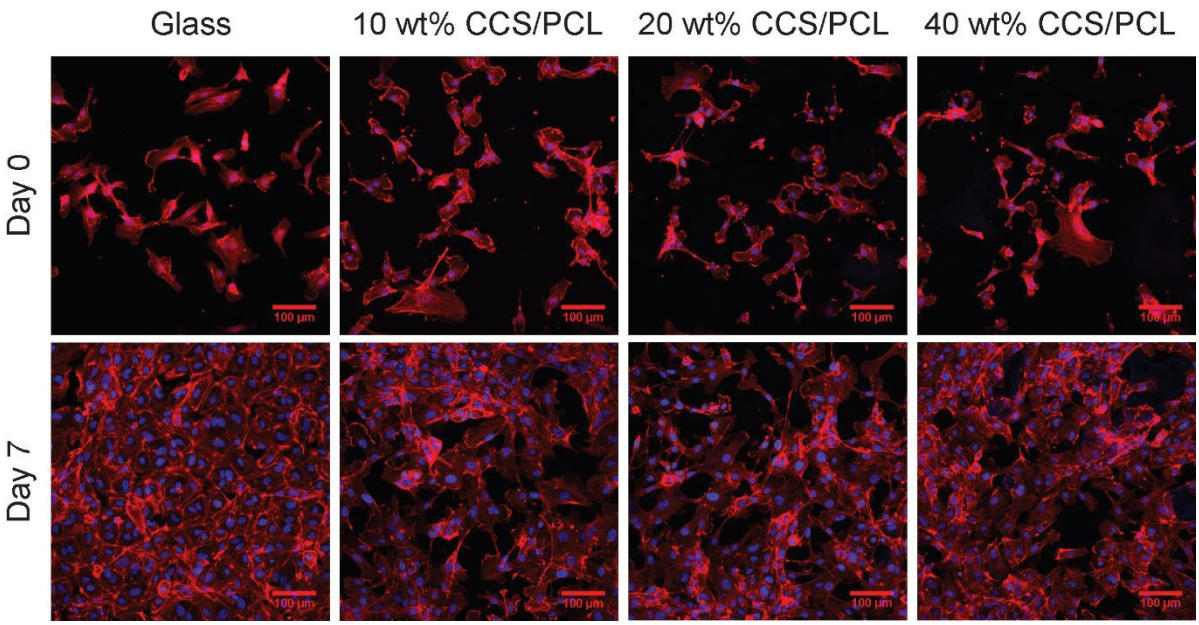

Figure 3.10: Representative images of HUVES adhesion and proliferation on various surfaces over 7 days. Scale bar represents 100 µm.

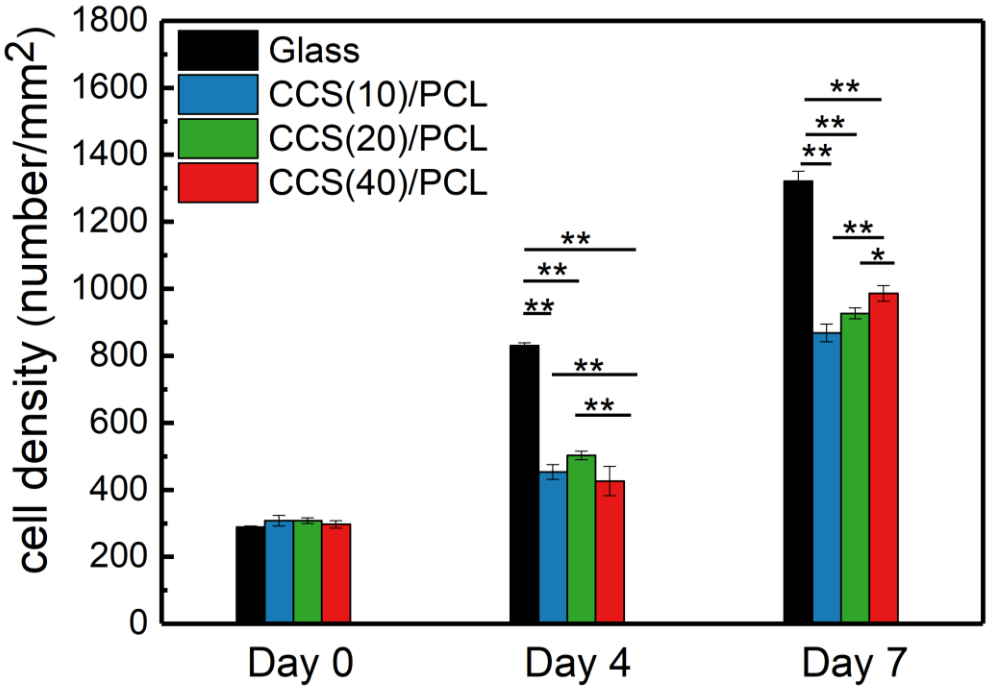

Figure 3.11: Quantification of HUVECs adhesion and proliferation over 7 days of culture. The cells were seeded at a density of 1.7×10^4 cells per cm^2. Asterisks (*) represent statistical difference where **P<0.01 and *P<0.05, (n= 3).

3.5. Conclusion

In conclusion, a class of core-cross linked star brush polymers have been successfully synthesized in this chapter. The synthesized systems were evaluated for drug loading and release of two clinically used antithrombotic drugs. Polymers exhibit hydrophobic PCL blocks in their outer parts, hydrophilic PEG MEA segments in their inner brushes, and hydrophilic PEGDA in their cores. The influence of the PEG brush length, cross-linker amount, as well as PCL arm length on the formation of star-brush polymers were investigated. Synthesized platforms were evaluated for encapsulation of anti-thrombotic drugs and showed drug loading contents 6.8 % and 5 % for dextran and heparin respectively. Drug loading efficiencies were found to be approximately 70 % and 50 % for dextran and heparin, respectively. Drug release profiles of both drugs were studied at pH = 5 and pH = 7.4 to better understand the influence of pH on drug release and degradation. Dextran was found to exhibit an increased drug release rate, with higher amount of drug released from the system, as compared to heparin. Biocompatibility of synthesized star-brush polymers was confirmed with the use of hUVECs. Adhesion and proliferation of hUVECs was studied on surfaces with varying content of synthesized CCSs in PCL matrix. Results show no difference in cell adhesion, and an increase in cell proliferation with increasing star content in PCL.

3.6. References

1. De Luca, L.; Musumeci, G.; Leonardi, S.; Gonzini, L.; Cavallini, C.; Calabro, P.; Mauro, C.; Cacciavillani, L.; Savonitto, S.; De Servi, S.; Investigators, E., Antithrombotic strategies in the catheterization laboratory for patients with acute coronary syndromes undergoing percutaneous coronary interventions: insights from the EmploYEd antithrombotic therapies in patients with acute coronary Syndromes HOspitalized in iTalian cardiac care units Registry. *J Cardiovasc Med (Hagerstown)* **2017,** *18* (8), 580-589.

2. Yang, X.; Ghobrial, J.; Pinto, D. S., Antithrombotic Therapy in Percutaneous Coronary Intervention. *Interv Cardiol Clin* **2016,** *5* (2), 239-247.

3. Nguyen, T. B. T.; Li, S.; Deratani, A., Reverse micelles prepared from amphiphilic polylactide-b-poly(ethylene glycol) block copolymers for controlled release of hydrophilic drugs. *Int J Pharm* **2015,** *495* (1), 154-161.

4. Nakayama, Y.; Yamaoka, S.; Nemoto, Y.; Alexey, B.; Uchida, K., Thermoresponsive heparin bioconjugate as novel aqueous antithrombogenic coating material. *Bioconjug Chem* **2011,** *22* (2), 193-9.

5. Go, D. H.; Joung, Y. K.; Park, S. Y.; Park, Y. D.; Park, K. D., Heparin-conjugated star-shaped PLA for improved biocompatibility. *J Biomed Mater Res A* **2008,** *86* (3), 842-8.

6. Gupta, A. S., Nanomedicine approaches in vascular disease: a review. *Nanomedicine* **2011,** *7* (6), 763-79.

7. Bardania, H.; Shojaosadati, S. A.; Kobarfard, F.; Dorkoosh, F., Optimization of RGD-modified Nano-liposomes Encapsulating Eptifibatide. *Iran J Biotechnol* **2016,** *14* (2), 33-40.

8. La, W. G.; Yang, H. S., Heparin-conjugated poly(lactic-co-glycolic acid) nanospheres enhance large-wound healing by delivering growth factors in platelet-rich plasma. *Artif Organs* **2015,** *39* (4), 388-94.

9. Bai, S.; Thomas, C.; Ahsan, F., Dendrimers as a Carrier for Pulmonary Delivery of Enoxaparin, a Low-Molecular Weight Heparin. *Journal of Pharmaceutical Sciences* **2007,** *96* (8), 2090-2106.

10. Feng, X.; Cheng, Y.; Yang, K.; Zhang, J.; Wu, Q.; Xu, T., Host−Guest Chemistry of Dendrimer−Drug Complexes. 5. Insights into the Design of Formulations for Noninvasive Delivery of Heparin Revealed by Isothermal Titration Calorimetry and NMR Studies. *The Journal of Physical Chemistry B* **2010,** *114* (34), 11017-11026.

11. Kasai, S.; Nagasawa, H.; Shimamura, M.; Uto, Y.; Hori, H., Design and synthesis of antiangiogenic/heparin-binding arginine dendrimer mimicking the surface of endostatin. *Bioorganic & Medicinal Chemistry Letters* **2002,** *12* (6), 951-954.

12. Gu, D.; Ladewig, K.; Klimak, M.; Haylock, D.; McLean, K. M.; O'Connor, A. J.; Qiao, G. G., Amphiphilic core cross-linked star polymers as water-soluble, biocompatible and biodegradable unimolecular carriers for hydrophobic drugs. *Polym. Chem.* **2015,** *6* (36), 6475-6487.

13. Kojima, C.; Kono, K.; Maruyama, K.; Takagishi, T., Synthesis of Polyamidoamine Dendrimers Having Poly(ethylene glycol) Grafts and Their Ability To Encapsulate Anticancer Drugs. *Bioconjugate Chemistry* **2000,** *11* (6), 910-917.

14. Wiltshire, J. T.; Qiao, G. G., Recent Advances in Star Polymer Design: Degradability and the Potential for Drug Delivery. *Australian Journal of Chemistry* **2007,** *60* (10), 699-705.

15. Khanna, K.; Varshney, S.; Kakkar, A., Miktoarm star polymers: advances in synthesis, self-assembly, and applications. *Polymer Chemistry* **2010,** *1* (8).

16. Blencowe, A.; Tan, J. F.; Goh, T. K.; Qiao, G. G., Core cross-linked star polymers via controlled radical polymerisation. *Polymer* **2009,** *50* (1), 5-32.

17. Burts, A. O.; Gao, A. X.; Johnson, J. A., Brush-first synthesis of core-photodegradable miktoarm star polymers via ROMP: towards photoresponsive self-assemblies. *Macromol Rapid Commun* **2014,** *35* (2), 168-173.

18. Liu, J.; Burts, A. O.; Li, Y.; Zhukhovitskiy, A. V.; Ottaviani, M. F.; Turro, N. J.; Johnson, J. A., "Brush-first" method for the parallel synthesis of photocleavable, nitroxide-labeled poly(ethylene glycol) star polymers. *J Am Chem Soc* **2012,** *134* (39), 16337-44.

19. Burts, A. O.; Liao, L.; Lu, Y. Y.; Tirrell, D. A.; Johnson, J. A., Brush-first and click: efficient synthesis of nanoparticles that degrade and release doxorubicin in response to light. *Photochem Photobiol* **2014,** *90* (2), 380-5.

20. Matyjaszewski, K., Atom Transfer Radical Polymerization (ATRP): Current Status and Future Perspectives. *Macromolecules* **2012,** *45* (10), 4015-4039.

21. Ribelli, T. G.; Lorandi, F.; Fantin, M.; Matyjaszewski, K., Atom Transfer Radical Polymerization: Billion Times More Active Catalysts and New Initiation Systems. *Macromol Rapid Commun* **2019,** *40* (1), e1800616.

22. Anastasaki, A.; Nikolaou, V.; Zhang, Q.; Burns, J.; Samanta, S. R.; Waldron, C.; Haddleton, A. J.; McHale, R.; Fox, D.; Percec, V.; Wilson, P.; Haddleton, D. M., Copper(II)/tertiary amine synergy in photoinduced living radical polymerization: accelerated synthesis of omega-functional and alpha,omega-heterofunctional poly(acrylates). *J Am Chem Soc* **2014,** *136* (3), 1141-9.

23. Boyer, C.; Derveaux, A.; Zetterlund, P. B.; Whittaker, M. R., Synthesis of multi-block copolymer stars using a simple iterative Cu(0)-mediated radical polymerization technique. *Polym. Chem.* **2012,** *3* (1), 117-123.

24. Tanabe, M.; Vandermeulen, G. W.; Chan, W. Y.; Cyr, P. W.; Vanderark, L.; Rider, D. A.; Manners, I., Photocontrolled living polymerizations. *Nat Mater* **2006,** *5* (6), 467-70.

25. Yamago, S.; Nakamura, Y., Recent progress in the use of photoirradiation in living radical polymerization. *Polymer* **2013,** *54* (3), 981-994.

26. Rzayev, J.; Penelle, J., HP-RAFT: a free-radical polymerization technique for obtaining living polymers of ultrahigh molecular weights. *Angew Chem Int Ed Engl* **2004,** *43* (13), 1691-4.

27. Magenau, A. J. D.; Strandwitz, N. C.; Gennaro, A.; Matyjaszewski, K., Electrochemically Mediated Atom Transfer Radical Polymerization. *Science* **2011,** *332* (6025), 81.

28. Pan, X.; Malhotra, N.; Simakova, A.; Wang, Z.; Konkolewicz, D.; Matyjaszewski, K., Photoinduced Atom Transfer Radical Polymerization with ppm-Level Cu Catalyst by Visible Light in Aqueous Media. *J Am Chem Soc* **2015,** *137* (49), 15430-3.

29. Fors, B. P.; Hawker, C. J., Inside Back Cover: Control of a Living Radical Polymerization of Methacrylates by Light (Angew. Chem. Int. Ed. 35/2012). *Angewandte Chemie International Edition* **2012,** *51* (35), 8901-8901.

30. Tasdelen, M. A.; Uygun, M.; Yagci, Y., Photoinduced controlled radical polymerization. *Macromol Rapid Commun* **2011,** *32* (1), 58-62.

31. Tasdelen, M. A.; Uygun, M.; Yagci, Y., Photoinduced Controlled Radical Polymerization in Methanol. *Macromolecular Chemistry and Physics* **2010,** *211* (21), 2271-2275.

32. Taskin, O. S.; Yilmaz, G.; Tasdelen, M. A.; Yagci, Y., Photoinduced reverse atom transfer radical polymerization of methyl methacrylate using camphorquinone/benzhydrol system. *Polymer International* **2014,** *63* (5), 902-907.

33. Tasdelen, M. A.; Ciftci, M.; Yagci, Y., Visible Light-Induced Atom Transfer Radical Polymerization. *Macromolecular Chemistry and Physics* **2012,** *213* (13), 1391-1396.

34. Konkolewicz, D.; Schröder, K.; Buback, J.; Bernhard, S.; Matyjaszewski, K., Visible Light and Sunlight Photoinduced ATRP with ppm of Cu Catalyst. *ACS Macro Letters* **2012,** *1* (10), 1219-1223.

35. Tsarevsky, N. V.; Matyjaszewski, K., "Green" Atom Transfer Radical Polymerization: From Process Design to Preparation of Well-Defined Environmentally Friendly Polymeric Materials. *Chemical Reviews* **2007,** *107* (6), 2270-2299.

36. Ciampolini, M.; Nardi, N., Five-Coordinated High-Spin Complexes of Bivalent Cobalt, Nickel, andCopper with Tris(2-dimethylaminoethyl)amine. *Inorganic Chemistry* **1966,** *5* (1), 41-44.

37. Tan, S.; Cui, J.; Fu, Q.; Nam, E.; Ladewig, K.; Ren, J. M.; Wong, E. H.; Caruso, F.; Blencowe, A.; Qiao, G. G., Photocontrolled Cargo Release from Dual Cross-Linked Polymer Particles. *ACS Appl Mater Interfaces* **2016,** *8* (9), 6219-28.

38. Klein M., D. R., Linhardt R., Langer R., A colorimetric assay for chemical heparin in plasma. *Analytical Biochemistry* **1982,** *124*.

39. Salamat-Miller, N.; Fang, J.; Seidel, C. W.; Smalter, A. M.; Assenov, Y.; Albrecht, M.; Middaugh, C. R., A network-based analysis of polyanion-binding proteins utilizing yeast protein arrays. *Mol Cell Proteomics* **2006,** *5* (12), 2263-78.

40. Zaman, P.; Wang, J.; Blau, A.; Wang, W.; Li, T.; Kohane, D. S.; Loscalzo, J.; Zhang, Y. Y., Incorporation of heparin-binding proteins into preformed dextran sulfate-chitosan nanoparticles. *Int J Nanomedicine* **2016,** *11*, 6149-6159.

41. Miao, Z. M.; Cheng, S. X.; Zhang, X. Z.; Wang, Q. R.; Zhuo, R. X., Degradation and drug release property of star poly(epsilon-caprolactone)s with dendritic cores. *J Biomed Mater Res B Appl Biomater* **2007,** *81* (1), 40-9.

42. Ranji-Burachaloo, H.; Karimi, F.; Xie, K.; Fu, Q.; Gurr, P. A.; Dunstan, D. E.; Qiao, G. G., MOF-Mediated Destruction of Cancer Using the Cell's Own Hydrogen Peroxide. *ACS Appl Mater Interfaces* **2017,** *9* (39), 33599-33608.

43. Shirbin, S. J.; Karimi, F.; Chan, N. J.; Heath, D. E.; Qiao, G. G., Macroporous Hydrogels Composed Entirely of Synthetic Polypeptides: Biocompatible and Enzyme Biodegradable 3D Cellular Scaffolds. *Biomacromolecules* **2016,** *17* (9), 2981-91.

44. Karimi, F.; McKenzie, T. G.; O'Connor, A. J.; Qiao, G. G.; Heath, D. E., Nano-scale clustering of integrin-binding ligands regulates endothelial cell adhesion, migration, and endothelialization rate: novel materials for small diameter vascular graft applications. *Journal of Materials Chemistry B* **2017,** *5* (30), 5942-5953.

45. Karimi, F.; Thombare, V. J.; Hutton, C. A.; O'Connor, A. J.; Qiao, G. G.; Heath, D. E., Beyond RGD; nanoclusters of syndecan- and integrin-binding ligands synergistically enhance cell/material interactions. *Biomaterials* **2018,** *187*, 81-92.

46. Vrignaud, S.; Benoit, J. P.; Saulnier, P., Strategies for the nanoencapsulation of hydrophilic molecules in polymer-based nanoparticles. *Biomaterials* **2011,** *32* (33), 8593-604.

47. Kailasan, A.; Yuan, Q.; Yang, H., Synthesis and characterization of thermoresponsive polyamidoamine–polyethylene glycol–poly(d,l-lactide) core–shell nanoparticles. *Acta Biomaterialia* **2010,** *6* (3), 1131-1139.

48. Cai, Q.; Zhao, Y.; Bei, J.; Xi, F.; Wang, S., Synthesis and Properties of Star-Shaped Polylactide Attached to Poly(Amidoamine) Dendrimer. *Biomacromolecules* **2003,** *4* (3), 828-834.

49. Sercombe, L.; Veerati, T.; Moheimani, F.; Wu, S. Y.; Sood, A. K.; Hua, S., Advances and Challenges of Liposome Assisted Drug Delivery. *Front Pharmacol* **2015,** *6*, 286-286.

50. Akbarzadeh, A.; Rezaei-Sadabady, R.; Davaran, S.; Joo, S. W.; Zarghami, N.; Hanifehpour, Y.; Samiei, M.; Kouhi, M.; Nejati-Koshki, K., Liposome: classification, preparation, and applications. *Nanoscale Res Lett* **2013,** *8* (1), 102-102.

51. Avila-Salas, F.; Pereira, A.; Rojas, M. A.; Saavedra-Torres, M.; Montecinos, R.; Bonardd, S.; Quezada, C.; Saldías, S.; Díaz Díaz, D.; Leiva, A.; Radic, D.; Saldías, C., An experimental and theoretical comparative study of the entrapment and release of dexamethasone from micellar and vesicular aggregates of PAMAM-PCL dendrimers. *European Polymer Journal* **2017,** *93*, 507-520.

52. Lukowiak, M. C.; Thota, B. N.; Haag, R., Dendritic core-shell systems as soft drug delivery nanocarriers. *Biotechnol Adv* **2015,** *33* (6 Pt 3), 1327-41.

53. Pedziwiatr-Werbicka, E.; Milowska, K.; Dzmitruk, V.; Ionov, M.; Shcharbin, D.; Bryszewska, M., Dendrimers and hyperbranched structures for biomedical applications. *European Polymer Journal* **2019,** *119*, 61-73.

54. Zhou, D.; Zeng, J.; Fu, Q.; Gao, D.; Zhang, K.; Ren, X.; Zhou, K.; Xia, Z.; Wang, L., Preparation and evaluation of a reversed-phase/hydrophilic interaction/ion-exchange mixed-mode chromatographic stationary phase functionalized with dopamine-based dendrimers. *J Chromatogr A* **2018,** *1571*, 165-175.

55. Dhanikula, R. S.; Hildgen, P., Synthesis and Evaluation of Novel Dendrimers with a Hydrophilic Interior as Nanocarriers for Drug Delivery. *Bioconjugate Chemistry* **2006,** *17* (1), 29-41.

56. Khoee, S.; Kavand, A.; Hashemi Nasr, F., Preparation of new dendrimer-like star-shaped amphiphilic poly(ethylene glycol)–poly(ϵ-caprolactone) copolymers for biocompatible and high-efficiency curcumin delivery. *Polymer International* **2015,** *64* (9), 1191-1201.

57. Chen, S.; Zhang, X.-Z.; Cheng, S.-X.; Zhuo, R.-X.; Gu, Z.-W., Functionalized Amphiphilic Hyperbranched Polymers for Targeted Drug Delivery. *Biomacromolecules* **2008,** *9* (10), 2578-2585.

58. Bulbake, U.; Doppalapudi, S.; Kommineni, N.; Khan, W., Liposomal Formulations in Clinical Use: An Updated Review. *Pharmaceutics* **2017,** *9* (2).

59. Alavi, M.; Karimi, N.; Safaei, M., Application of Various Types of Liposomes in Drug Delivery Systems. *Adv Pharm Bull* **2017,** *7* (1), 3-9.

60. Li, M.; Du, C.; Guo, N.; Teng, Y.; Meng, X.; Sun, H.; Li, S.; Yu, P.; Galons, H., Composition design and medical application of liposomes. *Eur J Med Chem* **2019,** *164*, 640-653.

61. Huang, W.; Shi, C.; Shao, Y.; Lam, K. S.; Luo, J., The core-inversible micelles for hydrophilic drug delivery. *Chem Commun (Camb)* **2013,** *49* (59), 6674-6.

62. Fan, X.; Li, Z.; Loh, X. J., Recent development of unimolecular micelles as functional materials and applications. *Polymer Chemistry* **2016,** *7* (38), 5898-5919.

63. Jones, M. C.; Gao, H.; Leroux, J. C., Reverse polymeric micelles for pharmaceutical applications. *J Control Release* **2008,** *132* (3), 208-15.

64. Lundy, B. B.; Convertine, A.; Miteva, M.; Stayton, P. S., Neutral polymeric micelles for RNA delivery. *Bioconjug Chem* **2013,** *24* (3), 398-407.

65. Luo, S.; Hu, X.; Zhang, Y.; Ling, C.; Liu, X.; Chen, S., Synthesis of thermoresponsive unimolecular polymeric micelles with a hydrophilic hyperbranched poly(glycidol) core. *Polymer Journal* **2010,** *43* (1), 41-50.

66. Trivedi, R.; Kompella, U. B., Nanomicellar formulations for sustained drug delivery: strategies and underlying principles. *Nanomedicine (Lond)* **2010,** *5* (3), 485-505.

67. Moya-Ortega, M. D.; Alvarez-Lorenzo, C.; Concheiro, A.; Loftsson, T., Cyclodextrin-based nanogels for pharmaceutical and biomedical applications. *Int J Pharm* **2012,** *428* (1-2), 152-63.

68. Kendre, P. N.; Satav, T. S., Current trends and concepts in the design and development of nanogel carrier systems. *Polymer Bulletin* **2018,** *76* (3), 1595-1617.

69. Lee, V. Y.; Havenstrite, K.; Tjio, M.; McNeil, M.; Blau, H. M.; Miller, R. D.; Sly, J., Nanogel star polymer architectures: a nanoparticle platform for modular programmable macromolecular self-assembly, intercellular transport, and dual-mode cargo delivery. *Adv Mater* **2011,** *23* (39), 4509-15.

70. Nukolova, N. V.; Oberoi, H. S.; Cohen, S. M.; Kabanov, A. V.; Bronich, T. K., Folate-decorated nanogels for targeted therapy of ovarian cancer. *Biomaterials* **2011,** *32* (23), 5417-5426.

71. Bharali, D. J.; Sahoo, S. K.; Mozumdar, S.; Maitra, A., Cross-linked polyvinylpyrrolidone nanoparticles: a potential carrier for hydrophilic drugs. *Journal of Colloid and Interface Science* **2003,** *258* (2), 415-423.

72. Chemelli, A.; Maurer, M.; Geier, R.; Glatter, O., Optimized loading and sustained release of hydrophilic proteins from internally nanostructured particles. *Langmuir* **2012,** *28* (49), 16788-97.

73. Chen, G.; Wang, Y.; Xie, R.; Gong, S., A review on core-shell structured unimolecular nanoparticles for biomedical applications. *Adv Drug Deliv Rev* **2018,** *130*, 58-72.

74. Fan, X.; Cheng, H.; Wu, Y.; Loh, X. J.; Wu, Y.-L.; Li, Z., Incorporation of Polycaprolactone to Cyclodextrin-Based Nanocarrier for Potent Gene Delivery. *Macromolecular Materials and Engineering* **2018,** *303* (9).

75. Lee, L.-C.; Xiao, C.; Huang, W.; Zhao, Y., Palladium–gold bimetallic nanoparticle catalysts prepared by “controlled release” from metal-loaded interfacially cross-linked reverse micelles. *New Journal of Chemistry* **2015,** *39* (4), 2459-2466.

76. Liu, J.; Huang, W.; Pang, Y.; Zhu, X.; Zhou, Y.; Yan, D., The in vitro biocompatibility of self-assembled hyperbranched copolyphosphate nanocarriers. *Biomaterials* **2010,** *31* (21), 5643-51.

77. Maglio, G.; Nicodemi, F.; Conte, C.; Palumbo, R.; Tirino, P.; Panza, E.; Ianaro, A.; Ungaro, F.; Quaglia, F., Nanocapsules based on linear and Y-shaped 3-miktoarm star-block PEO-PCL copolymers as sustained delivery system for hydrophilic molecules. *Biomacromolecules* **2011,** *12* (12), 4221-9.

78. Jones, M.-C.; Tewari, P.; Blei, C.; Hales, K.; Pochan, D. J.; Leroux, J.-C., Self-Assembled Nanocages for Hydrophilic Guest Molecules. *Journal of the American Chemical Society* **2006,** *128* (45), 14599-14605.

79. Lin, Y.; Liu, X.; Dong, Z.; Li, B.; Chen, X.; Li, Y.-S., Amphiphilic Core−Shell Nanocarriers Based On Hyperbranched Poly(ester amide)-star-PCL: Synthesis, Characterization, and Potential as Efficient Phase Transfer Agent. *Biomacromolecules* **2008,** *9* (10), 2629-2636.

80. Ghasdian, N.; Church, E.; Cottam, A. P.; Hornsby, K.; Leung, M.-Y.; Georgiou, T. K., Novel "core-first" star-based quasi-model amphiphilic polymer networks. *RSC Advances* **2013,** *3* (41), 19070-19080.

81. Wenn, B.; Martens, A. C.; Chuang, Y. M.; Gruber, J.; Junkers, T., Efficient multiblock star polymer synthesis from photo-induced copper-mediated polymerization with up to 21 arms. *Polymer Chemistry* **2016,** *7* (15), 2720-2727.

82. Chmielarz, P., Synthesis of α- d -glucose-based star polymers through simplified electrochemically mediated ATRP. *Polymer* **2016,** *102*, 192-198.

83. Liechty, W. B.; Kryscio, D. R.; Slaughter, B. V.; Peppas, N. A., Polymers for drug delivery systems. *Annu Rev Chem Biomol Eng* **2010,** *1*, 149-73.

84. Pang, X.; Zhao, L.; Akinc, M.; Kim, J. K.; Lin, Z., Novel Amphiphilic Multi-Arm, Star-Like Block Copolymers as Unimolecular Micelles. *Macromolecules* **2011,** *44* (10), 3746-3752.

85. Chmielarz, P., Synthesis of pyridoxine-based eagle-shaped asymmetric star polymers through seATRP. *Polymers for Advanced Technologies* **2017,** *28* (12), 1787-1793.

86. Ren, J. M.; McKenzie, T. G.; Fu, Q.; Wong, E. H. H.; Xu, J.; An, Z.; Shanmugam, S.; Davis, T. P.; Boyer, C.; Qiao, G. G., Star Polymers. *Chemical Reviews* **2016,** *116* (12), 6743-6836.

87. Han, Y.; Gao, C., Miktoarms hyperbranched polymer brushes: One-step fast synthesis by parallel click chemistry and hierarchical self-assembly. *Science China Chemistry* **2010,** *53* (12), 2461-2471.

88. Othman, M. H.; Zayed, G. M.; El Sokkary, G. H.; F Ali, U.; Abdellatif, A. A. H., Preparation and Evaluation of 5-Fluorouracil Loaded Microsponges for Treatment of Colon Cancer. *Journal of Cancer Science & Therapy* **2017,** *09* (01).

89. Basu, A.; Kunduru, K. R.; Abtew, E.; Domb, A. J., Polysaccharide-Based Conjugates for Biomedical Applications. *Bioconjug Chem* **2015,** *26* (8), 1396-412.

90. Sotomi, Y.; Onuma, Y.; Collet, C.; Tenekecioglu, E.; Virmani, R.; Kleiman, N. S.; Serruys, P. W., Bioresorbable Scaffold: The Emerging Reality and Future Directions. *Circ Res* **2017,** *120* (8), 1341-1352.

91. Siddiqi, O. K.; Faxon, D. P., Very late stent thrombosis: current concepts. *Curr Opin Cardiol* **2012,** *27* (6), 634-41.

92. Biran, R.; Pond, D., Heparin coatings for improving blood compatibility of medical devices. *Adv Drug Deliv Rev* **2017,** *112*, 12-23.

93. McKenzie, T. G.; Wong, E. H. H.; Fu, Q.; Lam, S. J.; Dunstan, D. E.; Qiao, G. G., Highly Efficient and Versatile Formation of Biocompatible Star Polymers in Pure Water and Their Stimuli-Responsive Self-Assembly. *Macromolecules* **2014,** *47* (22), 7869-7877.

94. Nimesh, S.; Manchanda, R.; Kumar, R.; Saxena, A.; Chaudhary, P.; Yadav, V.; Mozumdar, S.; Chandra, R., Preparation, characterization and in vitro drug release studies of novel polymeric nanoparticles. *Int J Pharm* **2006,** *323* (1-2), 146-52.

95. Watkins, K. A.; Chen, R., pH-responsive, lysine-based hydrogels for the oral delivery of a wide size range of molecules. *Int J Pharm* **2015,** *478* (2), 496-503.

96. Buwalda, S. J.; Bethry, A.; Hunger, S.; Kandoussi, S.; Coudane, J.; Nottelet, B., Ultrafast in situ forming poly(ethylene glycol)-poly(amido amine) hydrogels with tunable drug release properties via controllable degradation rates. *Eur J Pharm Biopharm* **2019,** *139*, 232-239.

97. Luo, X.; Qiu, D.; He, B.; Wang, L.; Luo, J., Biodegradable Heparin-Loaded Microspheres: Carrier Molecular Composition and Microsphere Structure. *Macromolecular Bioscience* **2006,** *6* (5), 373-381.

98. Tong, N.-A. N.; Nguyen, T. H.; Nguyen, D. H.; Nguyen, C. K.; Tran, N. Q., Preparation of the Cationic Dendrimer-Based Hydrogels for Controlled Heparin Release. *Journal of Macromolecular Science, Part A* **2015,** *52* (10), 830-837.

99. Lajunen, T.; Kontturi, L. S.; Viitala, L.; Manna, M.; Cramariuc, O.; Rog, T.; Bunker, A.; Laaksonen, T.; Viitala, T.; Murtomaki, L.; Urtti, A., Indocyanine Green-Loaded Liposomes for Light-Triggered Drug Release. *Mol Pharm* **2016,** *13* (6), 2095-107.

100. Saxena, V.; Gacchina Johnson, C.; Negussie, A. H.; Sharma, K. V.; Dreher, M. R.; Wood, B. J., Temperature-sensitive liposome-mediated delivery of thrombolytic agents. *Int J Hyperthermia* **2015,** *31* (1), 67-73.

101. Yamaguchi, N.; Chae, B.-S.; Zhang, L.; Kiick, K. L.; Furst, E. M., Rheological Characterization of Polysaccharide−Poly(ethylene glycol) Star Copolymer Hydrogels. *Biomacromolecules* **2005,** *6* (4), 1931-1940.

102. Brandl, F.; Kastner, F.; Gschwind, R. M.; Blunk, T.; Tessmar, J.; Gopferich, A., Hydrogel-based drug delivery systems: comparison of drug diffusivity and release kinetics. *J Control Release* **2010,** *142* (2), 221-8.

103. Li, W.; Liu, Q.; Zhang, P.; Liu, L., Zwitterionic nanogels crosslinked by fluorescent carbon dots for targeted drug delivery and simultaneous bioimaging. *Acta Biomater* **2016,** *40*, 254-262.

104. Meissner, Y.; Ubrich, N.; Ghazouani, F. E.; Maincent, P.; Lamprecht, A., Low molecular weight heparin loaded pH-sensitive microparticles. *Int J Pharm* **2007,** *335* (1-2), 147-153.

105. Reyes-Ortega, F.; Rodríguez, G.; Aguilar, M. R.; Lord, M.; Whitelock, J.; Stenzel, M. H.; San Román, J., Encapsulation of low molecular weight heparin (bemiparin) into polymeric nanoparticles obtained from cationic block copolymers: properties and cell activity. *Journal of Materials Chemistry B* **2013,** *1* (6), 850-860.

106. Tong, F.; Chen, X.; Chen, L.; Zhu, P.; Luan, J.; Mao, C.; Bao, J.; Shen, J., Preparation, blood compatibility and anticoagulant effect of heparin-loaded polyurethane microspheres. *Journal of Materials Chemistry B* **2013,** *1* (4), 447-453.

107. Ye, W.; Wang, N.; Hu, K.; Zhang, L.; Liu, A.; Pan, C.; Gong, T.; Liu, T.; Ding, H., Bio-inspired microcapsule for targeted antithrombotic drug delivery. *RSC Advances* **2018,** *8* (48), 27253-27259.

108. Wang, Q.; Wang, Y.; Guo, B.; Shao, S.; Yu, Y.; Zhu, X.; Wan, M.; Zhao, B.; Bo, C.; Mao, C., Novel heparin-loaded mesoporous tubular micromotors formed via template-assisted electrochemical deposition. *Journal of Materials Chemistry B* **2019,** *7* (16), 2688-2695.

109. Hallan, S. S.; Nidhi; Kaur, V.; Jain, V.; Mishra, N., Development and characterization of polymer lipid hybrid nanoparticles for oral delivery of LMWH. *Artificial Cells, Nanomedicine, and Biotechnology* **2017,** *45* (8), 1631-1639.

110. Lee, P.-C.; Zan, B.-S.; Chen, L.-T.; Chung, T.-W., Multifunctional PLGA-based nanoparticles as a controlled release drug delivery system for antioxidant and anticoagulant therapy. *Int J Nanomedicine* **2019,** *14*, 1533-1549.

111. İskenderoğlu, C.; Acartürk, F.; Erdoğan, D.; Bardakçı, Y., In vitro and in vivo investigation of low molecular weight heparin–alginate beads for oral administration. *Journal of Drug Targeting* **2013,** *21* (4), 389-406.

112. Patel, B.; Gupta, N.; Ahsan, F., Low-molecular-weight heparin (LMWH)-loaded large porous PEG-PLGA particles for the treatment of asthma. *J Aerosol Med Pulm Drug Deliv* **2014,** *27* (1), 12-20.

113. Hoffart, V.; Ubrich, N.; Simonin, C.; Babak, V.; Vigneron, C.; Hoffman, M.; Lecompte, T.; Maincent, P., Low Molecular Weight Heparin-Loaded Polymeric Nanoparticles: Formulation, Characterization, and Release Characteristics. *Drug Development and Industrial Pharmacy* **2002,** *28* (9), 1091-1099.

114. Sahoo, S. K.; De, T. K.; Ghosh, P. K.; Maitra, A., pH- and Thermo-sensitive Hydrogel Nanoparticles. *Journal of Colloid and Interface Science* **1998,** *206* (2), 361-368.

115. Gupta, A. K.; Gupta, M.; Yarwood, S. J.; Curtis, A. S., Effect of cellular uptake of gelatin nanoparticles on adhesion, morphology and cytoskeleton organisation of human fibroblasts. *J Control Release* **2004,** *95* (2), 197-207.

116. Cai, C.; Mao, S.; Germershaus, O.; Schaper, A.; Rytting, E.; Chen, D.; Kissel, T., Influence of morphology and drug distribution on the release process of FITC-dextran-loaded microspheres prepared with different types of PLGA. *J Microencapsul* **2009,** *26* (4), 334-45.

117. Maculotti, K.; Genta, I.; Perugini, P.; Imam, M.; Bernkop-Schnurch, A.; Pavanetto, F., Preparation and in vitro evaluation of thiolated chitosan microparticles. *J Microencapsul* **2005,** *22* (5), 459-70.

118. Yang, C.; Xie, R.; Liang, W.-G.; Ju, X.-J.; Wang, W.; Zhang, M.-J.; Liu, Z.; Chu, L.-Y., Beta-cyclodextrin-based molecular-recognizable smart microcapsules for controlled release. *Journal of Materials Science* **2014,** *49* (20), 6862-6871.

119. Nagahama, K.; Saito, T.; Ouchi, T.; Ohya, Y., Biodegradable Nano-aggregates of Star-Shaped 8-arm PEG-PLLA Block Co-polymers for Encapsulation of Water-Soluble Macromolecules. *J Biomater Sci Polym Ed* **2011,** *22* (1-3), 407-16.

120. Reyes-Ortega, F.; Parra-Ruiz, F. J.; Averick, S. E.; Rodríguez, G.; Aguilar, M. R.; Matyjaszewski, K.; San Román, J., Smart heparin-based bioconjugates synthesized by a combination of ATRP and click chemistry. *Polymer Chemistry* **2013,** *4* (9).

121. Park, K. D.; Joung, Y. K.; Bae, J. W.; Go, D. H., Heparin-Conjugated Nanointerfaces for Biomedical Applications. In *NanoScience in Biomedicine*, Shi, D., Ed. Springer Berlin Heidelberg: Berlin, Heidelberg, 2009; pp 247-271.

4. Additively manufactured multi drug eluting biodegradable reduced graphene oxide-polycaprolactone-star polymer coronary artery stents

4.1. Abstract

Coronary artery stents are intravascular medical devices to treat coronary heart disease. Current stents are drug-eluting, metallic, and permanent, and recipients require the need for life long anti-platelet therapy. The concept of biodegradable stents has emerged as an alternative to conventional stents, in which the stent degrades away leaving behind only the healed vessel. The first generation of biodegradable stents has been linked to higher rates of late stage thrombosis, and it has been suggested that this is due to increased strut thicknesses that cause disturbance to the laminar blood flow and result in activation of thrombogenic pathways. Current limitations in biodegradable scaffolds lie in fabrication of devices with low strut thickness, and long-term safety *in vitro* with low rates of scaffold thrombosis at later stages of a device lifetime, as compared to metallic devices.

In this study, we address these challenges by developing multi-drug eluting biodegradable PCL/rGO/CCS materials and confirming their printability utilizing additive manufacturing (MEW). We illustrate dual drug elution of an anti-thrombotic agent from the bulk of the material via heparin loaded star-brush polymers (hep load-CCS) embedded in PCL/rGO matrix, and elution of an anti-proliferative agent from the surface via a Rapamacyin (rapa)/PCL electrosprayed layer. Fabricated materials are characterized in terms of their mechanical performance, rheology, crystallinity, thermal behaviour, biological interactions, degradation as well as dual drug elution. These materials are fully biodegradable, deliver anti-proliferative

drugs through controlled release and anti-coagulating agents via slow release over time over their lifetime, and show excellent cytocompatibility *in vitro*.

4.2. Introduction

Cardiovascular diseases are number one cause of death globally, with coronary heart disease being one of the most deadly types of cardiovascular disseases [1]. Angioplasty is the most common treatment for coronary heart disease and involves the use of a coronary stent to open up the blocked artery [2]. The current generation of coronary artery stents are permanent, metallic, and are coated with a drug-impregnated and biodegradable polymer layer to allow short term drug elution. These devices elute drugs only through a surface coating, and do not provide bulk delivery of active ingredients from the bulk of a devive. While these devices have met with clinical success, the permanent nature of the metallic stent can lead to late-stage thrombosis and requires patients to remain on life-long antiplatelet therapy [3].

The diseased vessel can heal 6 months after the implantation of the coronary artery stent and does not require its permanent presence[4]. As such, biodegradable coronary artery stents have recently emerged as an attractive alternative with the potential to address the limitations associated with permanent stents. Specifically, these devices are designed to support the vessel for the required period and then degrade away, leaving behind a healed artery. This technology has the potential to alleviate the risk of late post-procedure complications and reduce the need for prolonged antiplatelet therapy [4].

The first clinically available bioabsorbable coronary artery stent has been linked to higher rates of late stage thrombosis, resulting in its removal from the market[5]. The failure of these devices

has been attributed to several factors including (1) changes to the shear stress experienced by the endothelium due to disturbance of laminar blood flow, (2) thrombogenicity of biodegradation products, and (3) the inflammatory response [6-8]. These challenges can be addressed though improved fabrication of devices, aiming at thin struts, which we presented in Chapter 2, or through careful design of drug delivery systems capable of delivery of anti-thrombotic molecules, which we presented in Chapter 3. In this chapter, we aim at approaching current limitations of biodegradable devices through the use of dual drug elution mechanism, which we hypothesize could allow us to elute anti-thrombotic agents from the bulk of the device, and anti-proliferative agents from the surface. This dual elution mechanism could address the limitations of current biodegradable devices by decreasing their thrombogenic potential.

In our previous work, we showed the feasibility of fabrication of stents with thin struts (as low as 60 µm) utilizing MEW and PCL-rGO (0.1 wt%) as the printing material. This fabrication process enabled us to fabricate devices with personalized pore size (strut spacing), strut thickness, diameter, and architecture, which are all important in the lesion coverage, stent implantation and long-term safety of a device[6-8]. Additionally, utilization of PCL-rGO as a printing material enabled us to fabricate devices with mechanical strength higher than that of pure PCL. Thin struts and personalized design of a scaffold are both crucial in successful development of biodegradable scaffolds as they prevent disturbances in laminar blood flow which can lead to thrombogenic eveents, and ensure proper lesion coverage depending on the patient's anatomy [6-7]. Furthermore, the addition of rGO into PCL enabled us to print devices with low strut thickness, high flexural stiffness, high tensile strength, which combined together

could promote endothelialization by decreasing the likelihood of mechanically induced causes of impaired neointimal coverage and re-endothelialization after implantation[6-7].

In this study, we investigate the addition of a drug-delivery system (heparin loaded star polymer) into the bulk of a material (PCL-rGO 0.1 wt%) to locally deliver an anti-thrombotic agent form the bulk of a device. To achieve this, we use the previously synthesized star-brush polymers (CCS) which exhibit hydrophobic exterior (PCL), hydrophilic shell (PEG MEA), and hydrophilic interior core (PEGDA) with loaded heparin. Previous reports show the release of anti-thrombotic agents from a vascular device such as vascular grafts via elution from a surface layer [9-10]. In this study, we investigate the concept of an anti-coagulant release from the bulk of the device rather than a surface, through embedding of loaded star polymers in the polymer matrix. Our hypothesis is that through incorporation of loaded star-brush polymers, which comprise of a hydrophilic interior and hydrophobic exterior, homogenous blending with the hydrophobic matrix will be achieved. Additionally, this approach is hypothesized to prolong the local release of anti-coagulant drug over time (> 1 month), therefore reduce likelihood of late stent thrombosis by ensuring that heparin release takes place in a slow, controlled manner over many months.

Rapamycin is an antiproliferative agent used to prevent in-stent restenosis (re-narrowing of the artery despite of the use of a stent) by slowing down the proliferation of smooth muscle cells after implantation of the scaffold. Rapamycin elution is required within short time frames after stent implantation to minimise in-stent restenosis and decrease the likelihood of need for the repeat procedures[2,4]. Heparin is an antithrombotic agent used intravenously following the angioplasty procedure to decrease the occurance of thrombus formation[9-10].

In the case of biodegradable stents, the long term safety issue lies in thrombogenic events such as an increased rate of late and very late scaffold thrombosis (30 days to 1 year after stent implantation) rather than early thrombosis (0 hours to 30 days after scaffold implantation) [6-7]. Therefore, we hypothesize that controlled release of antithrombotic agents from the bulk of a device could be beneficial to address the issue of late scaffold thrombosis (30 days or longer after scaffold implantation). The challenge to this approach lies in the design of a material which allows more robust release of rapamycin at the early stages (<1 month), and controlled slow release of heparin at later stages (>1 month).

Late stent thrombosis was previously correlated to thrombogenic events taking place in the artery due to thick struts (>80 μm), thrombogenicity of polymeric material, and degradation of stent in large bulks of polymer pieces[6-7]. Utilization of MEW to fabricate biodegradable stents could address these major issues through reduction of strut thickness and fabrication of a porous device which degrades in small fibre pieces rather than large chunks of polymer.

In this work, we combined our previous studies on MEW of PCL/rGO personalized coronary artery stents (**Chapter 2**) and synthesis of drug-delivery system for anti-thrombotic agents (**Chapter 3**) to develop multi-drug eluting, reduced graphene oxide-polycaprolactone-star polymer materials for application as coronary artery stents. The concentration of rGO in PCL was 0.1 wt% as we previously shown it is the most optimal in terms of printing, mechanical properties and biological behaviour (**Chapter 2**). Previously synthesized core-cross linked star polymers (CCS-PCL) (**Chapter 3**) with PEG length of approximately 20 repeat units and PCL length of approximately 30 units were used due to their low poly dispersity index (PDI) and highest conversion as shown in **Chapter 3**. These star polymers were loaded with anticoagulant

drug (heparin) and embedded into PCL-rGO (0.1 wt%) to melt electrowrite to confirm the printability of materials upon addition of CCS at the loading of 10 wt%. Following that, rapamycin (anti-proliferative drug for smooth muscle cells) in PCL was electrosprayed as an outer layer on the surface of the materials. Our work examined the feasibility of processing the material which is a PCL-reduced graphene oxide nanocomposite with dual drug elution mechanisms: 1) heparin elution through star polymers embedded in the bulk of a device 2) rapamycin elution through electro spraying on surface of melt electrowritten scaffolds. Fabricated materials with various star polymer content (10 wt%, 20 wt% and 40 wt%) in PCL-rGO (0.1wt%) matrix were investigated in terms of mechanical performance, rheological behaviour, crystallinity, thermal behaviour, and biological interactions. An accelerated degradation study was performed on scaffolds with different pore size and number of layers of deposited material. Dual drug elution was studied under physiological (pH = 7.4) and acidic conditions (pH = 5) to study the influence of pH on drug release and degradation of the materials. Cellular behaviour of hUVECs, SMCs, as well as platelets, upon contact with materials composed of CCS embedded in PCL, and PCL-rGO (0.1 wt%) was studied.

4.3. Methods

4.3.1. Materials

PCL pellets (average molecular weight 70,000 – 90,000 Da), basic alumina were purchased from Sigma-Aldrich, acetone from Chem Supply, graphene oxide (GO) (5 mg/ml in ethanol) from ACS Material LLC. ε-Caprolactone (97 %), Methanesulfonic acid (MSA, 98 %), Copper (II) bromide ($CuBr_2$), PEGDA (Mn = 250 Da), PEG MEA (Mn = 480 Da), 2 hydroxyethyl acetate, fluorescent isothiocyanate dextran (Mn = 20 kDa), heparin sodium salt from porcine mucosa (Grade I-A, ≥180 USP units/mg), Azure A chloride, Rapamycin (Sirolimus) were purchased from Sigma Aldrich. Toluene, DCM and CL were distilled over calcium hydride

before use. PEGDA (Mn = 250 Da) and PEG MEA (Mn = 480 Da) were deinhibited by passing through a basic alumina column before use as described in Chapter 3. HEBriB was synthesized via the esterification of 1,2-ethanediol with α-bromoisobutyryl bromide (98 %, Aldrich), purified by flash column chromatography, and characterized by ^{1}H and ^{13}C NMR as described in Chapter 3. Me_6TREN was synthesized following the previously published methods as described in Chapter 3**.**

4.3.2. Preparation and characterization of composites

Composites of 0.1 wt% PCL-rGO were prepared following the protocol reported in Chapter 2. rGO was used at 0.1 wt% concentration in PCL. Briefly, PCL pellets (2 g) were dissolved in acetone (5 mL) and a GO solution (5 mg/ml) was added to the PCL/acetone solution to obtain 0.1, 0.3, 0.6 and 1 wt% GO/PCL solutions. Solutions were continuosly stirred with a magnetic stirrer for 24h to allow dispersion of GO. GO was reduced to reduced graphene oxide (rGO) as described in Chapter 2. Previously synthesized and heparin loaded star polymers (Chapter 3) were blended with PCL-rGO (0.1 wt%) at the concentrations of 10 wt%, 20 wt% and 40 wt%.

4.3.3. Mechanical tests

4.3.3.1. Tensile tests

Samples were prepared using standardized moulds of a dog-bone shape with dimensions of approximately 10 mm height, 1.7 mm thickness and 1.5 mm width as described in Chapter 2 and following previously described protocols[11]. Briefly, PCL-rGO (0.1 wt%)-CCS composites at star content of 10 wt , 20 wt% and 40 wt% in PCL-rGO (0.1 wt%) were heated to 90 ºC and cast in the moulds. Tensile tests were performed using an Instron 5567 and 2 kN load cell at the strain rate of 0.1 mm/s until break following previously published protocols[11].

4.3.3.2. Compressive tests

Samples were prepared using standardized moulds of a disc shape with dimensions of approximately 1.45 mm height and 4 mm diameter as described in Chapter 2 and following the previous protocols[11]. Briefly, PCL-rGO (0.1 wt%)-CCS composites at star content of 10, 20 and 40 wt% in PCL-rGO (0.1wt%) were heated up to 90 ºC and cast in the moulds. Samples were compressed at a constant rate of 0.01 mm/s till the compression strain of approximately 40 %. All compression experiments were performed in PBS at 37 ºC using an Instron 5848 Microtester and 500 N load cell following previously published protocols[11]. For the quantitative analysis of the data, results were used from the compressive load of -0.5 N for all samples until the final data point as described previously[11].

4.3.4. Rheology

Rheology tests were performed using Twin Drive Rheometer MCR 702 (Anton Paar) on PCL-rGO (0.1 wt%)-CCS (10 wt%) and PCL-rGO (0.1 wt%) as described in Chapter 2. Viscosity was measured as a function of shear rate from 0.01 1/s till 1000 1/s at a temperature of 90 ºC (printing temperature). Temperature sweeps were performed at the frequency of 1Hz, shear strain of 1 % and the rate of 0.3 ºC/s. Frequency sweeps were performed from 0.01 Hz to 100 Hz, at the printing temperatures of the materials, 1 % shear strain (oscillatory). All measurements were performed using a cone and plate geometry with a measuring cone diameter of 25 mm, 2º angle and 0.102 mm gap.

4.3.5. Differential scanning calorimetry and Thermogravimetric analysis

DSC and TGA of the materials was performed using STA-8000 (Perkin Elmer) as described in Chapter 2. Dual DSC/TGA analysis was performed on approximately 10 mg of a sample at the heating/cooling rates of 10 ºC/min. Samples were allowed to reach thermal equilibrium for 30 min between the runs. 3 heating/cooling cycles were performed between 20 ºC to 150 ºC, followed by a thermogravimetric analysis from 20 ºC to 1000 ºC as described in the previous protocols[11]. Degree of crystallinity (X_c), was derived from the first heating cycle to include the thermal history after processing. X_c was calculated according to the following equation as described previously[11]:

$$X_c = \Delta H_f * \%PCL^{-1} * \Delta H^\circ_f{}^{-1} \quad (4.1)$$

Where ΔH_f and $\Delta H^\circ_f{}^{-1}$ are the measured heat of fusion of the samples (normalized to PCL content $\%PCL$ and the heat of fusion of 100 % crystalline PCL (136 J g^{-1}), respectively[11]. Melting and crystallization temperatures for each sample were obtained from 1st, 2nd and 3rd heating and cooling cycles respectively.

4.3.6. Melt electrowriting of stents

The custom-made MEW device with a high voltage source (DX250R, EMCO, Hallein, Austria) and a controller (Digit Multimeter 2100, Keithley, Cleveland, USA) was used with a gas-pressured feeding system as described in Chapter 2 and previously[11]. Materials containing PCL-rGO (0.1 wt%)-CCS(10 wt%) were melt electrowritten at the temperature of 90 ºC, pressure 2.5 bar, voltage 3.8 V. The deposition of materials was guided by the G-code (MACH

3 CNS software, ARTSOFT, Livermore Falls, USA) with a designed x,y pore sizes and architecture.

4.3.7. Rapamycin coating

0 mg, 2.5 mg and 5 mg of Rapamycin was dissolved in 0.5 mL dichloromethane (DCM) to prepare a stock solution of rapamycin/DCM. Following that, a stock solution containing 0 mg, 2.5 mg or 5 mg was added dropwise to previously prepared 15 wt% PCL solution in DCM (2.5 mL) under stirring. The mixture was stirred for 30 min prior to electrospinning. Electrospinning was performed on a custom-built electrospinning setup utilizing 18 G1/2 needle as a nozzle, 2 mL/h flow rate, 13 kV voltage, 10 cm distance, 1 mL syringe and 30 min of electrospinning time. PCL-rGO(0.1 wt%)-CCS(40 wt%) disc with dimensions of approximately 1.45 mm height and 4 mm diameter (mass ≈ 0.1g) was placed under the nozzle, at the distance of 10 cm, and electrospinning was performed onto the surface of a disc. Approximately 1000 µl of the PCL/rapamycin solution was electrospun onto the disc.

4.3.8. Drug elution

The *in vitro* dual drug elution was studied under physiological (pH = 7.4) and acidic conditions (pH = 5)[12]. Materials with varying heparin loaded star content in PCL/rGO 0.1 wt% matrix (hep loaded CCS 10 wt%, 20 wt% and 40 wt%) and electrospun rapamycin coating (mass rapamycin ≈ 1.2 mg) were prepared. Briefly, a piece of material (mass ≈ 0.1 g) was suspended in PBS (pH = 7.4 and pH = 5) and stirred at 37 ºC following previous protocols[12]. At certain time intervals, 2.0 mL aliquots were taken for ultraviolet/visible spectrophotometry (UV-VIS) and replaced with fresh PBS solution. UV-Vis spectrometric analysis was performed using a Shimadzu UV-2101 PC UV-Vis scanning spectrophotometer at a scan rate of 1 nm s^{-1}, with paired quartz cuvettes (Starna Pty Ltd) as described in Chapter 2. The concentrations of drugs

released were estimated via UV vis using the standard curves. Heparin concentration was obtained using Heparin-Azure A method as described in Chapter 2 and previous studies[13-16]. Briefly, the calibration curve was obtained with the use of Azure A to form heparin-azure A complex and enable calculation of remaining heparin concentration at 620 nm[13-16]. Rapamycin concentration was calculated using the standard curve and absorbance measured at 280 nm as described in previous studies[12, 17].

4.3.9. Degradation

The accelerated degradation of melt electrowritten scaffolds (PCL-rGO 0.1 wt%) with varying pore size (0.5 mm x 0.5 mm, 1mm x 1mm), and number of printed layers (3 layers, 5 layers), was studied following the previously developed protocols[11, 18]. Scaffolds were immersed in 5 M aqueous sodium hydroxide solution (10 mL) at 37ºC. At designated time points, materials were rinsed with deionized water several times and dried under pressure for 24 h. The decreasing mass of scaffolds was measured using an electronic balance (0.1 mg resolution). HIM images of scaffolds and their morphologies were taken using Helium Ion Bean Microscopy (HIM) (Zeiss, Germany). HIM was chosen as the imaging technique as it does not require sputtering of a conductive layer on the sample, which is required for SEM imaging, and it is also superior for imaging of surface roughness.

4.3.10. Biological interactions

4.3.10.1. Human umbilical vein endothelial cells

Surface preparation. Cell culture surfaces were prepared by coating the growth surfaces of 8-well Lab-Tek II chamber slides or Lab-Tek chambered coverglass (for confocal microscopy) with 25 µL of a 2% polymer solution in acetone. The chamber slides were then covered with aluminium foil and allowed to dry at ambient conditions for 48 h. Chamber slides were

sterilized through UV exposure for 1 h in a sterile biological safety cabinet. Wells were rinsed twice with PBS and incubated overnight in PBS at 37 °C before the introduction of cells.

Cell culture and maintenance. Pooled donor hUVECs were purchased from Lonza (Australia) and maintained in Clonetics™ EGM™-2 BulletKit™ containing Endothelial Basal Medium-2 (EBM™-2 Medium) supplemented with BulletKit™ as recommended by the supplier. Cells were cultured at 37 °C in a humidified 5 % CO_2 atmosphere. The culture medium was changed every other day. The cultures were passaged at 80 % confluence and lifted using 0.25 % trypsin-EDTA. For all tests, the cells between passages 3 and 5 were used [19-20].

Adhesion and growth of HUVECs. 500 µL of medium containing 1.7×10^4 cells per cm^2 was added to each well of polymer-coated chamber slides. Uncoated chamber slides were used as control. The HUVECs were cultured for 7 days, and the culture medium was changed every two days. Cell attachment and growth were determined for HUVECs after 4 h, 4 and 7 days using double stranded DNA (dsDNA) quantification by the Quant-iT™ PicoGreen® dsDNA Assay (Invitrogen) after digestion with papain as previously described [19-20]. Cell surface densities were determined by dividing the obtained cell number by the area of the test surface. Experiments were performed in triplicate.

The adherent endothelial cells were stained for the nuclei and actin cytoskeleton by using the FAK100 actin cytoskeleton/focal adhesion staining kit (Merck Millipore) as previously described[19-20]. Briefly, HUVECs were fixed after 4 h and 7 days and SMCs were fixed after 4 h and 4 days with 4% paraformaldehyde and were permeabilized with 0.1 % Triton X-100 in

PBS. The cells were stained with TRITC-phalloidin (1:500), and 4′,6-diamino-2-phenylindole (DAPI, 1:1000). The cells were finally washed and covered with PBS and imaged using a confocal laser scanning microscope (Nikon A1R) at 20× magnification. Images were generated by optical sectioning in the z-direction and were analysed using ImageJ software (NIH).

4.3.10.2. Smooth muscle cells

Surface preparation. Cell culture surfaces were prepared by coating the growth surfaces of 8-well Lab-Tek II chamber slides or Lab-Tek chambered cover glass (for confocal microscopy) with 25 µL of a 2 % polymer solution in acetone. The chamber slides were then covered with aluminium foil and allowed to dry at ambient condition for 48 h. Chamber slides were sterilized through UV exposure for 1 h in a sterile biological safety cabinet. Wells were rinsed twice with PBS and incubated overnight in PBS at 37 °C before the introduction of cells.

Cell culture and maintenance. SMCs were kindly donated from the O'Brien Institute (Melbourne, Australia) and maintained in smooth muscle cell growth medium 2 from PromoCell containing Fetal Calf Serum (FCS), human Epidermal growth factor (hEGF), human basic fibroblast growth factor (hbFGF-1), and insulin. Cells were cultured at 37 °C in a humidified 5 % CO_2 atmosphere. The culture medium was changed every other day. The cultures were passaged at 80 % confluence and lifted using 0.25 % trypsin-EDTA. For all tests, the cells between passages 3 and 5 were used.

Adhesion and growth SMCs. 500 µL of medium containing 1.7×10^4 cells per cm^2 was added to each well of polymer-coated chamber slides. The SMCs were cultured for 4 days and the culture medium was changed every two days. Cell attachment and growth were determined for SMCs after 4 h and 4 days using double stranded DNA (dsDNA) quantification by the Quant-

iT™ PicoGreen® dsDNA Assay (Invitrogen) after digestion with papain as previously described [19-20]. Cell surface densities were determined by dividing the obtained cell number by the area of the test surface. Experiments were performed in triplicate.

The adherent cells were stained for the nuclei and actin cytoskeleton by using the FAK100 actin cytoskeleton/focal adhesion staining kit (Merck Millipore) as previously described [19-20]. Briefly, SMCs were fixed after 4 h and 4 days with 4% paraformaldehyde and were permeabilized with 0.1% Triton X-100 in PBS. The cells were stained with TRITC-phalloidin (1:500), and 4′,6-diamino-2-phenylindole (DAPI, 1:1000). The cells were finally washed and covered with PBS and imaged using a confocal laser scanning microscope (Nikon A1R) at 20 × magnification. Images were generated by optical sectioning in the z-direction and were analysed using ImageJ software (NIH).

4.3.10.3. Platelet adhesion

Platelets were obtained from the Australian Red Cross Blood service. Precleaned 12-mm glass coverslips were dipcoated in 5 % polymer solution in acetone. Coverslips were dried overnight to remove residual solvent and then transferred to the wells of a 24-well plate. Well plates were sterilized through exposure to UV radiation for 2 h and equilibrated in PBS overnight. 0.3 mL of platelet suspension was pipetted onto each of the test surfaces and then incubated at 37 ºC for 1h. After that, samples were gently rinsed with phosphate buffered saline (PBS) to remove non adherent platelets. Adhered platelets on samples were fixed using 4% paraformaldehyde solution at room temperature for 2 h. Cultures were rinsed three times with deionized water to remove residual salt, dried and analyzed through HIM (ZEISS Microscopy GmbH, Germany). Images were taken of randomly selected five fields of view on each test surface. The number

of adherent platelets was counted and divided by the area of the image to calculate the adherent platelet density as decribed in Chapter 2.

4.3.11. Statistical analysis

All quantitative data are expressed as mean ± standard deviations with a minimum of n = 3 repeats. Student's t test and ANOVA one-way analysis of variances were used to analyse the statistical differences between samples and were considered significant at $^{**}P<0.01$ and $^{*}P<0.05$.

4.4. Results and Discussion

4.4.1. Mechanical tests

To better understand the influence of star addition on PCL-rGO properties, we characterized materials in terms of their mechanical properties (compressive and tensile). Composites of PCL-rGO (0.1 wt%) with star content of 10 wt%, 20 wt% and 40 wt% were prepared utilizing standardized moulds. Briefly, PCL-rGO (0.1 wt%), PCL-rGO (0.1 wt%)-CCS (10 wt%), PCL-rGO(0.1 wt%)-CCS(20 wt%) and PCL-rGO (0.1 wt%)- CCS(40 wt%) materials were heated up to 90 ºC and cast in standardized moulds. Mechanical characterization of composites in terms of tensile and compressive properties is presented in **Figure 4.1**.

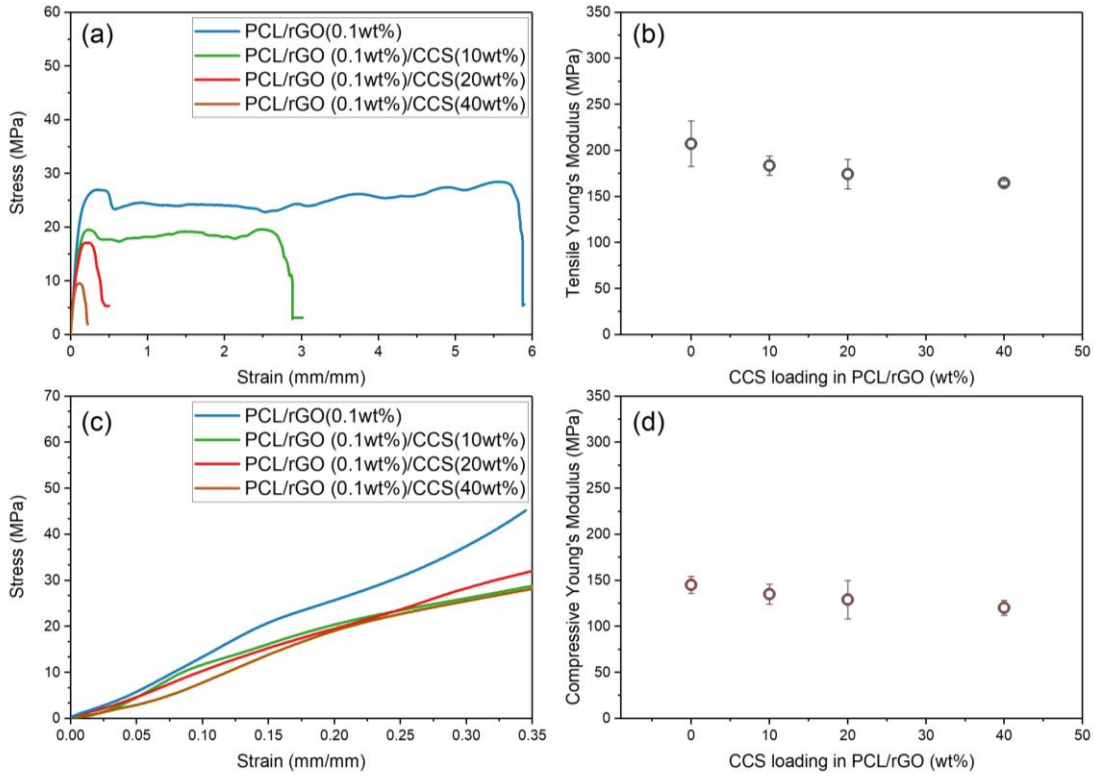

Figure 4.1: Mechanical characterization of CCS/PCL-rGO (0.1 wt%) composites. (a) Tensile stress-strain curves. (b) Tensile Young's Modulus for composites with varying content of CCS in PCL-rGO (0.1 wt%). (c) Compressive stress-strain curves (d) Compressive Young's Modulus for composites with varying content of CCS in PCL-rGO (0.1 wt%). All quantitative data are expressed as mean ± standard deviations with a minimum of n = 3 repeats.

The mechanical results illustrate dose dependent effect of star content on mechanical properties of materials both in terms of tension and compression (**Figure 4.1**). At a lower star loading (10 wt%) in PCL-rGO (0.1 wt%), there is a decrease in tensile Young's Modulus, elongation at break, ultimate tensile strength, stress at break and elongation at break as compared to PCL-rGO (0.1 wt%) as shown in **Table 4.1**. At a higher star loading in PCL-rGO (0.1 wt%) (20 wt%, 40 wt%), there is more profound decrease in both compressive and tensile Young's Modulus, tensile strength and stress at break. Additionally, materials have become more brittle after incorporation of star polymers into PCL-rGO (0.1 wt%), what can be seen in a significant decrease in elongation at break at higher concentrations of star polymers in PCL-rGO such as 20 wt%, 40 wt%. (**Table 4.1**). Higher loadings of stars in PCL-rGO (0.1 wt%) corresponds to

less graphene-based composite in a material, and more of the star polymer, which is composed of PCL arms, mPEG brush and PEGDA core. The core of the star used in this study is a gel-like polymer which has low mechanical performance in terms of its tensile and compressive strength. Due to this, a decrease in both tensile and compressive behaviour is seen at the higher star loading (20 wt%, 40 wt%). More detailed mechanical characteristics are presented in **Table 4.1.**

Table 4.1: Mechanical characterization of melt-cast PCL-rGO-CCS nanocomposites. All quantitative data are expressed as mean ± standard deviations with a minimum of n = 3 repeats.

Tensile properties of PCL-rGO-CCS nanocomposites

Material	Modulus (MPa)	Ultimate Tensile Strength (MPa)	Strain at break	Stress at break (MPa)
PCL/rGO (0.1 wt%)	207 ± 24	27.5 ± 2	5.9 ± 1.0	27.6 ± 2
PCL/rGO (0.1 wt%)/CCS(10 wt%)	184 ± 10	21.5 ± 2	3.6 ± 1.0	19.0 ± 1
PCL/rGO (0.1 wt%)/CCS(20 wt%)	174 ± 16	17.8 ± 6	0.8 ± 0.1	13.4 ± 7
PCL/rGO (0.1wt%)/CCS(40 wt%)	164 ± 3	10.2 ± 2	0.2 ± 0.1	8.2 ± 2

Compressive properties of PCL-rGO-CCS nanocomposites

Material	Modulus (MPa)	Stress at 10% strain (MPa)
PCL/rGO (0.1 wt%)	145 ± 9	11.3 ± 4
PCL/rGO (0.1 wt%)/CCS(10 wt%)	135 +11	10.9 ± 1
PCL/rGO (0.1 wt%)/CCS(20 wt%)	129 ± 21	10.1 ± 3
PCL/rGO (0.1 wt%)/CCS(40 wt%)	120 ± 8	9.2 ± 1

Results show that high loading of stars (20 wt%, 40 wt%) in PCL-rGO (0.1 wt%) lead to the loss of desired mechanical performance in terms of material stiffness, tensile and compressive strength, stress at break and elongation at break, therefore a low concentration of stars (10 wt%) was utilized for printing of stents (**Table 4.1**).

4.4.2. Rheology

The ability to melt electrowrite a material is dependent on its rheological properties. The melting point of PCL is ~ 60 ºC. The viscosity of PCL-rGO (0.1 wt%) was previously assessed (**Chapter 2**) at temperatures of 70 ºC, 90 ºC and 120 ºC relevant to MEW process. Additionally, the rheology data was previously collected for PCL-rGO (0.1 wt%) in frequency and temperature sweeps to better understand the behaviour of a material as a function of frequency and temperature (**Chapter 2, Figure 2.3).** In this study, we characterized the material chosen for printing (PCL-rGO (0.1 wt%)-CCS(10 wt%)) and compared it to PCL-rGO (0.1 wt%) in terms of its viscosity, as well as G' and G" characteristics over a range of temperatures and frequencies (**Figure 4.2).**

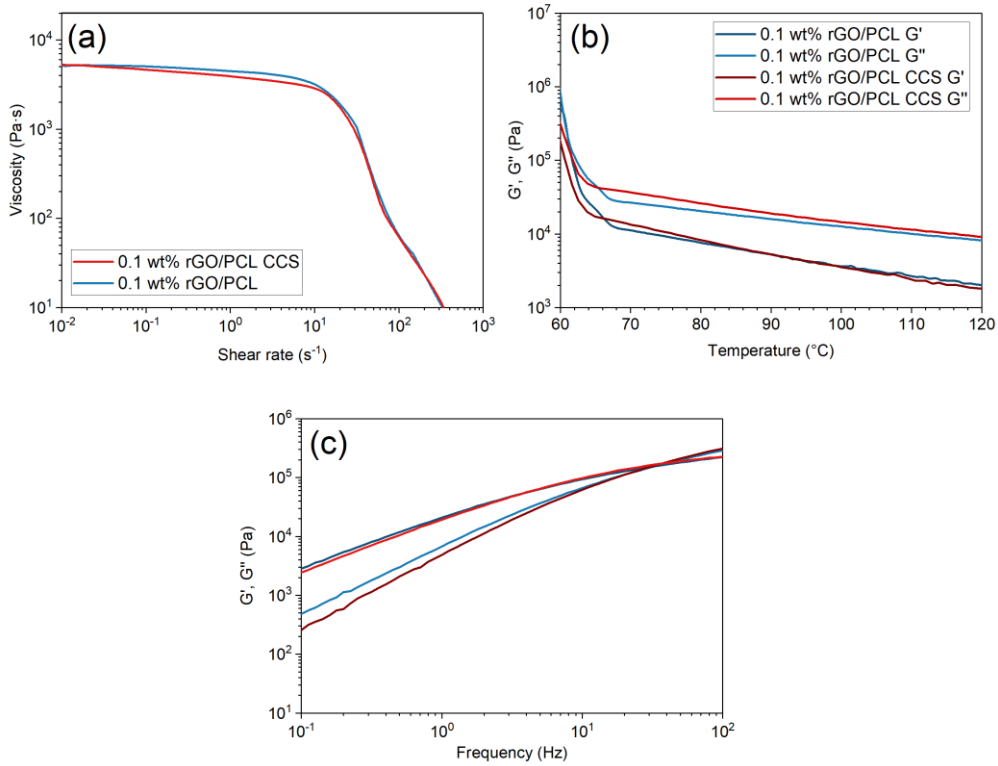

Figure 4.2: Rheology characterization of printing material. (a) Viscosity vs shear rate for PCL-rGO (0.1 wt%) and PCL-rGO(0.1 wt%)-CCS(10 wt%) at printing temperatures of 90 ºC(b) Temperature sweeps for PCL-rGO (0.1 wt%) and PCL-rGO(0.1 wt%)-CCS(10 wt%) (c) Frequency sweeps for PCL-rGO (0.1 wt%) and PCL-rGO(0.1 wt%)-CCS(10 wt%).

The results show almost identical behaviour in terms of viscosity, storage and loss moduli over a range of temperatures and frequencies. Similar to our results in Chapter 2, the viscosity of PCL-rGO (0.1 wt%)-CCS(10 wt%) was both temperature and shear rate dependent (**Figure 4.2**)**.** Specifically, the viscosity decreased with increasing temperature, and it dropped sharply from a rather steady value when the shear rate of 10 s^{-1} was exceeded. The storage modulus represents the energy stored in the elastic structure of the sample and gives information about the amount of structure in the sample. The loss modulus represents the viscous part, or the amount of energy dissipated in the sample. Above 60 ºC, both PCL-rGO (0.1 wt%) and PCL-rGO(0.1 wt%)-CCS(10 wt%) were characterized by higher loss moduli compared to its storage moduli, which is correlated to liquid-like behaviour and confirms their printability in that region (**Figure 4.2b**). Frequency sweeps were performed at printing temperatures of PCL-rGO(0.1 wt%) and PCL-rGO(0.1 wt%)-CCS(10 wt%) and showed that at lower frequencies storage moduli are higher than loss moduli (solid-like behaviour), while at higher frequencies loss moduli are higher than storage moduli (liquid-like behaviour) (**Figure 4.2c**). Our results indicated that PCL-rGO(0.1 wt%)-CCS(10 wt%) should be printable in conditions similar to that used for MEW of PCL-rGO (0.1 wt%).

4.4.3. Differential scanning calorimetry and Thermogravimetric analysis

In order to better understand the influence of star loading into the PCL-rGO(0.1 wt%), as well as the stability of drug used (heparin), DSC and TGA was performed on materials with varying star content (10 wt%, 20 wt%, 40 wt%) in PCL-rGO (0.1 wt%), PCL-rGO (0.1 wt%), heparin loaded CCS embedded in PCL-rGO (0.1 wt%) at the loading of 10 wt% and pure heparin (**Figure 4.3**).

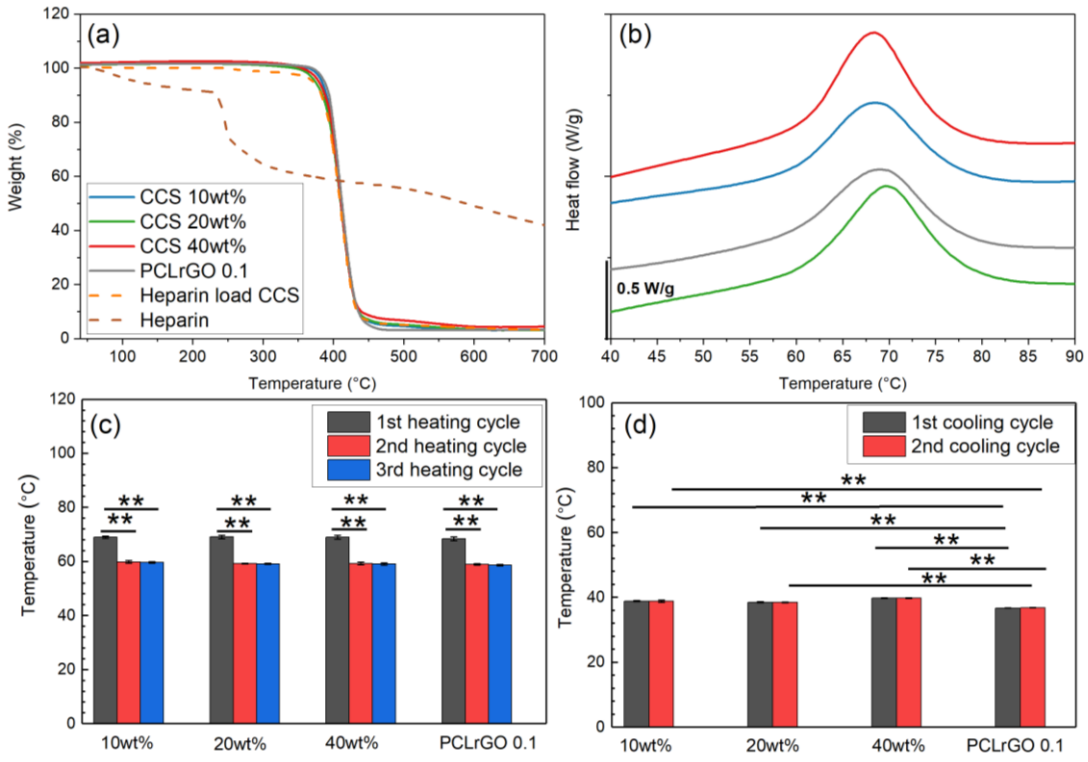

Figure 4.3: (a) TGA curves for CCS embedded in PCL-rGO (0.1 wt%) matrix at 10, 20 and 40 wt%, PCL-rGO (0.1 wt%), heparin loaded CCS (10 wt%) in PCL-rGO (0.1 wt%) matrix, and pure heparin. (b) Heat flow curves for PCL-rGO (0.1 wt%)-CCS(10 wt%), PCL-rGO (0.1 wt%)-CCS(20 wt%), PCL-rGO(0.1 wt%)-CCS(40 wt%), and PCL-rGO(0.1 wt%). (c) Melting temperatures for PCL-rGO (0.1 wt%)-CCS(10 wt%), PCL-rGO (0.1 wt%)-CCS(20 wt%), PCL-rGO(0.1 wt%)-CCS(40 wt%), and PCL-rGO(0.1 wt%) after 1st, 2nd and 3rd heating cycles. (d) Crystallization temperatures for PCL-rGO (0.1 wt%)-CCS(10 wt%), PCL-rGO (0.1 wt%)-CCS(20 wt%), PCL-rGO(0.1 wt%)-CCS(40 wt%), and PCL-rGO(0.1 wt%) after 1st, 2nd cooling cycles. Asterisks (*) represent statistical difference where **P<0.01 and *P<0.05, (n = 3).

Three heating cycles were run from 20 ºC to 150 ºC at the heating rate of 10 ºC/min, and two cooling cycles, to gain a better understanding of the effect of the thermal history of the materials, as well as the influence of printing on the degree of crystallinity and melting and crystallization temperatures. TGA results show that PCL-rGO (0.1 wt%), PCL-rGO (0.1 wt%)-CCS(10 wt%), PCL-rGO (0.1 wt%)-CCS(20 wt%), PCL-rGO (0.1 wt%)-CCS(40 wt%) and PCL-rGO (0.1 wt%)-heparin loaded CCS(10 wt%) have similar TGA curves and show the initial degradation at temperatures of approximately 375 ºC (**Figure 4.3a**).

TGA curve was additionally obtained for pure heparin to better understand its stability over a range of temperatures. Results indicate that heating up pure heparin up to 100 ºC has very little

effect on its thermal stability, with mass loss less than ≈ 2 - 3 %. This initial weight loss could be also associated with water loss. Higher temperatures (above 110 ºC), lead to more rapid loss of heparin mass suggesting its thermal degradation. Additionally, thermal analysis was obtained for PCL-rGO (0.1 wt%)-heparin loaded CCS(10 wt%) to investigate the influence of heating and printing temperature on material stability. Our results show that heparin loaded CCS (10 wt%), which are embedded into the PCL-rGO(0.1 wt%) matrix, do not degrade up until approximately 375 ºC, similarly to other materials (**Figure 4.3a**). From a thermal analysis point of view, it could be concluded that embedding heparin loaded CCS into PCL-rGO(0.1 wt%) enables retention of thermal stability of heparin, which is crucial during the printing process.

DSC results indicate that melting temperatures after 1st heating cycle were 68.5 ± 0.7 ºC, 69.0 ± 0.4 ºC, 69.1 ± 0.6 ºC and 68.9 ± 0.7 ºC for PCL-rGO (0.1 wt%), PCL-rGO (0.1 wt%)-CCS(10 wt%), PCL-rGO (0.1 wt%)-CCS(20 wt%) and PCL-rGO(0.1 wt%)-CCS(40 wt%) respectively (**Figure 4.3c).** After the 2nd heating cycle, melting temperatures were found to be lower in all groups as compared to 1st heating cycles (**Figure 4.3c**). There was no difference in melting temperatures between 2nd and 3rd heating cycles for all groups. Crystallization temperatures of PCL-rGO (0.1 wt%) after 1st and 2nd cooling cycles were found to be lower than those of PCL-rGO(0.1 wt%)-CCS(10 wt%), PCL-rGO(0.1 wt%)-CCS(20 wt%) and PCL-rGO(0.1 wt%)-CCS(40 wt%) **(Figure 4.3d**). No statistically significant difference was observed between crystallization temperature during the 1st cooling cycle and 2nd cooling cycle within each group (**Figure 4.3d**).

Degree of crystallinity (X_c) for all materials was estimated utilizing enthalpy obtained from DSC curves (**Figure 4.3b**, **Table 4.2**). Enthalpy (ΔH) of melting was approximated by integrating the heat flow of each sample as shown in the **Figure 4.3b**. Results indicated that after addition of CCS at low loading (10 wt%) into PCL-rGO (0.1 wt%) matrix, crystallinity decreased, which is hypothesized to be related to the change in the composition of the materials. CCS are composed of PCL arms, PEG MEA brush and PEGDA cores which are embedded into PCL-rGO(0.1 wt%) matrix. Addition of CCS into PCL-rGO (0.1 wt%) matrix introduced changes in microstructure of the material therefore changes in crystallinity.

Table 4.2: DSC characterization of PCL-rGO (0.1wt%) composited with varying content of CCS. ΔH – enthalpy; Xc – crystallinity.

Material	**ΔH (J/g)**	**X_c (%)**
PCL-rGO (0.1 wt%)	71 ± 24	52 ± 17
PCL-rGO (0.1 wt%)-CCS(10 wt%)	50 ± 1	37 ± 1
PCL-rGO (0.1 wt%)-CCS(20 wt%)	65 ± 5	48 ± 4
PCL-rGO (0.1 wt%)-CCS(40 wt%)	66 ± 1	54 ± 1

4.4.4. Melt electrowriting of stents

To confirm the printability of material upon addition of CCS into PCL-rGO (0.1 wt%) matrix, we prepared the composites of PCL-rGO(0.1 wt%)-CCS(10 wt%) and evaluated their printability utilizing MEW parameters previously optimized for printing of PCL-rGO (0.1 wt%). Briefly, we printed the material at 90 ºC, pressure of 2.5 bar, voltage of 3.8 V and confirmed its extrusion through the nozzle of 23 G as described in **Chapter 2**. In our previous work, we showed the feasibility of fabrication of personalized scaffolds with varying pore size

(strut spacing), number of printed layers (thickness), diameter, architecture and strut thickness, utilizing MEW. Scaffolds were printed with strut thickness as low as 60 μm to address the limitation of current technology and reduce the likelihood of scaffold thrombosis. In this study, we additionally embedded heparin-loaded CCS into PCL-rGO (0.1 wt%) to study heparin release from a bulk of a material and confirm the printability of material after CCS blending. Materials were successfully extruded with no signs of CCS blocking the nozzle or aggregating during printing as shown in the Video C1, Appendix C**.**

4.4.5. Rapamycin coating

In this study, our aim was to study dual elution of rapamycin and heparin from PCL-rGO(0.1 wt%)-CCS materials. To simplify the experiments, we fabricated discs with approximately 3 mm height and 4 mm diameter via melt-casting at 90 ºC utilizing PCL-rGO(0.1 wt%)-heparin loaded CCS. 0 mg, 2.5 mg and 5 mg of Rapamycin were dissolved in 0.5 mL DCM to prepare stock solutions of rapamycin/DCM mixture. Following that, a stock solution containing 0 mg, 2.5 mg or 5 mg of rapamycin was added dropwise to previously prepared 15 wt% PCL solution (2.5 mL) under stirring. The mixture was stirred for 30 min prior to electrospinning. Electrospinning was performed utilizing 18 G 1/2 needle as a nozzle, 2 mL/h flow rate, 13 kV voltage, 10 mm distance and 1 mL syringe. Briefly, a disc (PCL-rGO(0.1 wt%)-heparin loaded CCS) was placed under the nozzle at the distance of 10 cm, and approximately 1000 μl of a Rapamycin/PCL was electrospun onto the disc to allow a deposition of a layer of rapamycin loaded PCL fibres. Morphology of electrospun PCL/rapamycin fibres was characterized using HIM as shown in **Appendix Chapter 4** (**Figures C40-C41**). Upon the fabrication of PCL-rGO(0.1 wt%)-heparin loaded CCS discs with rapamycin/PCL outer layer, we studied drug elution from the materials.

Rapamycin concentration used in this study was based on previous reports which investigated rapamycin loading into the polymer fibres and therapeutic values required for prevention of in-stent restenosis[12,17]. We additionally studied the interaction of smooth muscle cells with rapamycin-PCL/rGO/CCS materials containing different rapamycin content (0 mg , 2.5 mg, 5 mg in 3 mL DCM), which correspond to initial concentrations of electrospinning solutions, to assess our chosen dosing. The study with smooth muscle cells showed that both rapamycin concentration (2.5 mg and 5 mg in 3 mL DCM) are effective in decreasing proliferation of smooth muscle cells (Section 4.4.8.2). However, to fully understand the required therapeutic dosage of rapamycin while delivered locally from our materials, further in-vitro experiments (e.g. under flow) and animal tests would be required.

In this study, we also simplified the experimental setup to minimize the use of rapamycin due to limited availability of a drug. Ideally, electrospinning of rapamycin should be undertaken directly onto the melt electrowriten scaffolds, rather than discs, by crimping them onto the collector. Melt electrowritten scaffolds would then rotate at the constant rotational speed, and rapamycin/PCL solution would electrosprayed onto the surface of the scaffold. This approach would allow uniform deposition of thin layer of Rapamycin/PCL fibres onto the surface of melt electrowritten devices.

4.4.6. Drug elution

Dual drug elution of heparin and rapamycin was studied in physiological (pH = 7.4) and acidic conditions (pH = 5). Materials with varying contents of heparin-loaded stars (hep-load CCS) embedded in PCL-rGO(0.1 wt%) were prepared at the ratios of 10 wt% CCS, 20 wt% CCS and 40 wt% CCS in PCL-rGO(0.1 wt%) by blending technique. Additionally, materials with

rapamycin/PCL coating (mass rapamycin ≈ 1.2 mg) were prepared with the bulk of the material composed of PCL-rGO(0.1 wt%)-CCS(40 wt%). For drug release, approximately 0.1 g of each material was suspended in PBS at 37 ºC in pH = 7.4 and pH = 5 to study heparin and rapamycin release at physiological and acidic conditions. Drug release profiles were obtained for all condition as shown in **Figure 4.4**.

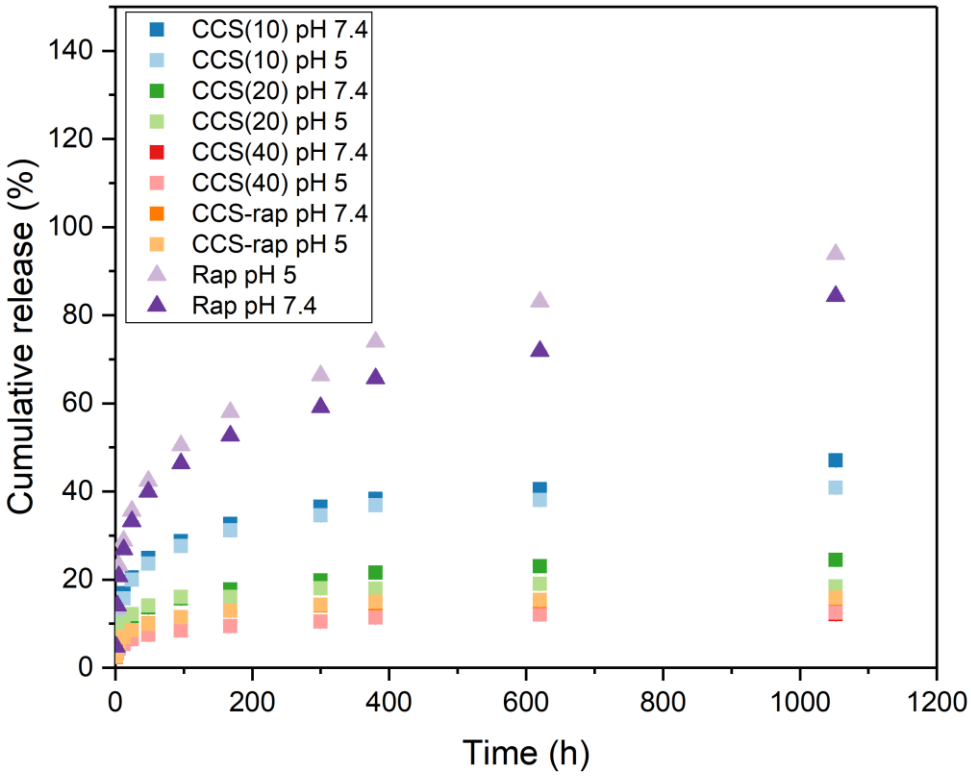

Figure 4.4: Drug release profiles of heparin and rapamycin at pH = 7.4 and pH = 5. All quantitative data are expressed as mean ± standard deviations with a minimum of n = 3 repeats. Square symbols show heparin release; triangle symbols show rapamycin release. Rap corresponds to rapamycin.

Our results show faster release of rapamycin at both physiological (pH = 7.4), and acidic (pH = 5) conditions. More than 50% of rapamycin was released from rapamycin/PCL coating within 200 h of drug elution, and approximately 80 % was released after approximately 1050 h (≈ 44 days). Rapamycin release was very rapid within first 200 h, with slower release towards

the end of the experiment. Additionally, more rapamycin was released under acidic conditions (pH = 5.0) which could be correlated to initial degradation of PCL fibres at longer time intervals. Release of rapamycin during the first 4 weeks after stent implantation is very important in anti-proliferation of smooth muscle cells to prevent in-stent restenosis after implantation of a device[16-17].

Heparin release was studied from heparin loaded CCS embedded in PCL-rGO(0.1 wt%) matrix at the ratios of 10 wt%, 20 wt% and 40 wt% (**Figure 4.4**). PCL-rGO(0.1 wt%)-CCS(10 wt%) materials had the lowest amount of heparin (≈ 0.9 mg) embedded within the matrix. Here, the release profile shows heparin release of approximately 30 % at 200 h for physiological and acidic pH conditions, increasing to approximately 47 % at 1050 h. For materials with 20 wt% CCS in PCL-rGO (0.1 wt%), a release of slightly less than 18 % of their drug content at 200 h was observed for both pHs, increasing to approximately 25 % of the drug content at 1050 h. Materials with 40 wt% of CCS embedded in PCL-rGO(0.1 wt%) showed release of approximately 10 % of drug content at 200 h, and of approximately 20 % at 1050 h for both pH levels. Materials with low content of heparin-loaded stars (10 wt%) embedded in PCL-rGO(0.1 wt%) matrix showed highest percentage of cumulative drug released due to their lowest initial content of the drug (≈ 0.9 mg) in the material. Similarly, materials with the highest CCS content (40 wt%) in PCL-rGO (0.1 wt%) showed the lowest percentage of cumulative drug released due to the highest initial amount of drug embedded in them (≈ 3.6 mg), and controlled release of drug over studied time (>1 month).

For all groups, heparin release was initially more rapid (from 1 h – 96 h), which was then followed by steady, controlled release with a lower slope. This trend continued until the final

data points (≈ 44 days) which showed steady, small increase in cumulative drug released. Although initially there is rapid release of heparin present in all groups with CCS embedded in PCL-rGO (0.1 wt%), more controlled, and slower release dominates after 96h of rapid release, as shown in **Figure 4.4**. Our results illustrate that electrospraying of rapamycin/PCL outer layer composed of nano-fibres on the bulk of PCL-rGO(0.1 wt%)-CCS material enables controlled release of rapamycin (anti-proliferative drug) and slower release of heparin.

Stars with higher content (40 wt%) in PCL-rGO(0.1 wt%) had approximately 80 % of drug left (≈ 2.9 mg) embedded in their matrices which continued to be slowly released over time. Stars with medium content (20 wt%) in PCL-rGO(0.1 wt%) had approximately 75% of drug left (≈ 1.3 mg) in their matrices and similarly to other material, continued to slowly release more drug beyond 1050 h. Stars with lower content (10 wt%) in PCL-rGO(0.1 wt%) had approximately 50 % of drug left (≈ 0.4 mg) embedded in their matrices which also continued to get slowly released. These drug release profiles for heparin and rapamycin show that by embedding heparin-loaded stars into PCL-rGO(0.1 wt%) matrix, heparin release can be controlled and prolonged (>1 month).

Heparin is usually administrated intravenously after angioplasty to prevent thrombogenic events, therefore no standardized information is present on desired therapeutic dosage while delivered locally from the scaffold[9-10]. Some companies developed heparin-coated vascular grafts (e.g., Gore® Acuseal Vascular Graft), which deliver heparin locally from a coating, and suggest that less than 1% of the intravenous dosage of heparin is required for its therapeutic activity[28]. In our study, it was approximated that star loading in the range of 10 wt% to 40 wt%, in PCL-rGO (0.1 wt%) would be required to deliver heparin at the therapeutic levels. Due to

this, we chose the loadings of 10 wt%, 20 wt%, 40 wt% in PCL-rGO (0.1 wt%) for our drug elution study. We approximated that at around 20 % - 30 % release of heparin loaded into the material with highest CCS content (40 wt%) in PCL-rGO (0.1 wt%), the desired therapeutic amount would be achieved. In this study, we reached a release of approximately 20 % at 1050 h (≈ 44 days). Further evaluations of a drug release at conditions closer to physiological (e.g., under flow) are required. This evaluation would enable critical approximation of released drug and its comparison to therapeutic value. Additionally, animal tests which evaluate the required therapeutic dosage would be necessary.

Our results also illustrate that by encapsulation of rapamycin into PCL fibres, and electro spraying of them as an outer material coating, controlled release of rapamycin could be achieved. Rapamycin release shows characteristic initial burst release profile followed by a decrease in the release rate which agrees with previous reports of drug release from electro sprayed coatings as described in Chapter 1, Section 1.4.1. The release of rapamycin could assure anti-proliferative effect on smooth muscle cells and prevent in-stent restenosis (narrowing of the artery despite of the use of stent). Conversely the slower, more controlled release of heparin at later times of devices lifetime, could potentially lead to anti-thrombotic effects therefore better long-term safety in vivo of the stent. However, animal tests and long-term evaluation of materials would be required to evaluate these hypotheses.

The kinetics of drug elution of heparin and rapamycin was estimated by mathematical modelling and fitting of the release data into various release mechanisms such as zero-order kinetic release, first-order release, Higuchi model, Power model, Hixon-Crowell model, Weibull model, Hopfenberg model and Exponential model [23-25] (**Appendix Chapter 4,**

Figures C1-C38). The zero-order kinetics model was not found to fit the release data as the relationship between the drug release and time was not linear both in case of heparin and rapamycin. Release data was then fit into the first-order kinetics model by plotting the log of cumulative percentage of drug remaining versus time and curve fitting [23-27]. For heparin release, first-order kinetics did not closely match the experimental data therefore other mechanisms of kinetics release were investigated. For rapamycin release, first-order kinetics matched the experimental data more closely as compared to heparin release therefore first order rate constants were estimated for rapamycin release (**Appendix Chapter 4, Figures C1-C2**). Following that, Higuchi model was used to fit experimental data and showed closer fit to rapamycin release, than to heparin, as presented in **Table 4.3** and **Appendix Chapter 4** (**Figures C3-C38**).

Table 4.3: Kinetics mechanism investigated for release of heparin and rapamycin. C_t – amount of the drug released at time t; C_0 – initial concentration of drug at time t = 0; K_0 – zero-order rate constant; t – time; K_t – first order rate constant; C- total amount of drug release; D – diffusion coefficient of the drug molecule; qt – total amount of drug in a unit volume of a matrix; C_s – dimensional solubility of drug in polymer matrix; C_t/C_∞ - fraction of drug release at time t; K – rate constant; n- release exponent; K_{HC} - Hixon-Crowell rate constant; T – lag time measured as a result of dissolution process; a – scale parameter that describes time dependence; b- shape of dissolution curve; C_L – initial drug loading through the system; n – exponent that varies with geometry; r – system half thickness; C_{max} – maximum dissolution; α - location/scale parameter; β - dissolution rate per unit of time (shape parameter)

Kinetics mechanism	Equation	Release mechanism	Ref
Zero-order	$C_t=C_0-K_0t$	Diffusion	23-27
First-order	$\log C=\log C_o-K_t/2.303$	Fick's first law, diffusion	23-27
Higuchi model	$C_t=[D(2qt-C_s)C_st]^{1/2}$	Diffusion medium based, Fick's first law	23-27
Korsemeyer-Peppas model (Power model)	$C_t/C_\infty=Kt^n$	Semi empirical, diffusion	23-27
Hixon-Crowell model	$C_0^{1/3}-C_t^{1/3}=K_{HC}t$	Erosion	23-27
Weibull model	$C_t=C_0\ [1-\exp[\frac{-(t-T)b}{a}]$	Empirical, life-time distribution function	23-27
Hopfenberg model	$C_t/C_\infty=1-[1-K_0t/C_Lr]^n$	Erosion	23-27
Gompertz model (Exponential model)	$C_t=C_{max}\exp[-\alpha e^{\beta \log t}]$	Dissolution	23-27

The power model, also known as Korsemeyer-Peppas Model, was used to model the release of heparin and rapamycin in the next stages. It showed close fit to heparin release with varying star content in polymeric matrix, and different experimental conditions of release (pH levels), as shown in **Table 4.3** and **Appendix Chapter 4** (**Figures C6-C15**). Rate constants and release exponents were approximated for different experimental conditions and both drugs (heparin and rapamycin) by fitting of experimental data into various kinetics models (**Figures C8-C38, Appendix Chapter 4**). The power model described the release of a drug from polymeric system and usually only the beginning of the release is used to model the data. This is due to the assumptions of the model that is applicable to short timespans. Experimental data shows a very close fit both for heparin and rapamycin release at short times of the release (up to 600 h), which agrees with the assumptions of the Power model. To evaluate other possible mechanisms of drug elution from the materials, additional release models were tested.

Hixon-Crowell model describes the drug elution via erosion mechanism therefore experimental data was evaluated for its fit into this model. In this model, the Hixon-Crowell constant (K_{HC}) combines the surface and volume relation [23-34]. Heparin release was not found to closely follow Hixon-Crowell kinetics, and rapamycin release exhibited a closer fit to this profile (**Appendix Chapter 4, Figures C16-C18)**. This suggests that heparin release primary follows the power law which is based on diffusion and dissolution of the polymer matrix. In rapamycin, the release profile was found to fit closely to power model, but additionally to other models such as first-order or Hixon-Crowell model which is erosion based. Furthermore, Weibull model of release was used to fit experimental data and showed a close fit with heparin release. However, this model is empirical and has several limitations such as lack of kinetics fundamental derivations[23-24].

Another kinetics model relevant for fitting into drug release in this study is the Exponential model (Gompertz model). The exponential model describes in-vitro dissolution profile utilizing the equation shown in **Table 4.3**. In this model, α determines the undissolved proportion at time 't = 1' which is also known as a location or scale parameter[23-24]. β parameter from the exponential model corresponds to the dissolution rate per unit of time and describes the shape parameter[23-24]. Heparin release at various star content values in the polymer matrix and rapamycin release were fit utilizing this model. Heparin release showed close fit to the exponential release profile at all conditions suggesting its release mechanism following dissolution. Rapamycin release showed a fit into this model as well heparin (**Appendix Chapter 4**, **Figures C29-C38**)

Combining all the results of mathematical modelling together, heparin release mechanism was found to be a combination of diffusion and dissolution mechanisms, while rapamycin release mechanism was found to be a combination of diffusion and erosion. The parameters of respective release models, together with statistical information on the fitting of our experimental data, are shown in **Appendix Chapter 4** (**Figures C8-C45**).

4.4.7. Degradation

To better understand the degradation behaviour of melt electrowritten scaffolds, we performed accelerated degradation experiments on scaffolds with varying pore size (0.5 mm x 0.5 mm, 1 mm x 1 mm) and number of printed layers (3 layers, 5 layers) (**Figure 4.5, Figure 4.6**). Scaffolds were immersed in 5 M aqueous sodium hydroxide solution (10 mL) at 37 ºC. At designated time points, materials were rinsed with deionized water several times and dried under vacuum for 24 h. The decreasing mass of scaffolds was measured (**Figure 4.5**) and HIM

images of scaffolds and their morphologies were taken using HIM (Zeiss, Germany) (**Figure 4.6**).

Our results showed that scaffolds with smaller number of printed layers (3 layers) degraded faster, as compared to scaffolds with 5 layers. This could be related to lower total mass of scaffolds with 3 layers as competed to scaffolds with 5 layers. PCL degradation takes place through a bulk degradation mechanism rather than surface erosion, and it is often determined by the total mass of the scaffold, as well as the surface area. In the case of this study, we observed that the total mass of the scaffold was the determining factor of the speed of the degradation, as shown by the difference in degradation time between scaffolds with 3 and 5 layers. Scaffolds with 0.5 mm x 0.5mm 5 layers degraded to less than 10 % of initial scaffold

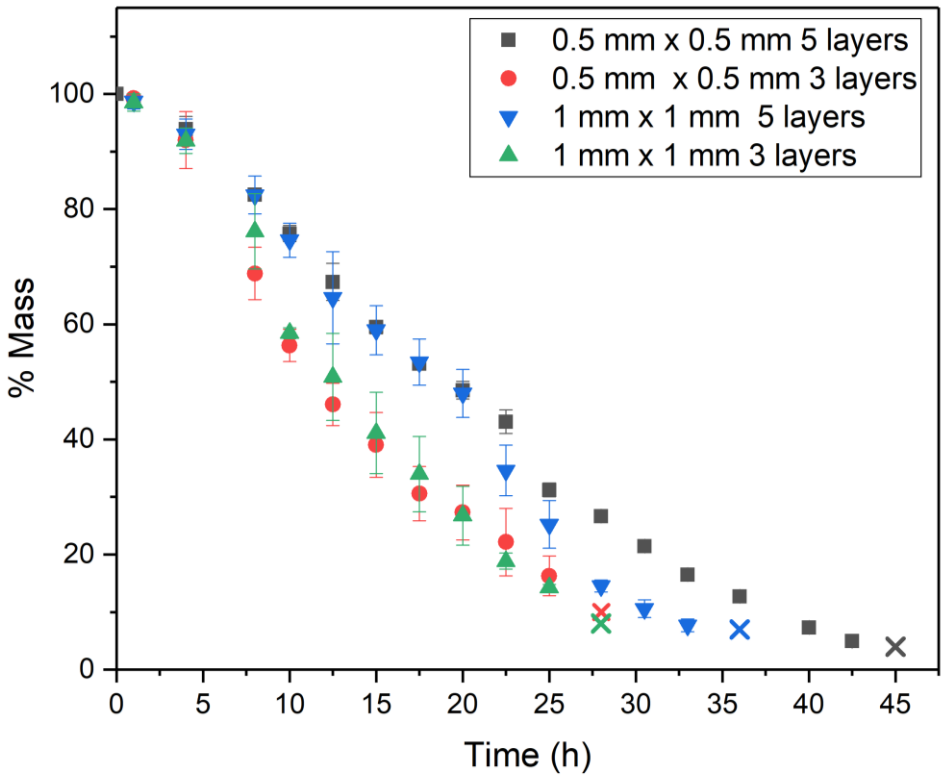

Figure 4.5: Degradation curves for melt electrowritten scaffolds with varying pore size and number of layers. All quantitative data are expressed as mean ± standard deviations with a minimum of n = 3 repeats. X corresponds to the data point at which the scaffold fully degraded into small fibre pieces and mass could not be measured.

mass at approximately 42.5 h of accelerated degradation, while scaffolds with 0.5 mm x 0.5 mm 3 layers degraded to less than 10 % of their initial mass after approximately 27.5 h of accelerated degradation. Similarly, stents with 1 mm x 1mm and 5 layers degraded to less than 10 % of their initial mass after approximately 36 h of accelerated degradation, while devices with 1mm x 1mm and 3 layers degraded to similar mass within 27.5 h of accelerated degradation. It can be also noted that devices with larger pore size (strut spacing) (1 mm x 1mm) degraded faster as compared to scaffolds with smaller pore size (0.5 mm x 0.5 mm). This can be seen by comparing 1mm x 1mm 5-layer degradation time to less than 10 % of scaffolds mass (36 h) to time required for 0.5 mm x 0.5 mm 5-layer scaffold to degrade to similar mass % (27.5 h). Similar trend can be seen between 1 mm x 1mm 3-layer scaffolds and 0.5 mm x 0.5 mm 3-layer scaffolds.

Figure 4.6 shows HIM images of scaffolds at different time intervals during accelerated degradation process. At t = 0 h, structures of printed scaffolds are intact and show no surface defects, with fibre surface showing very little roughness. After 10 h of accelerated degradation, changes can be seen both in terms of fibre roughness and initial loss of integrity of some parts of scaffolds. After 28 h of degradation, major changes in fibre roughness can be seen with surface becoming significantly rougher as compared to initial fibres. Additionally, major defects in the integrity of scaffold structure can be seen. Towards the end of the degradation, after 32 h, more defects can be seen with fibres being degraded and breaking into smaller pieces, as well as surface becoming very rough and degraded.

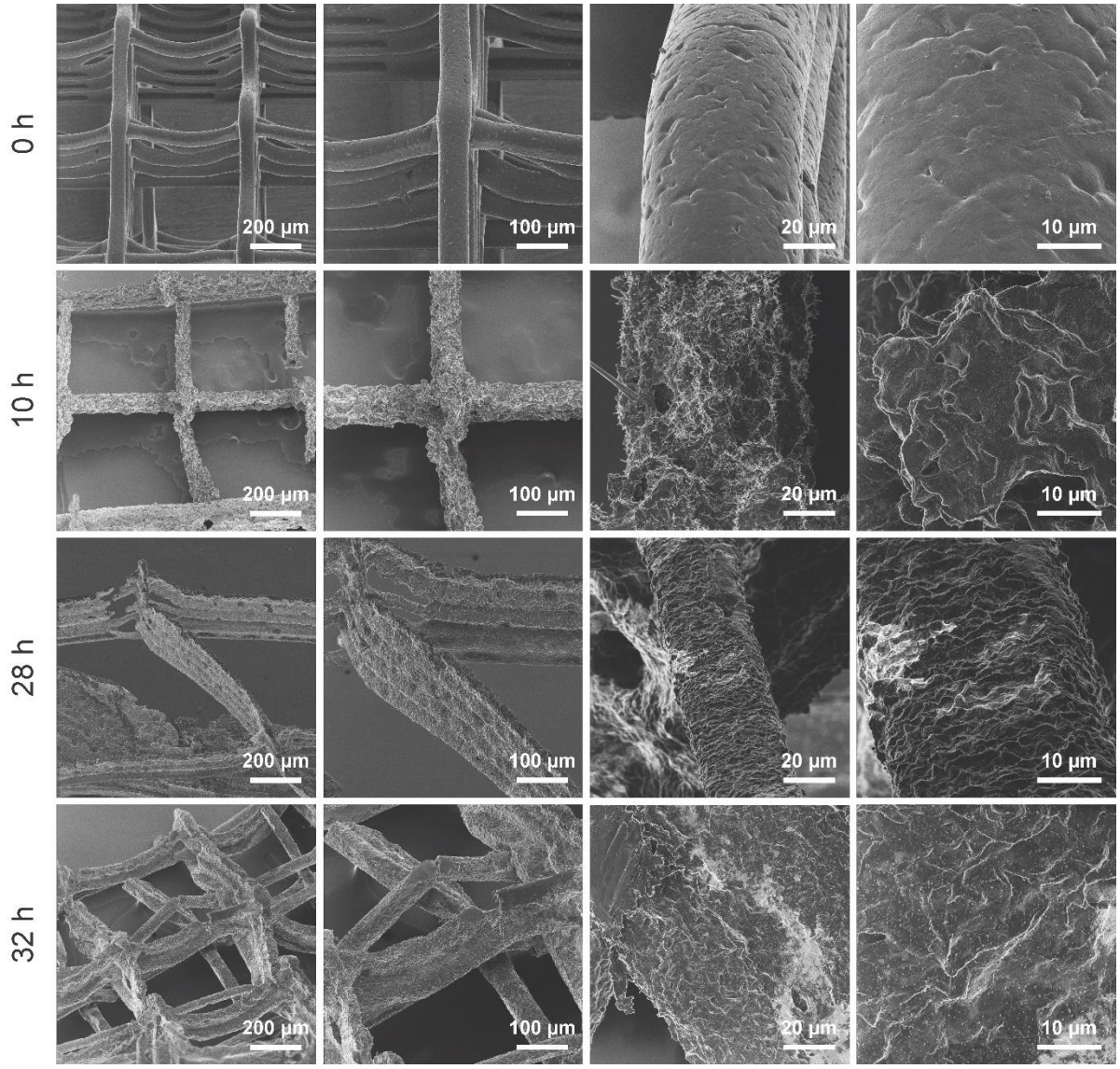

Figure 4.6: Representative images of accelerated scaffold degradation at 0 h, 10 h, 28 h, and 32 h of degradation.

4.4.8. Biological interactions

Fabricated materials were evaluated for the interactions with three different cell types (hUVECs, SMCs, platelets) to better understand the potential of their use in coronary artery stent application.

4.4.8.1. Human umbilical vein endothelial cells

Adhesion and proliferation of hUVECs surfaces with different rations of core-cross linked star polymers (CCS) in PCL and PCL-rGO (0.1 wt%) were studied. Adhesion of cells at day 0 and

proliferation at days 4 and 7 were quantified (**Figure 4.7, Figure 4.8**). No significant difference in cell adhesion was observed at day 0 between surfaces with different CCS content in PCL or PCL/rGO (0.1 wt%) (**Figure 4.8**). In terms of hUVECs proliferation, it was found that proliferation increases with star content in PCL at day 7 and is higher at surfaces with PCL-rGO(0.1 wt%). This agrees with our previous study which reports an increase of hUVECs proliferation at surfaces with rGO (0.1 wt%) content in PCL *(***Chapter 2, Figure 2.11, Figure 2.12**) . Different ratios of star in PCL or PCL-rGO (0.1 wt%) correspond to different hydrophilicity/hydrophobicity of surfaces as with increasing the CCS content in PCL or PCL-rGO(0.1 wt%) matrix, hydrophilicity increases as shown in **Chapter 3**. Also, the composition of material changes as more of PEG based methacrylates is incorporated into the materials with higher star content which affects cell interactions.

Our results show that PCL-rGO(0.1 wt%)-CCS(10 wt%) exhibits the highest proliferation of hUVECs , both at day 4 and day 7, as compared to other materials (**Figure 4.7, Figure 4.8**). This can be related to the highest content of PCL-rGO(0.1 wt%) in the material (90 wt%) as compared to other groups.

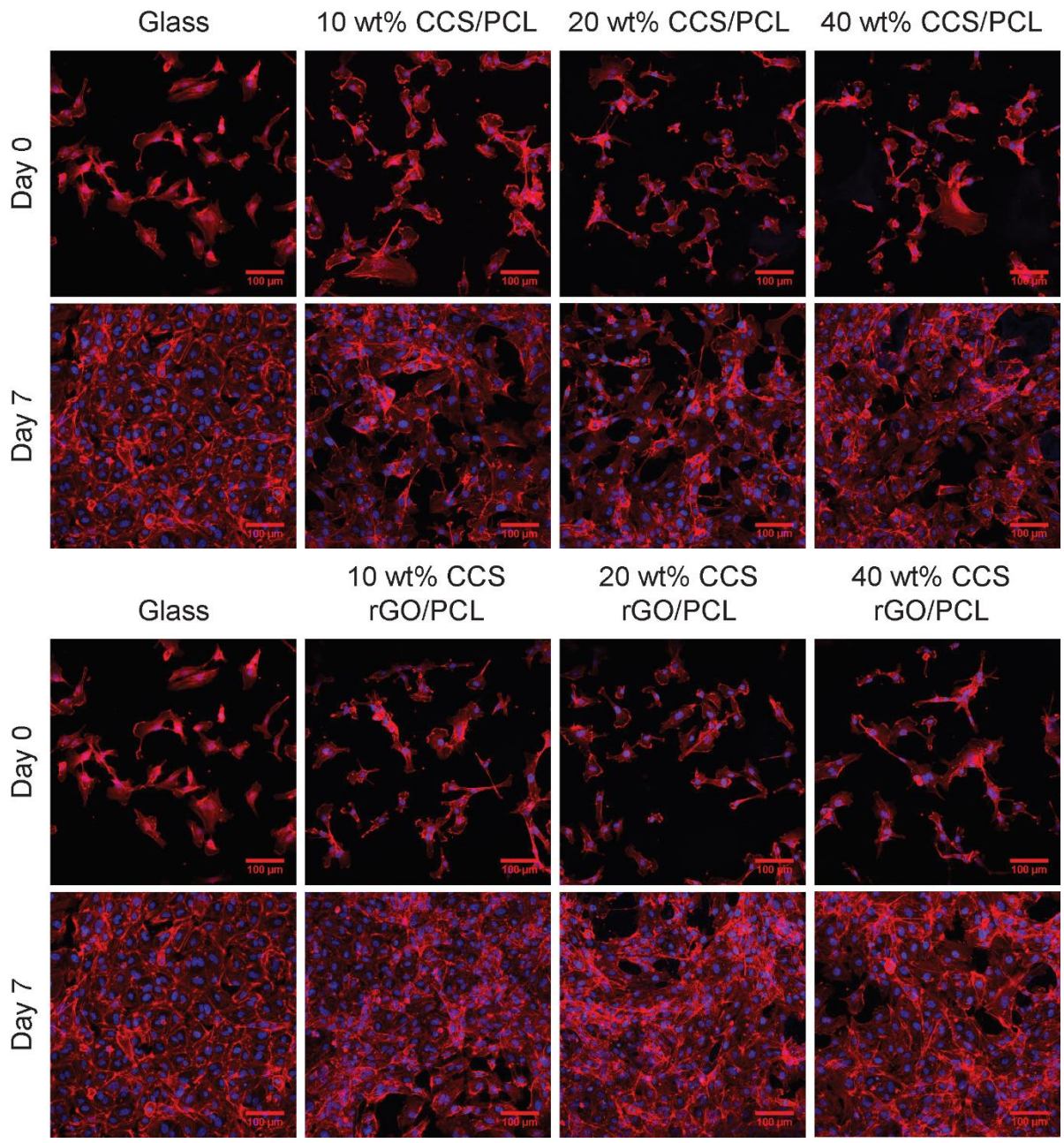

Figure 4.7: Representative images of hUVECS adhesion and proliferation on glass and materials with different CCS content in PCL, and PCL-rGO (0.1 wt%). Scale bars are 100 µm.

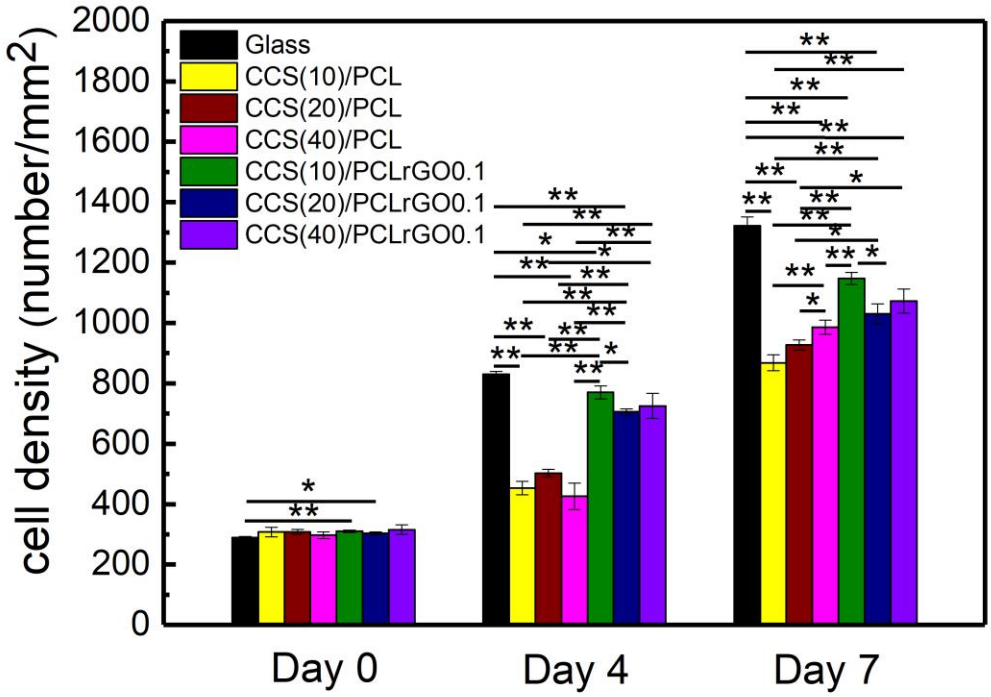

Figure 4.8: Quantification of hUVECs adhesion and proliferation over 7 days of culture. The cells were seeded at a density of 1.7×10^4 cells per cm^2. Asterisks (*) represent statistical difference where **P<0.01 and *P<0.05, (n = 3).

4.4.8.2. Smooth muscle cells

PCL-rGO(0.1 wt%)-CCS(10 wt%) was a material chosen for printing of final devices due to its best mechanical properties as compared to other groups (PCL-rGO(0.1 wt%)-CCS(20 wt%) and PCL-rGO(0.1 wt%)-CCS(40 wt%)), highest hUVECs proliferation at day 4 and 7, and desired rheological behaviour for printing process. SMCs adhesion and proliferation were studied on materials with PCL-rGO(0.1 wt%)-CCS(10 wt%) with rapamycin content of 0 mg, 2.5 mg (rap1) and 5 mg (rap2) in 3 mL of the initial electrospinning solution (**Figure 4.9**). These concentrations correspond to electrospun conditions and solutions used for electrospinning as described in the methods section for Rapamycin coating (Section 4.4.6).

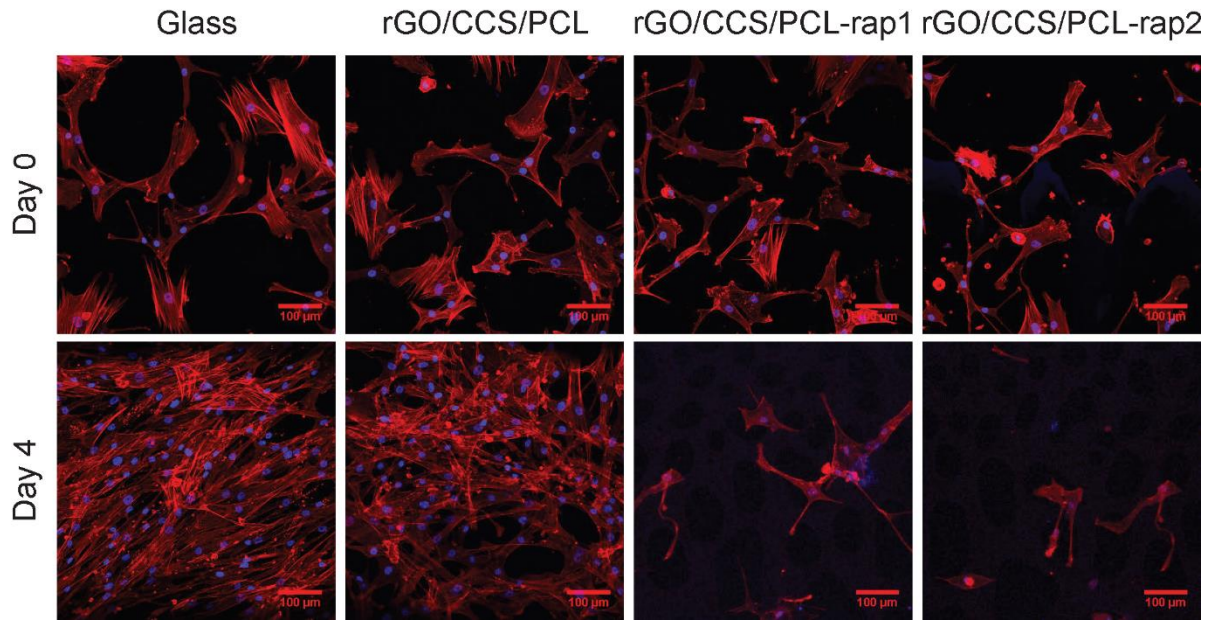

Figure 4.9: Representative images of SMCs adhesion and proliferation on various surfaces over 4 days. Scale bar represents 100 µm. rGO/CCS/PCL-rap1 corresponds to the 0.1 wt% rGO/CCS (10 wt%)/PCL material with 2.5 mg of rapamycin in 3 mL polymer solution in DCM. rGO/CCS/PCL-rap2 corresponds to the starting concentration of 5 mg of rapamycin in 3 mL polymer solution in DCM.

Results indicate that at day 0, rGO/CCS/PCL with highest rapamycin concertation (rapa2) shows decreased smooth muscle cell adhesion. Proliferation of smooth muscle cells was assessed at day 4 and showed significant reduction in cell number for materials with rapamycin (rGO/CCS/PCL-rap1 and rGO/CCS/PCL-rap2). Both materials, which had varying concentration of rapamycin, showed significant reduction in smooth muscle cell proliferation and confirmed the activity of the drug as well as its local dosing (**Figure 4.9, Figure 4.10**). Our results suggest that our chosen dosing for electrospun outer layer is efficient in decreasing the smooth muscle cell proliferation which confirms the activity of the drug. Inhibition of smooth muscle cell proliferation is critical in prevention of in-stent restenosis (re-narrowing of the artery despite of use of stent).

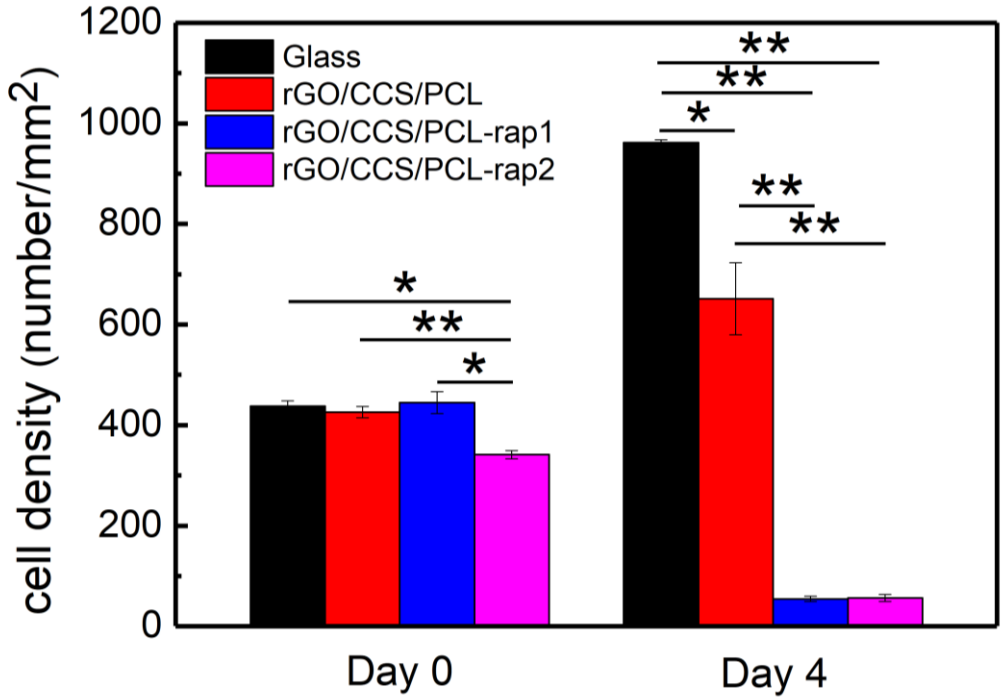

Figure 4.10: Quantification of SMCs adhesion and proliferation over 4 days of culture. The cells were seeded at a density of 1.7×10^4 cells per cm^2. rGO/CCS/PCL-rap1 corresponds to the 0.1 wt% rGO/CCS (10 wt%)/PCL material with 2.5 mg of rapamycin in 3 mL polymer solution in DCM. rGO/CCS/PCL-rap2 corresponds to the starting concentration of 5 mg of rapamycin in 3 mL polymer solution in DCM. Asterisks (*) represent statistical difference where **P<0.01 and *P<0.05 (n = 3).

4.4.8.3. Platelet adhesion

Platelet adhesion was assessed on materials with varying star content in PCL-rGO (0.1 wt%). Platelet adhesion was a very important aspect of a material's behaviour as it correlated to its thrombogenicity. In this study, we embedded heparin loaded stars into the polymer matrix and studied the platelet adhesion upon contact with the materials. Our results showed decreased platelet adhesion in all groups, as compared to pure PCL-rGO (0.1 wt%) studied in the previous part of this study (**Chapter 2**). The decrease was from approximately 2×10^{-4} adhered platelets per μm^2 of PCL-rGO (0.1 wt%) surface to approximately 1×10^{-4} adhered platelets per μm^2 on PCL-rGO(0.1 wt%)-CCS(10 wt%) and PCL-rGO (0.1 wt%)-CCS(20 wt%), and 9×10^{-5} adhered platelets per μm^2 on PCL-rGO(0.1 wt%)-CCS(40 wt%). Additionally, our results show

that at high star concentrations (40 wt%) in PCL-rGO (0.1 wt%), platelet adhesion decreased relative to low concentrations (10 wt%). (**Figure 4.11, Figure 4.12**). This reduction in platelet number was found to be statistically significant between CCS(10 wt%)/PCL-rGO (0.1 wt%) and CCS(40 wt%)/PCL-rGO(0.1 wt%) groups.

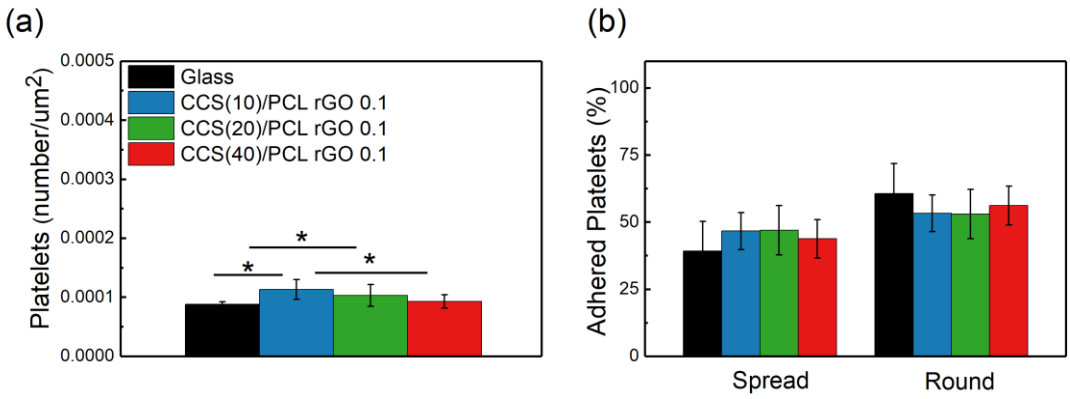

Figure 4.11: (a) Platelet adhesion on glass, PCL-rGO(0.1 wt%)-heparin loaded CCS(10 wt%), PCL-rGO(0.1 wt%)-heparin loaded CCS(20 wt%), and PCL-rGO(0.1 wt%)- heparin loaded CCS(40 wt%). (b) Morphology of adhered platelets on glass, PCL-rGO(0.1 wt%)-CCS(10 wt%), PCL-rGO(0.1 wt%)-CCS(20 wt%), and PCL-rGO(0.1 wt%)-CCS(40 wt%). Asterisks (*) represent statistical difference where **P<0.01 and *P<0.05, (n = 3).

Additionally, the shape and morphology of platelets were evaluated on different surfaces to better understand the influence of heparin elution on platelet morphology and activation (**Figure 4.11b, Figure 4.12).** Our data has shown that there was no significant difference between the materials with varying star content in PCL-rGO (0.1 wt%) matrix in terms of platelet morphology. The number of spread platelets and round platelets was found to not be statistically different.

.

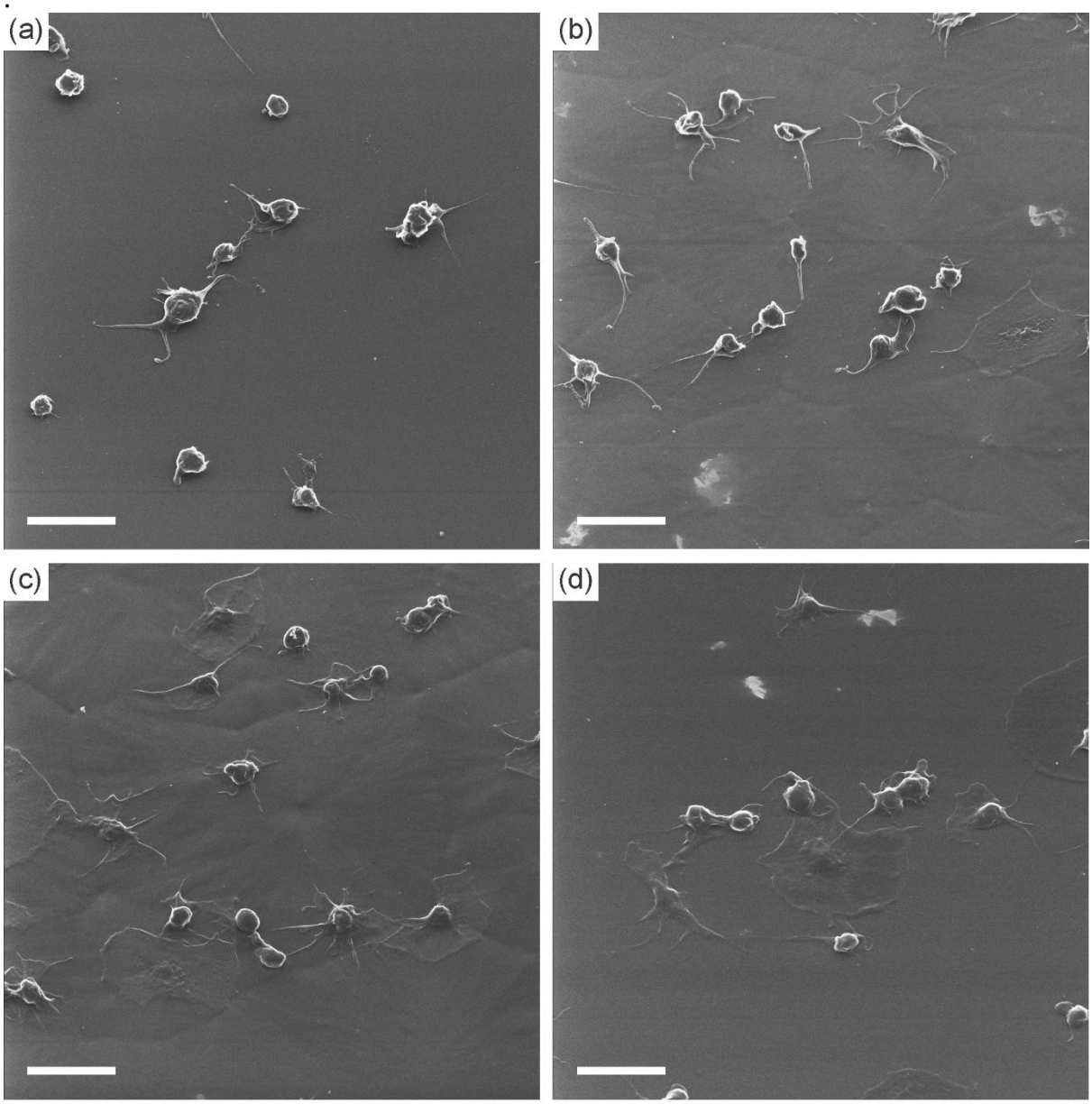

Figure 4.12: Representative images of platelet adhesion on (a) glass (b) PCL-rGO(0.1 wt%)-CCS(10 wt%) (c) PCL-rGO(0.1 wt%)-CCS(20 wt%) (d) PCL-rGO(0.1 wt%)-CCS(40 wt%). Scale bars are 5µm.

4.5. Conclusion

In conclusion, this study shows the development of PCL/rGO/CCS multi-drug eluting materials and their processing utilizing MEW. Previously synthesized CCSs, which are comprised of PCL outer block, inner PEG MEA brush, and core-cross linked PEGDA core, were heparin loaded and embedded into PCL-rGO (0.1 wt%) matrix. Synthesized materials were evaluated in terms of their printability, mechanics, rheology, crystallinity, thermal behaviour, degradation, drug elution and biological interactions. Our mechanical results illustrate that addition of CCS into PCL-rGO(0.1 wt%) matrix at a low star concentration (10 wt%) had a less profound effect on the material's compressive and tensile performance as compared to higher concentrations (20 wt%, 40 wt%). A decrease was observed in the compressive and tensile Young's Modulus at higher stat content (40 wt%). Dual drug elution of heparin and rapamycin was studied at pH = 7.4 and pH = 5, and results showed controlled release of both rapamycin and heparin. Materials were studied for their interaction with three types of cells: hUVECs, SMCs and platelets. Results showed that hUVECs proliferation was the highest on materials with CCS embedded in PCL-rGO (0.1wt%), as compared to materials embedded in PCL. PCL-rGO(0.1 wt%)-CCS(10 wt%) was found to have the highest proliferation of hUVECs at day 4 and 7. Smooth muscle cell adhesion and proliferation was studied on materials with varied rapamycin content in PCL. Results illustrated that rapamycin coating decreases smooth muscle cells and confirmed both activity and dosing of a drug. Incorporation of heparin loaded CCS into PCL-rGO (0.1 wt%) was found to decrease platelet adhesion, as compared to PCL-rGO (0.1 wt%) and was shown to decrease with increasing heparin-star content in PCL-rGO (0.1 wt%).

4.6. References

1. McAloon, C. J.; Boylan, L. M.; Hamborg, T.; Stallard, N.; Osman, F.; Lim, P. B.; Hayat, S. A., The changing face of cardiovascular disease 2000-2012: An analysis of the world health organisation global health estimates data. *Int J Cardiol* **2016,** *224*, 256-264.

2. Ho, M.-Y.; Chen, C.-C.; Wang, C.-Y.; Chang, S.-H.; Hsieh, M.-J.; Lee, C.-H.; Wu, V.; Hsieh, I. C., The Development of Coronary Artery Stents: From Bare-Metal to Bio-Resorbable Types. *Metals* **2016,** *6* (7).

3. Foin, N.; Lee, R. D.; Torii, R.; Guitierrez-Chico, J. L.; Mattesini, A.; Nijjer, S.; Sen, S.; Petraco, R.; Davies, J. E.; Di Mario, C.; Joner, M.; Virmani, R.; Wong, P., Impact of stent strut design in metallic stents and biodegradable scaffolds. *Int J Cardiol* **2014,** *177* (3), 800-8.

4. Kalra, A.; Rehman, H.; Khera, S.; Thyagarajan, B.; Bhatt, D. L.; Kleiman, N. S.; Yeh, R. W., New-Generation Coronary Stents: Current Data and Future Directions. *Curr Atheroscler Rep* **2017,** *19* (3), 14.

5. Jinnouchi, H.; Torii, S.; Sakamoto, A.; Kolodgie, F. D.; Virmani, R.; Finn, A. V., Fully bioresorbable vascular scaffolds: lessons learned and future directions. *Nat Rev Cardiol* **2019,** *16* (5), 286-304.

6. Sotomi, Y.; Suwannasom, P.; Serruys, P. W.; Onuma, Y., Possible mechanical causes of scaffold thrombosis: insights from case reports with intracoronary imaging. *EuroIntervention* **2017,** *12* (14), 1747-1756.

7. Sotomi, Y.; Onuma, Y.; Collet, C.; Tenekecioglu, E.; Virmani, R.; Kleiman, N. S.; Serruys, P. W., Bioresorbable Scaffold: The Emerging Reality and Future Directions. *Circ Res* **2017,** *120* (8), 1341-1352.

8. Ishibashi, Y.; Onuma, Y.; Muramatsu, T.; Nakatani, S.; Iqbal, J.; Garcia-Garcia, H. M.; Bartorelli, A. L.; Whitbourn, R.; Abizaid, A.; Serruys, P. W.; Investigators, A. E., Lessons

learned from acute and late scaffold failures in the ABSORB EXTEND trial. *EuroIntervention* **2014,** *10* (4), 449-57.

9. Hoshi, R. A.; Van Lith, R.; Jen, M. C.; Allen, J. B.; Lapidos, K. A.; Ameer, G., The blood and vascular cell compatibility of heparin-modified ePTFE vascular grafts. *Biomaterials* **2013,** *34* (1), 30-41.

10. Begovac, P. C.; Thomson, R. C.; Fisher, J. L.; Hughson, A.; Gallhagen, A., Improvements in GORE-TEX vascular graft performance by Carmeda BioActive surface heparin immobilization. *Eur J Vasc Endovasc Surg* **2003,** *25* (5), 432-7.

11. Hanßke, F.; Bas, O.; Vaquette, C.; Hochleitner, G.; Groll, J.; Kemnitz, E.; Hutmacher, D. W.; Börner, H. G., Via precise interface engineering towards bioinspired composites with improved 3D printing processability and mechanical properties. *Journal of Materials Chemistry B* **2017,** *5* (25), 5037-5047.

12. Zhu, Y.; Edmonds, L.; Zhao, X.; Chen, X.; Hu, C.; Cheng, Y.; Cui, W., In vitro and in vivo evaluation of Rapamycin-eluting nanofibers coated on cardia stents. *RSC Adv.* **2014,** *4* (65), 34405-34411.

13. Klein M., D. R., Linhardt R., Langer R., A colorimetric assay for chemical heparin in plasma. *Analytical Biochemistry* **1982,** *124*.

14. Kamiński, K.; Kałaska, B.; Koczurkiewicz, P.; Michalik, M.; Szczubiałka, K.; Mogielnicki, A.; Buczko, W.; Nowakowska, M., New arginine substituted derivative of poly(allylamine hydrochloride) for heparin reversal. *MedChemComm* **2014,** *5* (4).

15. Kalaska, B.; Kaminski, K.; Sokolowska, E.; Czaplicki, D.; Kujdowicz, M.; Stalinska, K.; Bereta, J.; Szczubialka, K.; Pawlak, D.; Nowakowska, M.; Mogielnicki, A., Nonclinical evaluation of novel cationically modified polysaccharide antidotes for unfractionated heparin. *PLoS One* **2015,** *10* (3), e0119486.

16. Salamat-Miller, N.; Fang, J.; Seidel, C. W.; Smalter, A. M.; Assenov, Y.; Albrecht, M.; Middaugh, C. R., A network-based analysis of polyanion-binding proteins utilizing yeast protein arrays. *Mol Cell Proteomics* **2006,** *5* (12), 2263-78.

17. Han, J.; Farah, S.; Domb, A. J.; Lelkes, P. I., Electrospun rapamycin-eluting polyurethane fibers for vascular grafts. *Pharm Res* **2013,** *30* (7), 1735-48.

18. Lam, C. X.; Savalani, M. M.; Teoh, S. H.; Hutmacher, D. W., Dynamics of in vitro polymer degradation of polycaprolactone-based scaffolds: accelerated versus simulated physiological conditions. *Biomed Mater* **2008,** *3* (3), 034108.

19. Karimi, F.; Thombare, V. J.; Hutton, C. A.; O'Connor, A. J.; Qiao, G. G.; Heath, D. E., Beyond RGD; nanoclusters of syndecan- and integrin-binding ligands synergistically enhance cell/material interactions. *Biomaterials* **2018,** *187*, 81-92.

20. Karimi, F.; McKenzie, T. G.; O'Connor, A. J.; Qiao, G. G.; Heath, D. E., Nano-scale clustering of integrin-binding ligands regulates endothelial cell adhesion, migration, and endothelialization rate: novel materials for small diameter vascular graft applications. *Journal of Materials Chemistry B* **2017,** *5* (30), 5942-5953.

21. Im, E.; Hong, M. K., Drug-eluting stents to prevent stent thrombosis and restenosis. *Expert Rev Cardiovasc Ther* **2016,** *14* (1), 87-104.

22. Iqbal, J.; Gunn, J.; Serruys, P. W., Coronary stents: historical development, current status and future directions. *Br Med Bull* **2013,** *106*, 193-211.

23. Baishya, H., Application of Mathematical Models in Drug Release Kinetics of Carbidopa and Levodopa ER Tablets. *Journal of Developing Drugs* **2017,** *06* (02).

24. Fu, Y.; Kao, W. J., Drug release kinetics and transport mechanisms of non-degradable and degradable polymeric delivery systems. *Expert Opin Drug Deliv* **2010,** *7* (4), 429-44.

25. 5 - Mathematical models of drug release. In *Strategies to Modify the Drug Release from Pharmaceutical Systems*, Bruschi, M. L., Ed. Woodhead Publishing: 2015; pp 63-86.

26. Siepmann, J.; Siepmann, F., Mathematical modeling of drug delivery. *Int J Pharm* **2008,** *364* (2), 328-43.

27. Lisik, A.; Musial, W., Conductomeric Evaluation of the Release Kinetics of Active Substances from Pharmaceutical Preparations Containing Iron Ions. *Materials (Basel)* **2019,** *12* (5).

28. Gore Medical Acuseal Vascular Graft Properties. https://www.goremedical.com/resource/AQ0107-EN5.

5. Conclusions and Future Perspectives

5.1. Thesis conclusions

This thesis reports the design and development of biodegradable, multi-drug eluting, customized vascular scaffold for application as a coronary artery stent. Additive manufacturing technique (MEW) was utilized to fabricate vascular scaffolds with varying designs and with the use graphene-based PCL composite as a printing ink. UV-ATRP polymerization and ROP polymerization were used to synthesize a class of star-brush polymers composed of hydrophilic PEGDA inner cores, hydrophilic PEG MEA inner brush-shells, and hydrophobic PCL outer arms. Synthesized polymers were evaluated for their drug loading and release properties of two antithrombotic drugs (dextran and heparin). These CCSs were incorporated into rGO-PCL nanocomposite and the materials were evaluated for their printability, drug-elution, mechanical performance, rheology, thermal and crystallinity, as well as biological interactions with three types of cells (hUVECs, SMCs, platelets) and proteins.

The first experimental part of this thesis (**Chapter 2**) presents the use of MEW to fabricate customized scaffolds composed of PCL/rGO with varying degree of curvature, design, diameter, pore size (strut spacing) and thickness (number of printed layers). The second part (**Chapter 3**) illustrates the synthesis of star-brush polymers with varying PEG brush length, cross-linker amount, and PCL length and their evaluation for drug loading and release of anti-thrombotic drugs. The last part (**Chapter 4)** presents the processing of biodegradable multi-drug eluting PCL/rGO/CCS material with focus on its mechanical, thermal, crystallinity, rheological, biological, degradation and drug-elution characterization.

In **Chapter 2**, biodegradable reduced graphene-oxide polycaprolactone stents were developed by utilization of MEW technology. Materials and scaffolds were characterized in terms of their

mechanics, rheology, crystallinity, thermal behaviour, and biological performance. Our mechanical tests showed an increase in Young's Modulus after incorporation of rGO into PCL by approximately 2 folds for PCL-rGO 0.1, 0.3, 0.6 and 1 wt%, as compared to PCL. Compression tests illustrated an increase in Compressive Young's Modulus of more than 1 fold for all PCL-rGO groups, as compared to PCL. Our tensile tests on PCL-rGO 0.1 wt% melt electrowritten fibers showed an increase of approximately 2 folds in Young's Modulus as compared to PCL melt electrowritten fibers. Thermal analysis showed no significant differences in thermal behaviour and degradation temperatures of PCL and PCL-rGO (0.1 wt%) before and after processing. Crystallinity studies showed an increase in the degree of crystallinity of PCL-rGO (0.1 wt%) compared to PCL. The results showed no significant difference in melting temperatures of PCL-rGO (0.1 wt%) and PCL before printing, however, a decrease in melting temperature of PCL-rGO (0.1 wt%) after printing. Moreover, a class of customized PCL-rGO 0.1 wt% stents have been fabricated using MEW system with varying pore size (strut spacing), diameter, strut thickness and architecture. Additionally, hUVECs cell culture was performed on PCL, PCL-rGO 0.1 and 0.3 wt% and demonstrated an increase in cell proliferation after incorporation of rGO into PCL which could potentially lead to better endothelialisation of a stent in-vivo, less thrombogenicity and better biological performance. Protein adsorption studies were performed on materials with varying content of rGO in PCL (0.1 wt% and 0.3 wt%) and revealed an increase in protein adsorption after incorporation of rGO into PCL. Platelet adhesion study revealed an increase of spread-like platelets on materials with the highest rGO content in PCL (0.3 wt%), as compared to PCL, suggesting activation of platelets. This study was the first to report the use of the MEW technique for fabrication of biodegradable coronary artery stents.

In **Chapter 3**, CCSs were synthesized via UV-ATRP and ROP polymerization. Synthesized CCSs exhibited hydrophobic PCL blocks in their outer shell, PEG MEA segments in their inner

brush shell and hydrophilic PEGDA in their cores. A class of stars and brushes was synthesized with varying PEG brush length, core-size (PEGDA amount), and PCL length to better understand the optimal conditions for synthesis of stars with low polydispersity (PDI) and high star conversion. These polymeric platforms were investigated for drug loading and release of two antithrombotic drugs (dextran, heparin). Drug loading study of fluorescent dextran and heparin demonstrated drug loading efficiencies of approximately 70 % for dextran and 50 % for heparin. Drug release profiles were obtained at physiological (pH = 7.4) and acidic (pH = 5) conditions. The release study showed controlled drug release of both heparin and dextran over time. Biocompatibility of synthesized CCSs was assessed through the cytotoxicity studies on human umbilical vein endothelial cells (hUVECs) and showed that synthesized stars are not cytotoxic. Proliferation and adhesion studies of HUVECs were performed on synthesized surfaces with varying ratios of CCSs in PCL and showed no difference in cell adhesion between groups and an increase of hUVECs proliferation with the increase of CCSs content in PCL matrix. These results illustrated that synthesized systems are easily tailorable for desired application and can be used as drug delivery platforms for anti-thrombotic drugs.

Finally, in **Chapter 4** previously synthesized CCSs polymers were incorporated into PCL/rGO matrix to fabricate a multi-drug eluting biodegradable material and assess its printability via MEW. The final material composed of heparin loaded CCS/rGO/PCL in a bulk and Rapamycin/PCL outer layer deposited via electrospinning. Materials were investigated in terms of their printability using MEW, mechanical performance, rheology, crystallinity, thermal behaviour, and biological interactions with three different cell types (hUVECs, SMCs, platelets). Results indicated that at lower CCS content in PCL/rGO matrix (10 wt%), less significant effect on mechanical properties was observed, as compared to higher concentrations (20 wt%, 40 wt%). At higher CCS loading (20 wt%, 40 wt%), more profound decrease in

tensile and compressive moduli was observed. Dual drug elution of heparin and rapamycin was studied at physiological (pH = 7.4) and acidic conditions (pH = 5). Adhesion and proliferation of hUVECs on materials with different CCSs ratio in PCL and PCL-rGO was studied and showed highest proliferation on materials with CCSs embedded in PCL-rGO at low CCS content (10 wt%). Additionally, the interaction of SMCs with materials containing rapamycin was investigated. Rapamycin coating was found to decrease SMCs proliferation and confirmed the activity as well as local dosing of the drug. Platelet adhesion and morphology studies were performed on materials with varying CCS ratio in PCL-rGO and revealed that incorporation of heparin loaded-CCSs decreased platelet adhesion with increasing CCS content. These results confirmed the feasibility of fabrication of multi-drug eluting biodegradable stent and illustrate that increasing star content has an impact on mechanical and biological performance. Additionally, these results confirmed that controlled dual drug elution can be achieved via incorporation of heparin-loaded stars into the bulk of the material and electrospinning of rapamycin as an outer layer on the material.

Taken together, these studies illustrate the development of a prototype of a biodegradable multi-drug eluting vascular scaffold for application as a coronary artery stent. A novel fabrication technique was utilized for the fabrication of biodegradable stents and allowed us to fabricate customized stents with a varying degree of curvature, design, diameter and strut thickness as low as 60 µm. Materials with varying ratio of rGO in PCL were evaluated in terms of their mechanical performance, rheology, thermal behaviour, crystallinity and biological interactions. We then designed and optimized the star synthesis pathway for synthesis of well-defined delivery systems and evaluated them for drug-release profiles. These delivery systems composed of outer hydrophobic PCL layer, and inner hydrophilic PEG based brush and hydrophilic PEGDA core. Synthesized systems were evaluated for their drug loading and

release properties of two antithrombotic drugs. Additionally, biocompatibility, adhesion and proliferation of hUVECs, while in contact with synthesized materials, was studied. Finally, we combined heparin loaded synthesized systems with PCL-rGO based nanocomposite to develop materials with enhanced mechanical properties and drug-eluting properties from the bulk of the material. Following that, we incorporated additional drug (rapamycin) via electro spraying as an outer layer coating. Dual drug elution from materials was evaluated and the most optimal ratio of star content in PCL/rGO matrix was found. Materials exhibited controlled release of anti-proliferative drug (rapamycin) and slower release of anti-coagulant (heparin). The study confirmed our hypothesis that by incorporation of heparin loaded systems into the hydrophobic matrix, a slow controlled release of heparin from the bulk of the material would take place. Additionally, by electropsraying of rapamycin/PCL as an outer layer, a controlled release of rapamycin was enabled. These results demonstrate that fabricated materials show potential for the use as coronary artery stents, however, further drug release studies under flow and *in-vivo* tests of materials are required.

5.2. Future perspectives

The results obtained in this thesis demonstrated development of biodegradable multi-drug eluting vascular scaffold for application as a coronary artery stent. Further work to translate this study into a commercial device and improve the technology could follow the below approaches.

In **Chapter 2**, scaffolds were fabricated utilizing a research grade PCL rather than clinical (medical) grade mPCL which differs in molecular weight, crystallinity and feasibility of clinical translation. Switching from research grade PCL into the medical grade PCL could be undertaken to facilitate translation from the laboratory to the clinic. Additionally, fabricated stents and materials were characterized in terms of tensile, compressive and flexural stiffness. An important test to be performed on fabricated scaffolds would be a radial compression test.

This characterization technique requires specialized equipment for testing of stents, which unfortunately was not available to us. Additionally, mechanical stability tests during degradation could be undertaken to provide insights on mechanical strength as a function of degradation time. Modelling tests could be performed to assess how thin struts could be fabricated based on available experimental data, and how this would correlate to commercial scaffolds such as BVS. Further studies to evaluate the *in-vivo* performance of fabricated stents should be explored. A pivot study on the biodistribution and degradation of stents could be performed in small animals (e.g., mice) to better understand the degradation mechanism of devices and biodistribution of graphene. Based on the results of the study, more detailed animal tests in larger animals (e.g., pigs) would be crucial to evaluate the behaviour of a device. Also, other carbon-based reinforcing additives (e.g., carbon nanotubes) or not carbon based (e.g., ions, nanofillers) could be evaluated for their influence on mPCL in terms of mechanical, rheology, thermal, crystallinity and biological performance. As of now, not many carbon-based nanocomposites were studied in terms of their printability utilizing MEW, therefore, studies with other nanofillers embedded in PCL could be undertaken.

In **Chapter 3**, star-brush polymers were synthesized which compromise of a PCL outer block, a PEG MEA inner brush and a PEGDA core. The study investigated the influence of a PEG brush, PEGDA amount, and PCL length on formation of a star-brush polymers, however, the study was limited to PEG based materials in their inner core and brush. Investigation of more broad range of materials such as PAMAM or PNIPAM as inner structures could lead to a broader range of synthesized polymers. This could require changes in synthesis pathway, however, investigation of these two polymers could enable enhancement in loading and release profiles. Both PAMAM and PNIPAM are cationic polymers, therefore, their incorporation into the core of star polymers could enhance the loading of heparin or other anionic drugs. Our

study showed the basic synthesis pathway of a system composed of hydrophobic outer layer-hydrophilic brush - hydrophilic core. Introduction of ionic, or more hydrophilic/hydrophobic spacers into the core could enable broader drug loading and release studies. Further studies to confirm the dosing of heparin *in-vivo* would be required to better understand the therapeutic value of eluted drug when delivered locally from a scaffold Additionally, investigation of synthesized stars as contrast agent loading molecules could be conducted. Providing radiopacity to the biodegradable implant is a current limitation in the field of biodegradable stents, therefore loading of synthesized stars with contrast agents and evaluating their loading and release profiles could be undertaken.

In **Chapter 4**, synthesized star-brush polymers were incorporated into PCL/rGO matrix and evaluated in terms of their printability, mechanical performance, rheology, thermal, crystallinity and biological interactions. Animal studies with fabricated scaffolds *in-vivo* could be performed to better understand the behaviour of the scaffold upon implantation and its long-term safety *in vivo*. Similarly, to **Chapter 2**, mechanical testing with stent specific equipment (e.q radial compression system) as well as mechanical stability testing during degradation should be performed to better evaluate the mechanical performance of devices. More comprehensive studies on dosing of eluted drugs as well as their therapeutic efficacy after processing would be required. Drug elution studies in conditions closer to human physiology (e.g., under flow) should be undertaken to better approximate actual amounts of eluted drugs. Additionally, more comprehensive studies on degradation of printed scaffolds could be performed. These could include more in depth studies on the influence of degradation on mechanical performance at various stages of the degradation, variability in scaffolds design and its influence on degradation, and different degradation conditions such as degradation under flow.

Our results showed activity of heparin while interacting with platelets, and activity of rapamycin while interacting with smooth muscle cells. However, these studies were performed *in-vitro*, and therapeutically applicable local dosing *in-vivo* would need to be established. Additionally, stability of the materials and drugs during degradation, both in terms of mechanical performance and biological activity, would need to be evaluated to ensure that drugs are stable and active within the desired timeframes.

The materials and scaffolds we designed and fabricated in this thesis were useful platforms for evaluation of materials properties and their printability. Further studies utilizing clinical grade materials (mPCL) are necessary to fully understand the potential of the MEW technology for fabrication of stents in the clinical application. Additionally, stability of fabricated devices during degradation as well as radial compressive performance would be crucial to evaluate. Similarly, *in-vivo* stability of synthesized materials (star-brush polymers) would need to be evaluated to better understand the behaviour of the materials while implanted in the body. Synthesized star polymers were compromised of PEG derivatives and stability of them in-vivo is yet to be understood. Finally, *in-vivo* tests in small animals should be performed to evaluate safety, degradation, and drug elution of devices.

Appendices

A. Chapter 2 Appendix

Table A.1: Protein adsorption on PCL, PCL-rGO (0.1 wt%), and PCL-rGO (0.3 wt%).

Material	Serum ΔF (Hz)
PCL	-29.9 ± 0.4
PCL-rGO (0.1 wt%)	-33.2 ± 0.2
PCL-rGO (0.3 wt%)	-40.0 ± 0.1

Supplementary files: Videos of three-point bending tests on printed scaffolds

These videos show three-point bending tests on printed stents with varying number of layers, pore size and stent-geometry.

Video A1 – 20le 0.5-0.5PS 3l s1 run1.wmv

Video A1 shows the three-point bending test on the printed scaffold with 0.5 x 0.5 mm pore size and 3 printed layers.

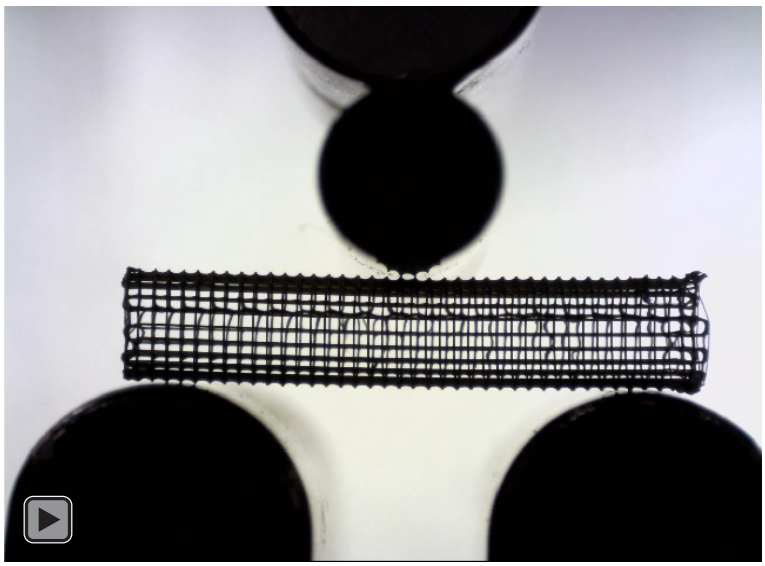

Video A2 - 20le 0.5-0.5PS 5l s1.wmv.wmv

Video A2 shows the three-point bending test on the printed scaffold with 0.5 x 0.5 mm pore size and 5 printed layers.

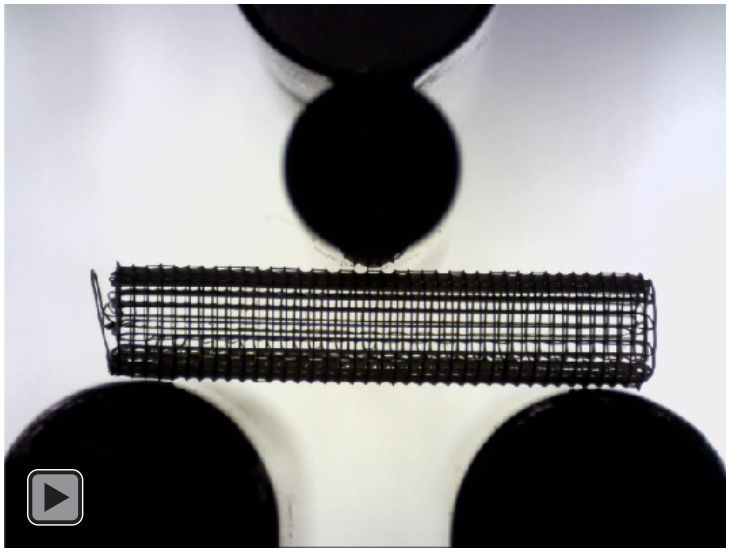

Video A3 - 20le 1-1PS 3l s1 run1.wmv

Video A3 shows the three-point bending test on the printed scaffold with 1 x 1 mm pore size and 3 printed layers.

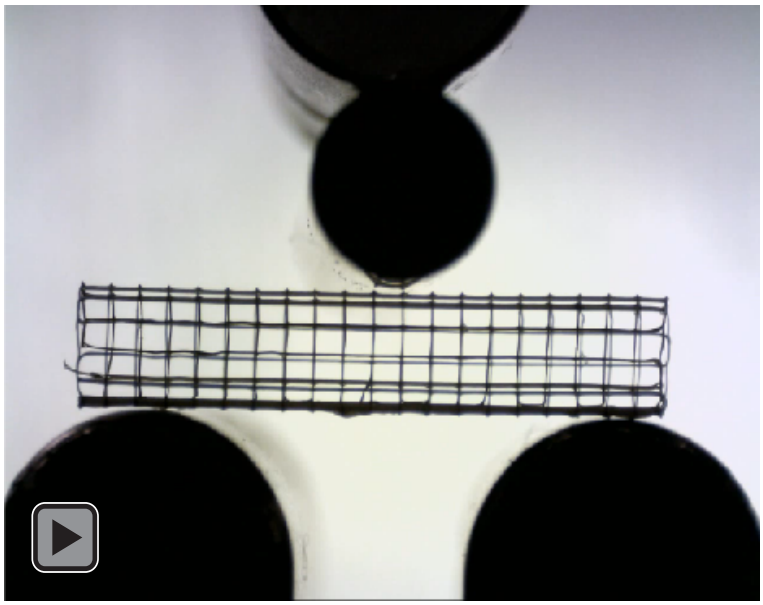

Video A4 - 20le 1-1PS 5l s2 run1.wmv

Video A4 shows the three-point bending test on the printed scaffold with 1 x 1 mm pore size and 5 printed layers.

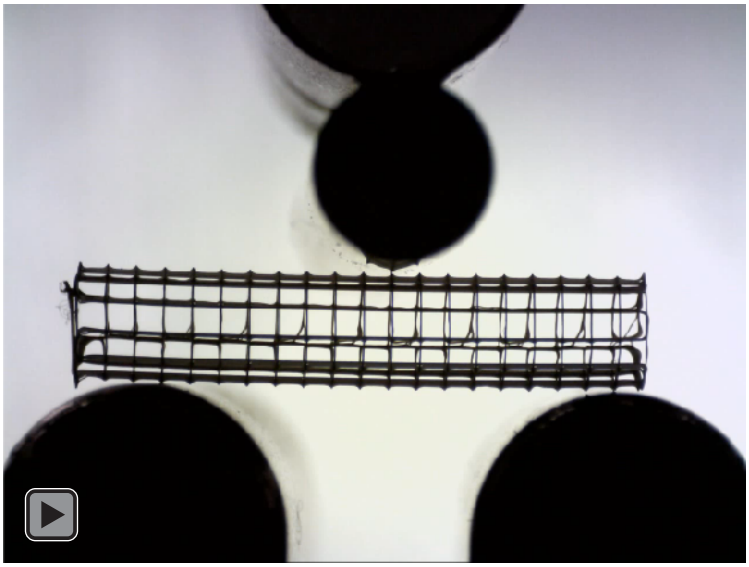

B. Chapter 3 Appendix

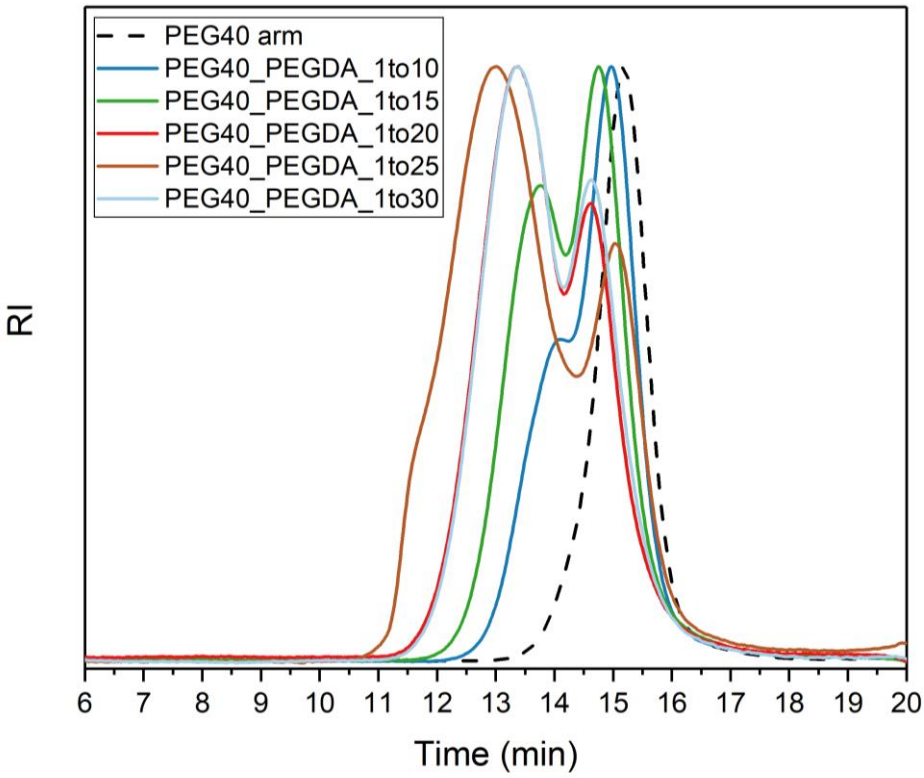

Figure B. 1: DMF GPC spectra of CCS-OH formed from PEG-40 arm with varying ratio of cross linker (PEG–diacrylate) to PEG brush (PEG40). PEG40 was used as a precursor brush and cross-linked with PEG diacrylate (PEGDA, MW=250 Da) at the ratios of PEF brush (PEG 40) : PEDGA (cross linker): 1:10, 1:15, 1:20, 1:25, 1:30.

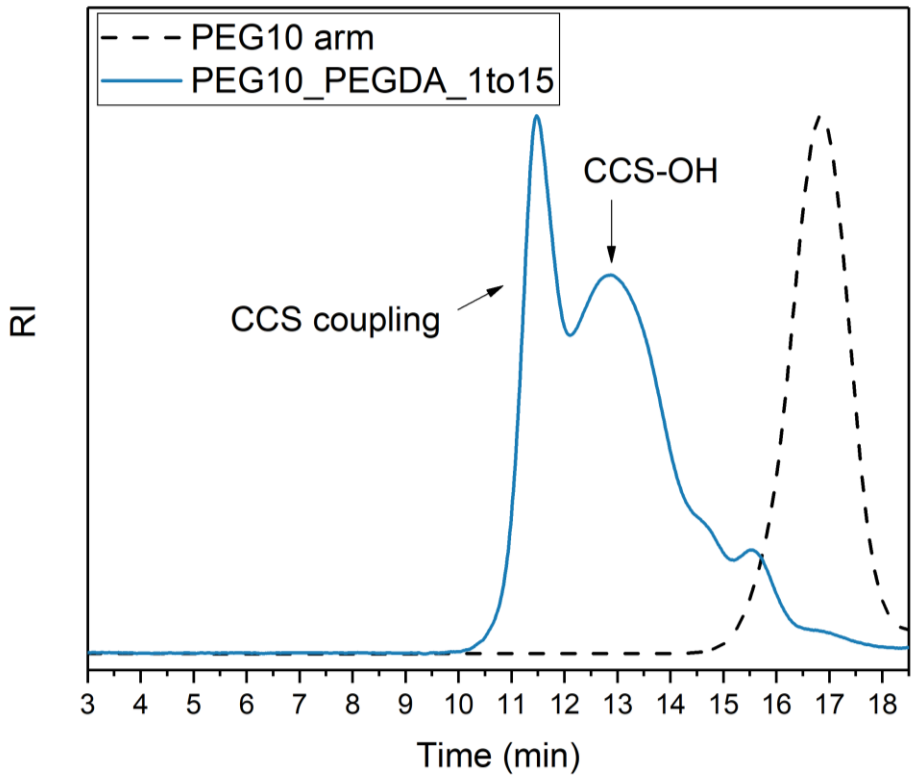

Figure B.2: DMF GPC of PEG10 arm and synthesized CCS after addition of cross-liner at the ratio of 1:15 [PEG10]:[PEGDA].

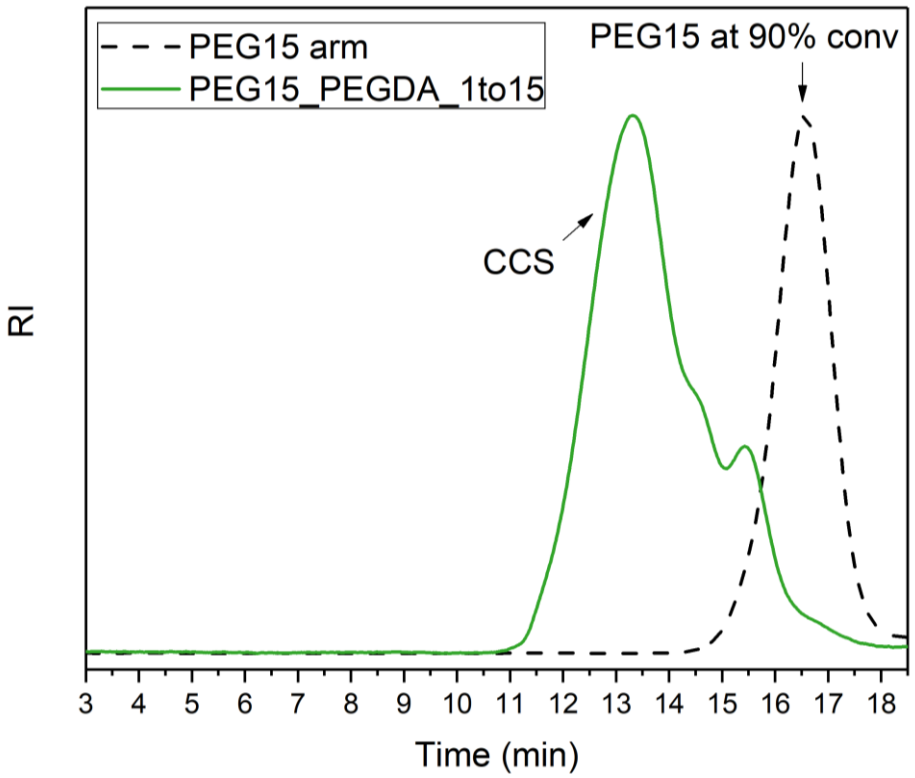

Figure B.3: DMF GPC of PEG15 arm and synthesized CCS after addition of cross linker at the ratio of 1:15 [PEG15]:[PEGDA].

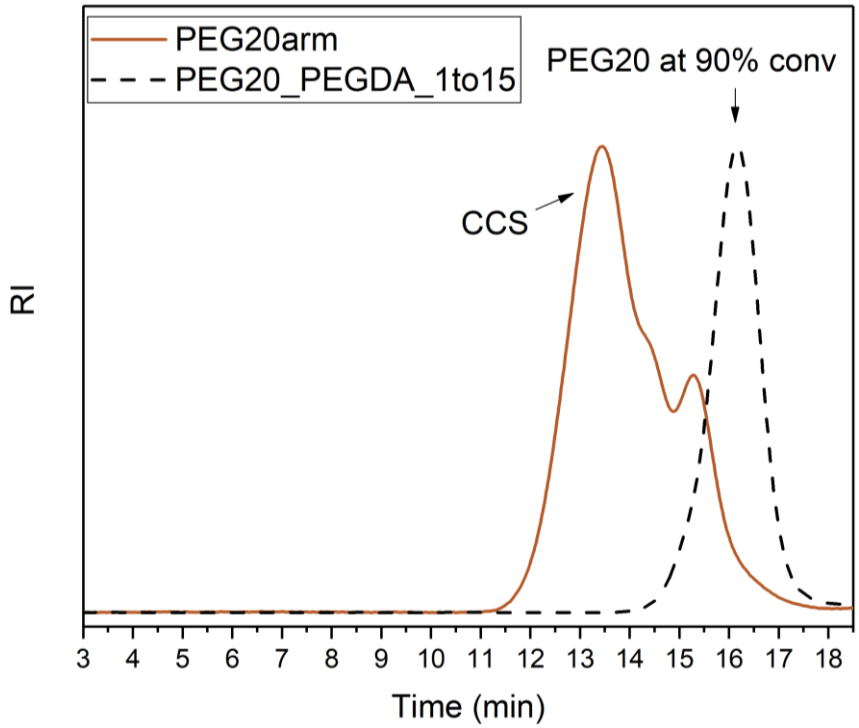

Figure B.4: DMF GPC of PEG20 arm and synthesized CCS after addition of cross linker at the ratio of 1:15 [PEG20]:[PEGDA].

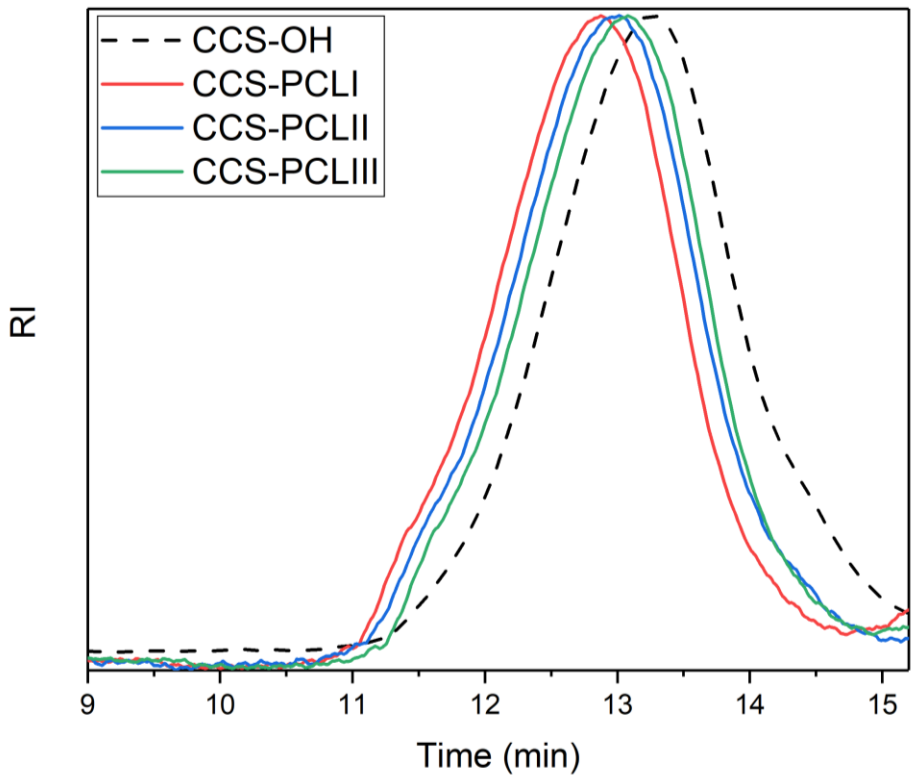

Figure B.5: DMF GPC spectra of CCS-PCL after ring opening polymerization of caprolactone utilizing CCS-OH as a precursor.

Table B.1: Characterization of synthesized CCS-PCL polymers. (a) [XL] = cross linker PEG diacrylate (MW = 250 Da) (b) Calculated from DMF GPC.

CCS-PCL	CCS-OH	[XL] : [B][a]	# PCL units	# Arm	≈ PCL unit/arm	Mw arm (kDa)	Mw (kDa)[b]	PDI
CCS-PCL_1	PEG_{20}-OH	15:1	731	15	50	5.6	207	1.5
CCS-PCL_2	PEG_{20}-OH	15:1	650	15	40	4.9	197	1.6
CCS-PCL_3	PEG_{20}-OH	15:1	441	15	30	3.4	174	1.4

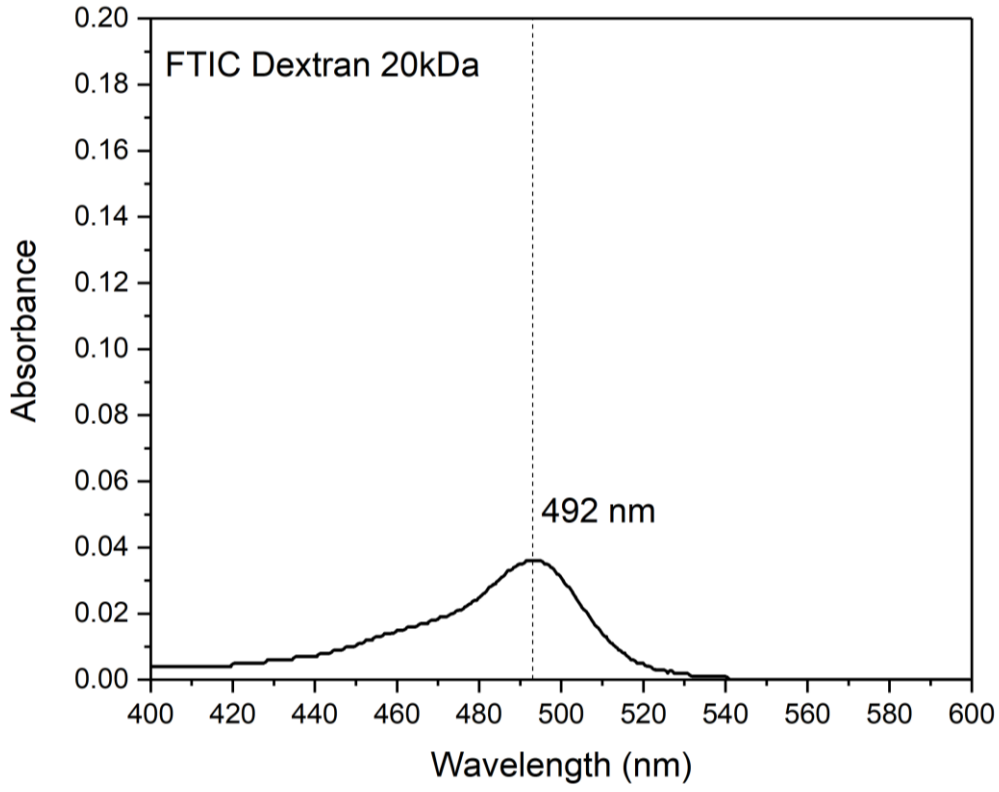

Figure B.6: UV-Vis spectrum of FTIC Dextran (Mw = 20 kDa) at 0.01 mg/ml.

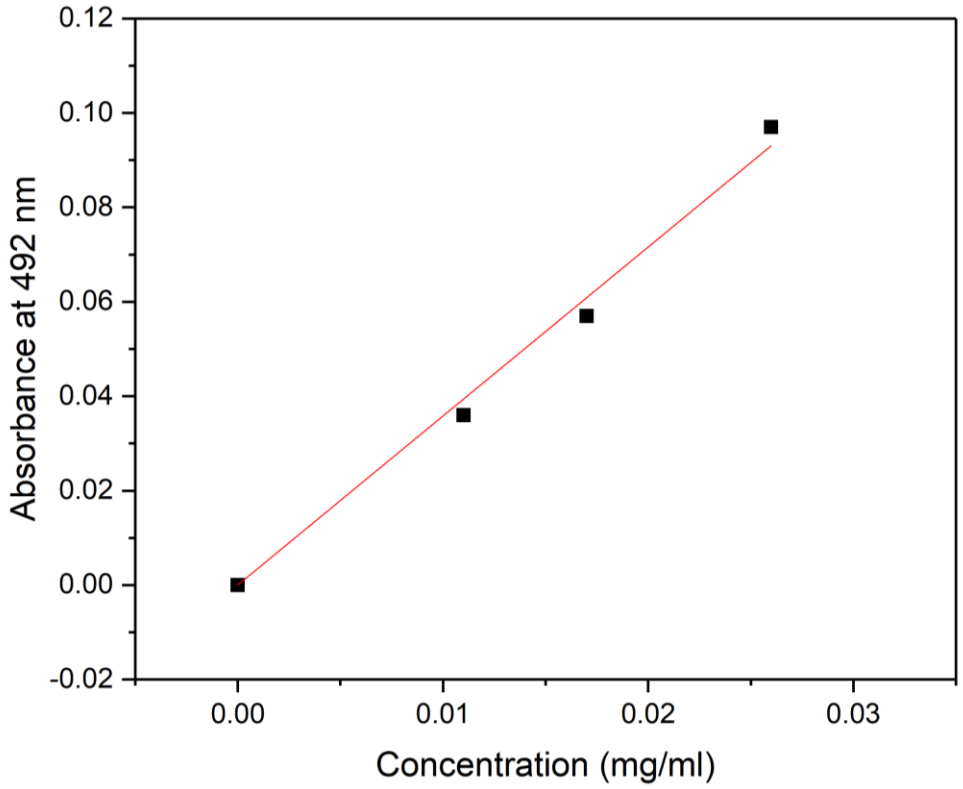

Figure B.7: Standard curve of FTIC Dextran (Mw = 20 kDa).

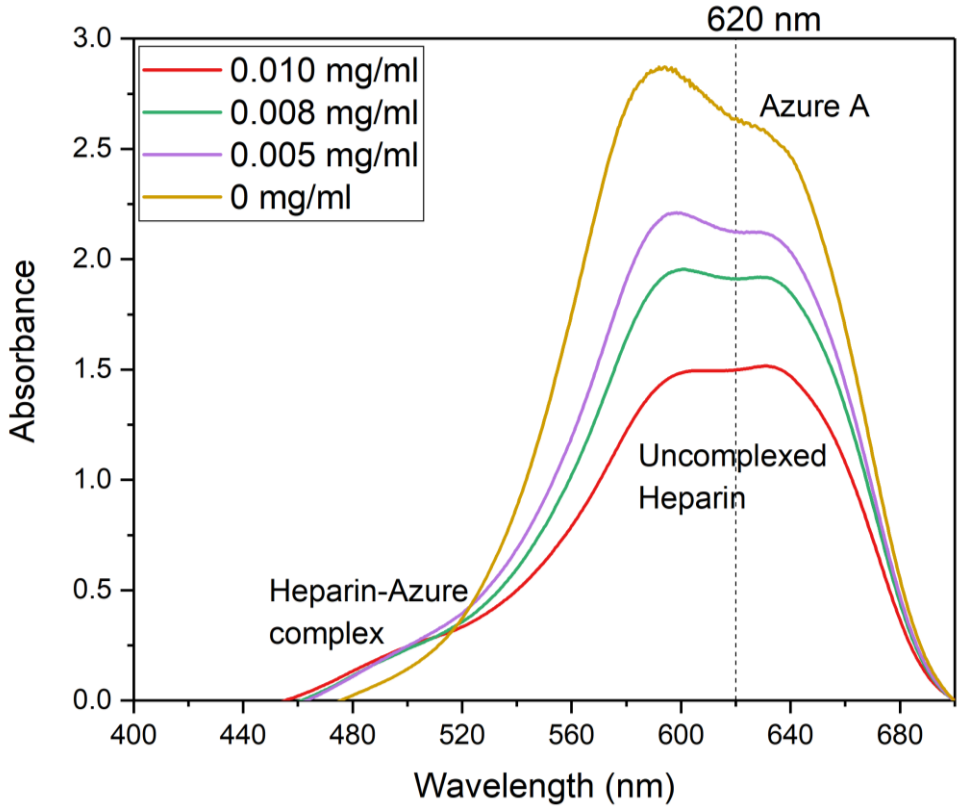

Figure B.8: UV-spectra of Heparin-Azure A complex. The band observed at approximately 510 nm corresponds to heparin-azure interactions. The band at 620 nm corresponds to uncomplexed heparin by Azure A dye. The absorption band at 620 nm decreases with increasing heparin concentration, due to the falling concentration of Azure A. The decrease in absorbance at 620 nm is proportional to the increase of free heparin concentration.

C. Chapter 4 Appendix

Supplementary file: Video of melt electrowriting of PCL-rGO(0.1 wt%)-CCS(10 wt%)

Video C1 – MEW PCLrGOCCS10wtp.mp4

The Video C1 shows extrusion of PCL-rGO(0.1 wt%)-CCS(10 wt%) material utilizing melt electrowriting setup. Due to the limited amount of synthesized material, the video only shows extrusion of small amount of material. The purpose of the experiment is to confirm material printability and lack of aggregation (blockage) of the nozzle after incorporation of CCS.

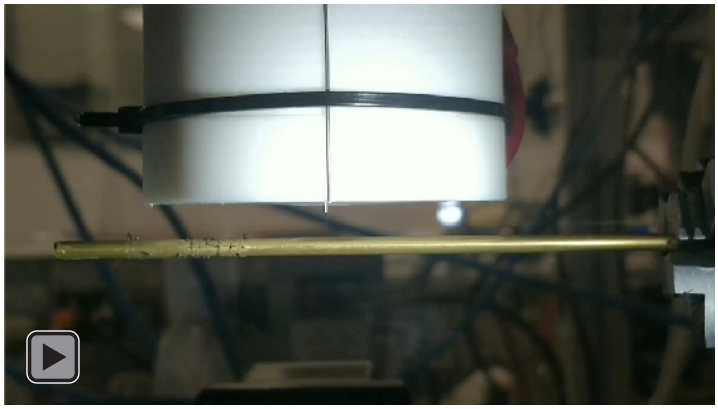

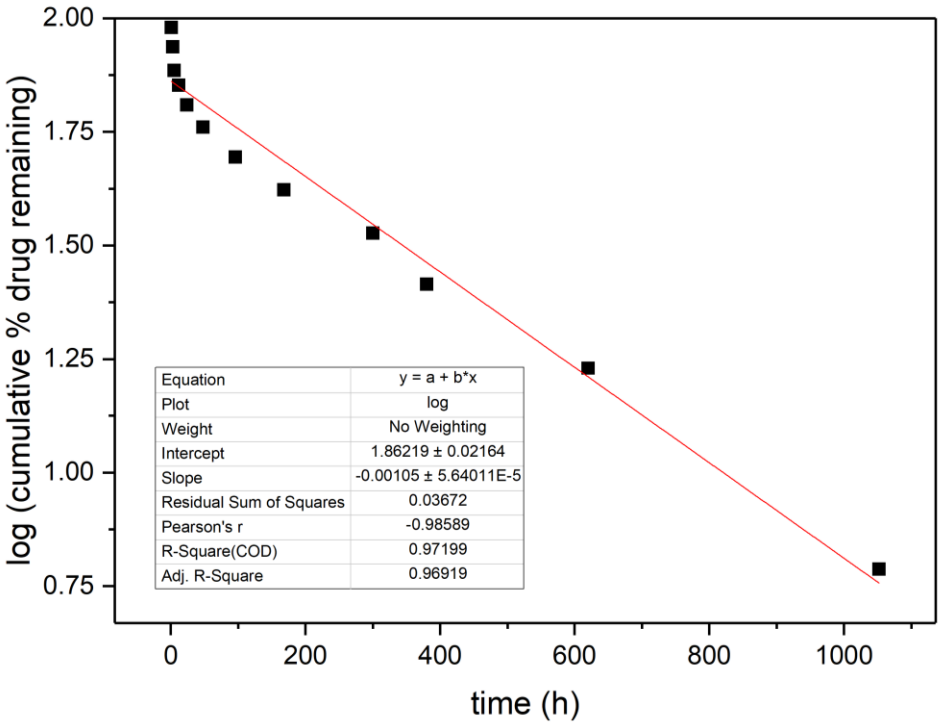

Figure C.1: Modelling of the kinetics release of rapamycin at pH = 5. Experimental data was fit into first-order kinetics model.

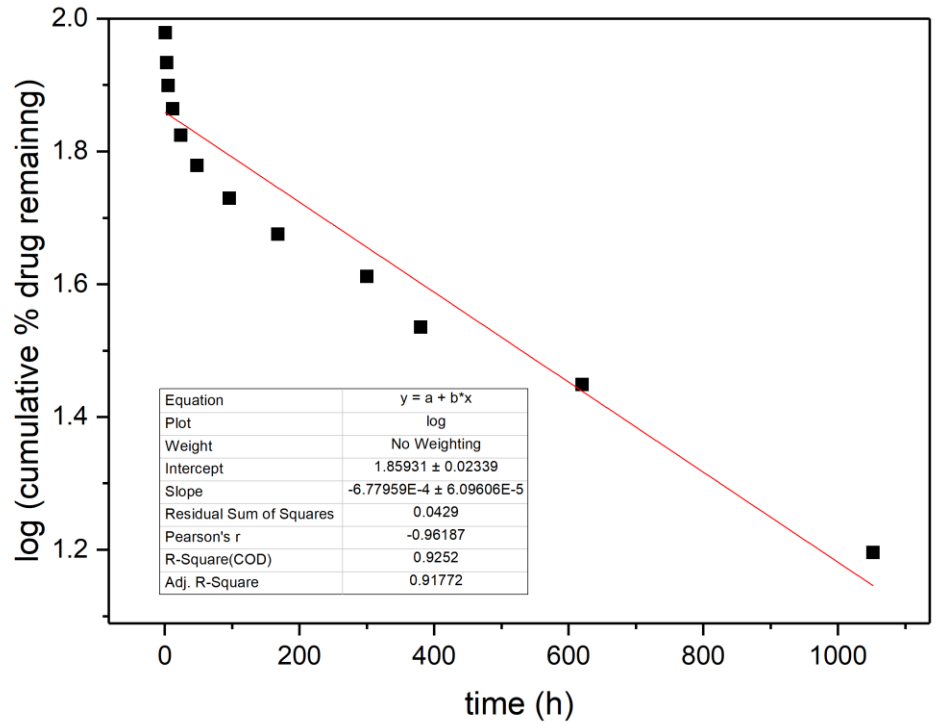

Figure C.2: Modelling of the kinetics release of rapamycin at pH = 7.4. Experimental data was fit into first-order kinetics model.

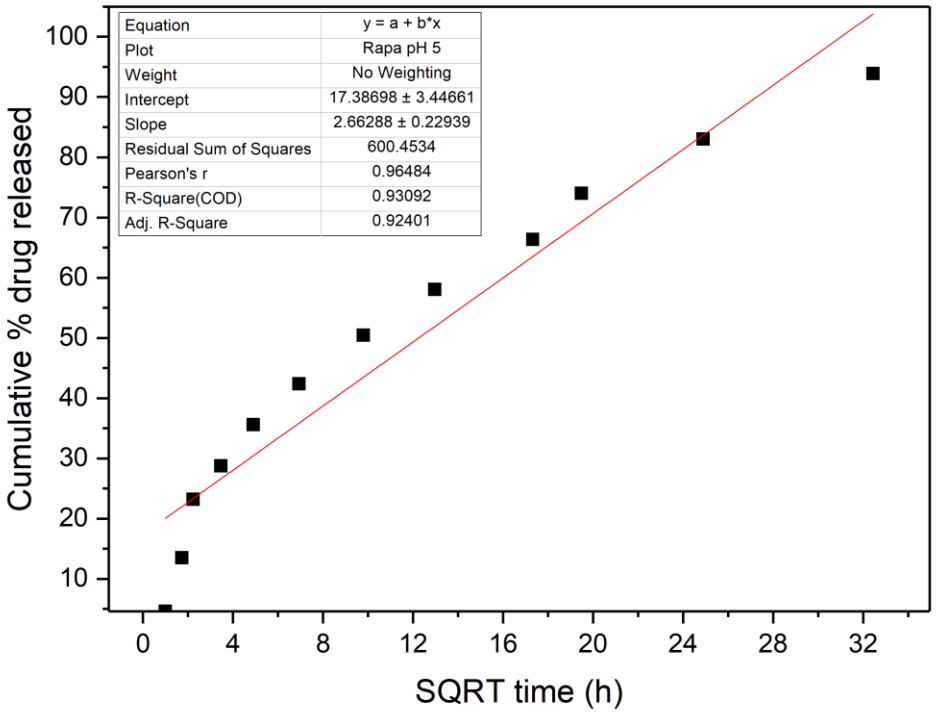

Figure C.3: Fitting of rapamycin release (pH = 5) into Higuchi model.

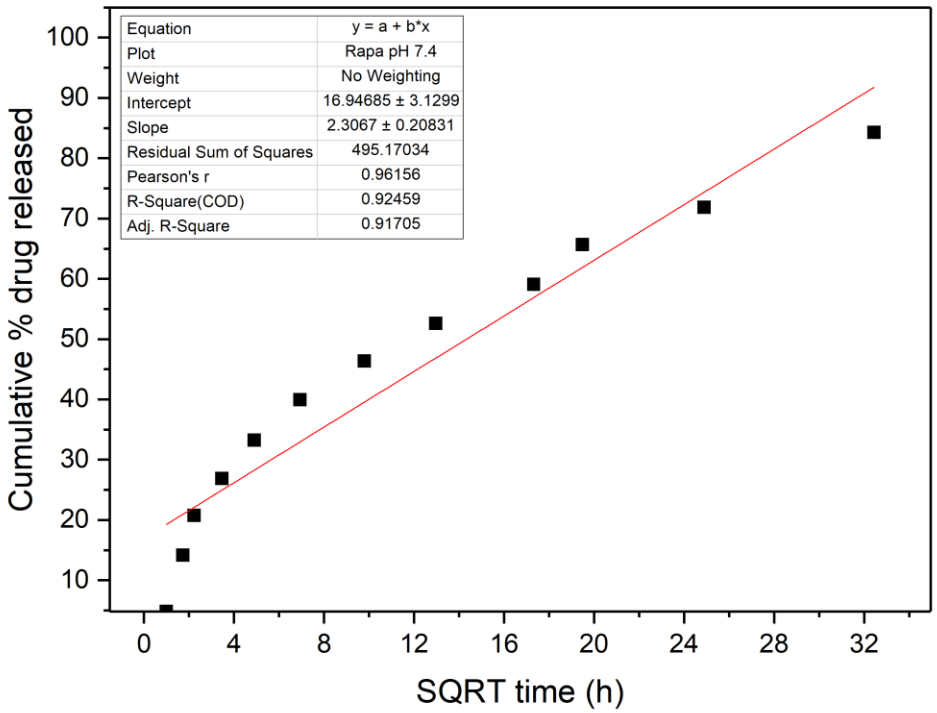

Figure C.4: Fitting of rapamycin release (pH = 7.4) into Higuchi model.

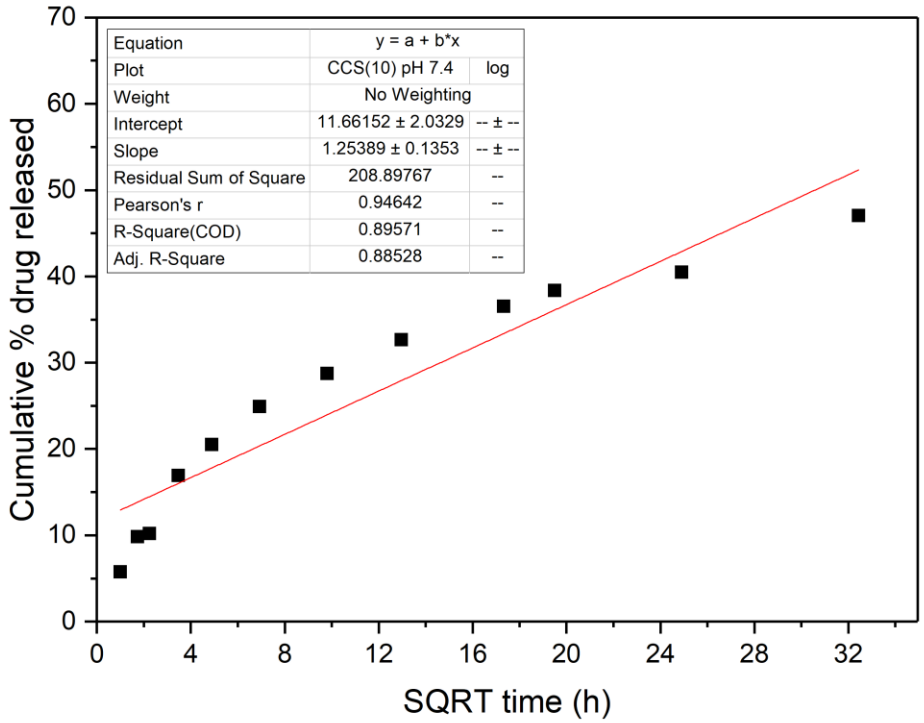

Figure C.5: Fitting of heparin release from CCS(10 wt%)/PCL-rGO at pH = 7.4 into Higuchi model.

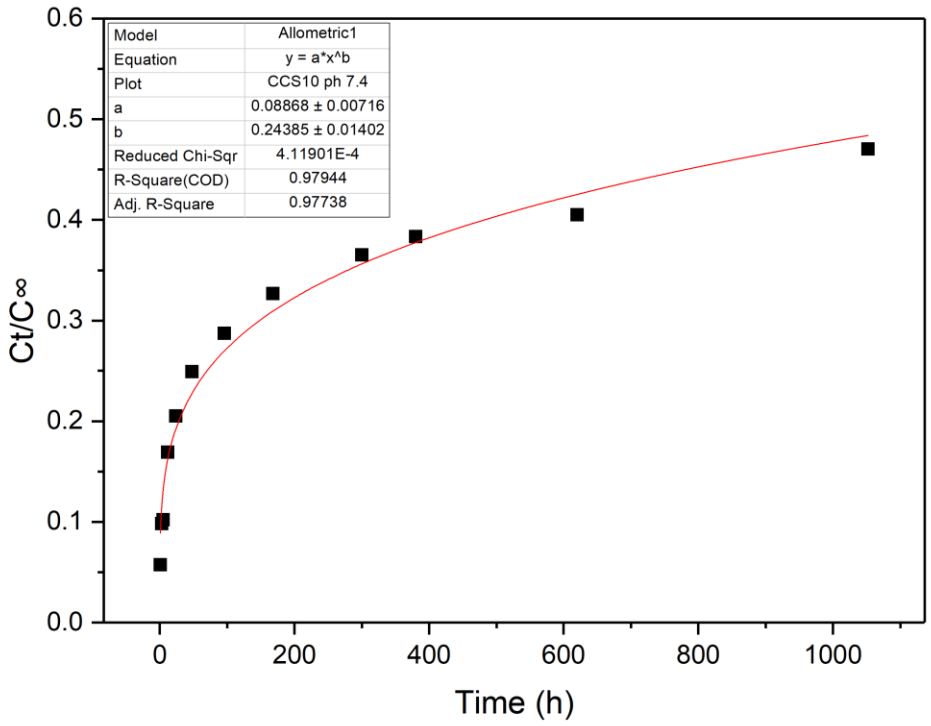

Figure C.6: Fitting of heparin release from CCS(10 wt%)/PCL-rGO at pH = 7.4 into the Power model.

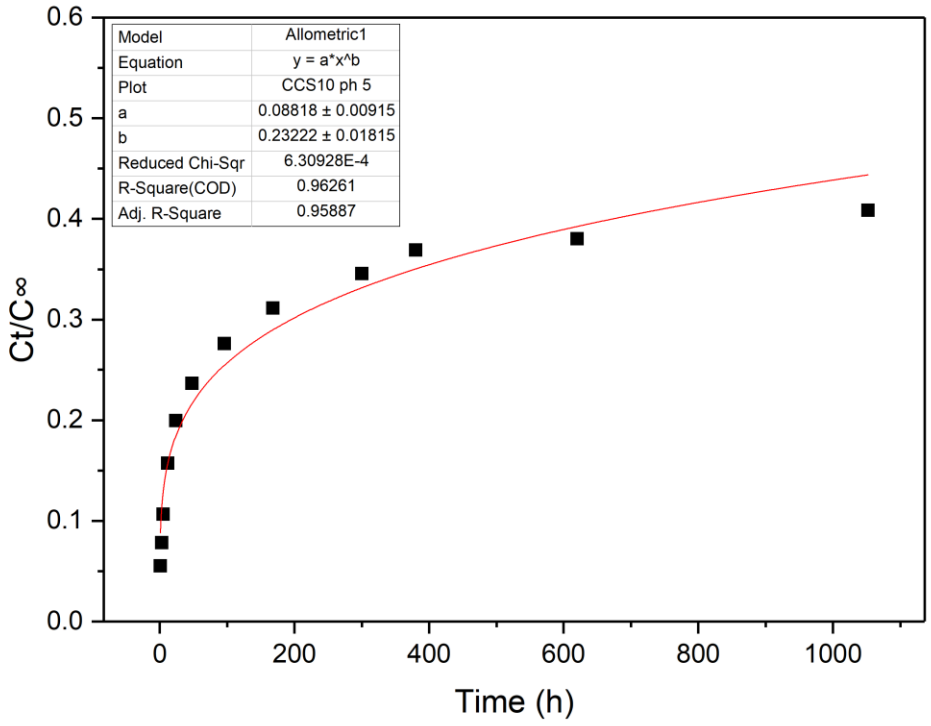

Figure C.7: Fitting of heparin release from CCS(10 wt%)/PCL-rGO at pH = 5 into the Power model.

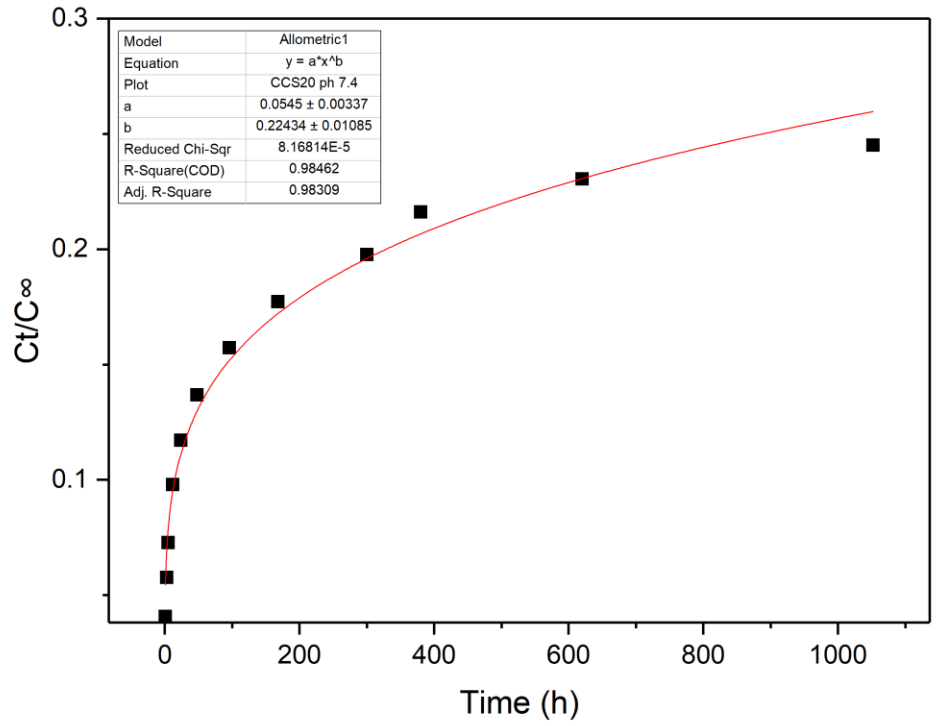

Figure C.8: Fitting of heparin release from CCS(20 wt%)/PCL-rGO at pH = 7.4 into the Power model.

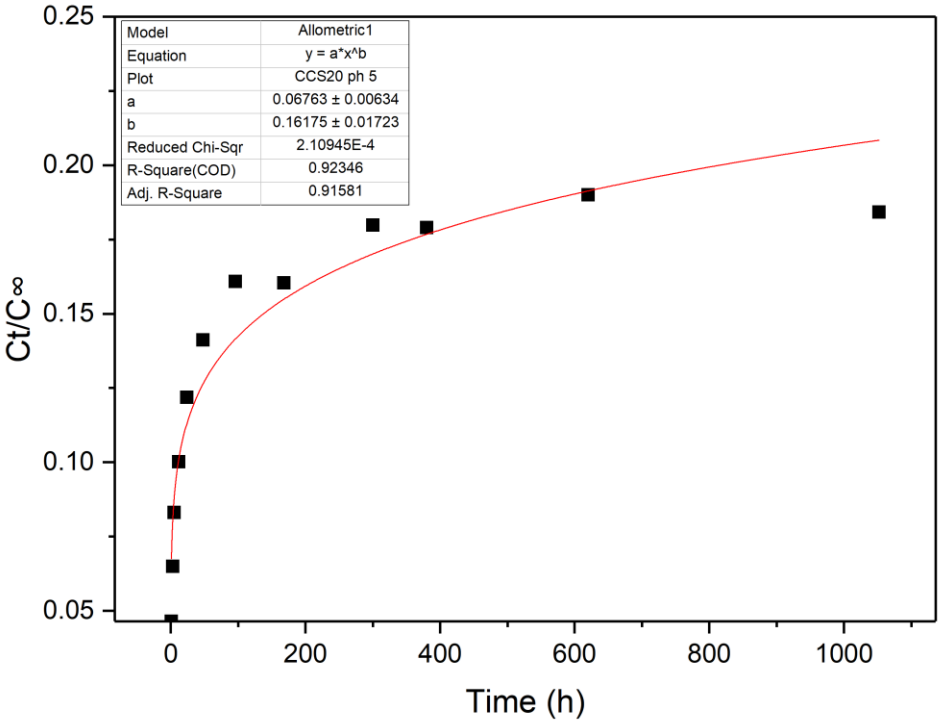

Figure C.9:Fitting of heparin release from CCS(20 wt%)/PCL-rGO at pH = 5 into the Power model.

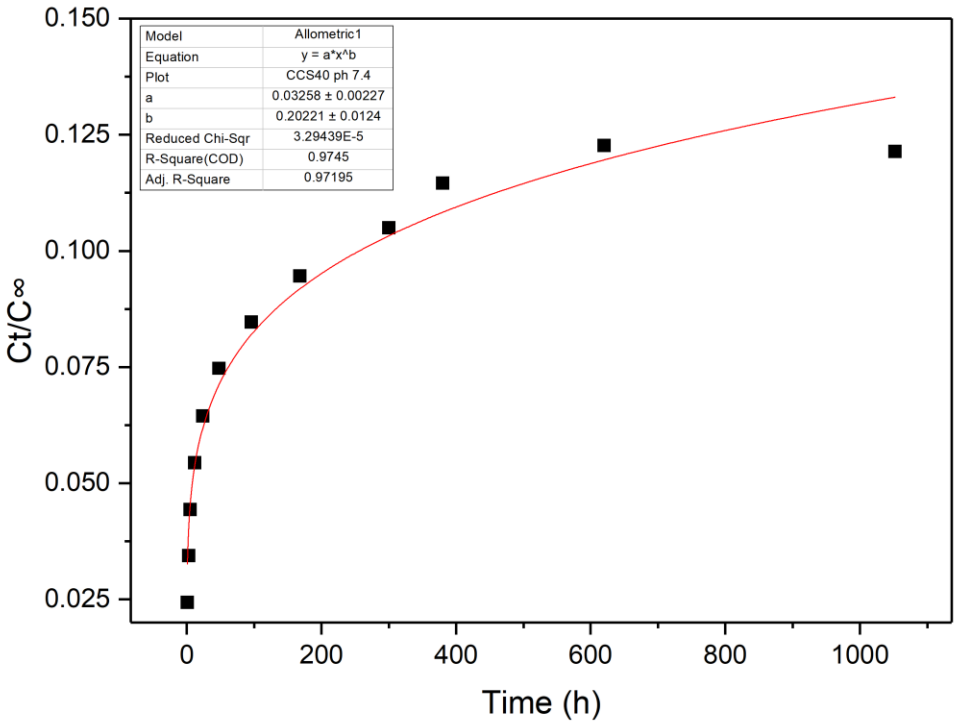

Figure C.10: Fitting of heparin release from CCS(40 wt%)/PCL-rGO at pH = 7.4 into the Power model.

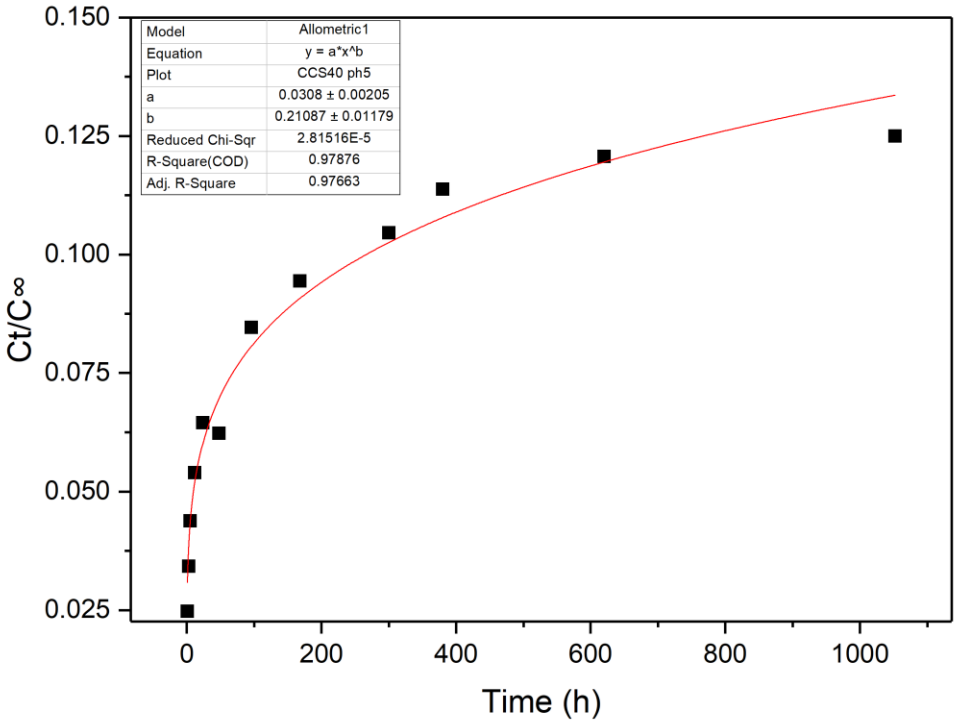

Figure C.11: Fitting of heparin release from CCS(40 wt%)/PCL-rGO at pH = 5 into the Power model.

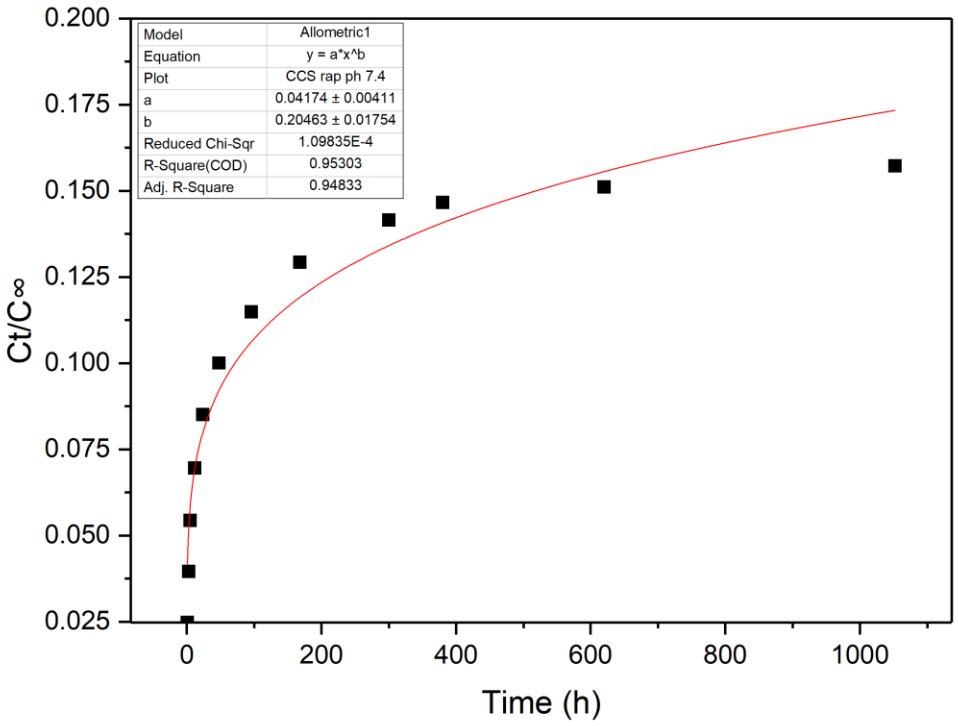

Figure C.12: Fitting of heparin release from CCS-rap/PCL-rGO at pH = 7.4 into the Power model.

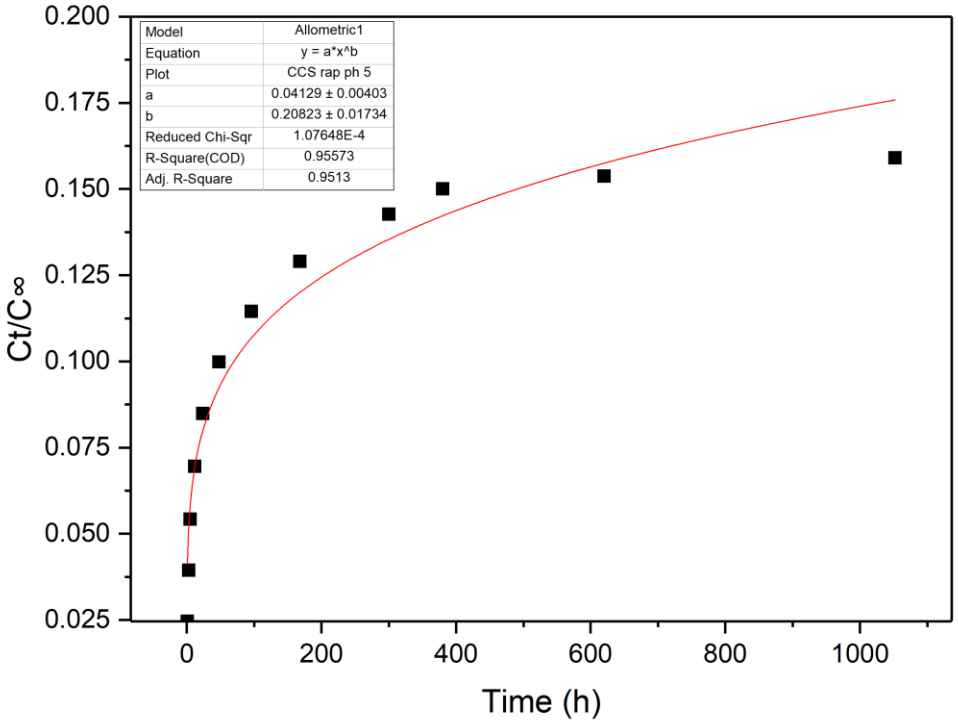

Figure C.13: Fitting of heparin release from CCS-rap/PCL-rGO at pH = 5 into the Power model.

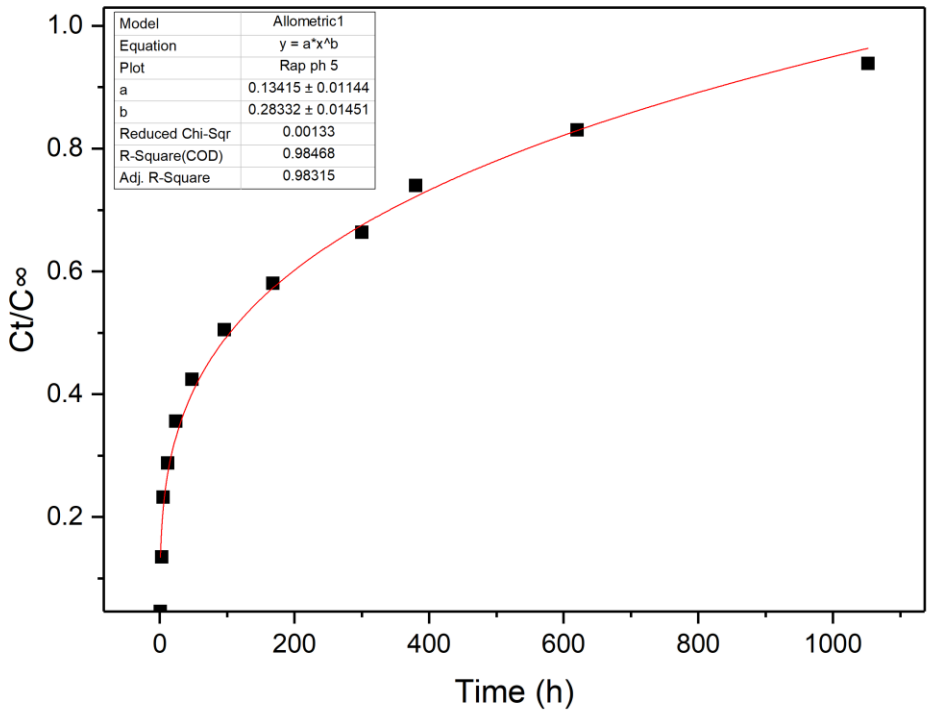

Figure C.14: Modelling of rapamycin release (pH = 5) using the Power model.

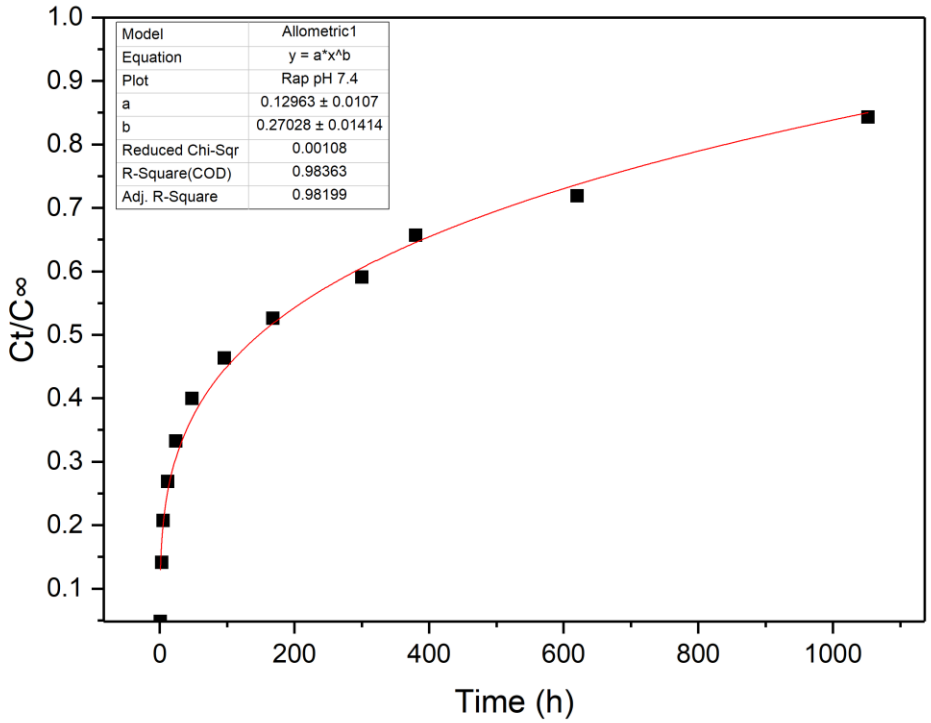

Figure C.15: Modelling of rapamycin release (pH = 7.4) using the Power model.

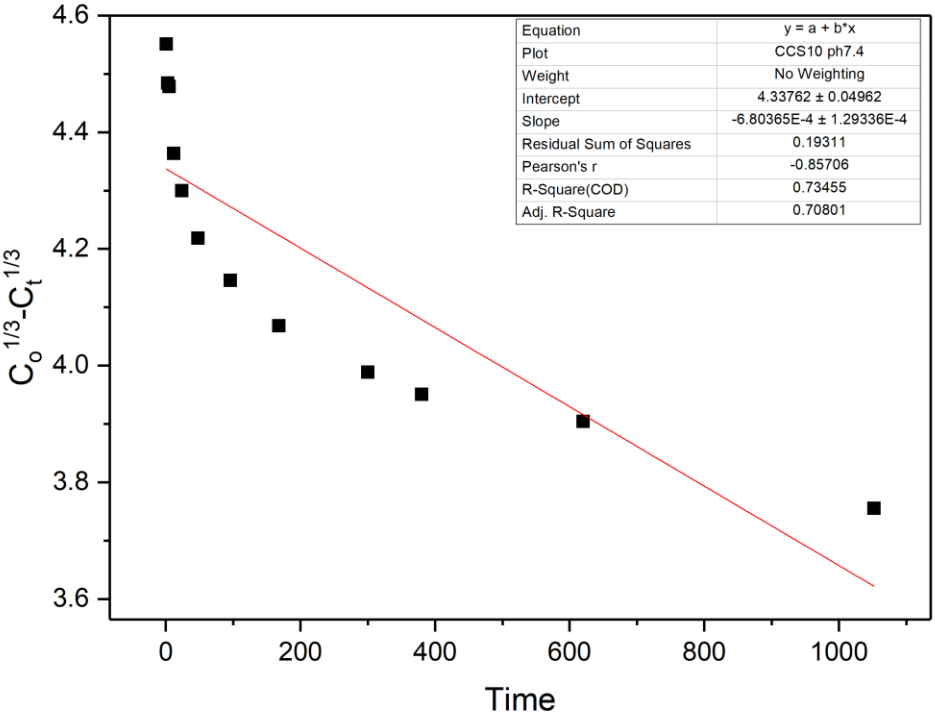

Figure C.16: Fitting of heparin release from CCS(10 wt%)/PCL-rGO at pH = 7.4 into the Hixon Crowell model.

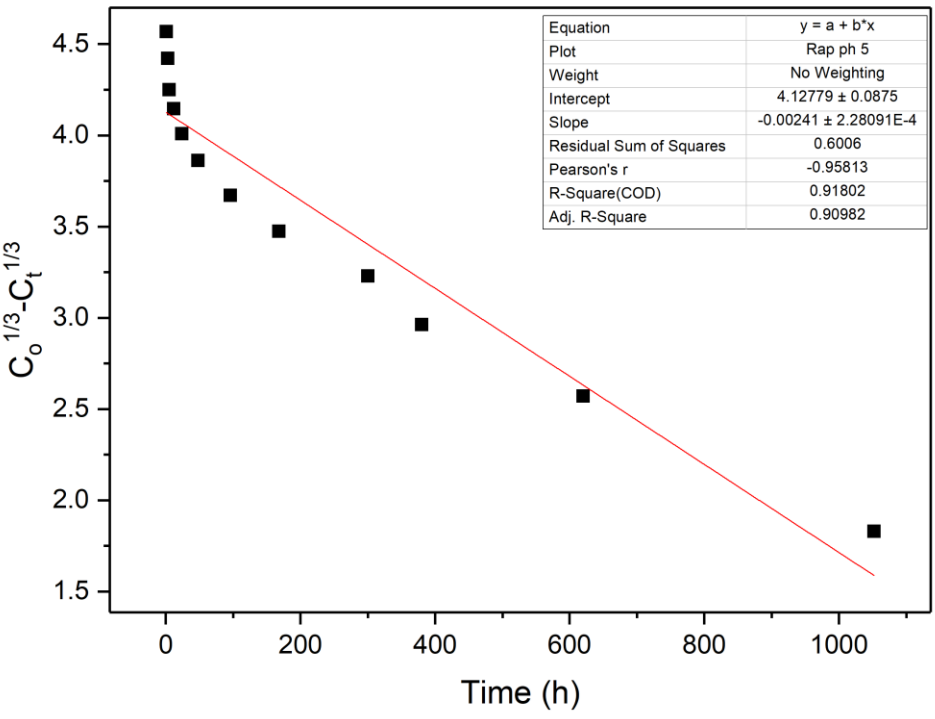

Figure C.17: Modelling of rapamycin release (pH = 5) using the Hixon-Crowell model.

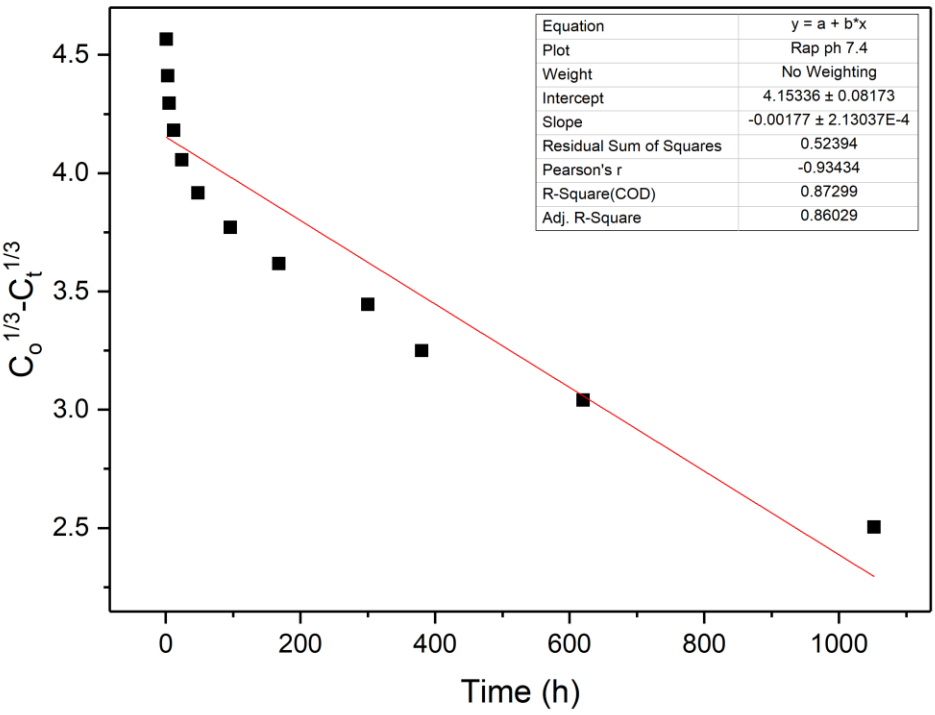

Figure C.18: Modelling of rapamycin release (pH = 7.4) using the Hixon-Crowell model.

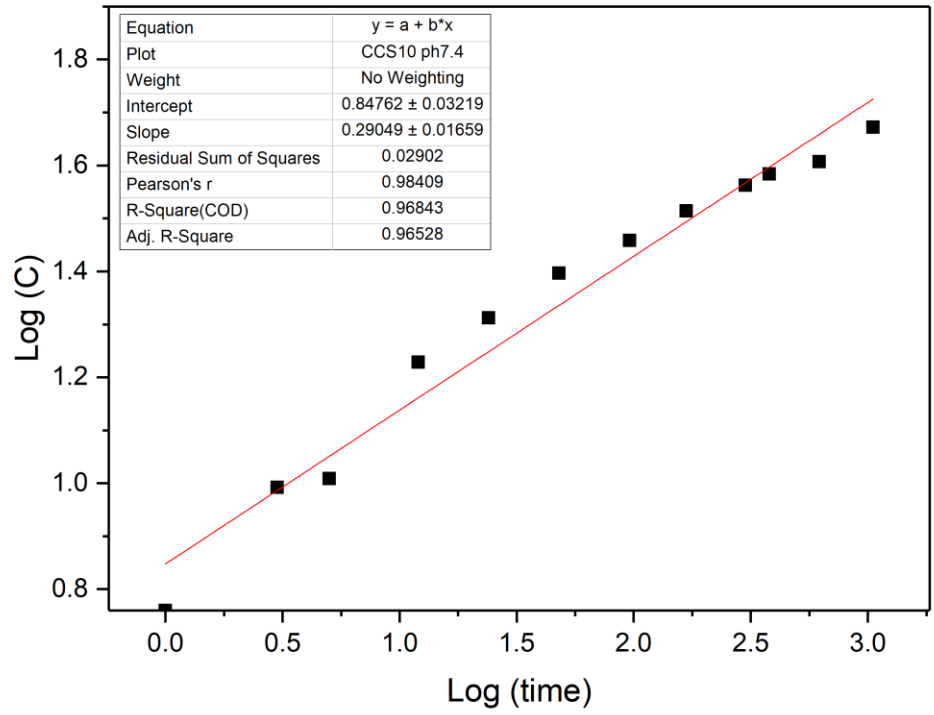

Figure C.19: Fitting of heparin release from CCS(10 wt%)/PCL-rGO at pH = 7.4 into the Weibull model.

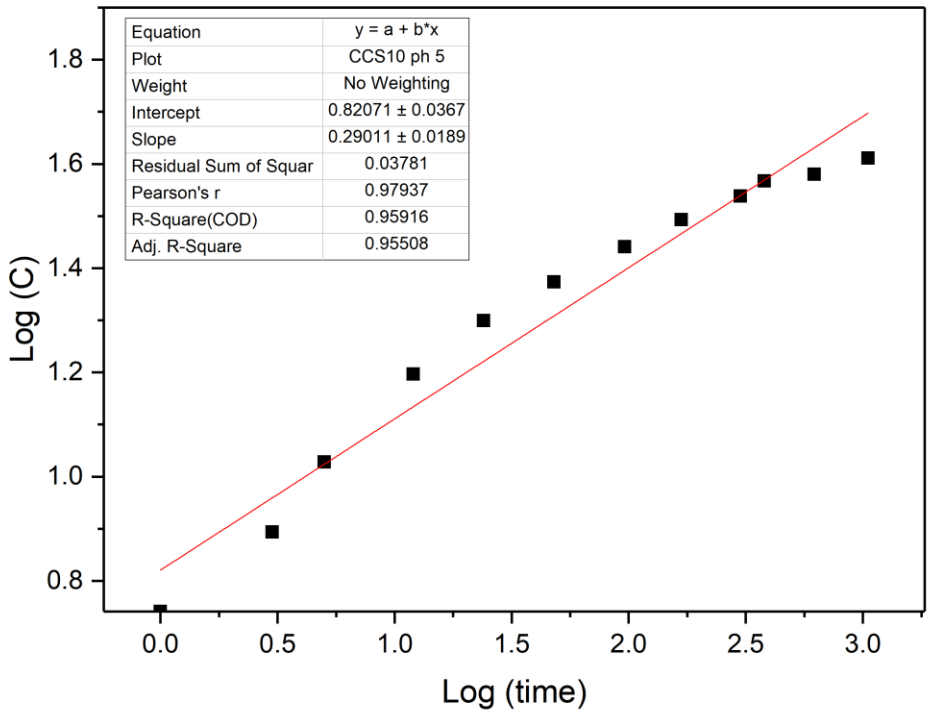

Figure C.20: Fitting of heparin release from CCS(10 wt%)/PCL-rGO at pH = 5 into the Weibull model.

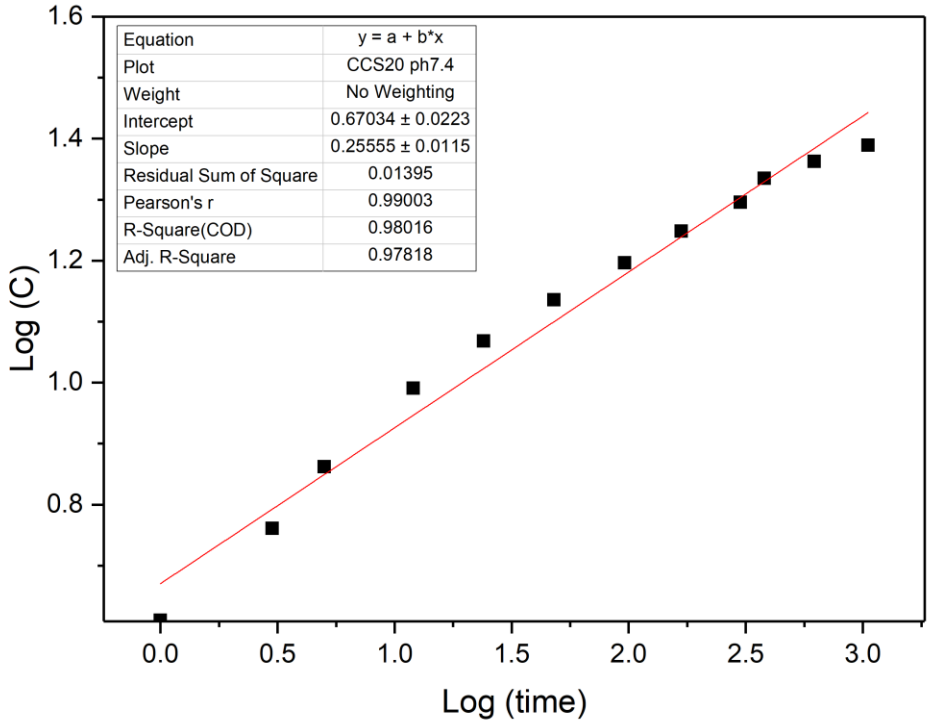

Figure C.21: Fitting of heparin release from CCS(20 wt%)/PCL-rGO at pH = 7.4 into the Weibull model.

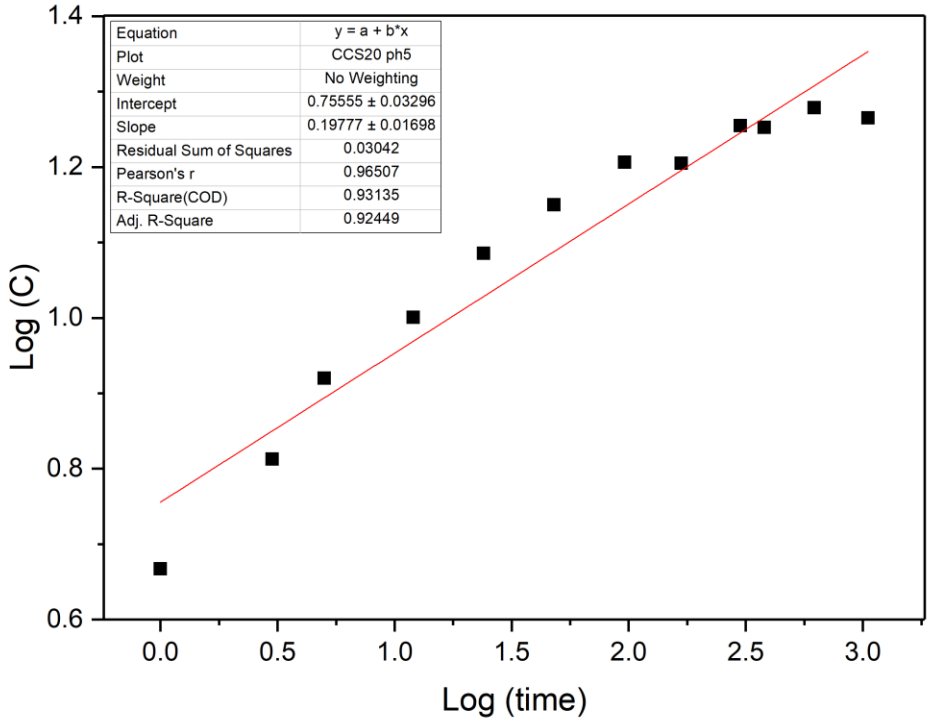

Figure C.22: Fitting of heparin release from CCS(20 wt%)/PCL-rGO at pH = 5 into the Weibull model.

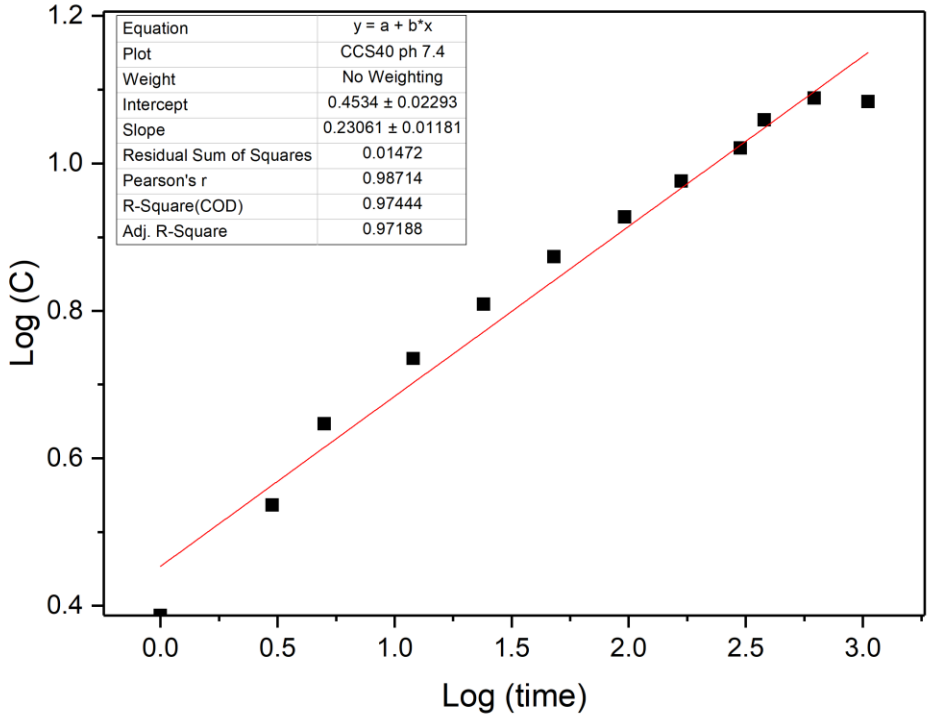

Figure C.23: Fitting of heparin release from CCS(40 wt%)/PCL-rGO at pH = 7.4 into the Weibull model.

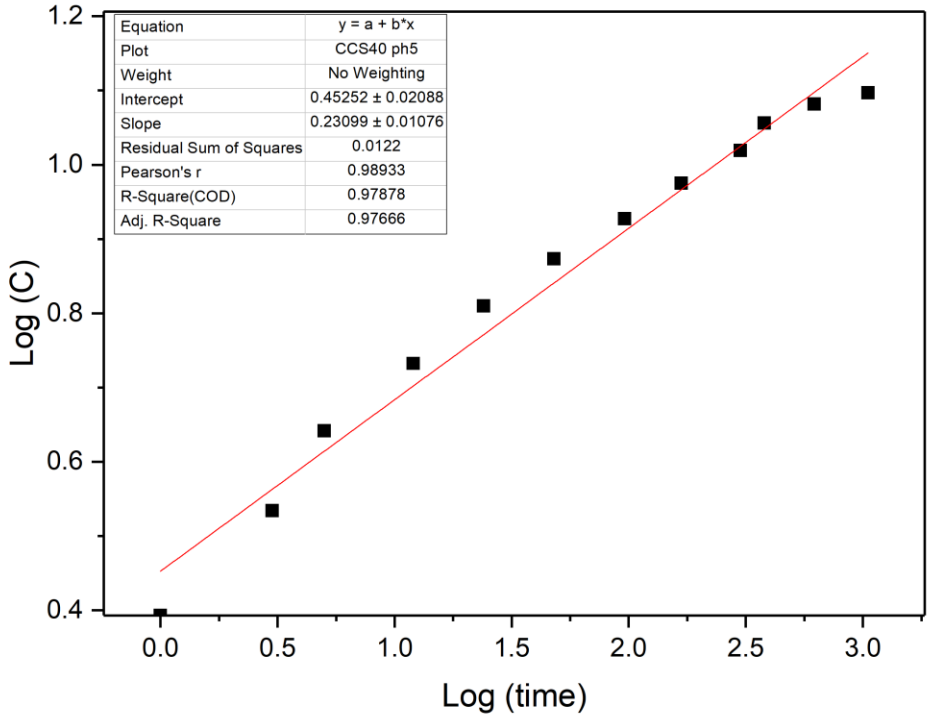

Figure C.24: Fitting of heparin release from CCS(40 wt%)/PCL-rGO at pH = 5 into the Weibull model.

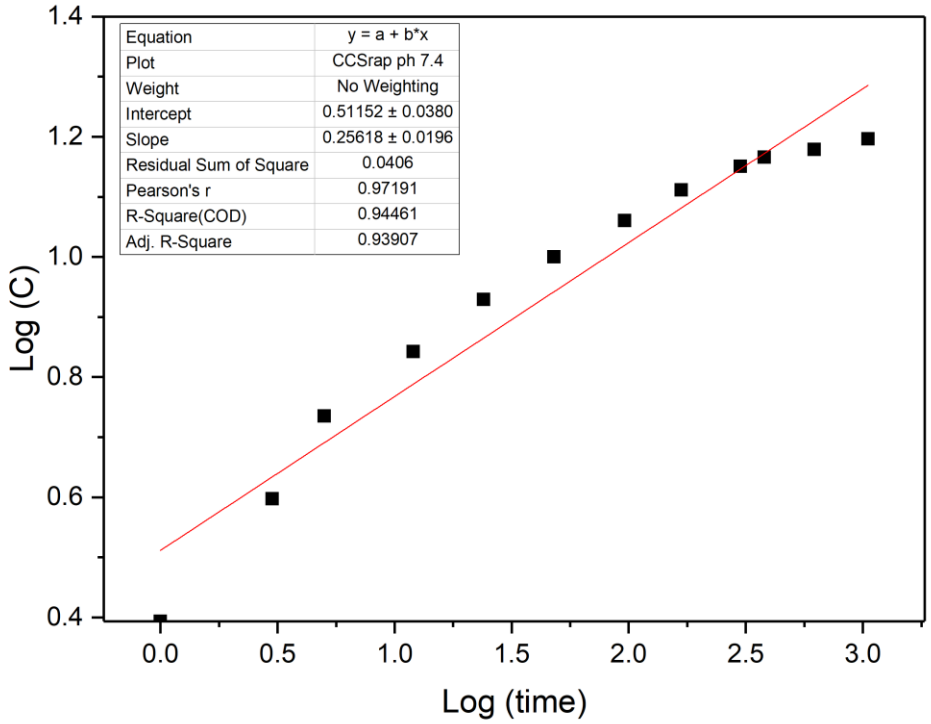

Figure C.25: Fitting of heparin release from CCS-rap/PCL-rGO at pH = 7.4 into the Weibull model.

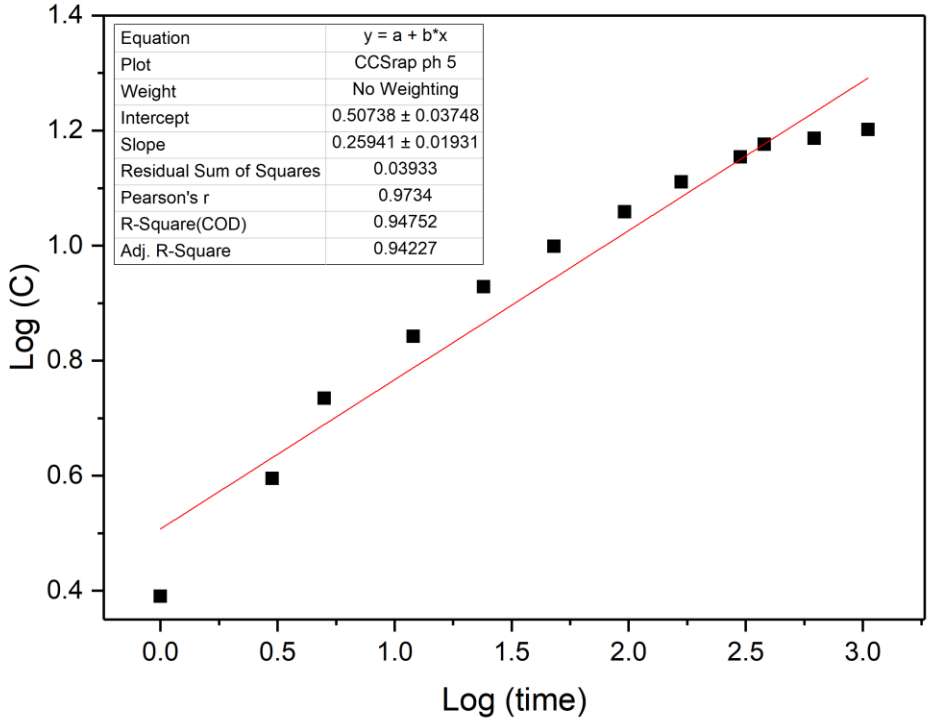

Figure C.26: Fitting of heparin release from CCS-rap/PCL-rGO at pH = 5 into the Weibull model.

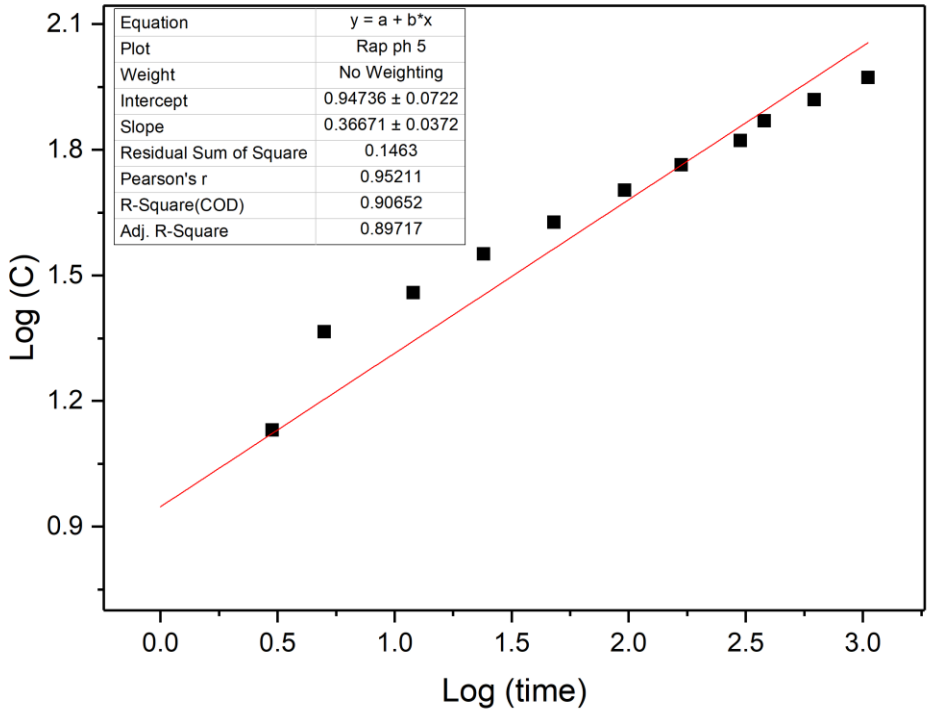

Figure C.27: Modelling of rapamycin release (pH = 5) using the Weibull model.

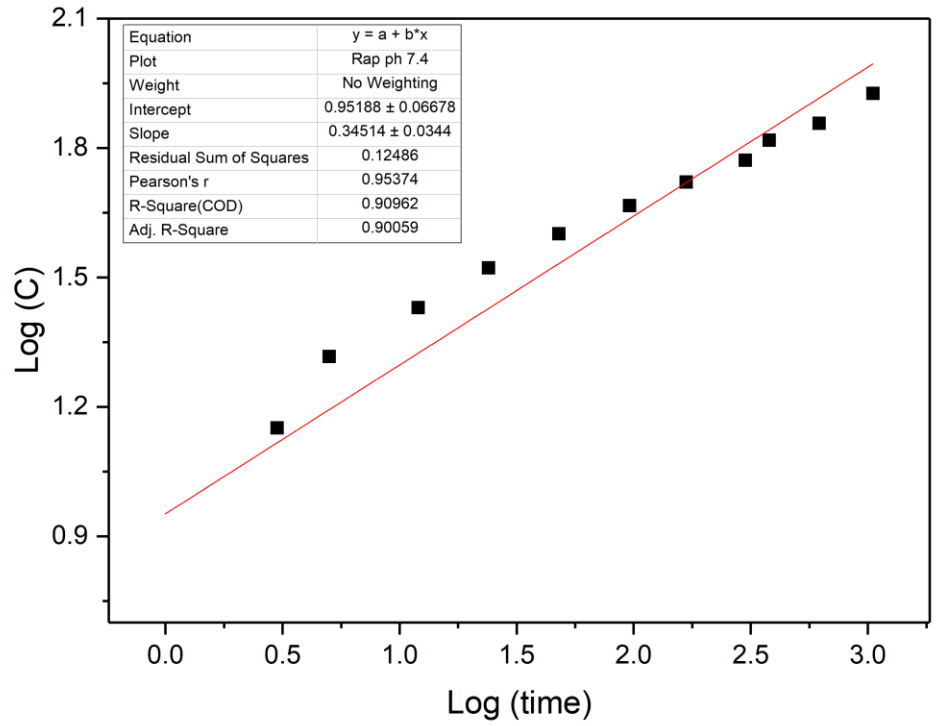

Figure C.28: Modelling of rapamycin release (pH = 7.4) using the Weibull model.

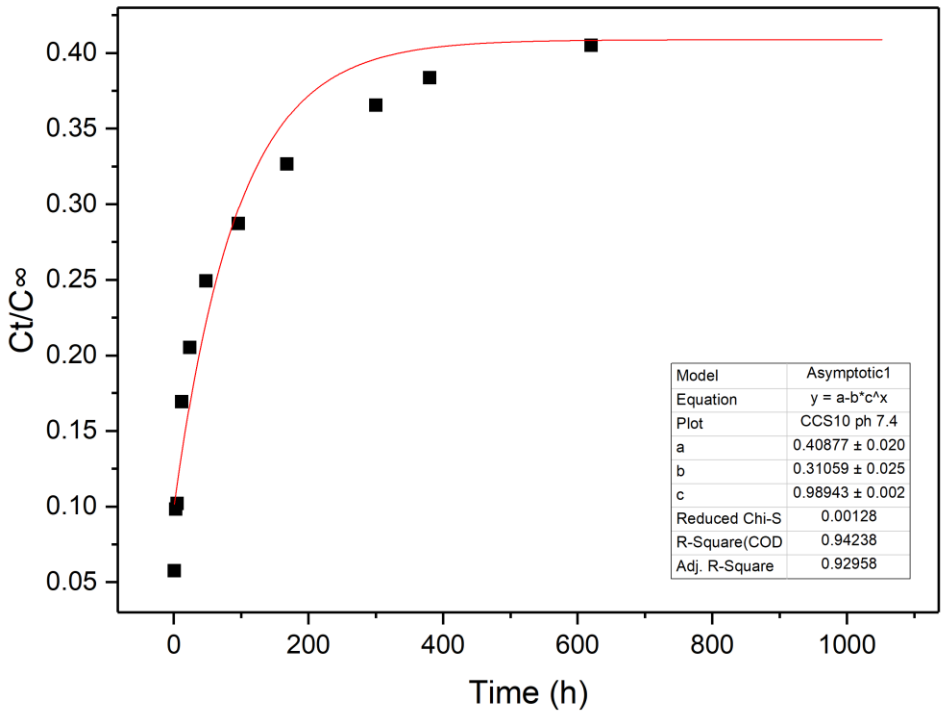

Figure C.29: Fitting of heparin release from CCS(10 wt%)/PCL-rGO at pH = 7.4 into the Exponential model.

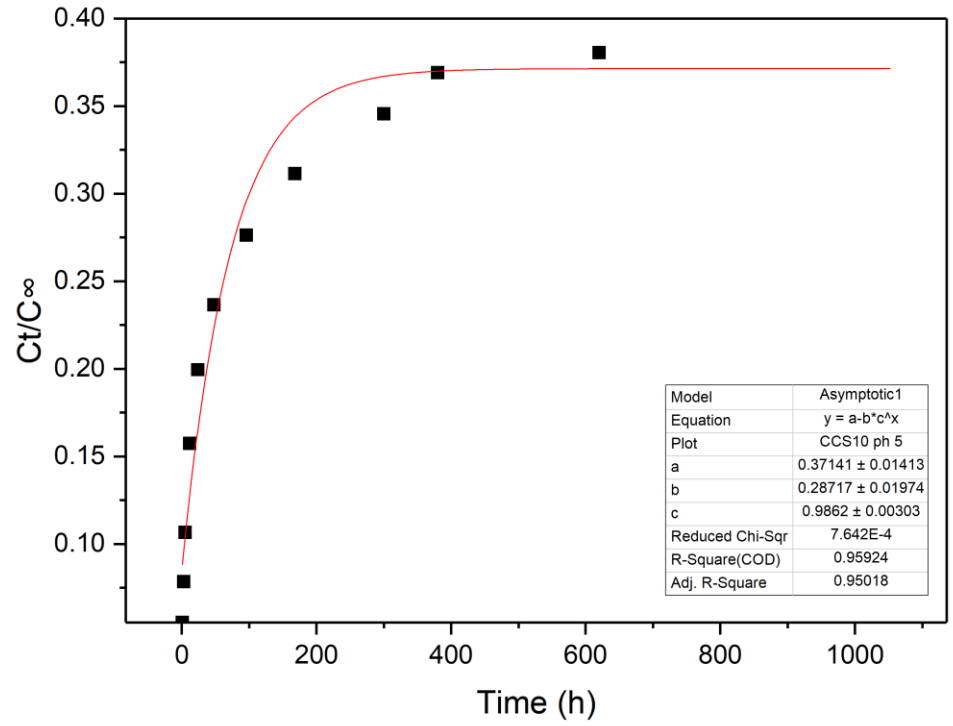

Figure C.30: Fitting of heparin release from CCS(10 wt%)/PCL-rGO at pH = 5 into the Exponential model.

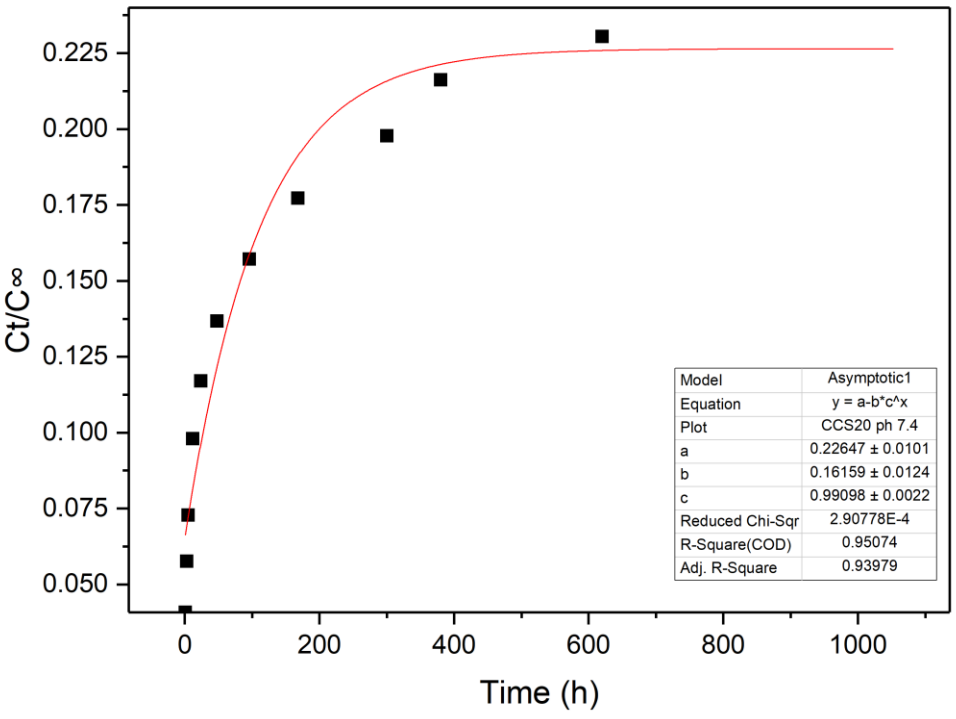

Figure C.31: Fitting of heparin release from CCS(20 wt%)/PCL-rGO at pH = 7.4 into the Exponential model.

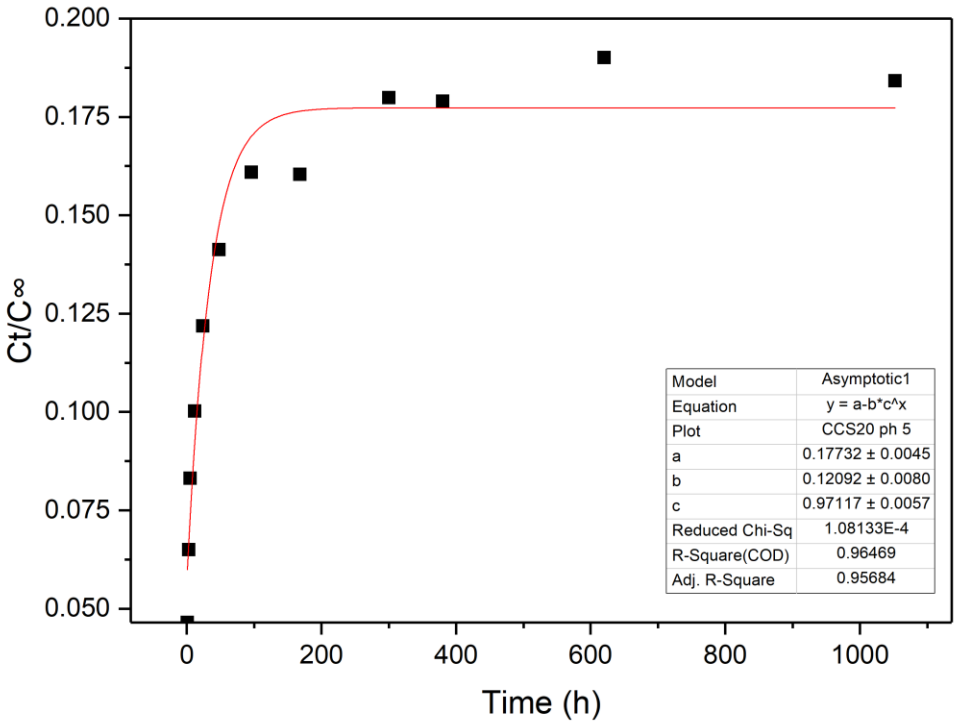

Figure C.32: Fitting of heparin release from CCS(20 wt%)/PCL-rGO at pH = 5 into the Exponential model.

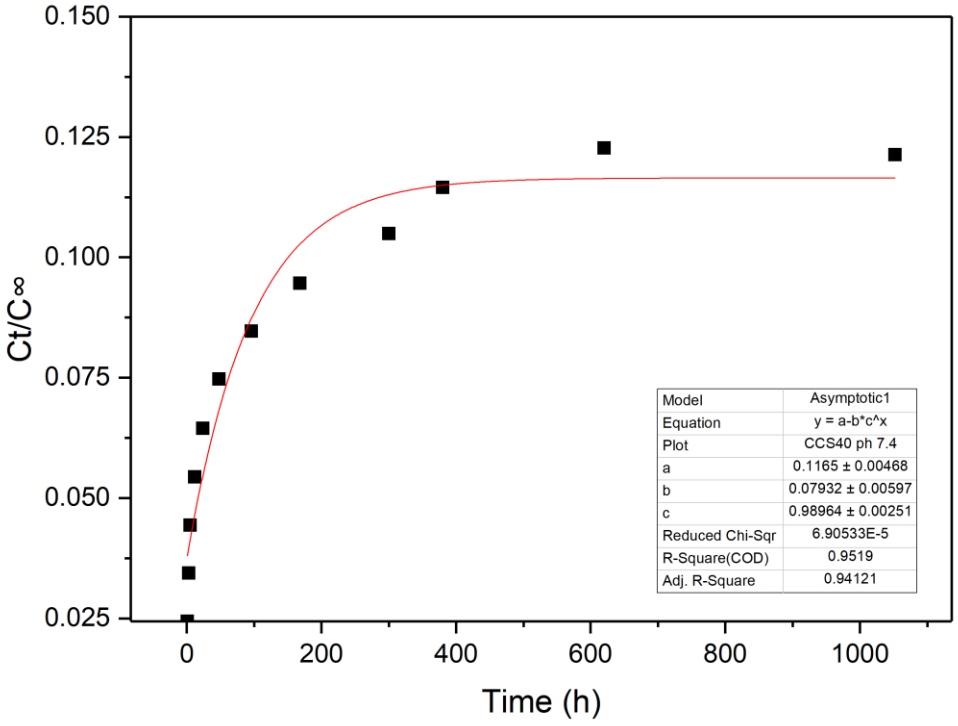

Figure C.33: Fitting of heparin release from CCS(40 wt%)/PCL-rGO at pH = 7.4 into the Exponential model.

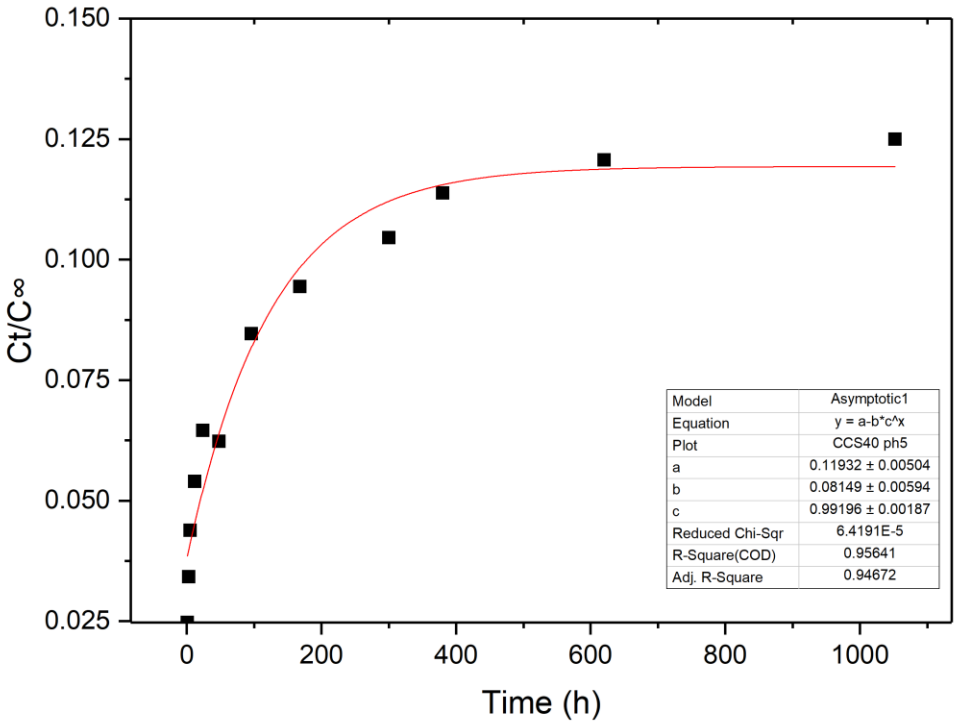

Figure C.34: Fitting of heparin release from CCS(40 wt%)/PCL-rGO at pH = 5 into the Exponential model.

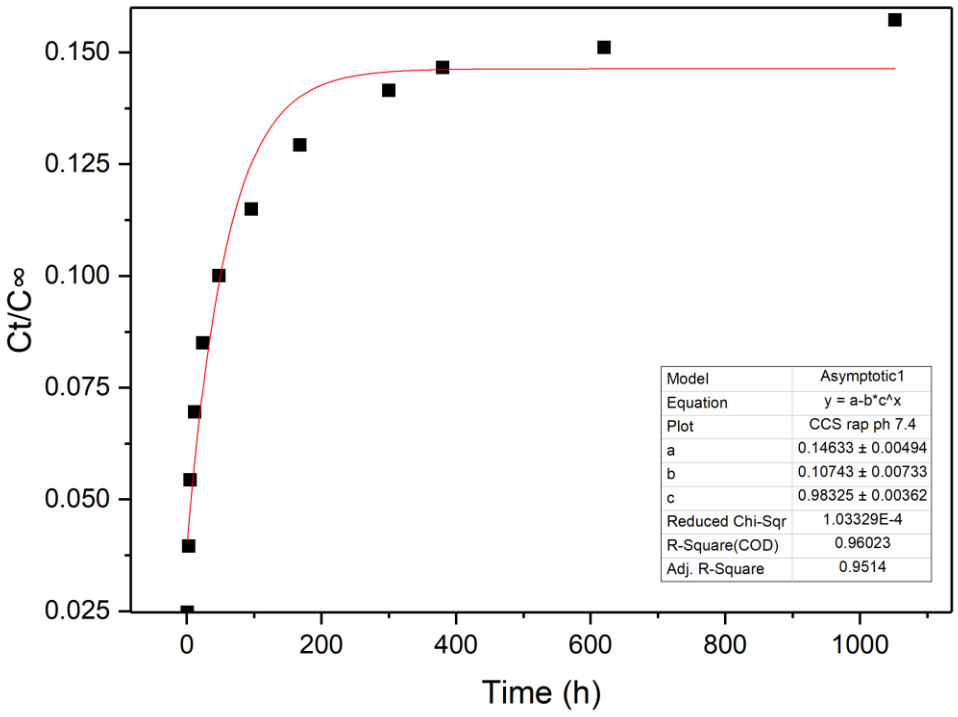

Figure C.35: Fitting of heparin release from CCS-rap/PCL-rGO at pH = 7.4 into the Exponential model.

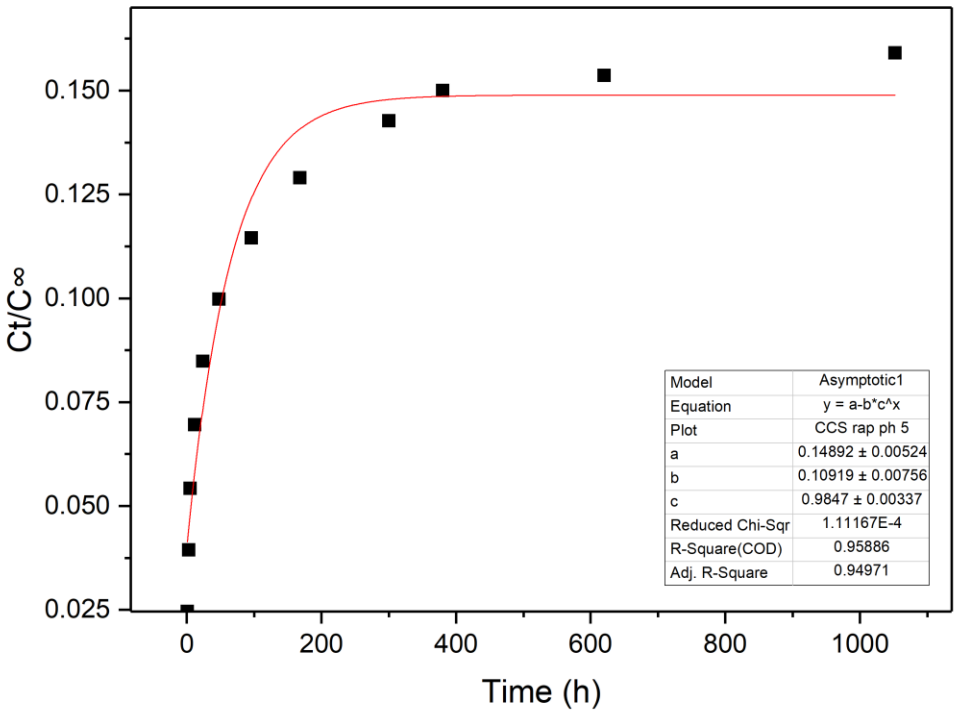

Figure C.36: Fitting of heparin release from CCS-rap/PCL-rGO at pH = 5 into the Exponential model.

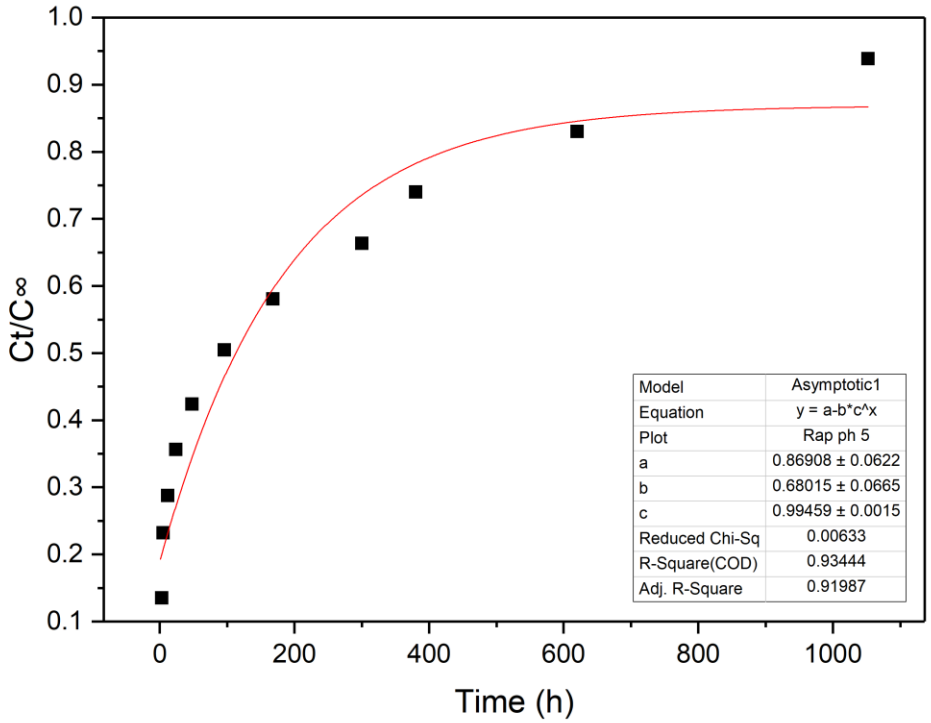

Figure C.37: Fitting of rapamycin release at pH = 5 into the Exponential model.

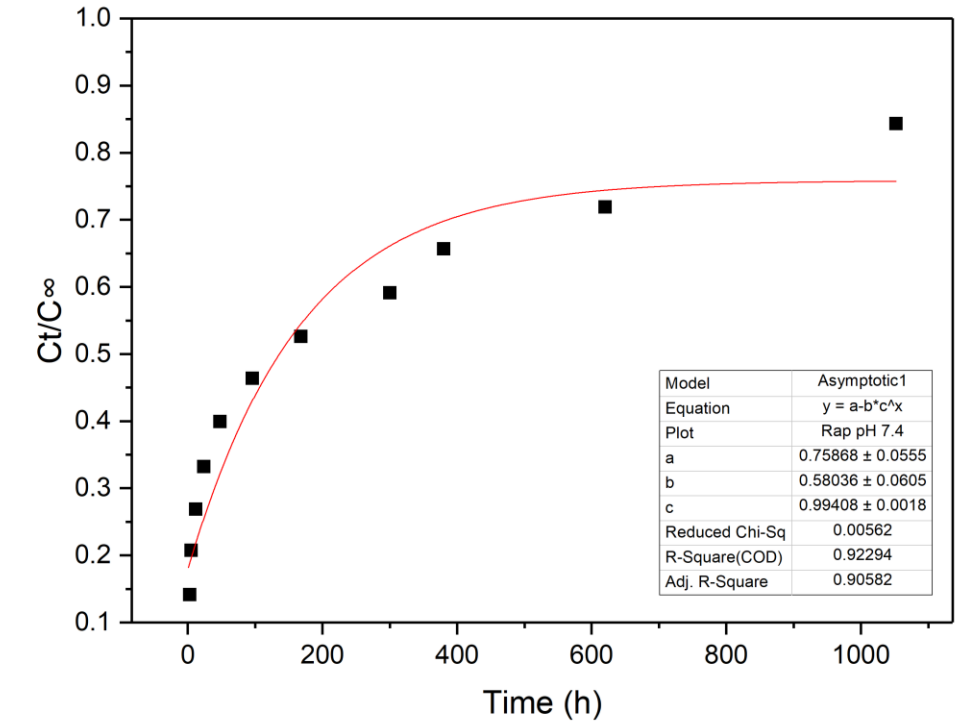

Figure C.38: Fitting of rapamycin release at pH = 7.4 into the Exponential model.

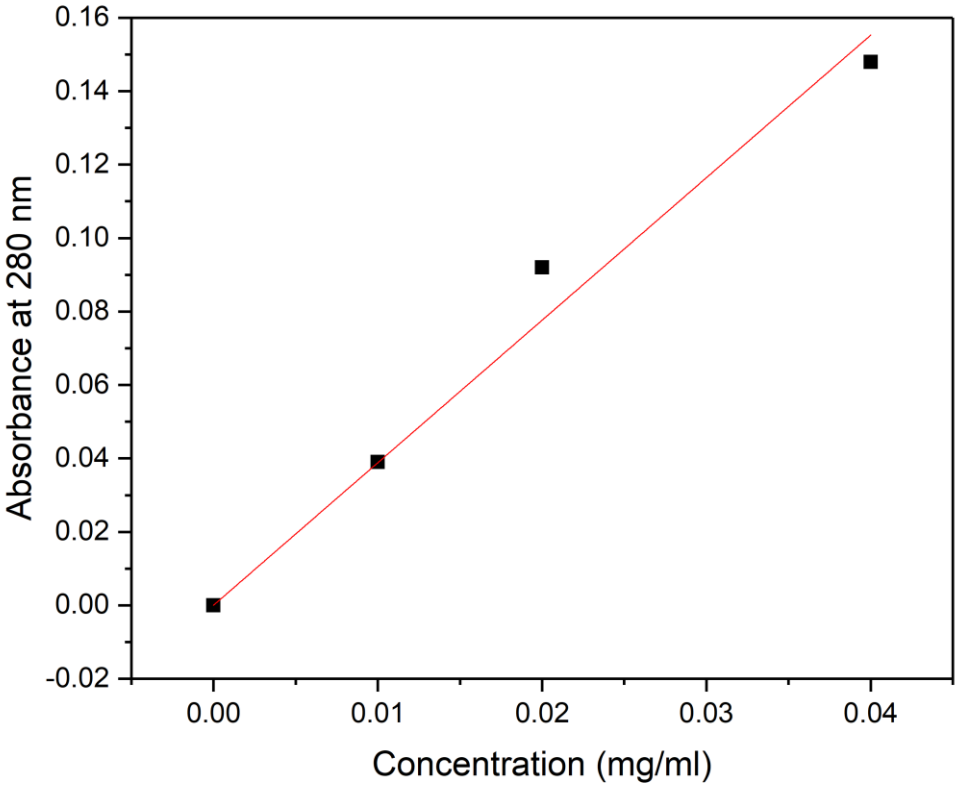

Figure C.39: Standard curve for Rapamycin measured at 280 nm.

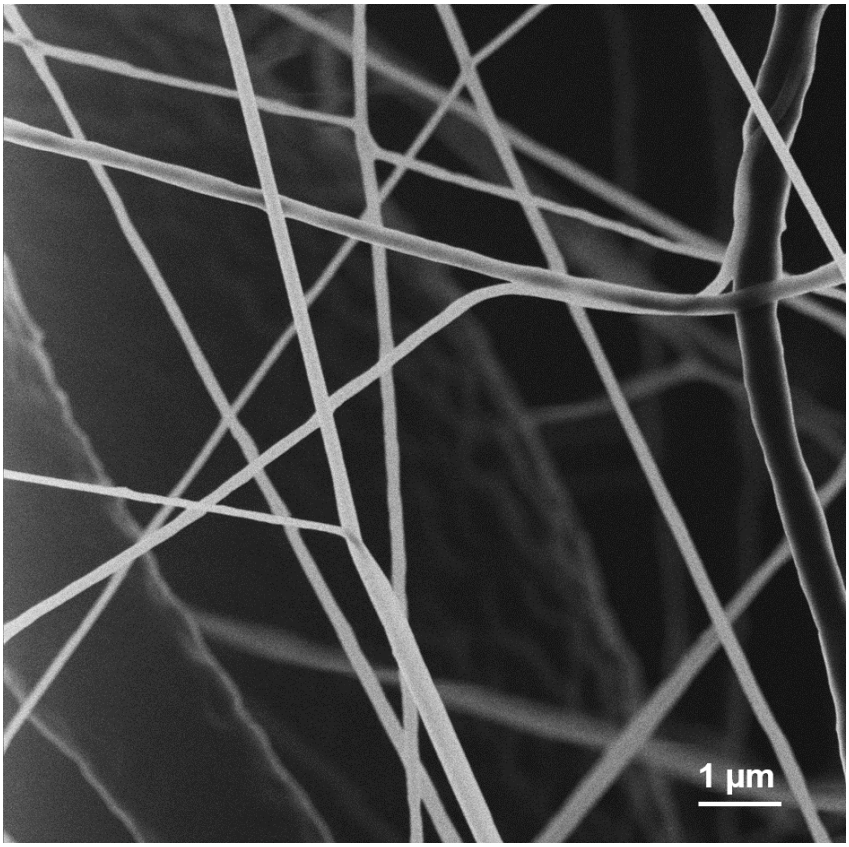

Figure C.40: Representative HIM image of electrospun PCL/rapamycin fibres. Scale bar corresponds to 1µm.

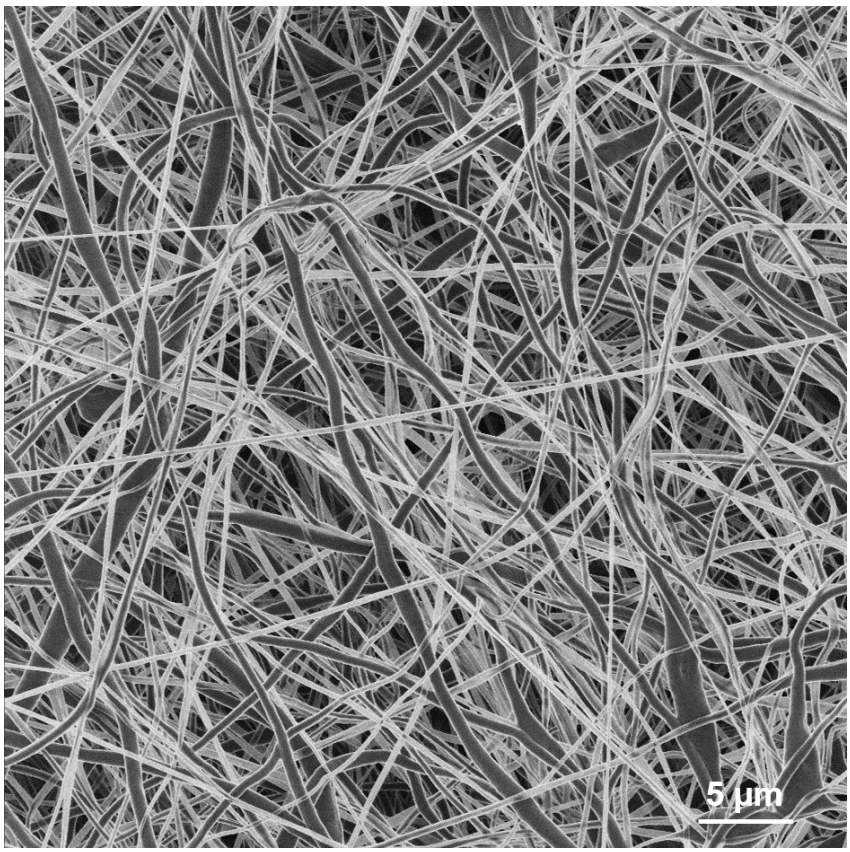

Figure C.41: Representative HIM image of electrospun PCL/rapamycin fibres. Scale bar corresponds to 5µm.